

**modern  
aspects  
of  
electrochemistry  
no. 34**

**Edited by J. O'M. BOCKRIS,  
B. E. CONWAY, and RALPH E. WHITE**

**MODERN ASPECTS OF  
ELECTROCHEMISTRY**

---

**No. 34**

# LIST OF CONTRIBUTORS

ZBIGNIEW KOCZOROWSKI

Department of Chemistry  
Warsaw University  
02-093 Warsaw, Poland

CLAUDE LAMY

Electrochimie et Interactions  
Université de Poitiers  
Poitiers, 86022 France

JEAN-MICHEL LÉGER

Electrochimie et Interactions  
Université de Poitiers  
Poitiers, 86022 France

BRENDA J. LITTLE

Department of Navy  
Naval Research Laboratory  
Stennis Space Center  
Mississippi 39529-5004

ISAO OKADA

Department of Chemistry  
Sophia University  
Tokyo 102-8554 Japan

MICHAEL SPIRO

Department of Chemistry  
Imperial College of Science, Technology &  
Medicine  
London SW72AY, United Kingdom

SUPRAMANIAN SRINIVASAN

Electrochimie et Interactions  
Université de Poitiers  
Poitiers, 86022 France

PATRICIA A. WAGNER

Department of Navy  
Naval Research Laboratory  
Stennis Space Center  
Mississippi 39529-5004

---

A Continuation Order Plan is available for this series. A continuation order will bring delivery of each new volume immediately upon publication. Volumes are billed only upon actual shipment. For further information please contact the publisher.

# **MODERN ASPECTS OF ELECTROCHEMISTRY**

---

**No. 34**

Edited by

**J. O'M. BOCKRIS**

*Molecular Green Technology  
College Station, Texas*

**B. E. CONWAY**

*University of Ottawa  
Ottawa, Ontario, Canada*

and

**RALPH E. WHITE**

*University of South Carolina, Columbia  
Columbia, South Carolina*

**Kluwer Academic Publishers**  
New York, Boston, Dordrecht, London, Moscow

eBook ISBN: 0-306-46923-5  
Print ISBN: 0-306-46462-4

©2002 Kluwer Academic Publishers  
New York, Boston, Dordrecht, London, Moscow

All rights reserved

No part of this eBook may be reproduced or transmitted in any form or by any means, electronic, mechanical, recording, or otherwise, without written consent from the Publisher

Created in the United States of America

Visit Kluwer Online at: <http://www.kluweronline.com>  
and Kluwer's eBookstore at: <http://www.ebooks.kluweronline.com>

## Preface

The current volume of this series continues to exhibit the main characteristic of the previous volumes: It covers the frontier in several widely differing sections of the huge area of modern electrochemistry.

Thus, the first chapter touches on an aspect of electrochemistry for which the author has become justly well known: application of the Wagner and Traud theorem of 1938 according to which electrochemical systems may function on a single electrode. In the next chapter, the article by Koczorowski treats a seldom-visited but truly fundamental area, that of voltaic measurements at liquid interfaces.

Chapter 3 is bound to attract the attention of the clean energy engineer because it concerns the ultimate fuel cell—one that uses the oxidation of an organic fuel directly without having to go through a reforming stage to produce the hydrogen fuel for the fuel cell. Success here would have a very significant effect upon the burgeoning enterprise of fuel cell-powered cars.

We are particularly pleased to welcome the article by Okada on dynamic processes in molten salts because it represents the culmination of the efforts of Professor Chemla at the Sorbonne to arrange such an article.

Finally, it is stimulating to read the article by Little and Wagner because of the prominence attached to microbial action in the electrochemistry of the 1990s and because it has hitherto been difficult to find an electrochemically oriented presentation of this topic.

J. O'M. Bockris

*Molecular Green Technology*  
*College Station, Texas*

B. E. Conway

*University of Ottawa*  
*Ottawa, Ontario, Canada*

Ralph E. White

*University of South Carolina*  
*Columbia, South Carolina*

*This page intentionally left blank.*

# Contents

## *Chapter 1*

### A CRITIQUE OF THE ADDITIVITY PRINCIPLE FOR MIXED COUPLES

Michael Spiro

I. Introduction . . . . .	1
II. The Additivity Principle . . . . .	1
III. Earlier Tests . . . . .	3
IV. Selected Corrosion and Electroless Plating Studies . . . . .	4
V. Heterogeneous Catalysis of Redox Reactions . . . . .	6
VI. Conclusions . . . . .	9
References . . . . .	11

## *Chapter 2*

### VOLTAIC CELLS IN ELECTROCHEMISTRY AND SURFACE CHEMISTRY OF LIQUIDS

Zbigniew Koczorowski

I. Introduction . . . . .	13
II. Electrified Interfaces and Their Electrical Potentials . . . . .	14
III. Volta Potential and Voltaic Cells . . . . .	16
IV. Experimental Methods for Investigating Voltaic Cells . . . . .	20
V. Volta Potential of the Metal/Solution Interface. . . . .	23
VI. Real Potentials of Ions in Electrolyte Solutions . . . . .	24
VII. Real Ion Activity. . . . .	26
VIII. Real Potentials of Ions in Solid Electrolytes . . . . .	27



IX. Voltaic Cells and Absolute Electrode Potentials . . . . .	29
X. Volta Potentials of <i>Ex Situ</i> and <i>Non-Situ</i> Electrodes . . . . .	31
XI. Voltaic Cells with Interfaces of Immiscible Electrolyte Solutions . . . . .	33
XII. Adsorption Potentials of Dipolar Compounds . . . . .	36
XIII. Adsorption Potentials of Surface-Active Electrolytes . . . . .	41
XIV. Adsorption Potentials of Inorganic Ions . . . . .	42
XV. Surface Potentials of Water and Organic Solvents . . . . .	43
XVI. Final Remarks . . . . .	48
References . . . . .	48

### Chapter 3

## DIRECT METHANOL FUEL CELLS: FROM A TWENTIETH CENTURY ELECTROCHEMIST'S DREAM TO A TWENTY-FIRST CENTURY EMERGING TECHNOLOGY

Claude Lamy, Jean-Michel Léger, and  
Supramaniam Srinivasan

I. A Synopsis of Fuel Cell Technologies—Background . . . . .	53
1. Energy Conservation and Environmental Friendliness— The Incentive for Fuel Cell Development . . . . .	53
2. Types of Fuel Cells . . . . .	54
3. Natural Gas—Its Important Role as a Primary Fuel for All Types of Fuel Cells . . . . .	55
4. Status of Fuel Cell Technologies . . . . .	57
5. Electrochemical vs. Other Methods of Energy Conversion . . . . .	62
II. Direct Methanol Fuel Cells . . . . .	65
1. Historical Development of DMFCs . . . . .	65
2. Principles of DMFCs . . . . .	67
3. Challenges in Developing DMFCs . . . . .	73
III. Electrode Kinetics and Electrocatalysis of Methanol Oxidation—Electrochemical and Spectroscopic Investigations . . . . .	73
1. Introduction . . . . .	73

2. Identification of the Reaction Products and the Adsorbed Intermediates . . . . .	75
3. How to Increase the Kinetics of the Electrooxidation of Methanol . . . . .	82
4. Structure and Composition of the Electrode in Relation to its Electroactivity . . . . .	83
5. Concluding Remarks on Mechanisms . . . . .	92
IV. Oxygen Electroreduction and Proton Exchange Membrane . . . . .	93
1. The Oxygen Electroreduction Reaction . . . . .	93
2. Concepts for New Oxygen Reduction Electrocatalysts . . . . .	96
3. Development of New Proton Exchange Membranes . . . . .	99
V. Progress in Technology . . . . .	100
1. Single-cell Investigations to Attain High Performance Levels . . . . .	100
2. Cell Stack Development and Demonstration . . . . .	111
VI. Prognosis—DMFCs for the 21st Century . . . . .	113
References . . . . .	115

## Chapter 4

### TRANSPORT PROPERTIES OF MOLTEN SALTS

Isao Okada

I. Introduction . . . . .	119
II. Database . . . . .	121
III. Electrical Conductance . . . . .	124
1. Electrolytic Conductivity . . . . .	124
2. Methods of Measuring Transport Numbers in Mixtures . . . . .	125
3. Pattern of the Isotherms in Binary Monovalent Cation Systems . . . . .	127
4. The Chemla Effect . . . . .	129
5. Empirical Equation for Internal Mobility . . . . .	131
6. Electrically Conducting Species . . . . .	146
7. Molecular Dynamics Simulation . . . . .	149
IV. Diffusion . . . . .	154
1. Macroscopic Description . . . . .	154
2. Measurement Methods . . . . .	157

3. Molecular Dynamics Simulation . . . . .	165
V. Viscosity . . . . .	167
1. Measurement Methods . . . . .	168
2. Bulk Viscosity . . . . .	174
3. Recommended Values . . . . .	176
4. Factors Determining Viscosity . . . . .	177
5. Molecular Dynamics Simulation . . . . .	180
VI. Thermal Conductivity . . . . .	182
1. Measurement Methods . . . . .	184
2. Evaluation of Experimental Data . . . . .	192
3. Molecular Dynamics Simulation . . . . .	195
VII. Conclusion . . . . .	196
References . . . . .	197

## Chapter 5

### APPLICATION OF ELECTROCHEMICAL TECHNIQUES TO THE STUDY OF MICROBIOLOGICALLY INFLUENCED CORROSION

Brenda J. Little and Patricia A. Wagner

I. Introduction . . . . .	205
1. Biofilm Formation. . . . .	205
2. MIC Mechanisms . . . . .	207
II. Techniques . . . . .	208
1. Redox Potential . . . . .	208
2. Polarization Resistance . . . . .	209
3. Open Circuit Potential . . . . .	213
4. Capacitance . . . . .	216
5. Microsensors . . . . .	223
6. Dual-Cell Technique . . . . .	226
7. Electrochemical Noise Analysis. . . . .	227
8. Electrochemical Impedance Spectroscopy. . . . .	233
9. Scanning Vibrating Electrode Techniques . . . . .	240
10. Large Signal Polarization Techniques . . . . .	240
III. Conclusions . . . . .	244
References . . . . .	245

<b>Contents</b>	<b>xi</b>
<i>Cumulative Author Index</i> .....	247
<i>Cumulative Title Index</i> .....	261
<i>Subject Index</i> .....	273

*This page intentionally left blank.*

# A Critique of the Additivity Principle for Mixed Couples

Michael Spiro

*Department of Chemistry, Imperial College of Science, Technology and Medicine,  
London SW7 2AY United Kingdom*

## I. INTRODUCTION

Wagner and Traud, in their seminal paper in 1938,<sup>1</sup> clearly enunciated the principle of adding current-potential curves when two (or more) couples are present together. Since then the additivity principle, sometimes called the *superposition or mixed potential theory*, has been applied throughout electrochemistry and has often been accepted almost as an article of faith. It has proved to be of particular importance in understanding such industrial processes as corrosion, mineral extraction, froth flotation, electroless plating, and photographic development.<sup>2</sup> It is surprising, then, that few unambiguous tests of the validity of the additivity principle have been available until recently. Evidence obtained in the past few years has now revealed cases in which previously unsuspected interactions occur between the couples or with the electrode. This evidence, described below, has now led to a reformulation of the additivity principle that extends its validity.

## II. THE ADDITIVITY PRINCIPLE

An electrode in a system containing two couples automatically adopts a mixed potential (or more correctly, a mixture potential)  $E_{\text{mix}}$ . At this

*Modern Aspects of Electrochemistry, Number 34*, edited by John O'M. Bockris *et al.*  
Kluwer Academic / Plenum Publishers, New York, 2001.

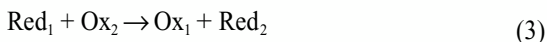
potential it acts simultaneously as an anode for the couple of lower Nernst potential



and as a cathode for the couple of higher Nernst potential



The anodic current due to couple 1 ( $I_{\text{mix}}$ ) and the cathodic current due to couple 2 ( $-I_{\text{mix}}$ ) exactly balance at  $E_{\text{mix}}$ , as illustrated in Fig.1. Each of these mixture currents also represents the rate  $\nu$  at which the reaction between the couples



takes place at the electrode surface, since by Faraday's law

$$\nu_{\text{mix}} = I_{\text{mix}}/F \quad (4)$$

Provided the additivity principle holds, the catalytic rate  $\nu_{\text{cat}}$  of reaction (3) at the surface should therefore be the same as the value  $\nu_{\text{mix}}$  predicted from the current-potential curves of the couples involved. Moreover, the measured potential  $E_{\text{cat}}$  of the catalyzed mixture should be

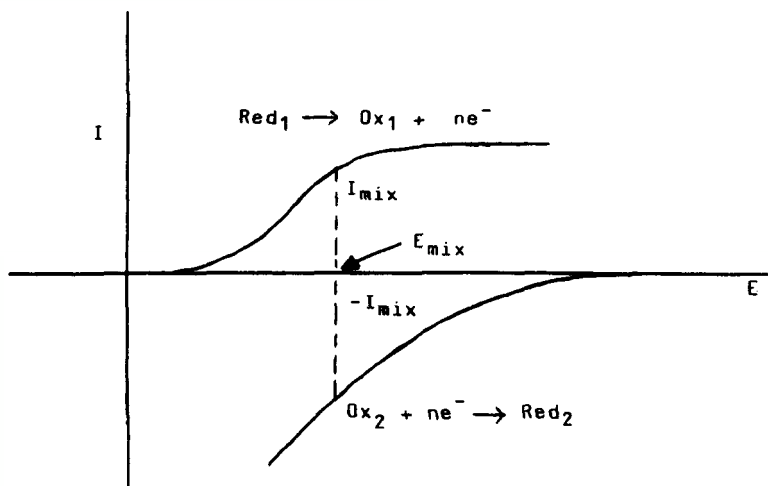


Figure 1. Schematic representation of two redox couples present at the same electrode.

the same as the value of  $E_{\text{mix}}$  obtained from adding the current-potential curves. However, it can be seen that the additivity principle, as normally applied, is actually a combination of two distinct premises<sup>3</sup>:

1. Each couple present is assumed to act independently so that its current-potential curve is unaffected by the presence of the other couple.
2. At any given potential, the observed current is assumed to equal the algebraic sum of the currents exhibited by each of the couples present. In particular, at  $E_{\text{mix}}$  the algebraic current sum is zero.

This distinction will be seen to be important in the following sections.

### III. EARLIER TESTS

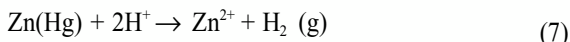
The main system chosen by Wagner and Traud themselves was the corrosion of zinc amalgam in aqueous HCl. They measured the current-potential curves of



in acetate buffer to avoid hydrogen evolution, and



in aqueous HCl at a mercury electrode to avoid zinc dissolution. On the assumption of the additivity of the curves of (5) and (6) in the mixture situation, they determined  $I_{\text{mix}}$  and hence by equation (4) predicted the rate of hydrogen evolution from the reaction



in aqueous HCl. The predicted rate agreed well with the experimentally measured rate of hydrogen evolution over a range of experimental conditions.

Despite the good agreement, there are two reasons why this test was flawed.<sup>4</sup> First, the anodic half-reaction (5) had of necessity to be carried out at a higher pH, and thus in a different medium from the overall reaction (7). Second, and even more important, the electrode surface in the cathodic half-reaction (6) was not the same as the amalgam surface in reaction (7). Hydrogen evolution could be affected by the presence of zinc sites on the



mercury surface since the exchange current density of the hydrogen couple is known to be larger on a zinc electrode than on one of mercury.<sup>5</sup>

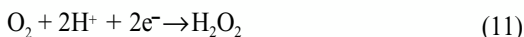
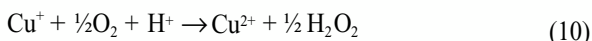
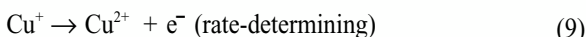
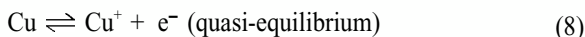
Several groups of workers in the literature have since tested the additivity principle. In most cases it, or corollaries based on it, were found to hold within the uncertainties of measurement. Modern texts on corrosion<sup>6,7</sup> take the additivity principle for granted throughout, while a recent compilation on electroless plating<sup>8,9</sup> cites various literature tests in this area, not all of them favorable. It is precisely in corrosion and in electroless plating that most doubt arises about the validity of the test. To be certain of the significance of the results, it is essential that each process be carried out on the same surface. But as shown for the zinc corrosion example, this cannot be done directly for one of the partial reactions: the reduction of the oxidant in corrosion or the oxidation of the reducing agent in electroless plating. Attempts to obtain the electrochemical information indirectly by studying the polarization curves over a much lower or much higher potential range, respectively, and extrapolating the current to the corrosion or plating potential, are not valid if the rate-determining step (and hence the Tafel slope) changes over the extrapolated section. They are also not valid if the catalytic properties of the surface change with potential over the region concerned.<sup>10</sup> Moreover, in both corrosion and plating the surface is continuously being regenerated, a point rarely taken into account.<sup>11</sup> In spite of these limitations, however, a small number of careful studies has shown clearly that the two partial reactions in corrosion or electroless plating are not always independent of each other. The main evidence from two major studies is summarized below.

#### IV. SELECTED CORROSION AND ELECTROLESS PLATING STUDIES

Andersen et al.<sup>10</sup> carried out a detailed investigation of the corrosion of copper in stirred oxygenated  $\text{H}_2\text{SO}_4$  solution at 25 °C. The stable corrosion products, at times up to 40 hr, were found to be equimolar amounts of  $\text{Cu}^{2+}$  ions and  $\text{H}_2\text{O}_2$ . The rates of copper oxidation at various potentials were determined by two independent methods: weight loss and polarization curves. The results of these two types of measurement agreed moderately well with  $\text{N}_2$ -saturated solutions whereas in  $\text{O}_2$ -saturated solutions the copper weight loss was always substantially larger than that derived from the current-potential curve and Faraday's law. Furthermore, the weight loss at the corrosion potential  $E_{\text{corr}}$  in oxygenated solutions was some ten

times larger than the value obtained from the anodic polarization curve for copper under nitrogen. These results are quite contrary to those expected from the additivity principle.

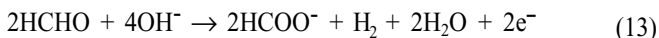
To explain their findings, the authors proposed the following mechanism:



For the additivity principle to hold, steps (8) and (9), the anodic processes taking place under nitrogen, would be coupled only with the cathodic reduction of oxygen in step (11). It is step (10), the attack by the constituents of the oxygen couple on the intermediate  $\text{Cu}^+$ , which lies outside the scope of the principle and which explains the observed findings.

Andersen et al. predicted that similar results would be expected for the corrosion of other multivalent metals oxidizing via lower oxidation states. They also pointed out that their interpretation was consistent with the kinetics of the corrosion of copper in oxygenated HCl solutions. Here the final product is  $\text{Cu}^+$  and thus there is no vulnerable intermediate. In consequence, the rate of copper dissolution from either  $\text{N}_2$ -saturated or  $\text{O}_2$ -saturated HCl solutions was the same at a given potential<sup>12</sup> in conformity with the additivity principle.

More recently, Wiese and Weil<sup>11</sup> reported a detailed study of the mechanism of electroless copper deposition with formaldehyde from alkaline ethylenediamine-tetraacetate (EDTA)-containing solutions. The partial reactions were expected to be



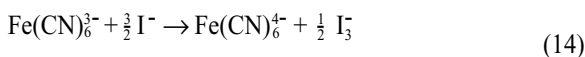
The hydrogen gas was later<sup>13</sup> shown to originate from the formaldehyde, not the water. Instead of cumbersome and slow *ex situ* weighing, Wiese and Weil measured the plating rate *in situ* with a quartz microbalance. They connected the electrode to a potentiostat to keep it at the plating

potential, and then rapidly replaced the plating mixture with a solution in which either cupric ions or formaldehyde was missing. If the additivity theory was correct, they reasoned, the current after such an exchange should be equivalent to the plating rate before the exchange and moreover this current should be constant with time. What they found was that on rapid removal of  $\text{Cu}^{2+}$  from the solution, the resulting formaldehyde oxidation current was indeed equal to the current corresponding to the plating rate. This proved that there was no non-electrochemical electron transfer to cupric ions. However, the formaldehyde current decreased gradually with time because copper ion reduction had activated the surface for HCHO oxidation.

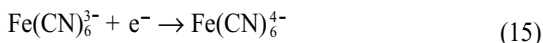
A more dramatic change occurred when the plating solution was rapidly replaced by a copper solution without formaldehyde: here the cupric ion reduction current quickly plummeted by an order of magnitude from the current equivalent to the plating rate. This was completely contrary to the prediction of the additivity theory. The authors concluded from this and other experiments that a catalytic organic species had been chemisorbed on the copper surface, and the pH dependence pointed to the active species being methanediolate,  $\text{H}_2\text{CO}(\text{OH})^-$ . Several other substances with a similar structure, or ones known to absorb specifically on copper, were also found to catalyze  $\text{Cu}^{2+}$  reduction from alkaline EDTA solutions. Thus the partial reactions (12) and (13) were not independent of each other as the principle demanded; indeed, the rate of one was increased by the other.

## V. HETEROGENEOUS CATALYSIS OF REDOX REACTIONS

The underlying problem in testing the validity of the additivity principle in corrosion, mineral extraction, and electroless plating is that the electrode metal itself forms part of one of the half-reactions involved, e.g., zinc in equation (5) and copper in equations (8) and (12). A much better test system is provided by the interaction of two couples at an inert metal electrode that does not form a chemical part of either couple.<sup>3,4</sup> A good example is the heterogeneous catalysis by platinum or a similar inert metal of the reaction



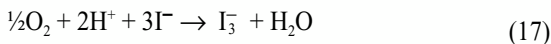
arising from the interaction between the couples



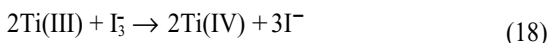
In such systems the researcher can electrochemically clean and precondition the metal electrode before each run to provide an identical surface for the anodic and the cathodic half-reactions as well as for the catalytic reaction between them. Use of a rotating disk electrode/catalyst also allows surface- and diffusion-controlled processes to be easily distinguished.<sup>14</sup>

Experiments by Freund and Spiro,<sup>4,15</sup> with the ferricyanide-iodide system showed that the additivity principle held within experimental error for both the catalytic rate and potential when the platinum disk had been anodically preconditioned, but not when it had been preconditioned cathodically. In the latter case the catalytic rate was *ca* 25% less than the value predicted from adding the current-potential curves of reactions (15) and (16). This difference in behavior was traced to the fact that iodide ions chemisorb only on reduced platinum surfaces. Small amounts of adsorbed iodide were found to decrease the currents of cathodic  $\text{Fe(CN)}_6^{3-}$  voltammograms over a wide potential range. The presence of the iodine couple (16) therefore affected the electrochemical behavior of the hexacyanoferrate (II, III) couple (15).

Iodide adsorbed on reduced platinum surfaces was found to affect several other systems. The most dramatic effect was shown when the couples  $\text{I}_2/\text{I}^-$  and  $\text{O}_2/\text{H}_2\text{O}$  were considered together. Addition of the current-potential curves of these two couples indicated that platinum should significantly catalyze the reaction



However, no such catalysis was detected.<sup>3</sup> The reason was that even very small amounts of iodide adsorbed on the platinum electrode strongly inhibited the electrochemical reduction of oxygen. A less dramatic but more instructive example was provided by Xiao and Spiro's study<sup>16</sup> of the reaction



catalyzed on a reduced platinum disk. As long as the anodic current-potential curve for Ti(III) as well as the cathodic curve for  $\text{I}_3^-$  had been carried

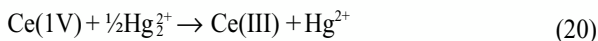
out in the same medium containing not only 0.1 M ( $M = \text{mol dm}^{-3}$ ) HCl + 0.8 M KCl but also 0.1 M KI, the additivity principle held very well for both the catalytic rate and potential. However, when the anodic Ti(III) curve had been determined in a medium without KI,  $v_{\text{mix}}$  was much greater than  $v_{\text{cat}}$  while  $E_{\text{mix}}$  was much less than  $E_{\text{cat}}$ . This illustrated once again that the adsorbed iodide, which was part of one of the couples, strongly influenced the electrochemical behavior of the other couple. The results also demonstrated that the current-potential curves *were* additive provided they had been obtained under the same conditions.

In contrast, the rate of the platinum-catalyzed reaction



was found by Creeth and Spiro<sup>3</sup> to be greater than expected from adding the current-potential curves of the reduction of  $\text{Fe}^{3+}$  and the oxidation of  $\text{I}^-$ . Once again adsorption of iodide on the reduced platinum surface was identified as the culprit. When a very small concentration of iodide ions had been added to the  $\text{Fe}^{3+}$  solution, the currents in the cathodic  $\text{Fe}^{3+}$  voltammogram became significantly larger. Superposition of this curve with the anodic voltammogram for  $\text{I}^-$  then yielded values for  $v_{\text{mix}}$  and  $E_{\text{mix}}$  that were in good agreement with  $v_{\text{cat}}$  and  $E_{\text{cat}}$ , respectively. These results, too, confirmed the additivity postulate underlying the Wagner and Traud principle, but again did not bear out the premise that the couples acted completely independently.

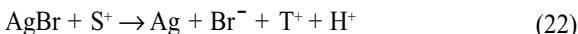
Some other types of interaction were reported by Garnica Meza and Spiro<sup>17</sup> in their study of the platinum-catalyzed reaction



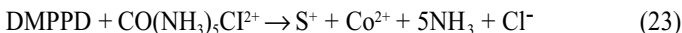
The additivity principle was well obeyed on adding the voltammograms of the two redox couples involved even though the initially reduced platinum surface had become covered by a small number of underpotential-deposited mercury monolayers. With an initially anodized platinum disk the catalytic rates were much smaller, although the decrease was less if the  $\text{Hg(I)}$  solution had been added to the reaction vessel before the  $\text{Ce(IV)}$  solution. The reason was partial reduction by  $\text{Hg(I)}$  of the oxide/hydroxide layer, so partly converting the surface to the reduced state on which catalysis was greater.

An industrial application is provided by a reaction important in photographic processing. On exposure to light, the silver halide in photo-

graphic film forms tiny silver specks called the *latent image*. These need to be greatly intensified by adding a developing agent such as *N,N*-dimethyl-*p*-phenylenediamine (DMPPD):



where  $\text{S}^+$  is the corresponding *p*-semiquinonediimine and  $\text{T}^+$  is the *p*-quinonediimine.<sup>14</sup> For color photography,  $\text{T}^+$  couples with certain organic compounds incorporated into the film to produce colored dyes. The dye intensity can be enhanced by forming more  $\text{S}^+$ , and then more  $\text{T}^+$  through the reaction



All these redox processes [(21)–(23)] are heterogeneously catalyzed by particles of silver.<sup>18</sup> To test the electrochemical model of the catalysis, Farchmin, Nickel, and Spiro<sup>19</sup> measured the rate of reaction (23), as well as the voltammograms of the couples involved, on rotating disks of silver, gold, and platinum. On the silver surface, the values of  $v_{\text{mix}}$  and  $E_{\text{mix}}$  obtained from the anodic current-potential curve of DMPPD and the cathodic curve for  $\text{CO}(\text{NH}_3)_5\text{Cl}_2^+$  agreed well with the values of  $v_{\text{cat}}$  and  $E_{\text{cat}}$  found directly from reaction (23). On gold and platinum surfaces, on the other hand,  $v_{\text{cat}}$  was much less than  $v_{\text{mix}}$ . This was shown to be due to adsorption of DMPPD on these metal surfaces, which decreased the cathodic current for the reduction of  $\text{Co}(\text{NH}_3)_5\text{Cl}_2^+$ . To allow for this effect, cathodic curves for  $\text{CO}(\text{NH}_3)_5\text{Cl}_2^+$  were measured in the presence of micromolar amounts of DMPPD. When these new curves were then combined with the anodic DMPPD curves, good agreement was obtained for both rates and potentials. Thus the additivity premise held, provided the interaction between the couples had been allowed for by superimposing only curves determined under circumstances that corresponded to those in the reaction mixture.

## VI. CONCLUSIONS

Although the original additivity principle of Wagner and Traud has been an immensely useful concept with applications in numerous fields,<sup>2</sup> carefully designed studies in recent years have revealed a number of exceptions. These have been described above and are summarized in

Table 1. The reasons for the apparent breakdown of the original principle have included chemical interaction between one couple and an intermediate species of the other, changes produced in the structure of the electrode surface and, most common of all, adsorption on the surface of a component of one couple that affected the electrode kinetics of the other. The underlying problem in these cases has been the untenable premise that each couple acts quite independently of the other and is not affected by the other's presence. However, as many of these studies have shown, the premise of additivity still applies whenever the interactions have been allowed for by carrying out the electrochemical experiments in an appropriate fashion. The validity of adding or superimposing electrochemical curves can therefore be considerably extended by restating the principle as follows:

**Table 1**  
**Summary of Recent Research to Test the Validity of the Wagner and Traud Additivity Principle**

Oxidant couple	Reductant couple	Electrode	$v_{\text{exp}}/v_{\text{mix}}$	Ref.
$\text{O}_2/\text{H}_2\text{O}_2$	$\text{Cu}/\text{Cu}^{2+}$	Corroding Cu	>1	10
$\text{Cu}(\text{EDTA})^{2-}/\text{Cu}$	$\text{HCHO}/\text{COO}^-$	Plating Cu	>1	11
$\text{Fe}(\text{CN})_6^{3-}/\text{Fe}(\text{CN})_6^{4-}$	$\text{I}^-/\text{I}_3^-$	Anodized Pt	1	4
		Reduced Pt	<1	4
$\text{Fe}^{3+}/\text{Fe}^{2+}$	$\text{I}^-/\text{I}_3^-$	Reduced Pt	>1	3
		Reduced Pt <sup>b</sup>	1	3
$\text{O}_2/\text{H}_2\text{O}$	$\text{I}^-/\text{I}_2$	Reduced Pt	0	3
		Reduced Pt <sup>b</sup>	(1)	3
$\text{I}_3^-/\text{I}^-$	$\text{Ti(III)}/\text{Ti(IV)}$	Reduced Pt	<1	16
		Reduced Pt <sup>b</sup>	1	16
$\text{Ce(IV)}/\text{Ce(III)}$	$\text{Hg}_2^{2+}/\text{Hg}^{2+}$	Reduced Pt	1	17
		Anodized Pt	<1	17
$\text{CO}(\text{NH}_3)_5\text{Cl}^{2+}/\text{Co}^{2+}$	DMPPD/ $\text{S}^+$	Ag	1	19
		Reduced Au or Pt	<1	19
		Reduced Au <sup>c</sup> or Pt <sup>c</sup>	1	19

<sup>a</sup> $v_{\text{exp}}$  equals  $v_{\text{corr}}$ ,  $v_{\text{plat}}$  or  $v_{\text{cat}}$ , depending on the reaction studied.

<sup>b</sup>With the addition of a small concentration of iodide to the noniodine couple.

<sup>c</sup>With the addition of a small concentration of DMPPD to the cobalt couple,

*The current-potential curve of a mixture of couples can be obtained by adding algebraically, at any potential, the currents given by each of the couples present, provided these have been determined in circumstances that correspond to those in the mixture.*

## REFERENCES

- <sup>1</sup>C. Wagner and W. Traud, *Z. Elektrochem.* **44** (1938) 391.
- <sup>2</sup>M. Spiro, *Chem. Soc. Rev.* **15** (1986) 141 and references therein.
- <sup>3</sup>A. M. Creeth and M. Spiro, *J. Electroanal. Chem.* **312** (1991) 165.
- <sup>4</sup>M. Spiro and P. L. Freund, *J. Electroanal. Chem.* **144** (1983) 293.
- <sup>5</sup>S. Trasatti, *J. Electroanal. Chem.* **39** (1972) 163.
- <sup>6</sup>H. H. Uhlig and R.W. Revie, *Corrosion and Corrosion Control*, 3rd ed., Wiley, New York, 1985.
- <sup>7</sup>L. L. Shreir, R. A. Jarman, and G. T. Burstein, eds., *Corrosion*, Vols. I and 2, 3rd ed., Butterworth-Heinemann, Oxford, 1994.
- <sup>8</sup>G. O. Mallory, in *Electroless Plating: Fundamentals and Applications*, Ed. by G. O. Mallory and J. B. Hajdu, American Electroplaters and Surface Finishers Society, Orlando, FL, 1990, p. 1.
- <sup>9</sup>P. Bindra and J. R. White, in *Electroless Plating: Fundamentals and Applications*, Ed. by G. O. Mallory and J. B. Hajdu, American Electroplaters and Surface Finishers Society, Orlando, FL, 1990, p. 289.
- <sup>10</sup>T. N. Andersen, M. H. Ghandebari, and H. Eyring, *J. Electrochem. Soc.* **122** (1975) 1580.
- <sup>11</sup>H. Wiese and K. G. Weil, *Ber. Bunsenges.* **91** (1987) 619.
- <sup>12</sup>B. Miller and M. I. Bellavance, *J. Electrochem. Soc.* **119** (1972) 1510.
- <sup>13</sup>Z. Jusys and A. Vaskelis, *Langmuir* **8** (1992) 1230.
- <sup>14</sup>M. Spiro, *Catalysis Today* **17** (1993) 517.
- <sup>15</sup>P. L. Freund and M. Spiro, *J. Chem. Soc. Faraday Trans. 1* **79** (1983) 491.
- <sup>16</sup>S. Xiao and M. Spiro, *J. Chem. Soc. Faraday Trans.* **90** (1994) 1983.
- <sup>17</sup>J. M. GamicaMeza and M. Spiro, *J. Chem. Soc. Faraday Trans.* **87** (1991) 1383.
- <sup>18</sup>U. Nickel and C.-Y. Liu, *J. Imaging Sci.* **34** (1990) 8.
- <sup>19</sup>R. O. Farchmin, U. Nickel, and M. Spiro, *J. Chem. Soc. Faraday Trans.* **89** (1993) 229.



*This page intentionally left blank.*

# Voltaic Cells in Electrochemistry and Surface Chemistry of Liquids

Zbigniew Koczorowski

*Department of Chemistry, University of Warsaw, ul.Pasteura I, 02-093 Warsaw Poland*

## I. INTRODUCTION

The Volta potential is defined as the difference between the electrostatic outer potentials of two condensed phases in equilibrium. The measurement of this and related quantities is performed using a system of voltaic cells. This technique, which in some applications is called the *surface potential method*, is one of the oldest but still frequently used experimental methods for studying phenomena at electrified solid and liquid surfaces and interfaces. The difficulty with the method, which in fact is common to most electrochemical methods, is lack of molecular specificity. However, combined with modern surface-sensitive methods such as spectroscopy, it can provide important physicochemical information. Even without such complementary molecular information, the voltaic cell method is still the source of much basic electrochemical data.

The aim of this review is to describe the fundamentals of the voltaic cell method and to outline its applications in electrochemistry. Only fragmentary information concerning this topic is available in books and articles.<sup>1-19</sup>

This review is arranged as follows. After a short review of the basic definitions and significance of the various potentials which are assumed to exist at free surfaces and interfaces, the nature and most important features of voltaic cells, including their measurement techniques, are

*Modern Aspects of Electrochemistry, Number 34*, edited by John O'M. Bockris *et al.*  
Kluwer Academic /Plenum Publishers, New York, 2001.

discussed. This is followed by a review of the use of voltaic cells to determine the real potentials of ions in liquid and solid systems; the Volta potentials of *in situ*, *ex situ*, and *non situ* electrodes and their importance in determining absolute electrode potential; and the Volta potentials of liquid-liquid systems. Finally, the surface potential change upon adsorption of various species and the surface potentials of pure solvents are discussed.

In addition, this review has been prepared to promote the term "voltaic cell" in honor of Alessandro Volta, the inventor of "the pile," i.e., an electrochemical generator of electricity. Up to now this name has been used in only a few papers.<sup>19-21</sup> This term is a logical analogue to the term "galvanic cell," particularly in discussions of "Volta potential" and "Galvani potential" concepts.

## II. ELECTRIFIED INTERFACES AND THEIR ELECTRICAL POTENTIALS

An electric potential drop across the boundary between two dissimilar phases as well as at their surfaces exposed to a neutral gas phase is the most characteristic feature of every interface and surface electrified due to ion separation and dipole orientation. This charge separation is usually described as an ionic double layer.

The system of distinctions and terminology of the thermodynamic and electric potentials introduced by Lange is still very useful and recommended for describing all electrified phases and interphases.<sup>1,13,22,23</sup> Therefore these potentials can be assigned to metal/solution (M/s), as well as the liquid/liquid boundaries<sup>15,16,24</sup> created at the interfaces of two immiscible electrolyte solutions: water (w) and an organic solvent (s).

The Volta potential,  $\Delta_S^M \Psi$ , very often called the *contact potential*, is the difference between the outer potentials of the phases, which are in electrochemical equilibrium in regard to the charged species, i.e., ions or electrons. Each two-phase electrochemical system, including a w/s system, may be characterized by the commonly known relation:

$$\Delta_S^M \Psi = -z_i F (\alpha_i^M - \alpha_i^s) \quad (1)$$

where  $\alpha_i^M$  and  $\alpha_i^s$  as are the real potentials of the charged species *i*, defined as the sum of its chemical potential and the electrical term containing the surface potential of the phase; e.g., for the solution:

$$\alpha_i^s = \mu_i^s + z_i F \chi^s \quad (2)$$

Relationships (1) and (2) together with

$$\Delta_S^M \Psi = \Delta_S^M \phi - \Delta_S^M \chi \quad (3)$$

where  $\Delta_S^M \phi$  is the difference in the inner potentials (i.e., the Galvani potential of a two-phase system), make it possible to find some important electrochemical information. This system, as illustrated in Fig. 1, is actually a three-phase system, since it includes the inert gas atmosphere of the environment.

The Volta potential, in contradiction to the Galvani potential, has the advantage of being measurable but also the disadvantage that it is not determined only by the chemical nature of the phases that create the interface, but also by the state at their surfaces, represented by the surface potentials, Eqs. (1) and (2).

In principle, the distribution of ions and dipoles at the M/s interface is different from that at the free M and s surfaces. Therefore the Galvani potential may also be written, in the absence of specific adsorption, as the sum of the charge and dipole components<sup>1,13,22,23</sup>

$$\Delta_S^M \phi = g_S^M(\text{ion}) + g_S^M(\text{dip}) \quad (4)$$

Usually  $g_S^M(\text{ion}) \neq \Delta_S^M \Psi$  and  $g_S^M(\text{dip}) \neq \Delta_S^M \chi$ . It appears that under accessible experimental conditions there is little or no dependence of  $\chi$  on  $\Psi$ , i.e., the surface potential is independent of the free charge of the phase,<sup>25</sup> but

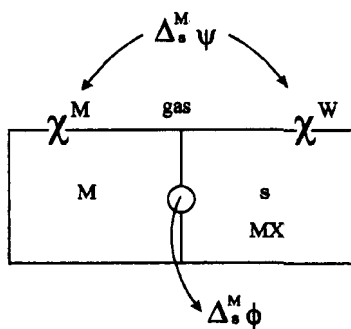


Figure 1. The electric potentials assumed to exist in a metal-electrolyte solution system.

the dependence of the dipole component of the Galvani potential at the metal/solution interface on the variation in charge [i.e.,  $g_s^M$  (ion) potential] is often observed experimentally.<sup>1,13,22,23</sup>

The common example of real potential is the electronic work function of the condensed phase  $x$ ,  $\phi_e^x$ , which is a negative value of  $\alpha_e^x$ . This term, which is usually used for electrons in metals and semiconductors, is defined as the work of electron transfer from the condensed phase  $x$  to a point in a vacuum in close proximity to the surface of the phase, but beyond the action range of purely surface forces, including image interactions. This point just outside of the phase is about 1  $\mu\text{m}$  in a vacuum. In other dielectric media, it is nearer to the phase by  $\epsilon$  times, where  $\epsilon$  is the dielectric constant.

A general discussion and attempts to clarify the definitions of electrochemical potential in light of recent theoretical results,<sup>26</sup> as well as the surface and Volta potentials<sup>27</sup> have been presented recently.

The surface potential of a liquid solvent  $s$ ,  $\chi^s$ , is defined as the difference in electrical potentials across the interface between this solvent and the gas phase, with the assumption that the outer potential of the solvent is zero. The potential  $\chi^s$  arises from a preferred orientation of the solvent dipoles in the free surface zone. At the surface of the solution, the electric field responsible for the surface potential may arise from a preferred orientation of the solvent and solute dipoles, and from the ionic double layer. The potential  $\chi^s$ , as the difference in electrical potential across the interface between the phase and gas, is not measurable. However, the relative changes caused by the change in the solution's composition can be determined using the proper voltaic cells (see Sections XII-XV).

### III. VOLTA POTENTIAL AND VOLTAIC CELLS

Volta potentials are measured by means of voltaic cells, i.e., systems composed of conducting, condensed phases in series, with a gas, liquid dielectric (e.g., decane) or a vacuum (in the case of solid conductors such as metals) gap situated between two condensed phases. The gap,  $g$ , may contain a gas such as pure air or nitrogen, saturated with vapors of the liquids present. Owing to the presence of a dielectric, special methods are necessary for the investigation of voltaic cells (see Section IV).

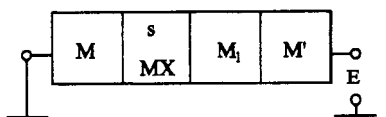
In the schemes shown in this chapter a single vertical bar (|) is used to represent a metal/metal-, metal/gas, metal/solutio/gas phase boundary,

while a dashed vertical bar ( : ) represents a junction between liquids. A double, dashed vertical bar ( :: ) represents a liquid junction in which the diffusion potential has been assumed to be eliminated.

The basic principle of every measurement of the Volta potential and generally of the investigations of voltaic cells too, in contrast to galvanic cells, may thus be presented for systems containing metal/solution (Fig. 2) and liquid/liquid interfaces (Fig. 3), respectively. This interface is created at the contact of aqueous and organic solutions (w and s, respectively) of electrolyte MX in the partition equilibrium.<sup>53,19</sup> Of course, electrolyte MX, shown in Fig. 2 and other figures of this chapter, may be different in organic (s) and aqueous (w) phases.

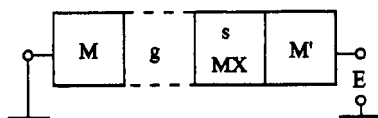
The compensating voltage,  $E$ , from a potentiometer is adjusted until the electric field strength in the gas space between the two condensed phases is zero. This state means that the Volta potential is zero, and simultaneously that the compensating voltage equals the sum of all Galvani potentials existing in the system (as is also true for every galvanic cell) plus the difference in surface potentials (instead of Galvani potential) between the conducting phases that contact the gas space. The use of two identical reference electrodes and the elimination of the liquid junction potentials by proper salt bridges (||) removes their contributions to the

### Galvanic cell



$$E = \Delta_{M'}^M \phi = \Delta_{M_1}^M \phi + \Delta_s^M \phi - \Delta_s^M \phi$$

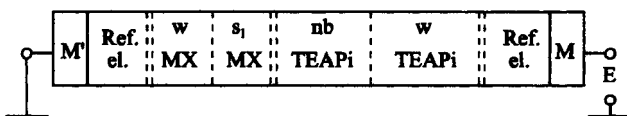
### Voltaic cell



$$E = \Delta_{M'}^M \phi = \Delta_s^M \phi + \chi^s - \chi^M = \Delta_s^M \psi$$

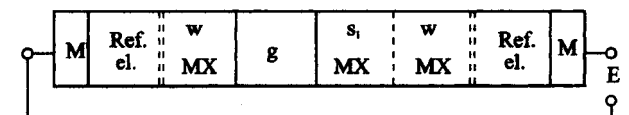
Figure 2. Comparison of galvanic and voltaic cells with metal/solution interfaces.

## Galvanic cell



$$E = \Delta_M^M \phi \simeq \Delta_w^s \phi (MX)$$

## Voltaic cell



$$E = \Delta_M^M \phi \simeq - \Delta_w^s \Psi (MX)$$

Figure 3. Comparison of galvanic and voltaic cells with liquid/liquid interfaces.

compensation potential. Using relation (3), after simple rearranging we have Fig. 2 and Fig. 3, respectively:

$$E = \Delta_S^M \Psi$$

$$\text{and } E = \Delta_M^S \Psi (MX) \quad (5)$$

Thus the Volta potential may be operationally defined as the compensating voltage of the cell. Very often the terms “Volta potential” and “compensation voltage” are used interchangeably. It should be stressed that the compensating voltage of a voltaic cell is not always the direct measure of the Volta potential.

In contradiction to the usual treatment, relation (5) is not general (see below). For this reason, as well as the lack of an exact thermodynamic relation with the changes in Gibbs energy, the term “compensation voltage” is also recommended instead of “emf,” which is commonly used for

reversible galvanic cells. The use of a two-phase salt bridge containing tetraethylammonium picrate (TEAPi), [e.g., water/nitrobenzene (w/nb)], in the galvanic cell shown in Fig. 3 is explained in Section XI.

Generally, the electrochemical information obtained from an investigation of voltaic cells depends on the composition, structure, and experimental conditions of the systems. It is easy to distinguish three basic groups of such information. The first (main) deals with the possibility of measuring the Volta potentials and the differences in real potentials of ions [Eq. (1)] for such two-phase systems as metal/metal, metal/liquid solutions of electrolytes (Sections V, VI, IX, X), metal/solid electrolytes (Section VIII), and electrolyte solutions in two solvents (Sections VI, XIII) or in the same solvent. The latter systems provide the basis for measuring so-called real activities (Section VII). The second group of information originates from the Volta potential measurements in systems where conditions are created to keep the bulk and surface properties of one phase consistent; the phase is treated as the reference. If the bulk properties of the second (i.e., investigated phase) are constant (second group), the changes in the surface potential caused, e.g., by adsorption can be measured (Section XII). This is the most popular application of voltaic cells. If the surface potential of the investigated phase is constant (third group), one can measure, for instance, partition (Section XIII), diffusion, and Donnan potentials.

In a discussion of liquid voltaic cells it is necessary to distinguish two groups of immiscible liquid/liquid interfaces: water/polar organic solvent (e.g., nitrobenzene) and water/nonpolar organic solvent, such as water/oil or water/hydrocarbon (e.g., decane- or octane-type systems). As is schematically shown in Fig. 4, the main difference is the presence of a dissociated electrolyte in the organic phase of the first group in contradiction to the second. As was clearly shown by Davies and Rideal,<sup>4</sup> this controls the character of the potential differences to be measured (see Fig. 4). If the organic phase constitutes the solution of the dissociated electrolyte, the ionic double layer is created there, and the Galvani potential changes may be measured. In the opposite case, the voltaic cell allows the surface potential changes to be measured. This behavior is fulfilled well for systems in an equilibrium state, which contain a nonpolar oil phase. Between these extremes lie the intermediate cases of very slightly polar solvents, to which belongs, for instance, the benzene phase saturated with water.<sup>4</sup> For these cases the results are dependent on the time and the measurement method.



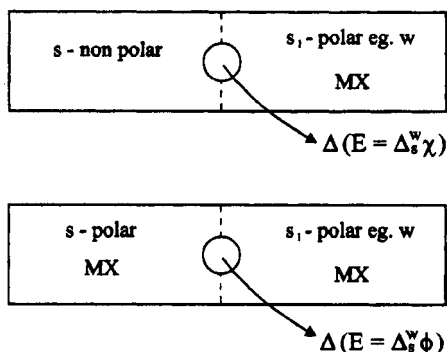


Figure 4. The potential changes measured at the interfaces formed by the nonpolar solvent–water and polar solvent–water systems.

#### IV. EXPERIMENTAL METHODS FOR INVESTIGATING VOLTAIC CELLS

The electronic work function may be found by either direct or indirect methods. The absolute value of  $\phi_e^x$  is determined by studying the emission of electrons from the given surface. The indirect methods [i.e., investigation of the external beam of electrons, or by measuring the Volta potentials (Sections II and III)] give the relative magnitudes (for example, the difference in the work functions of an investigated and a reference surface). It is worth noting that the voltaic cell gives the arithmetic mean work function of a heterogeneous surface (for example, in the presence of adsorbate), whereas direct methods give an average value that is weighted in favor of low work function paths. In contrast to the voltaic cell measurement, emission techniques are not equilibrium methods. Presentation of emission methods is outside the scope of this review.

The main difficulty in measuring the compensation voltage of voltaic cells is the very large resistance of the system caused by the presence of a dielectric gas phase. Therefore there are two possibilities for solving the problem: reduce this resistance or measure the work of the charge transfer across the dielectric. The first possibility is accomplished by the ionizing method and the second by condenser and jet methods.

The ionizing electrode method, also called the *radioactive* or *ionizing probe*, requires a radioactive source to ionize the gas gap and a high-

impedance electrometric device.<sup>4-17,28-30</sup> Usually gold foil coated with an alpha emitter (e.g., <sup>241</sup>Am) is used as the mediating air electrode. It ionizes the air gap between the air electrode and liquid surface so that a small current (a few picoamperes) can flow. The ionization of the gas, which is due to radiation, allows the direct compensation and measurement of the voltage of the investigated system. Modern experimental arrangements are presented in Refs. 28-29. The simultaneous use of two ionizing probes placed above the investigated and reference surfaces makes possible the direct differential measurement of  $\Delta\chi^W$ .<sup>29-30</sup>

In the dynamic condenser, or the vibrating plate or vibrating condenser method (Fig. 5), also called *Kelvin*, *Zisman*, or *Kelvin-Zisman probe*, the capacity of the condenser created by the investigated surface and the plate (vib. plate) is continuously modulated by periodical vibration (GEN.) of the plate. The ac output is then amplified and fed back to the condenser to obtain null-balance operation (E,V).<sup>4-7,31-36</sup>

In contrast to the ionizing electrode method, the dynamic condenser method is based on a well-understood theory and fulfills the condition of thermodynamic equilibrium. Its practical precision is limited by noise, stray capacitances, and variation of surface potential of the air-electrode surface, i.e., the vibrating plate. At present, the precision of the dynamic condenser method may be limited severely by the nature of the surfaces of the electrode and investigated system. In common use are adsorption-

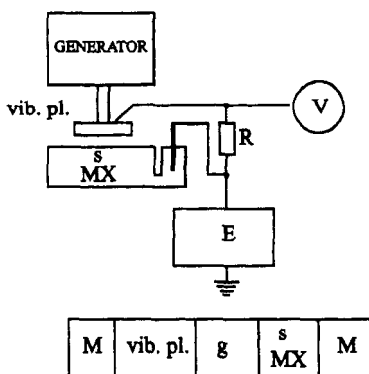


Figure 5. A block schematic diagram of the dynamic condenser method for voltaic measurements.

resistant air electrodes, often gold plated and protected with, e.g., a Teflon or Permaflon (FEP Teflon) layer. This minimizes the drift of the surface potential of the vibrating electrodes and ensures stable and reproducible results.<sup>34,37</sup>

Preparation of an uncontaminated surface of an aqueous solution is very difficult. Even minute traces of adsorbable organic impurities strongly influence the surface potential of water. Cleaning of the aqueous surface (e.g., by siphoning off the surface layer) is usually necessary, while for organic solutions it is usually not needed.<sup>34</sup>

It is now possible to construct a processor setup that combines good reproducibility and a low time constant with a theoretical sensitivity of  $\pm 0.05$  mV; for about a 0.5-mm air gap, changes in  $E$  equal to  $\pm 0.5$  may be detectable. Of course, it is easier for solid than for liquid surfaces.

Recently scanning Kelvin probes and microprobes have been developed as high-resolution surface analysis devices. They permit the investigation of the lateral distribution of work functions or the surface potentials of various phases.<sup>38-43</sup> Up to now, they were used for instance, for determining the corrosion potential profiles of metal and semiconductors under very thin films of electrolytic solution<sup>39</sup> and creating surface potential maps of Langmuir-Blodgett films<sup>42</sup> of charged ionomer-polymer blends.<sup>43</sup>

The static capacitor method is in principle the true original Kelvin technique. In this method, the tendency for charge to flow from the capacitor through the external circuit connecting the capacitor plates is detected, and then a backing-off potential is rapidly applied until charge ceases to flow.<sup>44-47</sup>

A theoretical approach that permits common discussion of the ionizing gap, as well as dynamic and static condenser methods, has been described.<sup>46</sup> The dynamic condenser method gives probably the most reliable results. However, the ionizing probe method appears to be experimentally simpler for investigation of liquid surfaces, in particular, owing to the delicate mechanical and vibrational or signal measuring problems involved with the condenser methods. It has been shown that the two techniques give similar results.<sup>25</sup>

The principle of the jet method, which also utilizes a condenser, was originated by Kenrick and improved by Randles<sup>48</sup> and later by McTigue et al.<sup>21</sup> It may be summarized as follows: A jet of one liquid is directed down the axis of a tube, the inner surface of which is covered by a stream of the second liquid. If the reference electrodes are the same and the outer

potentials at the two liquids are different, the Volta electric field exists in the gap between them. The droplets carry away the charge on the jet, so that there must be a continuous flow of charge into the jet. If this is connected, via suitable reference electrodes, to a high-impedance electrometering system, as in the ionizing method, and the liquid surrounding the jet is connected to a potentiometer, a condition may be established in which the outer potential of the jet equals that of the surrounding liquid. The continuous renewing of the surface, which is the principal virtue of the jet method, renders the method particularly suitable for solutions that do not contain spread monolayers. Kamiński has indicated that the dynamic jet method is reproducible, the purity of a free-flowing surface is ensured, no ionization occurs, and consequently the method is easy to handle.<sup>49</sup> The possibility of calculating the dynamic changes of  $\chi^W$  from the droplets' diameter has been also suggested.<sup>50</sup>

Experimental systems using a dynamic condenser in which the investigated solution is flowing horizontally or vertically have also been designed.<sup>51</sup>

## V. VOLTA POTENTIAL OF THE METAL/SOLUTION INTERFACE

The Volta potential at the metal/solution interface [Fig. 2, Eqs. (3) and (4)] may be described by the equation

$$\Delta_S^M \Psi = g_S^M (\text{ion}) + \delta\chi_{(s)}^M - \delta\chi_{(s)}^M \quad (6)$$

where  $\delta\chi_{(s)}^M$  and  $\delta\chi_{(M)}^S$  are the modifications relative to those at the surfaces of the separate phases and are caused by their physical contact and the creation of an interface.<sup>1,13,22,23</sup> Such voltaic measurements also include the zero charge potential [ $g_S^M (\text{ion}) = 0$ ], for which the Volta potential is equal to

$$(\Delta_S^M \Psi)_0 = \delta\chi_0^M - \delta\chi_0^S \quad (7)$$

Only this equation has been used in practice. For a mercury/water interface, the  $(\Delta_S^M \Psi)_0$  is equal to -0.25 V<sup>2,23</sup> or -0.22 V.<sup>52</sup> Its components [Eq. (7)] have been estimated to be -0.30 V and -0.05 V, respectively.<sup>2,23</sup> They show that in the presence of water, the electrons cannot expand freely as in a gas, but are pushed into mercury, and that the interaction of water

molecules with the metal is rather weak. The water dipoles are preferentially oriented with their protons toward the mercury.<sup>23</sup>

The standard Volta potential of the calomel electrode  $\Delta_{W}^{Hg} \Psi^0$  (Hg, Cl<sup>-</sup>) was determined for the first time by Klein and Lange, but the accepted and usually used value of this potential (equal to 0.207 V) was found by Randles.<sup>48</sup> Later measurements by Farrel and McTigue et al.<sup>21</sup> and Antropov et al.<sup>53</sup> gave 0.212 V and 0.220 V, respectively. In the methanol a value equal to 0.25 has been found.<sup>54</sup>

## VI. REAL POTENTIALS OF IONS IN ELECTROLYTE SOLUTIONS

The real energy of ion solvation,  $\alpha_i^s$ , defined by Eq. (2), expresses the change in ion energy upon its transfer from a gas phase into a solution. Unlike the chemical energy of solvation,  $\mu_{si}$ , the value of the real energy of solvation, also in the standard state, can be calculated from experimental data using the formula, e.g., for the hydration of the cation<sup>48,55</sup>:

$$-\alpha_M^{0,W} = F(E_{HgCl^-}^0 - E_{Me, \perp Me}^0 + \alpha_e^{Hg} + \Delta G_{subl}^0 + \Delta G_{ion}^{0,M} - F\Delta_{W}^{Hg} \Psi^0 \text{ (Hg, Cl-)} \quad (8)$$

where  $E^0$  denotes the standard electrode's potential relative to a given and calomel electrode,  $\alpha_e^{Hg}$  is the real potential of electron in mercury (i.e.,  $-\phi_e^{Hg}$ ), and  $\Delta G^0$  gives the standard Gibbs energies of sublimation and ionization of Hg. The latter three terms, according to the thermodynamic cycle, replace the real potential of ion in metal:

$$-\alpha_M^{M+} = \alpha_e^{Hg} + \Delta G_{subl}^0 + G_{ion}^{0,M} \quad (9)$$

Equation (8) may be easily found from the standard emf of the cell:

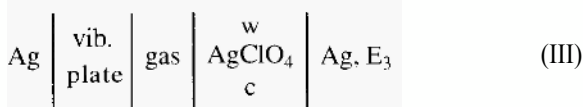
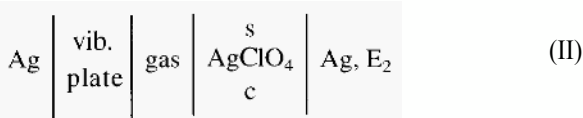


expressed as the difference in relative standard electrode potentials and the sum of the Volta potentials of the three interfaces, and using definition (I). It is worth noting that  $\Delta_s^M \phi$  or  $g_s^M$  (ion) potential differences fulfill the Nernst logarithmic dependencies.

Expression (8) can be used to calculate the real energy of ions in any solvent, provided the standard potential of the calomel electrode, and the standard potentials of the elements and the  $\Delta_s^{Hg}, \Psi^0$  (Hg, Cl<sup>-</sup>) under study

are known. However, it is difficult to determine this last value for organic solvents directly, owing to variations in the  $\chi^{\text{Hg}}$  caused by the adsorption of solvent vapors.<sup>34,54</sup> The simpler and more reliable method is to find the real energies of solvation from their differences measured relative to water.<sup>56-63</sup> This real medium effect (the real Gibbs energy of ion transfer, e.g., for  $\text{Ag}^+, \Delta_{\text{w}}^{\text{s}} \alpha \text{Ag}^+$ ) is determined by the compensation voltage of the proper voltaic cell (Fig. 6).

Applying the condenser or ionization methods (Section IV), the voltage  $E$  is determined as a difference in the compensating voltages of the following two cells:



The difference in the voltages expresses the formal real energy of transfer:

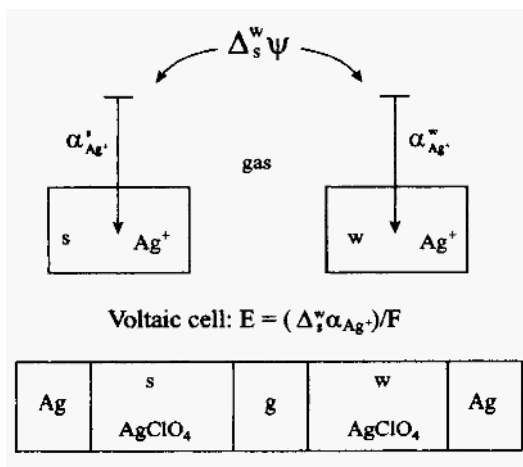


Figure 6. The differences of real potentials of the  $\text{Ag}^+$  ion in metal-solution systems.

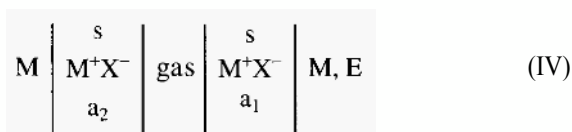
$$E = E_2 - E_3 = 1/F \Delta_{\mathcal{W}}^S \alpha_{\text{Ag}}^0 + RT/F \ln(a_{\pm}^S / a_{\pm}^{\mathcal{W}}) \quad (10)$$

at the same concentrations in both solvents and assumes that the surface potentials of the solvents are unmodified by the presence of low amounts of  $\text{AgClO}_4$  i.e.,  $<10^{-2}$  mol  $\text{dm}^{-3}$  (see Section XII). The method was applied to many solvents, among others, to methanol, ethanol, propanol, butanol, ethylene glycol, acetonitrile, acetone and  $\gamma$ -butyrolactane, as well as to mixtures of some organic solvents with waters<sup>56-63</sup>

According to Eq. (2), the real and chemical energies of transfer differ by the term containing the difference in surface potentials of a given solvent and water (see Section XIV).

## VII. REAL ION ACTIVITY

Rabinovich et al. have shown that it is possible to propose an extrathermodynamic definition of single-ion activity,  $a^*$ , as a function of the real potentials of those particles.<sup>64-66</sup> By carrying out the measurements of voltaic cells containing electrodes reversible to the same ionic species in solutions of different concentrations in the same solvent,



it is possible to find the ratio of the real activities of the  $\text{M}^+$  ions in both solutions:

$$E = RT/F \ln a_1/a_2 + \Delta_{a_2}^{a_1} \chi^S = RT/F \ln a_1^*/a_2^* \quad (11)$$

Therefore the real and chemical ionic activity coefficients are related by the formula:

$$\gamma_i^{*-1}/\gamma_i^{*-2} = \gamma_i/\gamma_i \exp z_i F \Delta_{a_2}^{a_1} \chi / RT \quad (12)$$

If the concentration change in the surface potential,  $\Delta_{a_2}^{a_1} \chi$ , is close to zero (see Section XII), the real and chemical activities are the same.

On the basis of this definition, one can determine, for instance, the activity of electrolytic solutions in terms of the "real" hydrogen ion activity.<sup>65</sup> Rybkin et al.<sup>66</sup> found that the  $\Delta\chi$  effect may be stabilized by adding surface-active substances in small quantities to the solution. Ac-

cording to their data, the value of  $\gamma_i^{*1}/\gamma_i^{*2}$  over wide ranges of HCl concentrations does not depend upon the presence of surface-active substances (e.g., *n*-heptyl and *n*-nonyl alcohols) in the experiments.

### VIII. REAL POTENTIALS OF IONS IN SOLID ELECTROLYTES

The possibility of measuring the Volta potential in the system metal–solid-state electrolyte and using the data obtained to determine ionic components of the free lattice energy has been shown in our papers.<sup>67–68</sup> Earlier, Copeland and Seifert<sup>69</sup> measured the Volta potential between Ag and solid AgNO<sub>3</sub> in the temperature range between 190 and 280 °C. They investigated the potential jump during the phase transition from solid to liquid salt.

Our measurements of the Volta potentials,  $\Delta_{MX}^M \Psi$ , in systems Ag–AgX and Cd–CdX (for X=Cl<sup>-</sup>, Br<sup>-</sup>, I<sup>-</sup>) were performed using voltaic cells; see Fig. 7 for an Ag–AgX system.

Applying the condenser or ionization methods (Section IV), the voltage *E* is determined as the difference in the compensating voltages

$$E = E_5 - E_6 = \Delta_{AgX}^{Ag} \Psi \quad (13)$$

of the following two cells:

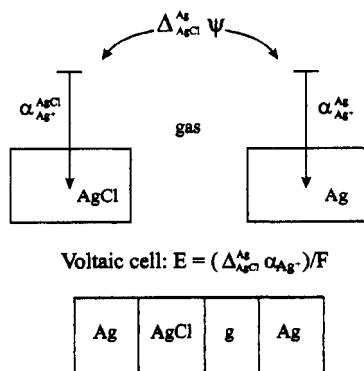
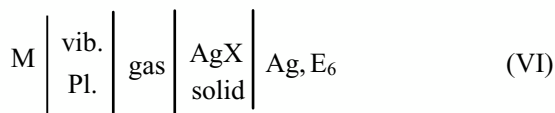
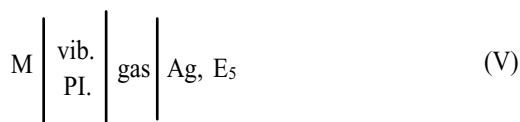
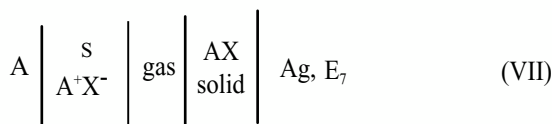


Figure 7. The differences of real potentials of the Ag<sup>+</sup> ion in metal–solid electrolyte systems.





An alternative method to experimentally determine the  $\alpha_M^{MX}$  potential is the measurement of the Volta potential for the system:



for which the voltage  $E$  may be found from the compensating voltages of cells (VI) and (III):

$$E_7 = E_6 - E_3 = \Delta_{\text{AgX,w}}^{\text{AgX,solid}} \Psi$$

The use of cell (VII) is experimentally much easier and more reliable than the cell presented in Fig. 7.

The data for  $\Delta\Psi$  make it possible to calculate  $\alpha_M^{MX}$  using Eq. (1) and  $\alpha_{M^+}$ , calculated according to the thermodynamic cycle, Eq. (9).

In the case of ionic solid substances, an important quantity is the free lattice energy  $\Delta G_{\text{solid}}^{MX}$ , i.e., the energy liberated when one type of crystalline substance is formed from its ionic constituents in the gas phase. This definition implies that this magnitude for a simple 1 : 1 solid electrolyte is a sum of the real potentials of cation and anion:

$$\Delta G_{\text{solid}}^{MX} = \alpha_{M^+}^{MX} + \alpha_X^{MX} \quad (15)$$

Therefore the investigation of proper voltaic cells makes it possible to determine ionic contributions to the energy of a crystalline lattice.

Voltaic cells have been used by Malov et al.<sup>69,70</sup> to investigate several silver salts, including superionic electrolytes synthesized on the basis of AgI, such as AgRbI<sub>5</sub>, AgSI, and Ag<sub>6</sub>WO<sub>4</sub>I<sub>4</sub>.

## IX. VOLTAIC CELLS AND ABSOLUTE ELECTRODE POTENTIALS

Knowledge of the Volta potential of a metal/solution interface is relevant to the interpretation of the absolute electrode potential. According to the modern view, the relative electrode potential (i.e., the emf of a galvanic cell) measures the value of the energy of the electrons at the Fermi level of the given metal electrode relative to the metal of the reference electrode. On the other hand, considered separately, the absolute value of the electrode potential measures the work done in transferring an electron from a metal surrounded by a macroscopic layer of solution to a point in a vacuum outside the solution.<sup>22,72,73</sup>

Therefore the absolute potential of a single electrode is its electron work function (Fig. 8), which may be expressed in the form

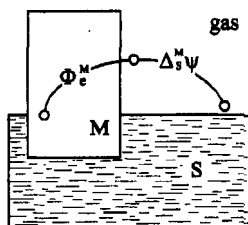
$$E(\text{abs}) = \phi_e^M / F + \Delta_S^M \Psi \quad (16)$$

or alternatively

$$E(\text{abs}) = \Delta_S^M \phi - \mu_e^M / F + \chi^s \quad (17)$$

It is clear that the Galvani potential,  $\Delta_S^M \phi$ , which is an electrostatic quantity, cannot be identified with the thermodynamic term called the *electrode potential*.

The absolute electrode may be expressed also in terms of thermodynamic quantities describing the electrode reaction by means of the Born-



$$E_{\text{abs}}^M = \Phi_e^M / F + \Delta_S^M \Psi$$

Figure 8. The physical meaning of the absolute electrode potential.

Haber–Fajans cycle, e.g., for the standard hydrogen electrode in the form<sup>22,73–75</sup>.

$$E_H^{0,W}(\text{abs}) = (\Delta G_{\text{at}}^0 + G_{\text{ion}}^0 + \alpha_H^{W+})/F \quad (18)$$

where the right side of the equation contains the energies of atomization (dissociation), ionization of hydrogen, and real hydration of the hydrogen ion.

On the basis of the above equations, the recommended absolute potential of the standard hydrogen electrode is<sup>22,73–75</sup>:

$$E_H^{0,W}(\text{abs}) = 4.44 \pm 0.02 \text{ eV} \quad (19)$$

In the calculation of  $E_H^{0,W}$  the standard Volta potential of the calomel electrode found by Randles has been used<sup>48</sup> (see Section V). The other estimators of  $E_H^{0,W}(\text{abs})$ ,<sup>76,78</sup> for instance,  $-4.73 \text{ V}$  by Gomer and Tryson<sup>76</sup> seem to be doubtful. A detailed discussion of this topic may be found in the papers by Trasatti.<sup>22,73–75</sup>

Knowledge of the value of  $E_H^{0,W}(\text{abs})$  makes it possible to convert all relative values of electrode potential to an absolute scale. For instance, the standard electrode potentials of the oxygen electrode, the zero charge of mercury, and the hydrated electron, in the absolute scale are equal to  $-5.67$ ,  $-4.25$ , and  $1.57 \text{ V}$ , respectively.<sup>73</sup>

Owing to the existence of relation (3), it is possible to define three other single (i.e., absolute) electrode potentials. However, only the potential defined by Eq. (16) has the reference state at a point close to the surface where the Volta potential is measured. This case corresponds to a truly universal absolute state (“electrons at rest in a vacuum”) adopted by physicists to measure electronic work functions.

The determination of the real energies of solvation from measurements of the voltaic cells (Section VI) makes it possible to find the absolute electrode potentials in nonaqueous solvents owing to the relation

$$E_H^{0,S}(\text{abs}) - E_H^{0,W}(\text{abs}) = (\alpha_H^{0,S} - \alpha_H^{0,W})/F \quad (20)$$

Some results of  $\alpha_H^{0,S}$  and  $E_H^{0,W}$  are presented in Table 1.<sup>79</sup>

The physical concept of a single electrode potential has been also discussed in terms of the energy levels of ions in electrode systems. This concept may be useful in the cases where the system has no electronic energy levels in a range of practical interest, such as in ionic solid crystalline and electronically nonconductive membrane electrodes.<sup>80</sup>

**Table 1**  
**Real Free Energy of Solvation of  $H^+$  and Absolute Potential of  $E_H^{0,W}(\text{abs})$  in Different Solvents<sup>79</sup>**

Solvent	$-\alpha_H^{0+}$ (kJ mol <sup>-1</sup> )	$-E^o$ (abs) (V)
Acetone	1118.± 6	4.13 ± 0.06
Acetonitrile	1073.5± 6	4.60 ± 0.10
Ethanol	1110.5± 6	4.21± 0.07
Formamide	1102.5± 6	4.29± 0.07
Methanol	1112.5± 6	4.19± 0.07
Water	1088.0± 2	4.44± 0.02

## X. VOLTA POTENTIALS OF *EX SITU* AND *NON-SITU* ELECTRODES

A relatively new arrangement for the study of the interfacial region is achieved by so-called emersed electrodes. This experimental technique developed by Hansen et al.<sup>81-84</sup> consists of fully or partially removing the electrode from the solution at a constant electrical potential. This *ex situ* experiment (Fig. 9), usually called an *emersion process*, makes possible an analysis of an electrode in an ambient atmosphere or an ultrahigh vacuum (UHV). Research using modern surface analysis such as electron spectroscopy for chemical analysis (ESCA), electroreflectance, as well as surface resistance, electrical current, and in particular Volta potential measurements, have shown that the essential features (e.g., the charge on

### Electrodes

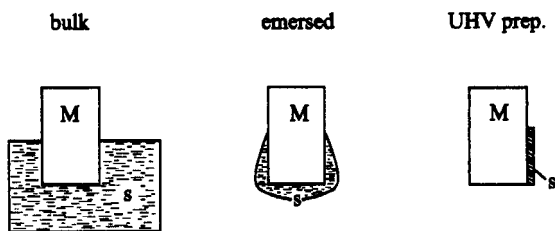


Figure 9. The electrodes investigated in voltaic cells.

the metal and the potential across the emerging double layer of the bulk electrode) transferred into an emersed state evidently remain intact.<sup>81-84</sup> The 1:1 correlation between the Volta and emersion potentials i.e., the potential supplied prior to emersion) presents a strong argument in favor of the above conclusion. However, the removal of the double layer becomes less perfect with decreasing ionic strength of the electrolyte ( $< 0.1 M$ ) because of the increasing extension of the diffuse part of the double layer. A 1:1 correlation of the Volta potential with the emersion potential has been found also for electrodes coated with exchange polymer membranes.<sup>85-86</sup>

The emersed electrode, in principle, may be treated as the experimental realization of a single electrode. However, it is doubtful whether its liquid layer has the same bulk properties. This is probably the main reason for the different results of  $E_H^0(\text{abs})$  found for emersed electrodes, e.g.,  $-4.85 V$ .<sup>83</sup> Samec et al.<sup>87</sup> have found that emersion of electrodes in a nitrogen atmosphere decreases the Volta potential and therefore the absolute electrode potential by ca.  $0.32 V$  relative to the value in solution. They have attributed this mainly to the reorientation of the water molecules at the free surface.

The non situ experiment pioneered by Sass<sup>88</sup> uses a preparation of an electrode in an ultrahigh vacuum through cryogenic coadsorption of known quantities of electrolyte species (i.e., solvent, ions, and neutral molecules) on a metal surface.<sup>88-91</sup> Such experiments serve as a simulation, or better, as a synthetic model of electrodes. The use of surface spectroscopic techniques makes it possible to determine the coverage and structure of a synthesized electrolyte. The interfacial potential (i.e., the electrode work function) is measured using the voltaic cell technique. Of course, there are reasonable objections to the UHV technique, such as too little water, too low a temperature, too small interfacial potentials, and lack of control of ionic activities.<sup>89,91</sup>

Non-situ and *ex situ* studies can provide important information for understanding the properties of metal/electrolyte interfaces. The applicability of these methods for fundamental studies of electrochemistry seems to be firmly established. The main differences between common electrochemical and UHV experiments are the temperature gap (ca.  $300$  vs.  $150 K$ ) and the difference in electrolyte concentration (very high concentrations in UHV experiments). In this respect, experimental research on double-layer properties in frozen electrolytes can be treated as a link between *in situ* experiments.<sup>92</sup> The measurements of the work functions

of emersed and UHV-prepared electrodes have suggested the  $E_{\text{H}}^{\circ}$  (abs) values to be ca. 4.8 V,<sup>89</sup> i.e., similar to that of the emersed systems.

## XI. VOLTAIC CELLS WITH INTERFACES OF IMMISCIBLE ELECTROLYTE SOLUTIONS

The interface separating two immiscible electrolyte solutions (e.g., one aqueous and the second based on a polar organic solvent) may be reversible in respect to one or many ions simultaneously as well as electrons. For symmetrical electrolytes of, e.g., type 1:1, such a liquid/liquid interface, in an equilibrium state, is characterized by the standard Galvani potential, usually called the *distribution potential*. This very important quantity can be expressed in three equivalent forms, i.e., (1) using the ionic standard potentials, (2) using standard Gibbs energies of transfer, (3) and employing the limiting ionic partition coefficients<sup>15,16,19</sup>:

$$\begin{aligned} \Delta_{\text{w}}^{\text{S}} \varphi^{\circ}(\text{MX}) &= \frac{1}{2} [\Delta_{\text{w}}^{\text{S}} \varphi^{\circ}(\text{M}^{+}) + \Delta_{\text{w}}^{\text{S}} \varphi^{\circ}(\text{X}^{-})] \\ &= \frac{1}{2F} [\Delta_{\text{S}}^{\text{w}} G_{\text{M}^{+}}^{\circ} - \Delta_{\text{S}}^{\text{w}} G_{\text{X}^{-}}^{\circ}] \\ &= \frac{RT}{2F} \ln \frac{B_{\text{w}}^{\text{S},0}(\text{M}^{+})}{B_{\text{w}}^{\text{S},0}(\text{X}^{-})} \end{aligned} \quad (21)$$

A water–nitrobenzene (NB) system containing tetraethylammonium picrate in the partition equilibrium state has been proposed by us as a convenient liquid junction bridge for the liquid galvanic and voltaic cells. The distribution potential of this system and the diffusion potential at the contact of nitrobenzene with many organic solvents are close to zero.<sup>93</sup> It should be stressed that the use of salt bridges, which provide practically constant or negligible liquid junction potentials, constitutes a nonthermodynamic procedure that is necessary in many electrochemical experiments. In the case of the investigation of interfaces between immiscible electrolyte solutions, only the cells with transport provide valuable information.<sup>15</sup>

The interface separating two immiscible electrolyte solutions may also be made virtually ideally polarized by a suitable choice of the electrolytes dissolved in the phases. For most of the water–nitrobenzene and water–1,2-dichloroethane systems studied, the presence of a tetrabutylammonium tetraphenylborate in the organic phase and a hydro-

phylic lithium chloride in water constitute, within certain potential limits, polarizable liquid/liquid interfaces.<sup>15-19</sup>

As pointed out in Section III, the compensation voltage does not always refer directly to the Volta potentials. The appropriate construction of voltaic cells, or more precisely, the proper mutual arrangements of phases, as well as the application of reversible electrodes or salt bridges in the systems, allows measurement of not only the Volta potential but also the surface and the Galvani potentials. The measurements of  $\Delta_S^w \chi$  and  $\Delta_S^w \phi$  potentials also include the potential of zero charge and make possible the estimation of the dipolar potentials  $\gamma_S^w$  (dipol), Eq. (4). These possibilities are schematically illustrated in Fig. 10. Of course, it should be remembered that these potential differences are only partially independent of one another because they are obtained using the same nonthermodynamic assumptions on negligible diffusion potentials, and usually the same salt bridges eliminating these potentials. As can be seen from the above discussion, only the use of liquid/liquid cells with transport allows one to obtain significant results. Therefore, as is generally known, the use of proper salt bridges, providing practically constant or negligible diffusion potentials, constitutes a nonthermodynamic procedure that is essential and necessary in many electrochemical experiments.<sup>15</sup>

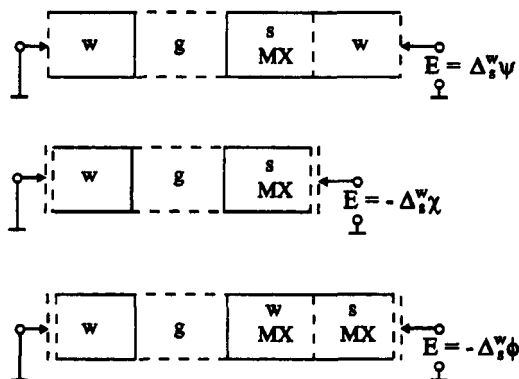


Figure 10. The potentials measured in various possible configurations of the voltaic cells with liquid/liquid interfaces.





where:  $E_{l,j}$  and  $E_{l,j}^*$  are common and real liquid junction potentials. There is no difference between the potentials if the influence of the electrolyte on the surface potential of the solvent in the concentration range investigated is negligibly small.

## XII. ADSORPTION POTENTIALS OF DIPOLAR COMPOUNDS

The adsorption of a dipolar organic compound B on a water surface can take place as the result of either spreading from the appropriate solution over water (i.e., formation of a Langmuir monolayer) or expelling the molecules of the considered compound from the bulk aqueous solution (i.e., formation of a Gibbs layer or monolayer).<sup>4-8</sup> The first method is used for relatively large, amphipathic molecules, i.e., molecules composed of a hydrophilic and a hydrophobic part, which is most commonly a flexible hydrocarbon chain with the number of carbon atoms in the chain greater than ten. There are also a large number of such compounds, including molecules of biological interest, with aromatic hydrophobic groups. The spreading solvent should be easily removed from the water surface by evaporation or/and dissolution. The total number of the adsorbed B molecules per 1 m<sup>2</sup> of the surface,  $N_B$ , may be easily evaluated from the amount of the spread compound. The second method is common for molecules that are easily soluble in water, and is called *adsorption from solution*. Surface tension measurements make it possible to calculate, from the Gibbs isotherm, the surface excess of substance B, which is a relative quantity.<sup>4,12</sup>

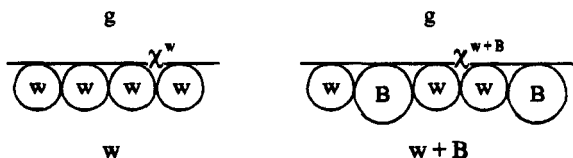
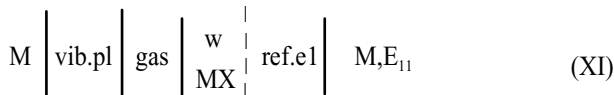
Replacement of gas by the nonpolar (e.g., hydrocarbon) phase (oil phase) has been sometimes used to modify the interactions among molecules in a spread film of long-chain substances.<sup>4-8,12,14-16</sup> The nonpolar solvent/water interface possesses an advantage over that between gas and water in that cohesion (i.e., interactions between adsorbed molecules) due to dipole and van der Waals's forces is negligible. Thus, at the oil/water interfaces, the behavior of adsorbates is much more ideal, but quantitative interpretation may be uncertain, in particular for the higher chains, which are predominantly dissolved in the oil phase to an unknown extent. The oil phase is poured on the surface of an aqueous solution. Thus, the hydrocarbon, such as heptane or decane, forms a membrane a few millimeters thick. It is thicker than the adsorbed monolayer. Owing to the small difference in dielectric constant between the air and a hydrocarbon oil, the

adsorption at the oil/air interface should be small and is practically negligible.

Adsorption of a dipolar substance at the w/a and w/o interfaces changes surface tension and modifies the surface potential of water<sup>19</sup> (Fig. 11). As seen in Fig. 11, the change in compensation voltage  $\Delta E$  due to adsorption is the surface potential difference, usually called the *surface potential*, or better the *adsorption potential*, and often indicated unnecessarily by  $\Delta V$ .<sup>4-8</sup>

$$\Delta E = \Delta\chi^w = \chi^w - \chi^{w+B} \tag{24}$$

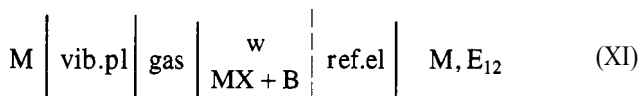
The experimental investigation of  $\Delta\chi^w$  may be performed directly as presented in Fig. 10 or by using two alternately measuring cells (XI) and (XII). In the first case, a voltaic cell with a differential ionizing probe or the jet method can be used. In the second case, the ionizing probe or vibrating plate method is applied (see Section IV). These probes are two versions of a so-called air electrode that assists in the measurement of a voltaic cell as illustrated in Fig. 10. The air electrode, e.g., the vibrating plate, creates in fact the two following cells:



**Voltaic cell:  $\Delta E = \Delta\chi^{w+B} = \Delta\chi^w$**

Ref. el.	w MX	g	w MX + B	Ref. el.
----------	---------	---	-------------	----------

Figure 11. Influence of the adsorbed molecules B on the surface potential of water.



and

$$\Delta E = E_2 - E_1 = \Delta\chi^w \quad (25)$$

The presence of the supporting electrolyte  $MX$  in the aqueous phases ensures the stability of the measurements. However,  $MX$  must not adsorb at the surface to avoid affecting the  $\Delta\chi^w$  potential.

Usually before adding a surfactant it is necessary to clean the surface of the water solution by siphoning off the top layers of water with a glass capillary until the constant compensation voltage is obtained. This is not done in the jet method.

The surface potential change, besides the surface pressure, is the most important quantity describing the surface state in the presence of an adsorbed substance. However, the significance in molecular terms of this very useful experimental parameter still remains unclear. It is common in the literature to link  $\Delta\chi^w$  with the properties of the neutral adsorbate by means of the Helmholtz equation<sup>4-14</sup>:

$$\bar{p} = P_B^{\perp} / \epsilon \epsilon_0 \quad (26)$$

where  $\epsilon_0$ , and  $\epsilon$  are the electric permittivity of the vacuum and the relative permittivity of the interfacial region, respectively, and  $p_B^{\perp}$  is the normal component of the molecular dipole moment of the substance B. Either from the known value  $N_B$ , or from the slope of the experimental relationship of  $\Delta\chi^w$  vs.  $N_B$ , the quantity  $\bar{p} = p_B^{\perp} / \epsilon_0 \epsilon$  can be derived. This quantity may be treated as the apparent surface dipole moment of the adsorbate.

As a rule, no information is available on the local value of  $\epsilon$ , which constitutes the main obstacle to an a priori calculation of  $\Delta\chi^w$ . In the fields of physics and surface chemistry, an assumption is often made that  $\epsilon = 1$  either because the molecules are treated as isolated entities or there is "lack of a better value."<sup>102</sup> It is known that  $\bar{p}$  values derived from experimental  $\Delta\chi^w$  data (e.g., for insoluble monolayers) with the assumption  $\epsilon = 1$  are substantially different from the dipole moment for the same molecule in the bulk of the solution.<sup>4</sup> The reasons offered to explain this difference are manifold, e.g., (1) inappropriate value of  $\epsilon$ , (2) reorientation of water molecules around the adsorbate, or (3) lateral interaction between adsorbed molecules in the monolayer.

Davies and Rideal proposed the  $\bar{p}$  term to consist of three components<sup>4</sup>:

$$\bar{p} = p_1^{\frac{1}{2}} + p_2^{\frac{1}{2}} + p_3^{\frac{1}{2}} \quad (27)$$

Later, Demchak and Fort<sup>102</sup> modified Eq. (27) with the aim of including effects (1)–(3):

$$\bar{p} = (p_1^{\frac{1}{2}}/\epsilon_1) + (p_2^{\frac{1}{2}}/\epsilon_2) + (p_3^{\frac{1}{2}}/\epsilon_3) \quad (28)$$

In Eqs. (27) and (28),  $p_1^{\frac{1}{2}}$  is the contribution of the substrate water molecules,  $p_2^{\frac{1}{2}}$  that of the adsorbate polar head, and  $p_3^{\frac{1}{2}}$  that of the hydrophobic moiety of the adsorbed molecules. Consistently,  $\epsilon_1$ ,  $\epsilon_2$ , and  $\epsilon_3$  are the effective local permittivities of the free surface of water and of the regions in the vicinity of the polar head and of the hydrophobic group, respectively. The models have been used in a number of papers on adsorbed monolayers<sup>18</sup> and on short-chain substances soluble in water.<sup>103–107</sup> Vogel and Möbius have presented a similar but more simplified approach in which  $p$  is split into two components only.<sup>108</sup> Recently some improvements to the analysis using Eq. (27) have been proposed.<sup>109</sup> An alternative approach suggesting the possibility of finding the values of the orientation angle of the adsorbate molecules instead of local permittivities has been also proposed.<sup>110</sup>

According to Frumkin and Damaskin,  $\Delta\chi^w$  at the air/solution interface changes linearly with composition, i.e., the interface behaves as two condensers in series.<sup>111,112</sup> On a molecular basis, this model is tantamount to assuming that an adsorbate and solvent do not interact in the interfacial zone, but create two homogeneous surface layers.

According to the macroscopic model, the adsorption potential shift is due to the removal of some solvent molecules,  $s$ , from the surface region and accommodating there the oriented molecules of adsorbate, B.<sup>113</sup> Using the assumptions listed in Ref. 114, the dependence for  $\Delta\chi^S$  is of the form

$$\Delta\chi^S = \left[ \frac{p_B}{\epsilon_0\epsilon_{B(S)}} - \frac{np_S}{\epsilon_0\epsilon_{S(B)}} \right] N_B + \left[ \frac{np_S}{\epsilon_0\epsilon_{S(B)}} - \frac{np_S}{\epsilon_0\epsilon_S} \right] N_B^0 \quad (29)$$

where  $p_B$ ,  $p_s$  and  $\epsilon_B$ ,  $\epsilon_s$  are the bulk dipole moment and relative dielectric constant for the solvent and substance B, respectively,  $\epsilon_0$  is the permittivity of the vacuum, and  $N_B$  is the surface amount of adsorbate. Parameter  $n$  is, in the limiting case, treated as the ratio of molar volumes, or better, partial molar volumes.

For  $N_B \rightarrow 0$ , the second term in Eq. (29) approaches 0, and we can obtain the slope of the relationship  $\Delta\chi^s = f(N_B)$ :

$$\left( \frac{\partial \Delta\chi}{\partial N_B} \right)_{N_B \rightarrow 0} = \text{const} \left[ \frac{P_B}{\epsilon_B} - n \frac{P_{sS}}{\epsilon_S} \right] = \text{const } \bar{p} \quad (30)$$

The expression in brackets is a more usable dependency [Eq. (30)] and describes the physical sense of the apparent dipole moment  $p$ . The model up to now has been used only for adsorption from solution.

The models presented above have also been reviewed in Ref. 18. Recently, an expression for the adsorption potential at the free water surface based on a combination of the electrostatic theory of dielectrics and classical thermodynamics has also been proposed.<sup>115</sup>

The popular applications of the adsorption potential measurements are those dealing with the surface potential changes at the water/air and water/hydrocarbon interface when a monolayer film is formed by an adsorbed substance.<sup>4-8,10-14,18,108,109</sup> Phospholipid monolayers, for instance, formed at such interfaces have been extensively used to study the surface properties of the monolayers. These are expected to represent, to some extent, the surface properties of bilayers and biological as well as various artificial membranes. An interest in a number of applications of ordered thin organic films (e.g., Langmuir and Blodgett layers) dominated research on the insoluble monolayer during the past decade.

Research on the adsorption potentials of aqueous solutions containing various short-chain organic compounds, developed mainly by Kamieński's school,<sup>49,116</sup> is still intensively continued by his successors.<sup>103-110</sup> The investigations also deal with mixed adsorbate systems.<sup>117,118</sup>

Our laboratory has investigated adsorption behavior at air/water and Hg/water interfaces, the adsorption potentials caused by the aliphatic nitriles,<sup>119</sup> dinitriles,<sup>120</sup> monoalkyl ethers,<sup>121</sup> dialkylethers,<sup>122</sup> propylglyl alcohol,<sup>123,124</sup> and dimethylsulfoxide.<sup>125</sup> The influence of the relative positions of two OH groups using the isomeric butanediols has been also studied.<sup>126</sup>

Adsorption potential shifts are higher at the air/solution than at the Hg/solution interface. This aspect has been discussed in terms of nonlocal electronic effects in the metal surface and different molecular orientation at the two interfacee.<sup>119-120</sup>

Recently, changes in the surface potential  $\Delta\chi^W$  of some organic solvents, specifically ethylene glycol,  $\gamma$ -butyrolactone,<sup>127</sup> and dimethylsulfoxide<sup>128</sup> upon adsorption of dipolar organic substances (e.g., chloroform and octanol) have been measured systematically for the first time.

### XIII. ADSORPTION POTENTIALS OF SURFACE-ACTIVE ELECTROLYTES

Equations (25) to (29) concern the case of neutral adsorbates, where there is no ionic double layer to contribute to the surface potential. In the case of charged (i.e., ionic) adsorbates, the measured potential  $\Delta\chi^W$  consists of two terms. The first term is due to dipoles oriented at the interface, which may be described by the above formulas, and the second term presents the potential of the ionic double layer at the interface from the aqueous side,<sup>4-8,11,12,14</sup>

$$\Delta\chi^W = \bar{p}/A_B + g^W(\text{ion}) \quad (13)$$

The  $g^W(\text{ion})$  is the electrical potential drop between the film of adsorbed long-chain ions and the bulk of aqueous solution.  $A_B$  is the reciprocal value of  $N_B$  and expresses the surface area per ion.

The physical meaning of the  $g^W(\text{ion})$  potential depends on the accepted model of an ionic double layer. The proposed models correspond to the Gouy-Chapman diffuse layer, with or without allowance for the Stern modification and/or the penetration of small counter-ions above the plane of the ionic heads of the adsorbed large ions.<sup>4-8</sup> The experimental data obtained for the adsorption of dodecyl trimethylammonium bromide and sodium dodecyl sulfate strongly support the Haydon and Taylor mode<sup>1,5,7,8,129</sup> According to this model, there is a considerable space between the ionic heads and the surface boundary between, for instance, water and heptane. The presence in this space of small inorganic ions forms an additional diffuse layer that partly compensates for the diffuse layer potential between the ionic heads and the bulk solution. Thus, the Eq. (31) may be considered as a linear combination of two linear functions, one of which  $[\Delta\chi^W - g^W(\text{dip})]$  crosses the zero point of the coordinates ( $\Delta\chi^W$  and  $1/A$  are equal to zero), and the other has an intercept on the potential axis. This, of course, implies that the orientation of the apparent dipole moments of the long-chain ions is independent of  $A$ .

The measurement of change in the surface potentials of aqueous solutions of electrolytes caused by adsorption of ionophore (e.g., crown ether) monolayers seems to be a convenient and promising method to ascertain selectivity and the effective dipole moments of the ionophore-ion complexes created at the water surface.<sup>130</sup>

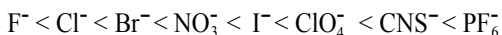
The presence of adsorbed Langmuir monolayers may induce very high changes in the surface potential of water. For example,  $\Delta\chi^W$  shifts attaining ca.  $-0.9$  (hexadecylamine hydrochloride) and ca.  $+1.0$  V (perfluorodecanoic acid) have been observed.<sup>2,118</sup>

Studies of the adsorption of surface-active electrolytes at the oil-water interface provide a convenient method for testing electrical double-layer theory and for determining the state of water and ions in the neighborhood of an interface. The change in the surface amount of the large ions modifies the surface charge density. For instance, a surface ionic area of  $100 \text{ \AA}^2$  per ion corresponds to  $16 \text{ \mu C}$  per square centimeter.<sup>4-8,11,12,14</sup>

The measurement of the concentration dependence of the changes in surface potential was also used to find critical concentration for forming a micellar solution. Near this critical concentration, one can observe a very strong fall in  $\Delta\chi$ .<sup>131</sup>

#### XIV. ADSORPTION POTENTIALS OF INORGANIC IONS

Investigations by Frumkin<sup>132</sup> and Randles<sup>3,10,133</sup> have shown that simple inorganic salts induce positive changes in the surface potential of water. These changes are small compared with the influence of surface-active additives, discussed above, and amount to several tens of millivolts, even at electrolyte concentrations reaching  $1 \text{ M}$ . In solutions of alkali metal salts, the value of  $\Delta\chi^W$  depends mainly on the anion and in a very small degree only on the cation. This was confirmed by other investigations.<sup>134-136</sup> Differences between the changes in the surface potentials induced by different simple salts led to the recognition of the following series of anions according to Refs. 133 and 134, arranged according to the magnitude of these changes, respectively:



and



These series are also consistent with increasing ionic radii, decreasing solvation energy, decreasing surface tension, and increasing probability of fractured hydrogen bonding between the molecules of water.<sup>3,10,132-136</sup> The cations of alkali metals do not markedly influence changes in  $\chi^W$ , but this influence becomes significant in solutions containing tetraalkylammonium ions<sup>137-139</sup> The tentative theoretical approach given by Randles to the variation in surface potential in terms of a simple model of the ionic double layer did not provide, according to the author,<sup>3,10,133</sup> a satisfactory explanation. The surface changes, however, do not appear to be a simple function of the hydration energy. The surface potential changes must also involve the orientation and structure of the water molecules at the water/air interface, which may be only partially dependent upon the ionic properties as determined in bulk solution.<sup>132-136</sup> Investigations of inorganic acids and tetraalkylammonium compound solutions confirm this statement.<sup>137-139</sup>

It was shown experimentally that inorganic acids change the surface potential of water more than do the corresponding alkali metal salts.<sup>132-133</sup> According to Randles, the most probable hypothesis explaining the large positive shift of surface potential,  $\Delta\chi^W$ , is the assumption that in solutions of acids  $\text{H}_3\text{O}^+$  ions easily penetrate into the uppermost molecular layer at the surface and are preferentially oriented with their protons directed into the liquid phase. It is also possible that the orientation of neighboring water molecules is influenced in such a way as to enhance the effect of the  $\text{H}_3\text{O}^+$  dipole itself.<sup>133</sup> This hypothesis seems to be confirmed by a comparison of the  $\Delta\chi^S$  values measured for acid solutions in methanol-water mixtures with the  $\Delta\chi^S$  values of the respective alkali-metal salts in the mixtures.<sup>140</sup>

Similarly as in water, small changes of  $\Delta\chi^S$  are observed in the case of nonaqueous solutions of inorganic salts, but the direction of change is opposite to that in water, i.e.,  $\Delta\chi < 0$  for solutions of electrolytes in solvents like methanol, ethanol, acetonitrile, and acetone.<sup>141</sup> The changes in the surface potential of aqueous, methanolic, and mixed solutions of tetramethylammonium chlorides, bromides and iodides were also measured. The sign of  $\Delta\chi^S$  in methanol is opposite to that in water.<sup>142</sup>

## XV. SURFACE POTENTIALS OF WATER AND ORGANIC SOLVENTS

The surface potential of water,  $\chi^W$ , as any other surface potential, is not measurable. Its probable value is inferred from indirect observations. Such a potential difference has been postulated because the tetrahedral charge



distribution of water molecules might lead to preferential orientation in the surface layer and thus to a dipole layer that would make the mean electrostatic potential at the surface different from that in the bulk. Consecutive reviews contain discussions of various attempts to estimate  $\chi^W$  and partly also the surface potentials of organic solvents,  $\chi^S$ , in particular that of methanol.<sup>142-144</sup>

Many attempts to estimate  $\chi^W$  on the basis of different nonthermodynamic assumptions have shown that the value of this potential is positive and that it is comparatively small. According to subsequent estimates by Frumkin,<sup>2,141</sup> Randles,<sup>3,10</sup> and Trasatti<sup>9,145</sup>  $\chi^W$  is equal to: +0.1, +0.08 ± 0.06, and +0.13 V, respectively. Dynamic experiments have confirmed this order of  $\chi^W$  value.<sup>146</sup> The time of establishing the equilibrium value has been found to be about 3 ms.

The impossibility of  $\chi^W$  being equal to about 1 V, as suggested by Kamienki,<sup>49,116</sup> has been demonstrated by Frumkin<sup>141</sup> on the basis of a discussion of the real energies of hydration.<sup>48</sup> Estimates from the variation in the solution surface potential with electrolyte molarity have yielded the value of +0.025 ± 0.010 V.<sup>21</sup> For methanol, the same method results in a value of -0.09 V.<sup>146</sup> Later the authors of that investigation stated that both estimated values should be understood as the lower limits of surface potentials of water and methanol.<sup>143</sup>

Therefore, it seems to be generally accepted that  $\chi^W$  has a positive value, 0.13 ± 0.02 V,<sup>9,144</sup> decreasing with increasing temperature. The negative value of the temperature coefficient of  $\chi^W$ , found experimentally<sup>147,148</sup> is important evidence in favor of a positive value of the surface potential of water. It implies that water molecules at the free surface have their proton ends oriented toward the bulk liquid, thus facilitating the formation of hydrogen bonds.<sup>149</sup> It is worth noting that the calculation of  $\chi^W$  from the simple Helmholtz equation (26), using the bulk solvent dielectric constant, leads to the value +0.09 to +0.113 V.<sup>114</sup> The arguments in favor of a comparatively high dielectric constant of the surface zone of a polar liquid have also been discussed.<sup>114,150</sup> A theoretical evaluation based on classical electrostatics has also confirmed the tendency for surface water molecules to orient their protons away from the vapor and into the water.<sup>151-153</sup>

Recent molecular dynamics studies of properties of the water surface have led to predictions of the surface potential of water that differ not only in magnitude but also in sign.<sup>21,154-157</sup> The main problem is connected with the difficulty of proper definition of the surface potential of a real polar

liquid, which must take into account the molecular nature of a liquid.<sup>21</sup> There is some evidence that the surface potential of very thin layers of water covering metal surfaces, for instance emersed electrodes, has a negative value.<sup>158</sup>

The published experimental estimates of the surface potentials of various organic solvents have been derived mainly from the data on the real, asi, and chemical,  $\mu_i^S$ , energies of solvation of ions:

$$F\chi^S = \alpha_i^S - \mu_i^S$$

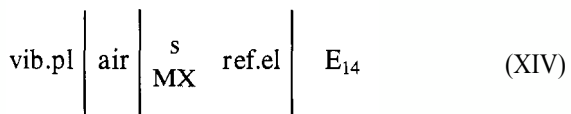
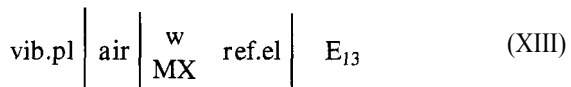
or from the differences of these energies in the solvent and water<sup>81-87</sup>

$$F\Delta_w^S \chi = \Delta_w^S \alpha_i - \Delta_w^S \mu_i \quad (32)$$

According to the above equations, the surface potential is the difference between the real and chemical potentials of charged particles dissolved in the liquid phase.

Trasatti has calculated the potentials ( $\chi^S$ ) of several organic solvents from Volta potentials and the partial surface potentials on the mercury solution phase boundaries at the potential of zero charge.<sup>79</sup>

The difference between the surface potentials of two solvents (e.g., an organic solvent and water) may also be measured by means of the following voltaic cells<sup>15,19,114,160</sup> (Fig. 12):



If both liquid junction potentials are eliminated and supporting electrolytes  $MX$  are not adsorbed at the free surfaces of solvents, the compensating voltage is

$$E = E_{14} - E_{13} = \Delta_w^S \chi \quad (33)$$

The liquid junction potential from the organic side may be negligible, owing to the use of a nitrobenzene-water partition system containing tetraethylammonium picrate as the salt bridge. The mobilities of both ions in nitrobenzene are similar, and they have similar Gibbs energies of

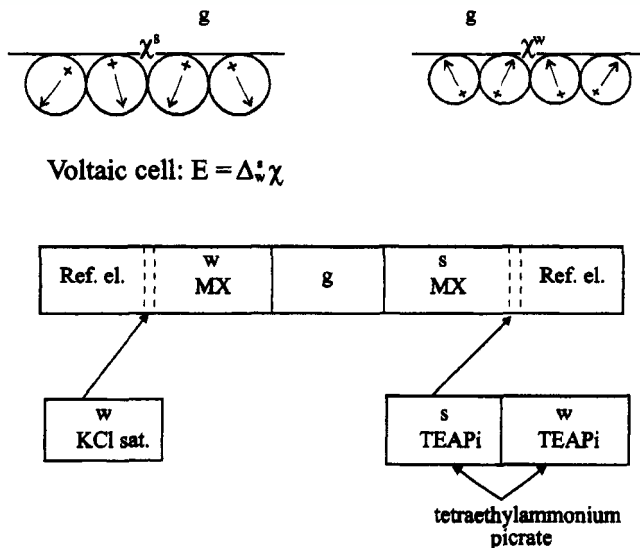


Figure 12. Difference between the surface potentials of water and an organic solvent.

transfer from water to nitrobenzene.<sup>15,19,93</sup> The voltaic cell presented in Fig. 12 has been used experimentally in the form of the above two cells.

The method has been used for about 20 organic solvents, including simple aliphatic alcohols, diols, alkoxyethanols, 1,2-dichloroethane (DCE), and nitroethane (NE).<sup>114,61,96-98</sup> Among them were the most intensively investigated solvents, such as methanol, ethanol, and acetonitrile. The surface potentials of all the solvents investigated were, as expected, negative, and equal to about 0.1–0.2 V. This is in agreement with direct measurement of the temperature coefficient of  $\chi^S$ , for example, of methanol.<sup>159</sup> The results are qualitatively the same as those found by other authors and as calculated by means of Eq. (26).<sup>114</sup>

This approach allowed us also to determine the difference in the surface potentials between mutually saturated water and an organic solvent: namely, nitrobenzene,<sup>96,97</sup> nitroethane and 1,2-dichloroethane,<sup>98</sup> and isobutyl methyl ketone (IBMK).<sup>61</sup> The qualitative data show a very strong influence of the added organic solvent on the surface potential of water, while the presence of water in the nonaqueous phase has practically no

effect on its  $\chi^S$  potential. In the case of NB, NE, and DCE solvents, the  $\Delta_{w\chi}^{w+s}$  values for the water phase saturated with these solvents are lower than  $\Delta_{w\chi}^S$ . For IBMK, the maximum is observed, which means that the surface orientation of the molecules of the solvent in water is larger than in pure IBMK. The information resulting from the surface potential measurements may be used in the analysis of the interfacial structure of liquid/liquid interfaces and their dipole and zero-charge potentials.<sup>24</sup> Also, among organic solvents that are fully miscible with water, monotonic changes have been observed for only a few systems, i.e., those containing methanol, ethanol, ethylene glycol, and 1,2-propylene glycol (Fig. 13).<sup>114</sup> For the majority of solvents investigated, the maximum of  $\Delta_{w\chi}^{w+s}$  is observed for a mole fraction smaller than 1 (Fig. 12).<sup>114</sup> This behavior indicates that the linear extrapolation of  $\Delta_{w\chi}^{w+s}$  sometimes used to estimate  $\chi^S$ <sup>59,60</sup> is not justified in every case.

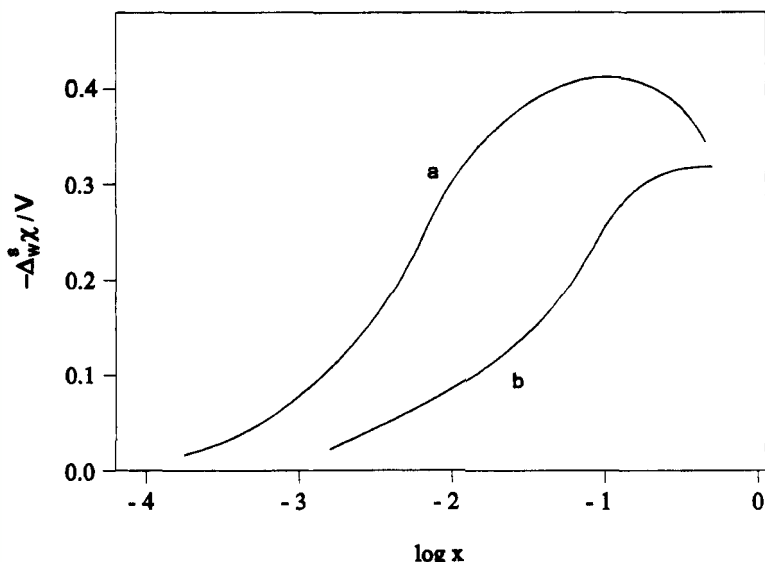


Figure 13. Two typical dependencies of  $-\Delta_{w\chi}^s$  on organic mole fraction in the mixture with water: (a) with (e.g., water + methoxyethanol) and (b) without (e.g., water + methanol) maximum, respectively.

## XVI. FINAL REMARKS

This review has been restricted mainly to clarification of the fundamentals and to presenting a coherent view of the actual state of research on voltaic cells, as well as their applications. Voltaic cells are, or may be, used in various branches of electrochemistry and surface chemistry, both in basic and applied research. They particularly enable interpretations of the potentials of various interphase and electrode boundaries, including those that are employed in galvanic and electroanalytical cells.

As stressed in the introduction, the main difficulty of the voltaic cell method of investigating systems is its lack of molecular specificity. Therefore, complementary information should be obtained by using techniques sensitive to the polar ordering and arrangement of molecules in a surface or interfacial layer, such as optical, spectroscopic, and scanning tunneling microscope methods.<sup>161-165</sup>

## ACKNOWLEDGMENT

The author is pleased to acknowledge financial support from the Polish Committee on Scientific Research (BST-592/19/99).

## REFERENCES

- <sup>1</sup>R. Parsons, in *Modern Aspects of Electrochemistry*, Vol. 1, Ed. by J. O'M. Bockris and B. M. Conway, Butterworths, London, 1954, Chap. 3.
- <sup>2</sup>A. N. Frumkin, X. A. Jofa, and M. A. Gerovich, *Zh. Fiz. Khim.* **30** (1956) 1456-1468.
- <sup>3</sup>J. E. B. Randles, *Adv. Electrochem. Eng.* **3** (1963) 1-30.
- <sup>4</sup>J. T. Davies and E. K. Rideal, *Interfacial Phenomena*, Academic Press, New York, 1963, Chaps. 2, 4, 5, and 6.
- <sup>5</sup>D. A. Haydon, in *Recent Progress in Surface Science*, Ed. by J. F. Danielli, K. G. A. Pankhurst, A. C. Riddiford, Academic Press, New York, 1964, Chap. 3.
- <sup>6</sup>G. L. Gaines, *Insoluble Monolayers at Liquid-Gas Interfaces*, Interscience, New York, 1966, Chaps. 4 and 5.
- <sup>7</sup>J. Llopis, in *Modern Aspects of Electrochemistry* Vol. 6, Ed. by J. O'M. Bockris and B. E. Conway, Plenum Press, New York, 1971, pp. 9-159.
- <sup>8</sup>R. Aveyard, and D. A. Haydon, *An Introduction to the Principles of Surface Chemistry*, Cambridge Univ. Press, London, 1973, Chaps. 2 and 3.
- <sup>9</sup>A. de Battisti and S. Trasatti, *Croat. Chem. Acta* **48** (1976) 607-622.
- <sup>10</sup>E. B. Randles, *Phys. Chem. Liq.* **7** (1977) 107-179.
- <sup>11</sup>A. W. Adamson, *Physical Chemistry of Surfaces*, Wiley-Interscience, New York, 1982, Chaps. 4 and 5.
- <sup>12</sup>D. K. Chattoray and K. S. Birdi, *Adsorption and Gibbs Surface Excess*, Plenum Press, New York, 1984, Chaps. 5 and 6.
- <sup>13</sup>S. Trasatti and R. Parsons, *Pure & Appl. Chem.* **58** (1986) 1251-1268.
- <sup>14</sup>K. S. Birdi, Plenum Press, New York, 1988, Chaps. 4 and 5.

- <sup>15</sup>Z. Koczorowski, in *The Interface Structure and Electrochemical Processes at the Boundary Between Two Immiscible Liquids*, Ed. by V. E. Kazarinov, Springer Verlag, Berlin, 1987, pp. 77–106.
- <sup>16</sup>L. I. Boguslavsky and A. G. Volkov, in *The Interface Structure and Electrochemical Processes at the Boundary Between Two Immiscible Liquids*, Ed. by V. E. Kazarinov, Springer Verlag, Berlin, 1987, pp. 143–178.
- <sup>17</sup>A. Ulman, *An Introduction to Ultrathin Organic Films: From Langmuir–Blodgett to Self-Assembly*, Academic Press, Boston, 1991.
- <sup>18</sup>P. Dynarowicz, *Adv. Colloid Interface Sci.* **45** (1993) 215–241.
- <sup>19</sup>Z. Koczorowski, *Liquid–Liquid Interfaces: Theory and Methods*, Ed. by A. G. Volkov and D. W. Deamer, CRC Press, Boca Raton, FL, 1996, pp. 19–37.
- <sup>20</sup>Ju. F. Rybkin, (in Russian) *Uspiechi Khim.* **44** (1975) 1345–1365.
- <sup>21</sup>J. R. Farrel and P. McTigue, *J. Electroanal. Chem.* **139** (1982) 37–56.
- <sup>22</sup>S. Trasatti, in *Electrified Interfaces in Physics, Chemistry and Biology*, Ed. by R. Guidelli, Kluwer Academic Publishers, London, 1992, pp. 229–244.
- <sup>23</sup>S. Trasatti, in *Electrified Interfaces in Physics, Chemistry and Biology*, Ed. by R. Guidelli, Kluwer Academic Publishers, London, 1992, pp. 245–273.
- <sup>24</sup>Z. Koczorowski, *J. Electroanal. Chem.* **190** (1985) 257–260.
- <sup>25</sup>B. A. Pethica, M. M. Standish, J. Mingins, C. Smart, D. H. Iles, M. E. Feinstein, S. A. Hossain, and J. B. Pethica, in *Advances in Chemistry*, No. 144, *Monolayers*, Ed. by E. Goddard, American Chemical Society, Washington, 1975, pp. 123–134.
- <sup>26</sup>D. Walz and S. R. Caplan, *Bioelectrochem. Bioenerg.* **28** (1992) 5–30.
- <sup>27</sup>L. R. Pratt, *J. Phys. Chem.* **96** (1992) 25–33.
- <sup>28</sup>D. Dragčević and M. Milunović, *Kem. Ind.* **36** (1987) 429439.
- <sup>29</sup>H. Hühnerfuss, *J. Colloid Interface Sci.* **128** (1989) 237–244.
- <sup>30</sup>M. Plaisance and L. Ter-Minassion-Saraga, (in French) *C. R. Acad. Sci. Paris* **270** (1970) 1269–1272.
- <sup>31</sup>H. G. Yamins and W. A. Zisman, *J. Chem. Phys.* **1** (1933) 656–661.
- <sup>32</sup>W. A. Zisman, *Rev. Sci. Instr.* **3** (1932) 367–370.
- <sup>33</sup>N. A. Surplice and R. J. D'Arcy, *J. Phys. E: Sci. Instrum.* **3** (1970) 477–482.
- <sup>34</sup>S. Minc, I. Zagórska, and Z. Koczorowski, *Roczniki Chem.* **41** (1983) 1983–1991.
- <sup>35</sup>H. A. Engelhardt, P. Feulner, H. Pfnür, and D. Menzel, *J. Phys. E: Sci. Instrum.* **10** (1970) 1133–1136.
- <sup>36</sup>L. B. Harris and J. Fiason, *J. Phys. E: Sci. Instrum.* **17** (1984) 788–792.
- <sup>37</sup>K. W. Benig and W. A. Zisman, *J. Phys. Chem.* **67** (1963) 130–135.
- <sup>38</sup>J. M. Palau and J. Bonnet, *J. Phys. E: Sci. Instrum.* **21** (1988) 674–679.
- <sup>39</sup>S. Yee, R. A. Orani, and M. Stratmann, *J. Electrochem. Soc.* **138**, (1991) 55–61.
- <sup>40</sup>H. D. Liess, R. Mäckel, H. Baumagärtner, and J. Ren, *Sensors Actuators B* **13–14** (1993) 739–740.
- <sup>41</sup>S. M. Huang, R. T. Atanasoski, and R. A. Oriani, *J. Electrochim. Soc.* **140** (1993) 1065–1067.
- <sup>42</sup>M. Fujihira and K. Hirotsuke, *Thin Solid Films* **242** (1994) 163–169.
- <sup>43</sup>M. T. Nguyen, K. K. Kanazawa, P. Brock, and A. E. Diaz, *Langmuir* **10** (1994) 597–602.
- <sup>44</sup>T. Delchar, A. Eberhagen, and F. C. Tomkins, *J. Sci. Instrum.* **40** (1963) 105–107.
- <sup>45</sup>J. L. M. Venselaar, A. J. Kruger, L. M. H. Verbakel, and J. A. Poulis, *J. Colloid Interface Sci.* **70** (1979) 149–152.
- <sup>46</sup>J. C. Jacobs, A. J. M. Buuron, P. J. M. Renders, and A. F. M. Snik, *J. Colloid Interface Sci.* **84** (1981) 270–271.
- <sup>47</sup>Yu. S. Gerasimenko and I. F. Khikh-Yalan, (in Russian) *Elektrokhimiya* **18** (1982) 15–19.
- <sup>48</sup>J. E. B. Randles, *Trans. Faraday Soc.* **52** (1956) 1573–1581.
- <sup>49</sup>B. Kamien'ski, in *Proc. 2nd Congr. Surf. Act.*, Vol. 3, J. H. Schulman (ed.), Butterworths, London, 1957, pp. 103–121.

- <sup>50</sup>S. W. Lopatenko, *Zh. Fiz. Khim.* **55** (1981) 2156–2157.
- <sup>51</sup>K. Doblhofer and M. Cappadonia, *J. Electroanal. Chem.* **243** (1988) 337–342.
- <sup>52</sup>L. I. Antropov, M. A. Gerasimenko, Yu. S. Gerasimenko, and I. E. Khirikh-Yalan, (in Russian) *Elektrokhimiya* **20** (1984) 1578–1582.
- <sup>53</sup>L. I. Antropov, M. A. Gerasimenko, I. F. Khirikh-Yalan, and E. E. Skholnaiya, *Elektrokhimiya* **20** (1984) 1357–1360.
- <sup>54</sup>L. I. Antropov, M. A. Gerasimenko, and I. F. Khirikh-Yalan, *Elektrokhimiya* **21** (1985) 59–597.
- <sup>55</sup>S. Minc and I. Zagórska, *Electrochim. Acta* **16** (1971) 609–613.
- <sup>56</sup>B. Case, N. S. Hush, R. Parsons, and M. E. Peover, *J. Electroanal. Chem.* **10** (1965) 360–370.
- <sup>57</sup>B. Case and R. Parsons, *Trans. Faraday Soc.* **63** (1967) 1224–1239.
- <sup>58</sup>I. Zagórska and Z. Koczorowski, *Roczniki Chem.* **44** (1970) 1559–1564.
- <sup>59</sup>B. Jakuszewski and H. Scholl, *Electrochim. Acta* **17** (1972) 1105–1111.
- <sup>60</sup>R. Parsons and B. T. Rubin, *J. Chem. Soc. Faraday Trans. 1*, **70** (1974) 1636–1648.
- <sup>61</sup>Z. Koczorowski and I. Zagórska, *J. Electroanal. Chem.* **193** (1985) 113–122.
- <sup>62</sup>V. I. Parfenyuk, J. A. Paramonov, T. I. Thankina, and G. A. Krestov, (in Russian), *Zh. Fiz. Khim.* **63** (1989) 1493–1497.
- <sup>63</sup>V. I. Parfenyuk and T. I. Thankina, *Elektrokhimiya* **32** (1996) 993–995.
- <sup>64</sup>V. A. Rabinovich, A. E. Nikerov, and V. P. Rotsein, *Electrochim. Acta* **12** (1967) 155–159.
- <sup>65</sup>Yu. F. Rybkin and M. G. Karpenko, *Electrochim. Acta* **11** (1966) 1135–1139.
- <sup>66</sup>V. A. Rabinovich, *Thermodynamic Activity of Ions in Electrolyte Solutions* (in Russian) Khimiya, Leningrad (1985).
- <sup>67</sup>Z. Koczorowski and I. Zagórska, *J. Electroanal. Chem.* **91** (1978) 395–397.
- <sup>68</sup>I. Zagórska and Z. Koczorowski, *J. Electroanal. Chem.* **101** (1979) 317–328.
- <sup>69</sup>J. L. Copeland and R. L. Seifert, *J. Electrochem. Soc.* **112** (1965) 813–36.
- <sup>70</sup>Yu. I. Malov, N. G. Bukun, and E. A. Ukshe, *Elektrokhimiya* **15** (1979) 422–424.
- <sup>71</sup>E. A. Ukshe, Yu. I. Malov, and N. G. Buku, *Elektrokhimiya* **24** (1988) 723–727.
- <sup>72</sup>E. A. Kaniewski, (in Russian) *Zh. Fiz. Khim.* **27** (1953) 296–309.
- <sup>73</sup>S. Trasatti, *Pure Appl. Chem.* **58** (1986) 955–966.
- <sup>74</sup>S. Trasatti, *Electrochim. Acta* **35** (1990) 269–271.
- <sup>75</sup>S. Trasatti, *J. Electroanal. Chem.* **52** (1974) 313–329.
- <sup>76</sup>R. Gomer and G. Tryson, *J. Chem. Phys.* **66** (1977) 4413–4424.
- <sup>77</sup>H. Reiss and A. Heller, *J. Chem. Phys.* **89** (1985) 4207–4213.
- <sup>78</sup>H. Reiss, *J. Electrochem. Soc.* **135** (1988) 247c–258c.
- <sup>79</sup>S. Trasatti, *Electrochim. Acta* **32** (1987) 843–850.
- <sup>80</sup>N. Sato, *Russ. J. Electrochem.* **31** (1995) 906–914.
- <sup>81</sup>W. N. Hansen, C. L. Wang, and T. W. Humphrerys, *J. Electroanal. Chem.* **93** (1978) 87–98.
- <sup>82</sup>W. N. Hansen and D. M. Kolb, *J. Electroanal. Chem.* **100** (1979) 493–500.
- <sup>83</sup>W. N. Hansen, *J. Electroanal. Chem.* **150** (1983) 133–140.
- <sup>84</sup>G. J. Hansen and W. N. Hansen, *J. Electroanal. Chem.* **150** (1983) 193–200.
- <sup>85</sup>M. Cappadonia, K. Doblhofer, and M. Jauch, *Ber. Bunsenges. Phys. Chem.* **92** (1988) 903–908.
- <sup>86</sup>K. Doblhofer and M. Cappadonia, *Colloids and Surfaces* **41** (1989) 211–222.
- <sup>87</sup>Z. Samec, B. W. Johnson, and K. Doblhofer, *Surf. Sci.* **264** (1992) 440–448.
- <sup>88</sup>J. K. Sass, D. Lackey, and J. Scott, *Electrochim. Acta* **36** (1991) 1883–1887.
- <sup>89</sup>F. T. Wagner, in *Structure of Electrified Interfaces*, Ed. by J. Lipkowski and P. N. Ross, VCH, New York, 1993, pp. 309–400.
- <sup>90</sup>E. M. Stuve, A. Krasnopoler, and E. D. Sauer, *Surf. Sci.* **335** (1995) 177–185.
- <sup>91</sup>S. Trasatti, *Surf. Sci.* **335** (1995) 1–9.
- <sup>92</sup>Z. Borkowska and U. Stimming, in *Structure of Electrified Interfaces*, Ed. by J. Lipkowski and P. N. Ross, VCH, New York, 1993, pp. 277–307.

- <sup>93</sup> Z. Koczorowski, *J. Electroanal. Chem.* **127** (1981) 11–16.
- <sup>94</sup> S. Minc and Z. Koczorowski, *Electrochim. Acta* **8** (1963) 575–582.
- <sup>95</sup> Z. Koczorowski and S. Minc, *Electrochim. Acta* **8** (1963) 645–649.
- <sup>96</sup> Z. Koczorowski and I. Zagórska, *J. Electroanal. Chem.* **159** (1983) 183–193.
- <sup>97</sup> I. Zagórska and Z. Koczorowski, *J. Electroanal. Chem.* **204** (1986) 273–279.
- <sup>98</sup> I. Zagórska, Z. Koczorowski, and I. Paleska, *J. Electroanal. Chem.* **282** (1990) 51–58.
- <sup>99</sup> K. Doblhofer, in *The Electrochemistry of Novel Materials*, Ed. by J. Lipkowski and P. N. Ross, VCH, New York, 1994, pp. 141–205.
- <sup>100</sup> M. M. Mueller, *Diss. Abs.* **20** (1959) 901.
- <sup>101</sup> Z. Koczorowski, doctoral thesis, Warsaw Univ., 1961.
- <sup>102</sup> R. J. Demchak and T. Fort, Jr., *J. Colloid Interface Sci.* **46** (1974) 191–202.
- <sup>103</sup> P. Dynarowicz and M. Paluch, *J. Colloid Interface Sci.* **107** (1985) 75–80.
- <sup>104</sup> M. Paluch and P. Dynarowicz, *J. Colloid Int. Sci.* **115** (1987) 307–311.
- <sup>105</sup> M. Paluch and P. Dynarowicz, *J. Colloid Int. Sci.* **115** (1989) 379–383.
- <sup>106</sup> P. Dynarowicz, *Colloid Polym. Sci.* **267** (1989) 941–945.
- <sup>107</sup> M. Paluch and J. Rybska, *J. Colloid Int. Sci.* **145** (1991) 219–223.
- <sup>108</sup> V. Vogel and D. Möbius, *J. Colloid Interface Sci.* **126** (1988) 408–420.
- <sup>109</sup> O. N. Oliveira, Jr., A. Riul, and Leal G. F. Ferreira, *Thin Solid Films* **242** (1994) 239–242.
- <sup>110</sup> P. Dynarowicz, *Colloid and Surfaces* **59** (1991) 371–376.
- <sup>111</sup> A. N. Frumkin, B. B. Damaskin, and A. A. Survila, *J. Electroanal. Chem.* **16** (1968) 493–.
- <sup>112</sup> B. B. Damaskin, A. N. Frumkin, and A. Chizhov, *J. Electroanal. Chem.* **28** (1970) 93–.
- <sup>113</sup> Z. Koczorowski, S. Kuroski, and S. Trasatti, *J. Electroanal. Chem.* **329** (1992) 25–34.
- <sup>114</sup> Z. Koczorowski, I. Zagórska, and A. Kalinska, *Electrochim. Acta.* **34** (1989) 1857–1862.
- <sup>115</sup> P. Nikitas and A. Pappa-Louisi, *J. Electroanal. Chem.* **385** (1995) 257–263.
- <sup>116</sup> B. Kamieński, *Electrochim. Acta* **1** (1959) 272–277.
- <sup>117</sup> P. Dynarowicz, M. Paluch, and B. Walińska, *Tenside Surf. Det.* **27** (1990) 184–186.
- <sup>118</sup> M. Paluch and B. Gzyl, *J. Colloid Interface Sci.* **179** (1996) 51–56.
- <sup>119</sup> A. Daghetti, S. Trasatti, I. Zagórska, and Z. Koczorowski, *J. Electroanal. Chem.* **129** (1981) 253–264.
- <sup>120</sup> S. Mingozzi, A. Daghetti, S. Trasatti, I. Zagórska, and Z. Koczorowski, *J. Chem. Soc. Faraday I*, **79** (1983) 2801–2812.
- <sup>121</sup> A. Daghetti, S. Trasatti, I. Zagórska, and Z. Koczorowski, *J. Electroanal. Chem.* **204** (1986) 299–313.
- <sup>122</sup> A. Daghetti, S. Trasatti, I. Zagórska, and Z. Koczorowski, *Electrochim. Acta* **33** (1988) 1705–1711.
- <sup>123</sup> A. Daghetti, S. Trasatti, G. Rochini, I. Zagórska, and Z. Koczorowski, *Colloids and Surfaces* **41** (1989) 135–147.
- <sup>124</sup> A. Daghetti, S. Trasatti, I. Zagórska, and Z. Koczorowski, *Colloids and Surfaces* **51** (1990) 29–36.
- <sup>125</sup> J. Dpbkowski, I. Zagórska, M. Dpbkowska, Z. Koczorowski, and S. Trasatti, *J. Chem. Soc. Faraday Trans.* **92** (1996) 3873–3878.
- <sup>126</sup> I. Zagórska, Z. Koczorowski, and S. Trasatti, *J. Electrochem. Chem.* **366** (1994) 211–218.
- <sup>127</sup> Z. Koczorowski, I. Zagórska, R. Pruszkowska-Drachal, and S. Trasatti, *Russian J. Electrochem.* **31** (1995) 822–827; *Elektrokhimija* **31** (1995) 89–891.
- <sup>128</sup> J. Dgbkowski, M. Dgbkowska, R. Pruszkowska-Drachal, Z. Koczorowski, and S. Trasatti, *Electrochim. Acta* **42** (1997) 2899–2905.
- <sup>129</sup> S. Minc and Z. Koczorowski, *Roczniki Chem.* **39** (1965) 469–478.
- <sup>130</sup> Z. Koczorowski, I. Zagórska, I. Paleska, E. Luboch, and J. E. Biernat, *Polish J. Chem.* **68** (1994) 1245–1251.
- <sup>131</sup> A. N. Frumkin, (in German), *Z. Physik. Chem.* **109** (1924) 34–48,
- <sup>132</sup> J. E. B. Randles, *Discuss. Faraday Soc.* **24** (1957) 197–199.
- <sup>133</sup> N. L. Jarvis and M. A. Scheiman, *J. Phys. Chem.* **72** (1968) 74–78.



- <sup>134</sup>N. L. Jarvis, *J. Geophys. Res.* **77** (1972) 5177–5182.
- <sup>135</sup>D. Chartier and B. Fotouhi, *J. Chim. Phys.* **71** (1974) 335–345.
- <sup>136</sup>B. B. Damaskin, R. I. Kaganovich, W. M. Gerovich, and S. L. Diatkina, (in Russian) *Elektrokhimija* **5** (1969) 507–511.
- <sup>137</sup>R. Benes and B. E. Conway, *Can. J. Chem.* **59** (1981) 1978–1986.
- <sup>138</sup>V. P. Rudy, M. V. Orinyak, A. V. Smogorshersky, and T. S. Slipenyuk, (in Russian), *Koll. Zh.* **46** (1984) 951–954.
- <sup>139</sup>I. Zagórska and Z. Koczorowski, *J. Electroanal. Chem.* **58** (1975) 251–253.
- <sup>140</sup>I. Zagórska and Z. Koczorowski, *Roczniki Chem.* **48** (1974) 57–61.
- <sup>141</sup>A. N. Frumkin, *Electrochim. Acta* **2** (1960) 351–354.
- <sup>142</sup>L. I. Kristhalik, N. M. Alpatova, and E. V. Ovsyannikova, *J. Electroanal. Chem.* **329** (1992) 1–8.
- <sup>143</sup>C. G. Barraclough, P. T. McTigue, and Y. Ieung Ng, *J. Electroanal. Chem.* **329** (1992) 9–24.
- <sup>144</sup>S. Trasatti, *J. Chem. Soc. Faraday Trans. I.* **70** (1974) 1752–1768.
- <sup>145</sup>N. N. Kochurova and A. I. Rusanov, *J. Colloid Interface Sci.* **81** (1981) 297–303.
- <sup>146</sup>C. G. Barraclough, A. Borazio, P. T. McTigue, and B. Verity, *J. Electroanal. Chem.* **243** (1988) 353–365.
- <sup>147</sup>J. E. B. Randles and D. J. Schiffrin, *J. Electroanal. Chem.* **10** (1965) 480–484.
- <sup>148</sup>J. R. Farrell and P. McTigue, *J. Electroanal. Chem.* **163** (1984) 129–136.
- <sup>149</sup>J. Goodisman, *Electrochemistry: Theoretical Foundations*, Wiley-Interscience, New York, 1987, p. 132.
- <sup>150</sup>B. E. Conway, *Croat. Chem. Acta* **48** (1976) 573–596.
- <sup>151</sup>N. N. Fletcher, *Phil. Mag.* **18** (1968) 1287–1300.
- <sup>152</sup>F. H. Stillinger, Jr. and A. Ben-Naim, *J. Chem. Phys.* **47** (1967) 4431–4437.
- <sup>153</sup>W. G. Madden, R. Gomer, and M. J. Mandell, *J. Phys. Chim.* **81** (1977) 2652–2657.
- <sup>154</sup>G. Aloisi, R. Guidelli, R. A. Jackson, S. M. Clark, and P. Barnes, *J. Electroanal. Chem.* **206** (1986) 131–137.
- <sup>155</sup>M. Matsumoto and Y. Kataoka, *J. Chem. Phys.* **88** (1988) 3233–3245.
- <sup>156</sup>M. A. Wilson and A. Pohorille, *J. Chem. Phys.* **88** (1988) 3281–3285.
- <sup>157</sup>A. Pohorille and M. A. Wilson, *J. Mol. Struct. (Theochem.)* **284** (1993) 271–298.
- <sup>158</sup>Z. Samec, B. W. Johnson, M. Cappadomia, M. Jauch, and K. Doblhofer, *Sensors and Actuators B* **13–14** (1993) 741–742.
- <sup>159</sup>Z. Koczorowski and I. Zagórska, *Roczniki Chem.* **44** (1976) 911–913.
- <sup>160</sup>S. Minc and I. Zagórska, *Electrochim. Acta* **16** (1971) 1213–1216.
- <sup>161</sup>B. B. Sauer, Y. Chen, G. Zograf, and H. Yu, *Langmuir* **4** (1988) 111–117.
- <sup>162</sup>M. C. Goh, J. M. Hicks, K. Kemnitz, G. R. Pinto, K. Bhattacharyya, K. B. Eisenthal, and T. F. Heinz, *J. Phys. Chem.* **92** (1988) 5074–5075.
- <sup>163</sup>V. Vogel, C. S. Mullin, and J. R. Shen, *Langmuir* **7** (1991) 1222–1224.
- <sup>164</sup>F. Bökman, O. Bohman, and H. O. G. Siegbahn, *Chem. Phys. Lett.* **189** (1992) 414–419.
- <sup>165</sup>R. Garcia-Garcia and J. J. Sáenz, *Surf. Sci.* **251/252** (1991) 223–227.

# **Direct Methanol Fuel Cells: From a Twentieth Century Electrochemist's Dream to a Twenty-first Century Emerging Technology**

Claude Lamy, Jean-Michel Léger, and  
Supramaniam Srinivasan\*

*Laboratory of Electrocatalysis, UMR CNRS N°6503, Université de Poitiers, Poitiers  
Cédex, France*

## **I. A SYNOPSIS OF FUEL CELL TECHNOLOGIES—BACKGROUND**

### **1. Energy Conservation and Environmental Friendliness—the Incentive for Fuel Cell Development**

The fuel cell is a nineteenth century invention; in the twentieth century it became the “heart” of an electrochemical power plant and power source, which is now in a stage of advanced technology development. Its first and only application since the early 1960s, has been as an auxiliary power source for space flights by the National Aeronautics and Space Administration (NASA). During the past decade, development for terrestrial (civilian and defense) applications has led to its commercialization and research on utilization in a variety of applications. Programs in the United States, Japan, Europe, and some other countries are focused on the development of fuel cell power plant/power sources for (1) base-load,

\*Present address: Center for Energy and Environmental Studies, Princeton University, Princeton, NJ, 08544-5263.

*Modern Aspects of Electrochemistry, Number 34*, edited by John O'M. Bockris *et al.*  
Kluwer Academic /Plenum Publishers, New York, 2001.

intermediate-load, peak-load, and dispersed electric utility power generation; (2) cogeneration (electricity plus heat for chemical industries, apartment buildings, hospitals, shopping centers); (3) transportation and electric vehicles (cars, motorcycles, buses, trucks, military vehicles, fleet vehicles, submarines, trains, ships); and (4) portable power sources (for remote areas or backpack power sources for soldiers).

Since the advent of the space era in the 1960s there has been an exponential growth in the number of publications each year on fuel cell R&D topics. The energy era, stimulated by the energy crisis of 1973, further enhanced the growth of such publications. However, in the early 1980s energy economists forecast an abundance of oil and natural gas reserves, and low energy prices (which was confirmed by lower prices of gasoline, diesel fuel, jet fuel, and heating oil in the 1980s and 1990s than in the 1940s, taking into consideration the changing value of the U.S. dollar). The incentive in the late 1980s and early 1990s for fuel cell R&D was environmental pollution, so that there is now an environmental era for the development of fuel cells. In the United States, emissions (CO, NO<sub>x</sub>, O<sub>3</sub>, particulates, SO<sub>2</sub>, etc.) from power plants and transportation vehicles are at about a similar level and account for over 90% of air pollutants.

## 2. Types of Fuel Cells

This introductory section presents a brief review of the articles on fuel cell R&D published during the space, energy, and environmental eras. The reader is referred to selected publications for more details.<sup>1-10</sup> Several classifications of the types of fuel cells have appeared in the voluminous literature (books, chapters in books, reviews and original articles in journals, and proceedings of conferences and meetings). These classifications have mainly been done according to (1) type of fuel, (2) operating temperature range and/or electrolyte, or (3) direct or indirect utilization of fuel. For fuel cells operating at low (<100 °C) and intermediate temperatures (up to 200 °C), H<sub>2</sub> and H<sub>2</sub>-CO<sub>2</sub> (with minimal amounts of CO) are the ideal fuels; the H<sub>2</sub>-CO<sub>2</sub> gas mixture is produced by steam reforming/shift conversion, or partial oxidatiod/shift conversion of the primary or secondary organic fuels. Hydrogen is a secondary fuel, and like electricity, is an energy carrier. On a large scale, hydrogen is produced from the primary fuels, natural gas, coal, or oil. For high-temperature fuel cell systems (>650 °C), a mixture of H<sub>2</sub>, CO, and CO<sub>2</sub> produced by steam reforming can be used in fuel cells quite efficiently (a power plant

efficiency of over 50%). These fuels (pure  $H_2$ ,  $H_2-CO_2$ ,  $H_2-CO-CO_2$ ) can also be produced from renewable energy sources: biomass, solar, wind-mills, and hydroelectric. Pure  $H_2$  can also be generated using nuclear power plants. Hydrogen is the most electroactive fuel for fuel cells operating at low and intermediate temperatures. Methanol is the most electroactive organic fuel, and when it is electrooxidized directly at the fuel anode (instead of being transformed in a hydrogen-rich gas), the fuel cell is called a *direct methanol fuel cell* (DMFC).

### 3. Natural Gas—Its Important Role as a Primary Fuel for All Types of Fuel Cells

During the energy era and the energy crisis, energy conservation was one of the main objectives. Thus there was considerable interest in producing  $H_2$ ,  $H_2-CO_2$ , or  $H_2-CO_2-CO$  from petroleum for utilization in fuel cells, which are the only energy conversion devices that convert chemical energy directly into electrical energy. Thus, unlike the case of thermal engines, the second law of thermodynamics, which limits the efficiency of energy conversion, does not apply. Hence, in principle the free energy change in the fuel cell reaction can be converted to electrical energy, which corresponds to a theoretical energy conversion efficiency of over 80%. In view of the abundance of natural gas resources found since the 1980s, and natural gas being a considerably cleaner fuel than petroleum or coal for the fuel processors, the main goals of the major worldwide fuel cell programs are to develop fuel cell power plants and portable power sources using natural gas or natural gas-derived fuel cells. A chart of all types of fuel cells using natural gas as a fuel is presented in Fig. 1; the applications being considered for the different types of fuel cells are also indicated. The most advanced type of fuel cell is the phosphoric acid fuel cell (PAFC) system, which operates at about 473 K. However, in order to make this fuel cell system reasonably efficient, it is necessary to steam reform the fuel and use a shift converter to reduce the carbon monoxide levels to about 1 to 2%. With natural gas as the fuel, the high temperature systems (i.e., molten carbonate and solid oxide fuel cells, MCFC and SOFC, respectively) are more attractive because of the following advantages: (1) carbon monoxide is a reactant and not a poison, (2) noble metal electrocatalysts are not required, and (3) the waste heat from these fuel cells, which is of sufficiently high quality, can be used for cogeneration or transferred to a bottoming cycle gas turbine to produce more electricity.

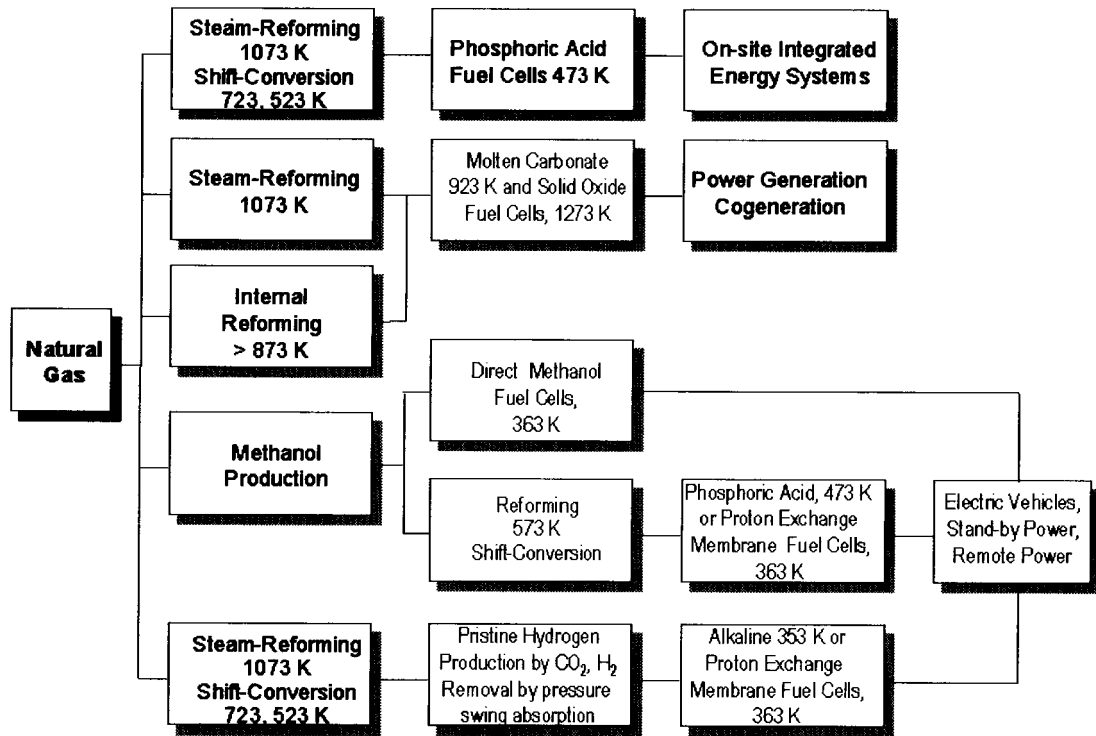


Figure1. Schematic Representation of the methods utilization of natural gas in fuel cells and fuel applications

For a transportation application, methanol is an ideal fuel. Even though its energy content is half of that of gasoline, a methanol fuel cell vehicle could have the same range (driving distance) as a gasoline internal combustion engine (ICE) or diesel-powered vehicle for the same volume of fuel carried on board the vehicle. This is because the fuel cell could operate at twice the efficiency of the ICE or diesel engine. Increasing concern about global warming has stimulated the utilization of pristine hydrogen as a fuel to be carried on board electric vehicles. It is also the only fuel for space fuel cells. Pristine hydrogen can also be produced by steam reforming, shift conversion, and pressure-swing absorption for the complete removal of  $\text{CO}_2$ . If the problems of hydrogen storage, in respect to energy density, specific energy, and safety, can be solved, the alkaline fuel cell (AFC) or the proton exchange membrane fuel cell (PEMFC) will be ideal candidates for terrestrial applications. An advantage of the alkaline system is that there is no noble metal requirement, but a great disadvantage is that even with air as a cathodic reactant, a small amount of  $\text{CO}_2$  carbonates the electrolyte, lowering the conductivity of the electrolyte, altering its pH, and depositing insoluble carbonates in the porous gas diffusion electrode.

With a methanol-fed fuel cell, there are two schemes that look promising. One method is to feed either a PAFC or a PEMFC with hydrogen produced by on-board methanol steam reforming; the second is to use it directly as the anodic reactant in a DMFC. The PAFC has the advantage that because of good thermal matching between the temperatures for the endothermic steam-reforming reaction and the exothermic fuel cell reaction, the heat required for the former process can effectively be utilized from the waste heat generated during the fuel cell reaction. However, the fuel cell researcher's dream is to develop a DMFC, since in such a fuel cell a heavy and bulky fuel-processing system is not required. The PEMFC has a considerably better prospect of attaining high power densities and a faster startup time than the PAFC and is thus the more favored power source for an electric vehicle.

#### 4. Status of Fuel Cell Technologies

An attempt has been made in Table 1 to present the status of fuel cell technologies. For terrestrial applications, the PAFC power plant is the most advanced, and a 200-kW system manufactured by ONSI, a division of United Technologies, Inc., has reached commercialization. Its main applications are focused on on-site integrated energy systems that could

**Table 1**  
**Status of Fuel Cell Technologies**

Type of fuel cell <sup>a</sup> Operating fuel and temperature	Power rating <sup>b</sup> (kW)	Fuel efficiency <sup>c</sup> (%)	Power density <sup>b</sup> (mW/cm <sup>2</sup> )	Lifetime <sup>c</sup> (hr)	Capital cost <sup>c</sup> (\$/kW)	Applications
PAFC; CH <sub>4</sub> , CH <sub>3</sub> OH, oil 200 °C	200-10,000	40-45	200-300	30,000-40,000	200-3000	On-site integrated energy systems, transportation (fleet vehicles), load leveling
MCFC; CH <sub>4</sub> , Coal? 650 °C	100-5000	50-55	150-300	10,000-40,000	1250	Base load and intermediate load power generation, cogeneration
SOFC; CH <sub>4</sub> , Coal? 800-1000 °C	25-5000	50-60	200-400	8,000-40,000	1500	Base load and intermediate load power generation, cogeneration
PEMFC; H <sub>2</sub> , CH <sub>3</sub> OH 25-100 °C	0.1-200	40-50	500-1000	10,000-100,000	50-2000	Transportation, standby power, portable power, space station
DMFC; CH <sub>3</sub> OH 25-150 °C	0.1-10	30-45	50-200	1,000-10,000	1000	Portable power, standby power, transportation (?)
AFC; H <sub>2</sub> 80 °C	20-100	65	250-400	3,000-10,000	1000	Space flights, space stations, transportation

<sup>a</sup>PAFC, phosphoric acid fuel cell; MCFC, molten carbonate fuel cell; SOFC, solid oxide fuel cell; PEMFC, proton exchange membrane fuel cell; DMFC, direct methanol fuel cell; AFC, alkaline fuel cell.

<sup>b</sup>Higher values are projected.

<sup>c</sup>Tower values are projected.

provide electricity and heat for apartment buildings, hospitals, shopping centers, etc. Overall efficiencies higher than 85% for fuel consumption (natural gas  $\rightarrow$  electricity plus heat) have been demonstrated in these power plants. In the U.S. Department of Energy-sponsored fuel cell program, PAFC systems are also being considered as power plants for fleet vehicles (buses, trucks, delivery vehicles) and 100-kW units have been installed and tested in buses; the performance of these buses is quite promising. Apart from the ONSI program, the most active PAFC development and commercialization programs are in Japan and conducted by Fuji, Toshiba, and Mitsubishi.

Molten carbonate fuel cells have the advantages of (1) not requiring noble metal electrocatalysts, (2) efficient heat transfer from the exothermic fuel cell reaction to the endothermic fuel-processing reaction (internal reforming), (3) CO being a reactant and not a poison, and (4) the rejected heat from the MCFC power plant being of high enough quality to produce electricity in a gas turbine or steam in a steam turbine (for cogeneration). The active MCFC developers are (1) Energy Research Corporation and M-C Power Corporation in the United States; (2) ECN and Ansaldo in Europe; and (3) IHI, Toshiba, Mitsubishi, Hitachi, and Sanyo in Japan. Power plants with power ratings of 100 kW to 2 MW have been constructed and tested.

The solid oxide fuel cells have practically the same advantages as the MCFCs for applications in electric utility companies and chemical industries. An additional advantage is that because the SOFC power plant is a two-phase system (gas, solid) whereas all other types of fuel cells are three-phase systems (gas, liquid, and solid), the complex problems associated with liquid electrolytes are eliminated and mass transport problems are thus greatly minimized. The world leader in this technology is Westinghouse Electric Corporation in the United States. The materials used in the electrochemical cell stack are relatively inexpensive, but the costs of fabrication of thin-film structures are prohibitive. The Westinghouse power plants (100 kW) with a tubular structure have reached the performance goals and shown promise of reaching the lifetime goals. Flat-plate designs are more desirable than a tubular one for the SOFCs from the points of view of scale up to megawatt sizes and marked lowering of the capital cost. Siemens in Germany is at the most advanced state in developing the flat-plate design. Other companies working in this area are IHI in Japan and ZTEK, Allied Signal, SOFCO, and MTI in the United States.



The fuel cell power plant that has drawn the most attraction since the mid- 1980s is the one with a proton exchange membrane as the electrolyte. This was the first type of fuel cell to find an application (i.e., as an auxiliary power source for NASA's Gemini space flights in the 1960s). This technology was developed by General Electric Company in the United States. Since the AFCs were more energy efficient and could attain the higher power densities required for the subsequent manned space flights, the PEMFC technology became dormant after the Gemini flights until the mid-1980s. Since then, Ballard Power Systems, Inc. in Canada has made major strides in this technology, particularly for electric vehicle applications. The Ballard/Daimler-Benz/Ford venture for the development and commercialization of PEMFC-powered electric vehicles has provided great enthusiasm for this technology. As may be seen from Table 1, the significant advantage of this technology is that it has the greatest potential for attaining the highest power densities and the longest lifetime. An attractive feature of a PEMFC is that it uses an innocuous electrolyte (a perfluorosulfonic membrane). The potential for reducing the platinum loading by more than a hundred times (compared with that used in the Gemini fuel cells) has been demonstrated in high power density PEMFCs. There are good prospects of further reducing the platinum loading to an even lower value (about 0.3 g/kW), so that the Pt cost could be as low as US\$ 5/kW. Ballard/Daimler-Benz have demonstrated 60-kW PEMFC-powered automobiles, and Ballard has also been sponsored by California and Illinois state agencies to develop and test 120-kW PEMFC-powered buses.

The cost target in the U.S. Partnership for a New Generation of Vehicles (PNGV) Program to develop hybrid electric vehicles that have three times the efficiency of fuel consumption and meet the same performance characteristics as conventional vehicles is most challenging; it is US\$ 3–50/kW, and is thus a factor of 100 lower than that of ONSI's 200-kW commercialized PAFCs. The R&D projects to advance the PEMFC technology in industries, universities, and government laboratories are at a peak level. Practically all the automobile companies (Daimler-Benz, GM, Ford, Chrysler, Toyota, Honda, and Nissan) are collaborating with (1) chemical industries (Du Pont, W.L. Gore and Assoc., Asahi Chemical, Asahi Glass, Solvay, Hoechst) to develop advanced proton-conducting membranes for electrolytes and (2) high-technology engineering companies [Ballard; International Fuel Cells (IFC), Energy Partners, Allied Signal, MTI, H-Power in the United States; Siemens in Germany; De Nora

in Italy; and Fuji, Mitsubishi, and Sanyo in Japan] to develop and manufacture high-performance PEMFCs.

As stated earlier, the fuel cell researcher's dream is to develop DMFCs. Until recently (i.e., the early 1990s), most of the efforts to develop DMFCs had used sulfuric acid as the electrolyte. Recent success with a proton-conducting membrane (perfluorosulfonic acid membrane) in PEMFCs has steered DMFC research toward the use of this electrolyte. The positive feature of a liquid feed to a DMFC is that it eliminates the humidification subsystem, which is required for a PEMFC with gaseous reactants. Another advantage is that the DMFC does not require a heavy and bulky fuel processor. Two problems continue to be challenging in the projects to develop DMFCs: (1) The exchange current density for methanol oxidation, even on the best electrocatalyst to date (Pt-Ru), is  $10^5$ – $10^6$  times lower than that for the electrooxidation of hydrogen. (2) The transport of methanol through the membrane, from the anode to the cathode side, reduces the Coulombic efficiency for methanol utilization by about 30%. However, a compensating feature of DMFCs compared with PEMFCs is that they eliminate the fuel processor, and a lower performance of the electrochemical cell stack may still be acceptable for some applications, e.g., portable power sources.

The DMFC projects are still at an infant stage, but the progress made toward their development by fuel cell companies (IFC, Sanyo, Fuji, Siemens, Giner, Inc.), government laboratories [Jet Propulsion Laboratory (JPL), Los Alamos National Laboratory (LANL), Osaka National Research Institute, Consiglio Nazionale delle Ricerche (CNR) Messina] and universities (Université de Poitiers, University of Newcastle, University of Bonn, Case Western Reserve University, University of Southern California, Yamanashi University) gives some food for thought. According to some projections, the energy densities of DMFCs could be considerably higher than those of even lithium ion batteries, so that DMFCs could find low-power applications (laptop computers, backpack power sources for soldiers). International Fuel Cells and Siemens have designed, constructed, and tested kilowatt-sized DMFC power plants. Research studies in the above-mentioned government laboratories, universities, and industries have shown prospects of attaining a current density of 400 mA/cm<sup>2</sup> at a cell potential of 0.5 V.

### 5. Electrochemical vs. Other Methods of Energy Conversion

In order to evaluate fuel cells in comparison with other methods of energy conversion, an attempt is made in this subsection to base an evaluation on the following types of applications: electric power generation and transportation. The resulting technoeconomic assessment is presented in Tables 2A and B. Definitive performance and cost parameters are available for conventional thermal power plants. However, this is not the case for advanced methods of energy conversion. As seen from Table 2A, for electric power generation, the main advantages of electrochemical energy conversion over the conventional methods are higher efficiency, ultra-low levels of emissions of environmental pollutants and thus minimal health hazards, and low noise levels because of few moving parts. It is difficult to envisage high power-rated fuel cell power plants (>100 MW), as in the case of the thermal and nuclear plants. MCFC and SOFC fuel cell power

**Table 2A**  
**Electrochemical vs. Other Methods of Energy Conversion (Electric Power Generation)**

Energy conversion method	Efficiency (%)	Power range (MW)	Lifetime (years)	Cost (\$/kW)	Environmental Safety
Fuel cells					
PAFC	40–45	0.2–10	5 <sup>a</sup>	1500 <sup>a</sup>	<i>b,c,d</i>
MCFC	50–55 <sup>a</sup>	1–100 <sup>a</sup>	5 <sup>a</sup>	1000 <sup>a</sup>	<i>b,c,d</i>
SOFC	50–60 <sup>a</sup>	1–100 <sup>a</sup>	5 <sup>a</sup>	1000 <sup>a</sup>	
Conventional thermal coal, oil, gas	25–35	≈1000	> 20	1500	<i>b<sub>γ</sub>d<sub>γ</sub></i>
Gas turbines		100–1000	>20	> 50	<i>b,d<sub>γ</sub></i>
Hydroelectnc		0.1–1000	>20	1500	<i>b,c,d</i>
Nuclear		≈1000	>20	2000	<i>b</i>
Photovoltaic		0.1–1 <sup>a</sup>	>10 <sup>a</sup>	5000	<i>b,c,d</i>
Wind		0.1–1	>10 <sup>a</sup>		<i>b,c,d</i>
MHD		0.1–100 <sup>a</sup>	>10 <sup>a</sup>	2000	<i>b,c,d</i>

<sup>a</sup>Projected

<sup>b</sup>Below environmentally acceptable emission levels

<sup>c</sup>Below environmentally acceptable noise levels

<sup>d</sup>Minimal health hazards

plants could play a role in dispersed power generation and cogeneration, at a level of 1–100 MW; PAFCs are being commercialized for on-site integrated energy systems (200 kW). In the case of fuel cell power plants, the parameters most difficult to forecast are the lifetime and capital cost. Even though nuclear energy conversion plays a dominant role in some countries and a minor to midlevel role in a few other countries, the strong antinuclear lobby in most countries will in all probability slow down the construction of new nuclear power plants. It is rather difficult for fuel cells to compete with hydroelectric power plants. The disadvantages of the latter are that hydropower resources are limited in most countries in the world and in other countries are already well developed, and their construction causes severe environmental problems (large land requirements, building of new bridges, roads). Photovoltaic and wind energy conversion systems are in an advanced state of development and in some countries are already utilized for power generation on a relatively large scale. The problems with these systems are interruptible duty cycles (weather and/or time dependent), large land area requirements, and high capital cost. It is most likely that electrochemical energy conversion may play a greater role in power generation than these two technologies. The R&D programs on magnetohydrodynamic (MHD) electric power generators in the United States and Russia showed very promising results. There are serious problems of finding materials stable at the high operating temperature needed (3000–4000 °C) and more so because it utilizes hot ionized gases.

With respect to an analysis of electrochemical vs. other methods of energy conversion for transportation applications (Table 2B), one must take into consideration that fuel cell technology is quite immature compared with internal combustion and diesel engine technologies, which have been intensively developed since the beginning of the twentieth century at a cost of several billions of dollars. The most important performance characteristics of power sources for automobile application are efficiency, power density, specific power, energy density, and specific energy. These characteristics are vitally important to meet the performance and cost goals of automobiles. In spite of the fact that development of fuel cells for electric vehicles started only in the late 1970s in several countries (predominantly the United States, Germany, and Japan) and the investment in R&D has been less than US\$10<sup>9</sup>, Table 2B shows that PEMFCs for automobiles and PAFCs for fleet vehicles may be able to compete with IC engine- and diesel engine-powered vehicles in performance characteristics. However, meeting the cost target in the near future is a major

**Table 2B**  
**Electrochemical vs. Other Methods of Energy Conversion (Transportation)**

Energy conversion method/fuel	Efficiency (%)	Power (kW)	Specific power (W/kg)	Power density (W/liter)	Range automobiles (km)	Cost (\$/kW)	Environmental safety
Fuel cells							
PEMFC/pure H <sub>2</sub> or H <sub>2</sub> from methanol	55/H <sub>2</sub> ; 45/C <sub>3</sub> OH <sup>a</sup>	10-200	400-1000 <sup>a</sup>	600-1500 <sup>a</sup>	500		<i>b,c,d</i>
PAFC/methanol	40	20-200	100-200 <sup>a</sup>	150-300 <sup>a</sup>	300 <sup>a</sup>		<i>b,c,d</i>
DMFC	30 <sup>a</sup>	20-30	100-200 <sup>a</sup>	150-300 <sup>a</sup>	500 <sup>a</sup>		<i>b,c,d</i>
Internal combustion Engine/gasoline, C <sub>2</sub> H <sub>5</sub> OH	25-30	10-100	> 1000	> 1000	600	50	
Diesel engine/diesel oil	30-35	10-200	>1000	> 1000	800	60	<i>b,d</i>
Gas turbine/natural gas	35-40	10-200 <sup>a</sup>	>1000 <sup>a</sup>	>1000 <sup>a</sup>			<i>b,c,d</i>
Battery <sup>e</sup>	65	10-100 <sup>a</sup>	100-400 <sup>a</sup>	250-750 <sup>a</sup>	200-300 <sup>a</sup>	100	<i>b,c,d</i>
Hybrid electric vehicle	40-50	10-100 <sup>a</sup>	>200 <sup>a</sup>	> 500 <sup>a</sup>	500 <sup>a</sup>		<i>b,c,d</i>

<sup>a</sup>Projected.

<sup>b</sup>Below environmentally acceptable emission levels.

<sup>c</sup>Below environmentally acceptable noise levels.

<sup>d</sup>Minimal health hazards.

<sup>e</sup>A battery is an energy storage system. However on board a vehicle, it is a power source.

challenge. One option for a fuel cell-powered vehicle to attain high power and energy levels on a gravimetric and volumetric basis is to develop fuel cell/battery hybrid vehicles as in the United States PNGV program. The competition in the case of hybrid vehicles is from diesel engines. Even though gas turbines are also being considered as candidates for hybrid electric vehicle applications in the PNGV program, they are not in as advanced a state as fuel cells. On the other hand, the prospects are very low for battery-powered vehicles to meet both the performance and cost goals.

## II. DIRECT METHANOL FUEL CELLS

### 1. Historical Development of DMFCs<sup>3</sup>

Since methanol is a relatively inexpensive and reactive fuel for DMFCs, its electrooxidation has been studied for more than three decades.<sup>11</sup> One of the first investigations was in 1954 by Pavela, who demonstrated interest in methanol as a soluble fuel in aqueous electrolytes.<sup>12</sup> Methanol and other small organic fuels are more reactive in alkaline media than in acid media, so that the first attempts to build a DMFC used concentrated NaOH or KOH as electrolytes which also contained the fuel. One of the first such systems, described in 1955 by Justi and Winsel, used DSK nickel electrodes, porous nickel for the methanol anode, or porous nickel–silver for the oxygen cathode.<sup>13</sup> A similar unit constructed by Wynn in 1960 consisted of a platinized porous carbon anode and a porous carbon cathode impregnated with silve–cobalt–aluminum mixed oxides.<sup>14</sup> Using air as the cathodic reactant, this cell yielded 8 mA/cm<sup>2</sup> at 0.35 V. During this period, the first methanol-fed PEMFC was conceived by Hunger, who built a cell with an anion exchange membrane on both sides of which porous catalytic electrodes were pressed.<sup>15</sup> However, the performance was quite low: 1 mA/cm<sup>2</sup> at 0.25 V at room temperature with methanol and air as the reactants.

The first DMFC power source operating at a reasonably high power level and using an alkaline electrolyte (5 M KOH) was constructed in 1963 by Murray and Grimes at Allis-Chalmers Manufacturing Co.<sup>16</sup> It consisted of a 40-cell stack operating at 50 °C. Each cell in the stack consisted of a nickel sheet anode on which was deposited a platinum–palladium electrocatalyst and a porous nickel sheet cathode impregnated with silver. The open circuit voltage was 22 V and the maximum power output was 750 W

at 9 V and 83 A (ie., 180 mA/cm<sup>2</sup> and 40 mW/cm<sup>2</sup>), so that the power density and specific power at the maximum power level were 21 W/dm<sup>3</sup> and 11 W/kg, respectively (Fig. 2).

However, one major drawback of fuel cells with an alkaline electrolyte is the carbonation of the electrolyte caused by the complete oxidation of the fuel in carbon dioxide. This decreases the fuel cell efficiency owing to both a decrease in the electrolyte conductivity and an increase in concentration polarization, mainly at the oxygen electrode. Furthermore, from a practical point of view, the carbonate has to be replaced and regenerated, leading to an increase in the operating cost of the fuel cell. Therefore the succeeding developmental projects of DMFCs made use of strong acid electrolytes, which are carbon dioxide rejecting. New problems still arose, owing to the lower reactivity of methanol in acid media, which could only be overcome with relatively large amounts of noble metal electrocatalysts, and corrosion problems with the fuel cell materials.

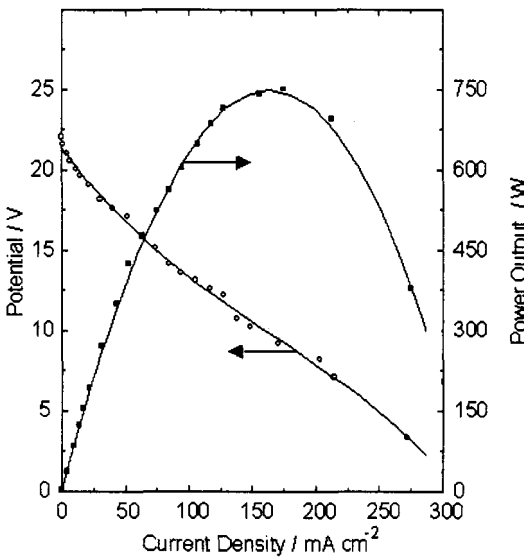


Figure 2. Current-voltage characterization of the 40-module methanol-air fuel cell developed by Allis-Chalmers. (From J. N. Murray and P. G. Grimes in *Fuel Cells*, p. 57, 1963; reproduced with permission of the AICHE).

DMFC stacks using concentrated sulfuric acid as electrolyte were developed in the 1970s and early 1980s by Shell Research Centre in England<sup>17</sup> and Hitachi Research Laboratories in Japan.<sup>18</sup> In both cases the anode electrocatalysts consisted of Pt–Ru alloys, which are much more active than pure Pt in oxidizing methanol. The cathode electrocatalyst was carbon-supported platinum mixed with Teflon for the Hitachi DMFC, whereas it was an iridium chelate in the case of the Shell DMFC. The platinum loadings were very high (around 10 mg/cm<sup>2</sup>) and the performance was quite low. In terms of quantity of platinum per kilowatt, it could be as high as 400 g/kW, and the cost of Pt about US\$ 6000/kW, which would prevent any commercial development. Relatively large stacks (up to 5 kW by Hitachi) were built, but these DMFCs working at 60 °C, to avoid high methanol pressure, led to rather similar electrical performances, with a maximum power density of 25 mW/cm<sup>2</sup> (at 0.3 V for Shell and 0.4 V for Hitachi).

Recent development of the DMFC was made possible by using the concept of PEMFC in which the acid electrolyte is a proton exchange membrane (PEM). This approach is beneficial from the point of view of building rather compact stacks in which the methanol could be fed either in gas or liquid phase. In both cases, it has been shown that raising the temperature to 130 °C greatly improves the electrical performance (a power density of 250 mW/cm<sup>2</sup> with air at 3 bar pressure was attained). The first programs at the beginning of this decade, particularly in Europe, were carried out in academic laboratories (University of Newcastle, University of Bonn, University of Poitiers) and in an industrial company (Siemens). The Joule program, funded by the European Union, led to the building, in 1994, of small stacks (with electrodes of 250 cm<sup>2</sup> surface area) working at 130 °C with vapor-fed methanol under a pressure of 4 bar.<sup>19</sup>

In the United States, the Department of Defense (DOD) and the Department of Energy (DOE) promoted in 1992 the Defense Advanced Research Project Agency (DARPA) program to develop a DMFC for portable and mobile applications.<sup>20</sup> Several institutions are involved (IFC, JPL, LANL, Giner, Inc.) and small stacks (up to 10 elementary cells) were built by IFC and JPL. The performances are quite encouraging, with power densities of 250 mW/cm<sup>2</sup> at 0.5 V. More details are given in Section V.2.

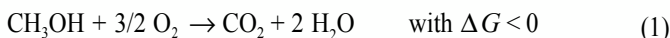
## 2. Principles of DMFCs<sup>21,22</sup>

A direct methanol fuel cell consists of two electrodes—a catalytic methanol anode and a catalytic oxygen cathode—separated by an ionic conduc-



tor, preferably an acid electrolyte, for the purpose of rejecting the carbon dioxide produced (Fig. 3). Great progress was recently made by feeding methanol directly in a proton exchange membrane fuel cell in which the protonic membrane (e.g., Nafion) plays the role of an acidic medium and of a separator between the two electrode compartments (Fig. 4). This technology has the added advantage of thin elementary cells and hence of compact stacks.

In such a device, the electrons liberated at the anode by the oxidation of methanol circulate in the external electrical circuit, producing electrical energy, and reach the cathode, where they reduce the oxidant, usually oxygen from air. The overall reaction thus corresponds to the catalytic combustion of methanol with oxygen, i.e.,



The electrochemical oxidation of methanol occurs on the anode electrocatalyst (e.g., dispersed platinum), which constitutes the negative electrode of the cell:

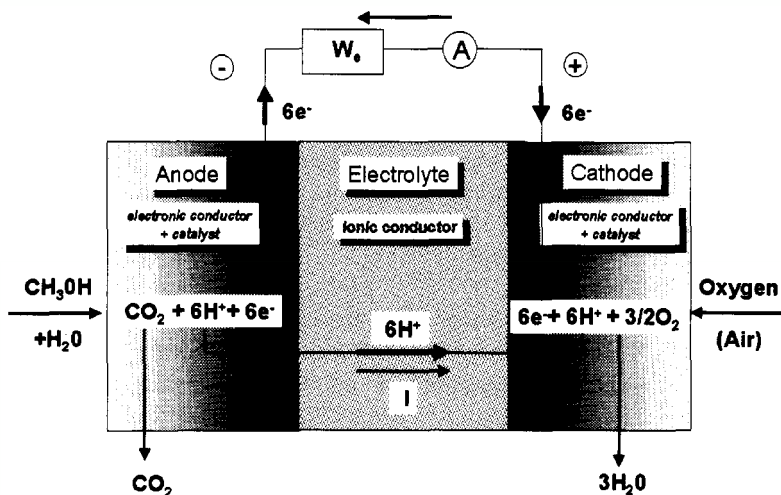
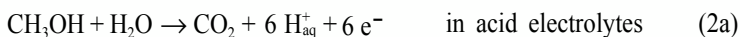


Figure 3. Schematic diagram of a direct methanol fuel cell working in an acidic medium.

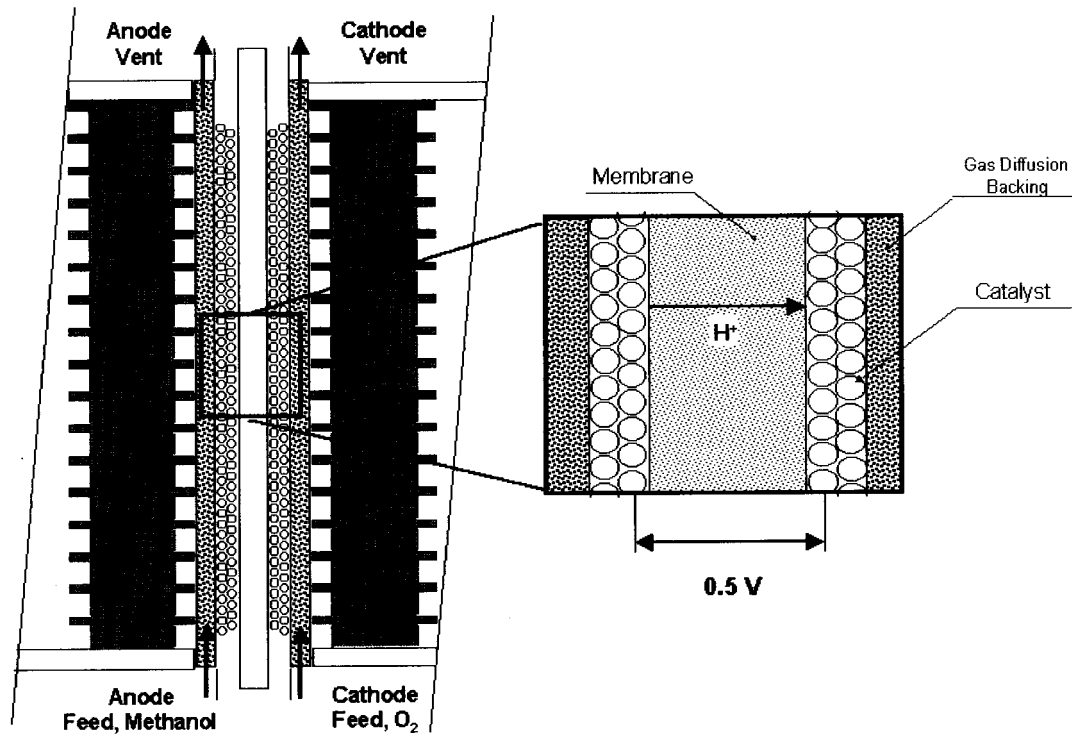
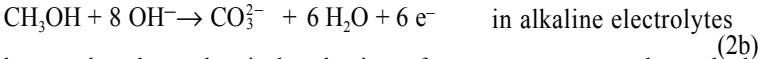
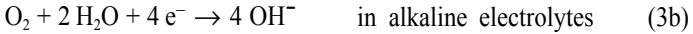
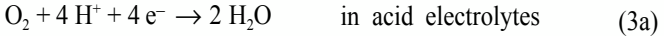


Figure 4. Schematic design of a proton exchange membrane fuel.



whereas the electrochemical reduction of oxygen occurs at the cathode (also containing a platinum-based catalyst), which corresponds to the positive electrode of the cell:



The cell potential  $E$  is thus equal to the difference between the electrode potentials of each electrode:

$$E = E_c^+ - E_a^- \quad (4)$$

where the electrode potentials  $E_i$  are defined as the difference of internal potential at each electrode/electrolyte interface.

One main advantage of such a power source is the direct transformation of the chemical energy of methanol combustion into electrical energy. Hence, the reversible cell potential,  $E_r$ , can be calculated from the Gibbs energy change,  $\Delta G$ , associated with the overall combustion reaction of methanol (1), by the equation:

$$\Delta G + nF E_r = 0 \quad \text{leading to } E_r > 0 \text{ with } \Delta G < 0 \quad (5)$$

where  $F$  is the Faraday constant ( $F = 96,500 \text{ C}$ ) and  $n$  is the number of faradays (per mole of methanol) involved in the half-cell reactions. Under standard conditions ( $25^\circ\text{C}$ ), the heat of combustion, i.e., the enthalpy change for reaction (1),  $\Delta H^\circ$ , is  $-726 \text{ kJ/mole}$  of methanol, and the Gibbs energy change,  $\Delta G^\circ$ , is  $-702 \text{ kJ/mole}$  of methanol. This corresponds to a standard reversible potential for the cell, as given by the equation:

$$E_r^\circ = E_c^\circ - E_a^\circ = - \frac{\Delta G^\circ}{nF} = \frac{702 \times 10^3}{6 \times 96,500} = 1.21 \text{ V} \quad (6)$$

where  $E_c^\circ$ ,  $E_a^\circ$  are the standard potentials of each electrode.

The main attractions of the DMFC are its high specific energy ( $W_s$ ) and high energy density ( $W_e$ ), the values of which are calculated as follows:

$$W_s = \frac{(-\Delta G^\circ)}{3600 \times M} = \frac{702 \times 10^3}{3600 \times 0.032} = 6.09 \text{ kWhr kg}^{-1} \quad (7)$$

and  $W_e = W_s \times \rho = 4.82 \text{ kWhr dm}^{-3}$ , where  $M = 0.032 \text{ kg}$  is the molar weight of methanol and  $\rho = 0.7914 \text{ kg dm}^{-3}$  is its density.

Under the standard reversible conditions (25 °C), the energy efficiency is very high:

$$\epsilon_{\text{rev}} = \frac{W_e}{(-\Delta H^0)} = \frac{nFE_r^0}{(-\Delta H^0)} = \frac{\Delta G^0}{\Delta H^0} = \frac{702}{726} = 96.7\% \quad (8)$$

This is considerably higher than that of an  $\text{H}_2\text{-O}_2$  fuel cell (i.e., 83%). However, under normal operating conditions, at a current density  $j$ , the electrode potentials deviate from their equilibrium values as a result of large overpotentials,  $\eta_i$ , at both electrodes (Fig. 5):

$$\eta_a = E_a^-(j) - E_r^- \geq 0 \quad \text{at the methanol anode} \quad (9a)$$

$$\eta_c = E_c^+(j) - E_r^+ \geq 0 \quad \text{at the oxygen cathode} \quad (9b)$$

This results from the slow kinetics of methanol oxidation and oxygen reduction. An additional loss is due to the cell resistance  $R_e$  (arising mainly

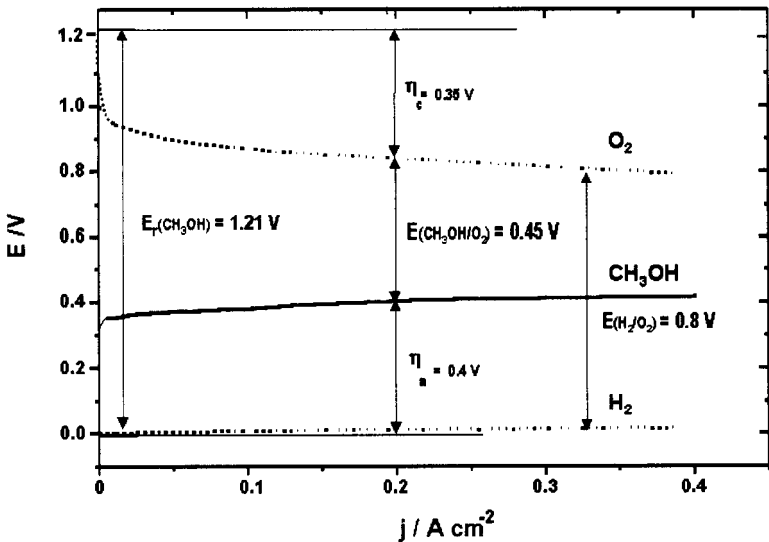


Figure 5. Typical half-cell potentials vs. current density curves for an  $\text{H}_2\text{-O}_2$  fuel cell and a DMFC.

from the proton conducting membrane). The cell potential under working conditions is

$$E(j) = E_c^+(j) - E_a^-(j) - R_e j = E_r - (|\eta_c| + |\eta_a| + R_e j) \leq E_r \quad (10)$$

Thus the energy efficiency will be decreased proportionally to the so-called voltage efficiency:

$$\epsilon_E = E(j)/E_r \quad (11)$$

For a DMFC working at 200 mA/cm<sup>2</sup> and 0.5 V, this ratio will be

$$\epsilon_E = 0.5/1.21 = 41.3\% \quad (12)$$

and the overall efficiency of the fuel cell will be

$$\epsilon_{\text{cell}} = \epsilon_{\text{rev}} \times \epsilon_E = 0.967 \times 0.413 \approx 40\% \quad (13)$$

assuming a Coulombic efficiency of 100%, i.e., a complete combustion of methanol. This is acceptable for an autonomous power source when the oxidation reaction is complete, i.e., it gives a theoretical number of faradays  $n_{\text{th}} = 6$  F per mole of methanol. However, for a methanol fuel cell, the complete oxidation of CH<sub>3</sub>OH to CO<sub>2</sub> (involving  $n = 6$  faradays per mole) is rarely complete, so that a Coulombic efficiency is introduced:

$$\epsilon_F = n_{\text{exp}}/n_{\text{th}} \quad (14)$$

where  $n_{\text{exp}}$  is the number of faradays effectively exchanged in the half-cell reaction, and  $n_{\text{th}} = 6$  is the number of faradays exchanged for a complete combustion.

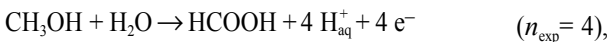
The overall energy efficiency becomes

$$\epsilon_{\text{cell}} = \frac{W_e}{(-\Delta H)} = \frac{n_{\text{exp}} F E(j)}{(-\Delta H)} = \frac{n_{\text{th}} F E_r}{(-\Delta H)} \times \frac{E(j)}{E_r} \times \frac{n_{\text{exp}}}{n_{\text{th}}} = \epsilon_{\text{rev}} \times \epsilon_E \times \epsilon_F \quad (15)$$

Therefore the overall efficiency may be dramatically decreased, e.g., if the electrooxidation stops at the formaldehyde stage:



or at the formic acid stage:



thus leading, respectively, to a Coulombic efficiency:

$$\epsilon_F = \frac{n_{\text{exp}}}{n_{\text{th}}} = \frac{2}{6} = 33.3\% \quad \text{or} \quad \epsilon_F = \frac{n_{\text{exp}}}{n_{\text{th}}} = \frac{4}{6} = 66.6\%,$$

and to an overall efficiency:

$$\epsilon = \epsilon_{\text{rev}} \times \epsilon_E \times \epsilon_F \approx 13.3\% \quad \text{or} \quad \epsilon = \epsilon_{\text{rev}} \times \epsilon_E \times \epsilon_F \approx 26.6\%. \quad (16)$$

### 3. Challenges in Developing DMFCs

From the above discussion, it is clear that the main objectives of fundamental investigations on the direct methanol fuel cell are to:

decrease the overvoltages  $\eta_i$ , and hence to increase the reaction rates at both the methanol anode and the oxygen cathode,

increase the reaction selectivity toward complete oxidation to  $\text{CO}_2$ ,

find methanol-tolerant oxygen cathodes (e.g., transition metal macrocycles), and

decrease the effects of methanol crossover through the ionic membrane by developing advanced membranes with optimum structures and compositions.

These main objectives can be reached only by modifying the structures and compositions of primarily the anode (methanol electrode) and secondarily the cathode (oxygen electrode) as discussed in Sections III and IV, respectively. In addition, Section IV discusses the conception of new proton exchange membranes with lower methanol permeability in order to improve the cathode characteristics. Section V deals with the progress in the development of DMFCs, while in Section VI the authors attempt to make a prognosis on the status of DMFC R&D and its potential applications.

## III. ELECTRODE KINETICS AND ELECTROCATALYSIS OF METHANOL OXIDATION—ELECTROCHEMICAL AND SPECTROSCOPIC INVESTIGATIONS

### 1. Introduction

Methanol can be considered as a hydrogen carrier in a fuel cell. Conventionally, methanol has been reformed/shift converted to produce hydrogen. A low concentration of carbon monoxide formed during this process leads to a strong poisoning of the anode, and even after cleaning of the

reformate, a low level of CO is still present in the hydrogen-rich gas. In order to avoid the complexity of the fuel processing and the consequences of weight, particularly for electric vehicle applications, the direct oxidation of methanol is a simple and attractive way to directly convert the chemical energy of the methanol oxidation reaction to electricity. The direct electrooxidation of methanol is advantageous for a fuel cell application only if the reaction is complete and leads to the formation of carbon dioxide and water at low anode potentials. Platinum is the best electrocatalyst in an H<sub>2</sub>-O<sub>2</sub> PEMFC, but in a DMFC it is subjected to poisoning by CO; the challenge is thus to develop electrocatalysts able to oxidize methanol without poisoning its surface at such low potentials.

The overall reaction for methanol electrooxidation is expressed by Eq. (1) and its standard reversible potential by Eq. (6). The value of  $E_r^\circ = 1.21$  V for the methanol oxidation reaction is very close to that for a hydrogen-oxygen fuel cell (e.g., 1.23 V). Under standard equilibrium conditions, an anode potential  $E_a^\circ$  of 0.016 V vs. SHE can be easily calculated from thermodynamic data. This means that theoretically methanol can be oxidized at very low potentials. Conversely, it is well known that methanol is only oxidized at potentials greater than 0.5 V, in acid medium on a platinum electrocatalyst, owing to the slow kinetics of its electrooxidation reaction, which results in high overpotentials. The challenge—to increase the methanol oxidation kinetics at an electrode/electrolyte interface—has been most difficult for practically all electrochemists working in this field, and even at present, this irreversible loss due to activation overpotential is high for several mechanistic reasons.

Thus, worldwide efforts have focused on the elucidation of the reaction mechanism. For this purpose, knowledge about the following items is vital: (1) identification of reaction products and the electrode kinetics of the reactions involved, (2) identification of adsorbed intermediate species and their distribution on the electrode surface, and (3) dependence of the electrode kinetics of the intermediate steps in the overall and parasitic reactions on the structure and composition of the electrocatalyst. It is only after a better knowledge of the reaction mechanisms is obtained that it will be possible to propose modifications of the composition and/or structure of the electrocatalyst in order to significantly increase the rate of the reaction.

## 2. Identification of the Reaction Products and the Adsorbed Intermediates

The electrocatalytic oxidation of methanol has been thoroughly investigated during the past three decades (see reviews in Refs. 21–27), particularly in regard to the possible development of DMFCs.<sup>21,22,25,27</sup> The oxidation of methanol, the electrocatalytic reaction, consists of several steps, which also include adsorbed species. The determination of the mechanism of this reaction needs two kinds of information: (1) the electrode kinetics of the formation of partially oxidized and completely oxidized products (main and side products) and (2) the nature and the distribution of intermediates adsorbed at the electrode surface.

### (i) Experimental Methods

#### (a) Analysis of reaction products

The quantitative analyses of reaction products due to partial or complete oxidation can be performed by different methods. This type of determination is essential to improve electrode composition. Apart from a decrease in the Coulombic efficiency (see Section II.2), the formation of partially oxidized products can be deleterious for the DMFC application because some of these products (e.g., formic acid) may be in liquid form and are corrosive.

Quantitative analysis can be carried out by chromatography (in gas or liquid phase) during prolonged electrolysis of methanol.<sup>24,28,29</sup> The main product is carbon dioxide,<sup>24,28,29</sup> which is the only desirable oxidation product in the DMFC. However, small amounts of formic acid and formaldehyde have been detected, mainly on pure platinum electrodes. The concentrations of partially oxidized products can be lowered by using platinum-based alloy electrocatalysts; for instance, the concentration of carbon dioxide increases significantly with Pt-Ru and Pt-Ru-Sn electrodes,<sup>22</sup> which thus shows a more complete reaction with alloy electrocatalysts.

*In situ* analysis of the reaction products can also be carried out by mass spectrometry, using the differential electrochemical mass spectrometry (DEMS) technique.<sup>30</sup> This technique permits the detection of gaseous products since they are produced and captured through a porous electrode. It has been confirmed that carbon dioxide is the main reaction product. With this technique, it is also possible to determine the production of CO<sub>2</sub>



as a function of potential. Such information is valuable for comparing the behavior of different kinds of electrodes.

Reaction products can also be identified by *in situ* infrared reflectance spectroscopy (Fourier transform infrared reflectance spectroscopy, FTIRS) used as single potential alteration infrared reflectance spectroscopy (SPAIRS). This method is suitable not only for obtaining information on adsorbed products (see below), but also for observing infrared (IR) absorption bands due to the products immediately after their formation in the vicinity of the electrode surface. It is thus easy to follow the production of CO<sub>2</sub> versus the oxidation potential and to compare the behavior of different electrocatalysts.

### *(b) Identification of the adsorbed intermediates*

It is only since 1980 that *in situ* spectroscopic techniques have been developed to obtain identification of the adsorbed intermediates and hence of reliable reaction mechanisms.<sup>31</sup> These new infrared spectroscopic *in situ* techniques, such as electrochemically modulated infrared reflectance spectroscopy (EMIRS), which uses a dispersive spectrometer, Fourier transform infrared reflectance spectroscopy, or a subtractively normalized interfacial Fourier transform infrared reflectance spectroscopy (SNIFTIRS), have provided definitive proof for the presence of strongly adsorbed species (mainly adsorbed carbon monoxide) acting as catalytic poisons.<sup>30,31</sup> Even though this chapter is not devoted to the description of *in situ* infrared techniques, it is useful to briefly note the advantages and limitations of such spectroscopic methods.

The objective is to identify species present at the electrode/aqueous electrolyte interface. Owing to the water absorption limitations, the spectroscopic signal from the adsorbed layer is very weak and most of the information contained in the reflected signal arises from the water layer. However, such problems were overcome by using different approaches.<sup>31</sup> The first was to decrease the thickness of the electrolyte layer. The EMIRS and SNIFTIRS techniques have been used to extract the useful information from the signal. In all cases, signal averaging of spectra was necessary to improve the signal-to-noise ratio. The improvements made in the experimental techniques permit the detection of the adsorbed species, not only on a smooth pure platinum electrode (Fig. 6) or a bulk alloy (such as a Pt-Ru alloy, Fig. 7), but also in the case of metallic particles dispersed in a carbon powder (Pt-Ru particles deposited on carbon, Fig. 8).<sup>32</sup> The *in situ* IR techniques are at present sufficiently powerful to observe such poor

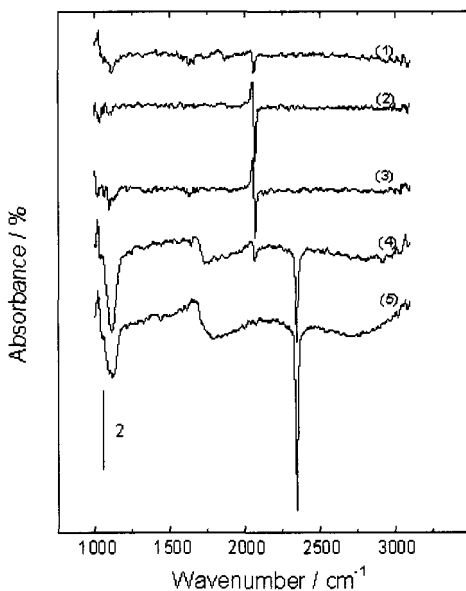


Figure 6. SNIFTIR spectra of the adsorbed intermediates involved in the oxidation of  $0.1\text{ M CH}_3\text{OH}$  in  $0.5\text{ M HClO}_4$  on a smooth Pt electrode (p-polarized light; modulation potential  $\Delta E = 0.3\text{ V}$ ; averaging of 128 interferograms). Electrode potential (mV/RHE): (1) 370, (2) 470, (3) 570, (4) 670, (5) 770.

reflective surfaces and to extract information on the formation of carbon dioxide as a function of electrode potential. The main results obtained in the case of alloys and particles are presented in Section III.4.

### (ii) Reaction Mechanism

From the results obtained with *in situ* reflectance spectroscopy and on-line analytical methods, investigators at Université de Poitiers proposed a complete mechanism for the electrooxidation of methanol at a platinum electrode.<sup>24</sup> The first step of the electrooxidation reaction is the dissociative adsorption of methanol, leading to several species according to the following equations:

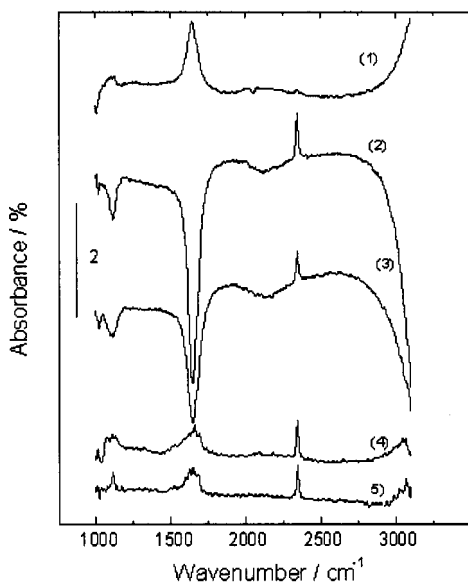
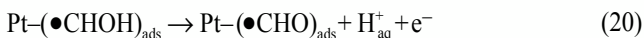
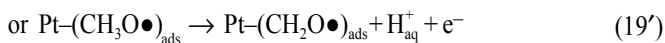
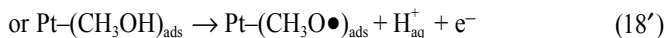
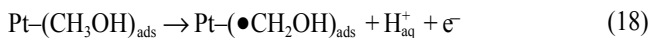
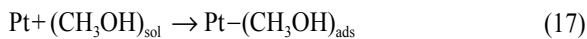


Figure 7. SNIFTIR spectra of the adsorbed intermediates involved in the oxidation of 0.1 M CH<sub>3</sub>OH in 0.5 M HClO<sub>4</sub> on a smooth Pt<sub>0.9</sub>Ru<sub>0.1</sub> bulk alloy (p-polarized light; modulation potential  $\Delta E = 0.3$  V averaging of 128 interferograms). Electrode potential (mV/RHE); (1) 370, (2) 470, (3) 570, (4) 670, (5) 770.



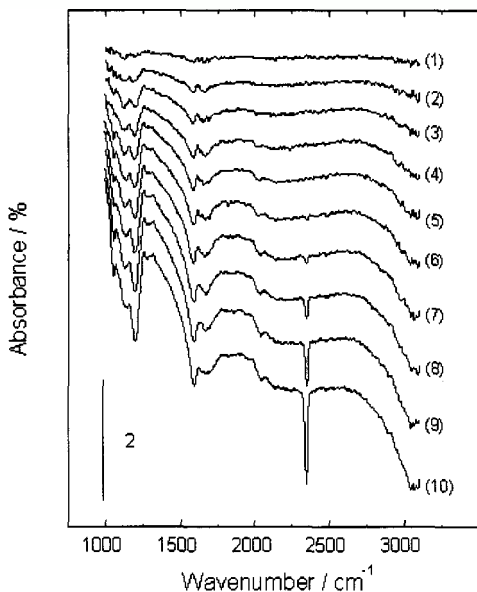
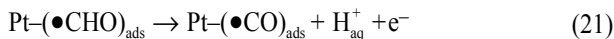


Figure 8. SPAIR spectra of the adsorbed intermediates involved in the oxidation of 0.1 M CH<sub>3</sub>OH in 0.5 M HClO<sub>4</sub> on a Pt<sub>0.9</sub>Ru<sub>0.1</sub> alloy dispersed electrode (p-polarized light; modulation potential  $\Delta E = 0.3$  V; reference spectrum taken at 50 mV/RHE; averaging of 128 interferograms). Electrode potential (mV/RHE): (1) 100, (2) 150, (3) 200, (4) 250, (5) 300, (6) 350, (7) 400, (8) 450, (9) 500, (10) 550.



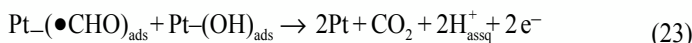
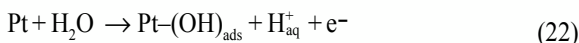
The different species formed by steps (18) to (20) or (18') to (20') have been detected by *in situ* infrared reflectance spectroscopy, and such dissociative steps are now widely accepted even if the exact nature of the species formed during (20) or (20') is still a subject of discussion. Several groups proposed the species (COH)<sub>ads</sub> as the main, strongly adsorbed species on the platinum surface,<sup>30,33</sup> even though no absorption infrared band can be definitely attributed to (COH)<sub>ads</sub>. However, the formyl-like species (•CHO)<sub>ads</sub> has been formally identified, since it gives an IR absorption band at around 1690 cm<sup>-1</sup>.<sup>34</sup>

After the reactions (20) or (20'), the formyl-like species is spontaneously dissociated on platinum according to the reaction:

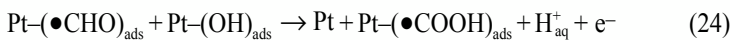


The strongly adsorbed CO species was identified as the main poisoning species blocking the electrode active sites from further adsorption of intermediates formed during methanol oxidation.<sup>35</sup> The reaction represented by Eq. (21) is a rather fast process and it is the main reason for the fast poisoning phenomena observed on a platinum surface. The configuration of the adsorbed CO species depends on the electrode coverage and on the electrode structure. On a smooth platinum polycrystalline electrode, linearly bonded CO is the main species at intermediate to high coverages (which prevails under operating conditions of a DMFC), whereas bridge and multibonded CO are clearly seen at low coverages.<sup>34</sup> Linearly bonded CO is the main species adsorbed on Pt(110), whereas multibonded CO is mainly formed on Pt(111).<sup>36</sup>

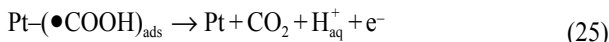
The vital step in the reaction mechanism appears to be the formation of the intermediate  $(\bullet\text{CHO})_{\text{ads}}$ , which facilitates the overall reaction. The kinetics of its further desorption and/or oxidation into reaction products are the key steps of the mechanism, leading to complete oxidation. An alternative path to the spontaneous formation of the poisoning species, Eq. (21), is its oxidation, with OH species arising from the dissociation of water according to the following reactions:



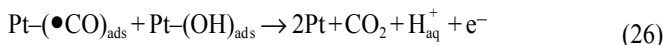
One other reaction has been observed:



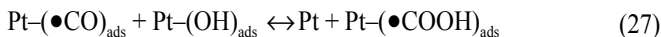
then leading also to the formation of carbon dioxide:



On the other hand, adsorbed CO can be oxidized through the reactions:



or:



followed by Eq. (25).

This mechanism takes into account the formation of all the products detected:  $\text{CO}_2$  from steps (23), (25), or (26), formation of formaldehyde after steps (19) or (19') and (20) or (20'), and formation of formic acid after steps (24) or (27).

The infrared spectra exhibit the absorption bands corresponding to all these species. Adsorbed CO is detected as IR absorption bands around  $2050 \text{ cm}^{-1}$  for the linearly bonded species and  $1870 \text{ cm}^{-1}$  for the bridge-bonded species. The presence of  $\text{CO}_2$  is clearly indicated by the sharp band at  $2345 \text{ cm}^{-1}$ , which appears at higher potentials; the formation of  $(\bullet\text{CHO})_{\text{ads}}$  is evidenced by the band at  $1690 \text{ cm}^{-1}$ , while that of  $(\bullet\text{COOH})_{\text{ads}}$  by weak absorption bands around  $1720 \text{ cm}^{-1}$  (see Figs. 6 to 8).

The crucial aspect is thus to determine the fate of the  $(\bullet\text{CHO})_{\text{ads}}$  species. Possible mechanisms for its oxidative removal are schematically shown in Fig. 9. From this scheme, it appears that the desorption of the formyl species can follow different pathways through competitive reactions. This schematic illustrates the main problems and challenges in improving the kinetics of the electrooxidation of methanol. On a pure platinum surface, step (21) is spontaneously favored, since the formation of adsorbed CO is a fast process, even at low potentials. Thus, the coverage

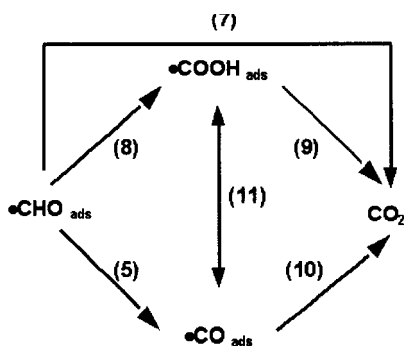


Figure 9. Mechanism of the oxidation of  $(\bullet\text{CHO})_{\text{ads}}$  (schematic representation).

of adsorbed CO is high and explains the poisoning phenomena encountered at a platinum electrode. This poisoning species can be removed [by oxidation through step (26) into CO<sub>2</sub>] only at potentials at which oxygenated species are present at the electrode surface. For platinum, such oxygenated species, arising from the dissociation of water, step (22), appear only for potentials greater than 0.5 to 0.6 V.<sup>37,38</sup> An alternative route is the direct oxidation of (•CHO)<sub>ads</sub> into CO<sub>2</sub> by step (23) or through step (24) followed by step (25). In both cases, the reaction again needs the presence of an oxygen atom, which can be provided only by the dissociation of water at the platinum surface.

### 3. How to Increase the Kinetics of the Electrooxidation of Methanol

Platinum is the only acceptable electrocatalyst for most of the primary intermediate steps in the electrooxidation of methanol. It allows the dissociation of the methanol molecule by breaking the C–H bonds during the adsorption steps. However, as seen earlier, this dissociation leads spontaneously to the formation of CO, which is due to its strong adsorption on Pt; this species is a catalyst poison for the subsequent steps in the overall reaction of electrooxidation of CH<sub>3</sub>OH. The adsorption properties of the platinum surface must be modified to improve the kinetics of the overall reaction and hence to remove the poisoning species. Two different consequences can be envisaged from this modification: prevention of the formation of the strongly adsorbed species, or increasing the kinetics of its oxidation. Such a modification will have an effect on the kinetics of steps (23) and (24) instead of step (21) in the first case and of step (26) in the second case.

The rate-determining step (rds) of the reaction on platinum is the oxidation of adsorbed CO with adsorbed hydroxyl species [step (26)]. The current density of the methanol electrooxidation can be obtained from the following equation<sup>39–41</sup>:

$$j = n F k \theta_{\text{res}} \theta_{\text{OH}} \exp(\alpha n_{\text{rds}} FE/RT) \quad (28)$$

where  $\theta_{\text{res}}$  and  $\theta_{\text{OH}}$  are the coverages in the adsorbed residues of methanol and in hydroxyl groups (arising from water dissociation),  $n$  and  $n_{\text{rds}}$  are the numbers of electrons involved in the overall reaction and in the rate-determining step;  $k$  is the rate constant,  $F$  the Faraday constant,  $\alpha$  the transfer coefficient, and  $E$  the electrode potential. The coverages in

methanol residues and in hydroxyl species can be expected to depend on the electrode potential. However, in the case of CO adsorbed on platinum, the  $\text{CO}_{\text{ads}}$  coverage is high and rather constant over a large potential range from 0.1 to 0.7 V vs. RHE. Thus, one may infer that the current density versus potential relation is dependent mainly on the coverage in adsorbed OH. As a consequence, the first approach to improving the overall kinetics is to increase the adsorbed OH coverage at low potentials. This can be done by increasing the dispersion of platinum (i.e., by decreasing the particle sizes) or by adding to platinum a second metal more easily oxidized at lower potentials. These two possibilities are discussed in the next section.

In Eq. (28), the methanol residue is mainly adsorbed CO. As discussed earlier, other kinds of adsorbed species can also be present on the electrode surface. The different species and their degree of coverage on the Pt surface depend on the electrode potential and also on the nature and the structure of the electrode surface. For the sake of simplicity, if only two types of adsorbed species,  $\text{CO}_{\text{ads}}$  and  $\text{CHO}_{\text{ads}}$ , are considered, Eq. (28) becomes:

$$j = nF \theta_{\text{OH}} [k_{10} \theta_{\text{CO}} \exp(\alpha_{10} n_{10} FE/RT) + k_7 \theta_{\text{CHO}} \exp(\alpha_7 n_7 FE/RT)] \quad (29)$$

where  $k_i$ ,  $\alpha_i$ , and  $n_i$  are the corresponding parameters for steps (23) and (26), respectively. For this simple model, an optimized electrocatalyst is one with a  $\theta_{\text{CO}}$  value as low as possible, and with  $\theta_{\text{CHO}}$  and  $\theta_{\text{OH}}$  each being equal to 0.5 at low potentials. Since it is impossible to avoid the formation of adsorbed CO on pure platinum, it is obvious that at least a second metal is necessary to fulfill the conditions of optimal coverage.

#### 4. Structure and Composition of the Electrode in Relation to its Electroactivity

##### (i) *Effect of the Platinum Crystallographic Structure*

Since oxidation of methanol is an electrocatalytic reaction with different adsorption steps, interactions of the adsorbed species with the metallic surface are important. Using platinum single-crystal electrodes, it has been proven that the electrooxidation of methanol is a surface-sensitive reaction.<sup>23,24</sup> The initial activity of the Pt(110) plane is much higher than that of the other low-index planes, but the poisoning phenomenon is so rapid that it causes a fast decrease in the current densities. The



structural effect was confirmed by *in situ* infrared spectroscopy which showed a high coverage of adsorbed CO on a Pt(110) plane: conversely, on the other single-crystal planes, a distribution of different species is clearly visible.<sup>36,42,43</sup> Further, strong lateral interactions between the different adsorbed species on Pt(100) lead to very low activity of this electrode at low potentials.<sup>36</sup>

### (ii) *Effect of Particle Size and Carbon Support*

The effects of dispersion of the electrocatalyst and of particle size on the kinetics of electrooxidation of methanol have been the subject of numerous studies because of the utilization of carbon support in DMFC anodes. The main objective is to determine the optimum size of the platinum anode particles in order to increase the effectiveness factor of platinum. Such a size effect, which is widely recognized in the case of the reduction of oxygen,<sup>44,45</sup> is still a subject of discussion for the oxidation of methanol. According to some investigators,<sup>46</sup> an optimum of 2 nm for the platinum particle size exists, but studying particle sizes up to 1.4 nm, other authors observed no size effect.<sup>47</sup> According to a recent study,<sup>48</sup> the rate of oxidation of methanol remains constant for particles greater than 4.5 nm, but decreases with size for smaller particles (up to 2.2 nm).

Such information can be obtained from cyclic voltammetric measurements.<sup>49</sup> It is possible to determine the quantity of electricity involved in the adsorption of hydrogen, or for the electrooxidation of previously adsorbed CO, and then to estimate the real surface area and the roughness factor ( $\gamma$ ) of a Pt-C electrode. From the real surface area and the Pt loading, it is possible to estimate the specific surface area,  $S$  (in  $\text{m}^2 \text{g}^{-1}$ ), as follows:

$$S = 100 \gamma / W \quad (30)$$

where  $W$  (in  $\mu\text{g cm}^{-2}$ ) is the Pt loading of the carbon powder (referred to the geometric surface area) and  $\gamma$  is the roughness factor, i.e., the ratio of the real surface area  $A_r$  to the geometric surface area  $A_g$ . This specific surface area is useful for easily characterizing the dispersed catalyst. Using the simple idea that all the particles can be assumed to be hemispherical, the particle diameters  $d$  in nanometers can be obtained from the value of  $S$  by:

$$d = \frac{60W}{\gamma_p} = \frac{6000}{S_p} \quad (31)$$

with  $\rho$  the density of the platinum ( $21.4 \text{ g cm}^{-3}$ ). The estimated value of  $d$  can be then compared with the size observed by microscopic techniques.

It is also convenient to compare the behavior of different dispersed catalysts with the help of the two following quantities: the mass activity,  $MA$ , in  $\text{Ag}^{-1}$ , and the specific activity,  $SA$ , in  $\mu\text{A cm}^{-2}$ .<sup>49</sup> The values of  $MA$  and  $SA$  of different dispersed Pt-carbon powders for the electrooxidation of methanol are given in Table 3. Both  $MA$  and  $SA$  increase with the amount of surface oxides on the carbon powder.  $MA$  does not depend on the platinum-specific surface area, but depends on the carbon structure only.  $SA$  decreases with an increase in the platinum-specific surface area (Table 3; see Ref. 49). In this study, it was also reported that the oxidation state of the carbon powder support has a greater effect than that of the particle size on the kinetics of electrooxidation of methanol at platinum particles.<sup>49</sup> This analysis could explain the discrepancies encountered in the literature. When the high surface area carbon powder (which is the support commonly used for the electrocatalyst) is partially covered by

**Table 3**  
**Specific Activity ( $SA$ ) and Mass Activity ( $MA$ ) of Pt Electrocatalysts Supported on Different Carbon Powders Characterized by Specific Surface Area ( $S$ ) and Particle Size ( $d$ )**

Sample	$S(\text{m}^2\text{g}^{-1})$	$d(\text{nm})^a$	$SA(\mu\text{A cm}^{-2})$	$MA(\text{A g}^{-1})$
Vulcan <sup>b</sup>	64	4.5	37	24
	38	7.5	68	26
	32	9.0	75	24
	19	14.0	137	26
Vulcan <sup>c</sup>	31	9.0	126	39
	15	18.5	240	36
HSAG <sup>d</sup>	73	4.0	67	49
	37	7.5	127	41
	25	11.0	196	49
E-TEK	112	2.5	41	46
Bulk Pt	—	—	78	—

<sup>a</sup>Calculated assuming spherical particles.

<sup>b</sup>As received.

<sup>c</sup>Oxidized.

<sup>d</sup>High surface area graphite (from Lonza Co.)

oxidized groups, the strength of the Pt–O bonds on the particle surface can be modified. From this point of view, adsorbed OH species are necessary for the rate-determining step of methanol oxidation; the particle size effects, as observed in the results of this study, are quite valuable.

Another convenient way to disperse platinum-based electrocatalysts is to use electron-conducting polymers, such as polyaniline (PAni) or polypyrrole (PPy), which play the role of a three-dimensional electrode.<sup>50,51</sup> In such a way very dispersed electrocatalysts are obtained, with particle sizes on the order of a few nanometers, leading to a very high activity for the oxidation of methanol (Fig. 10).

Finally, a simple method for a rapid evaluation of the activity of high surface area electrocatalysts is to observe the electrocatalytic response of a dispersion of carbon-supported catalyst in a thin layer of a recast proton exchange membrane.<sup>52</sup> This type of electrode can be easily obtained from a solution of Nafion. As an example, Fig. 11 gives the comparative

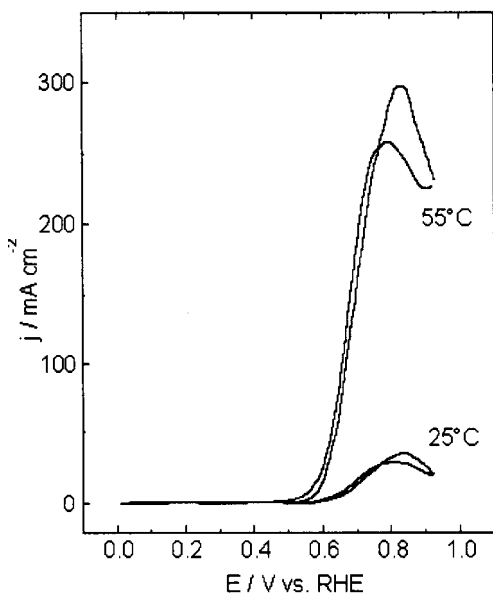


Figure 10. Electrocatalytic oxidation of 1 M CH<sub>3</sub>OH in 0.5 M HClO<sub>4</sub> on a platinum electrode dispersed in polyaniline (Pt loading 5 mg cm<sup>-2</sup>, sweep rate 5 mV s<sup>-1</sup>).

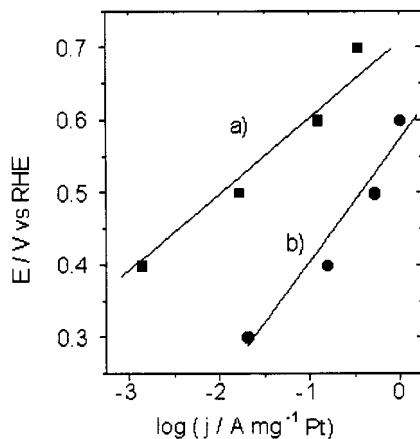


Figure 11. Tafel plots for methanol oxidation on (a) an E-Tek Pt-C electrode and (b) an E-Tek Pt<sub>0.5</sub>Ru<sub>0.5</sub>-C electrode (1 M CH<sub>3</sub>OH in 0.5 M HClO<sub>4</sub>, 50 °C, metal loading 0.1 mg cm<sup>-2</sup>).

behavior of Pt-C and Pt-Ru-C electrodes toward the electrooxidation of methanol at 50 °C. The mass activities found are in agreement with the results published in the literature for fuel cell electrodes,<sup>53</sup> which demonstrates the advantage and the accuracy of the method.

### (iii) Bimetallic Electrodes

In spite of the extent of dispersion of Pt particles on pretreated carbon powder, the poisoning effect has still been observed. An alternative approach is thus to add a second component (a promoter) to platinum to decrease the formation of poisoning species or to promote their oxidation at lower potentials. Since this latter process needs the presence of oxygenated species, numerous types of components have been explored to generate O or OH species at lower potentials on the platinum surface. Historically, systematic screening of the possible metals shows that only a few metals led to positive results.<sup>54</sup> Ruthenium, tin, and molybdenum were the most promising ones. In a more recent systematic study, theoretical calculations were carried out to determine the effects of alloying platinum with transition metals in groups 4 to 6 on the ease of formation

of OH-adsorbed species.<sup>55</sup> Such calculations can only provide an insight on this effect, but not on the stability of the selected alloys. According to the authors of this study, Ru and Cr are potentially interesting alloying components, while in general all the elements in the left part of the periodic table may also show some prospects. A crucial remark on such a type of estimation is that in a DMFC, the electrolyte is acidic and thus a highly corrosive medium environment prevails, so that a more noble environment (e.g., Pt with Ru) is necessary.

*(a) Nature of the promoter*

A third way to increase both the active surface area and the number of oxygenated species at the electrode surface is to prepare alloy particles or deposits and then to dissolve the non-noble metal component.<sup>33</sup> This technique, which is similar to that used to prepare Raney-type catalysts, yields very high surface area electrodes and hence some improvements in the electrocatalytic activities compared with those of pure platinum. However, it is always difficult to be sure whether the mechanism of enhancement of the activities is due to this effect or the possible presence of remaining traces of the dissolved metal. Results with Pt<sub>3</sub>Cr and Pt<sub>3</sub>Fe were encouraging,<sup>33</sup> although the effect of iron is still under discussion. From studies in a recent work<sup>33</sup> on the behavior of Pt-Fe particles for methanol electrooxidation, it was concluded that the electrocatalytic effect is due to the Fe alloyed to platinum.<sup>56</sup>

The use of adatoms of foreign metals obtained by underpotential deposition on the platinum surface is another convenient method for investigating the effect of a promoter on the electrocatalytic properties of platinum.<sup>23,24</sup> However, the effect of adatoms in this case has been shown to be not as effective for electrooxidation of methanol as for the oxidation of other organic molecules such as formic acid; adatoms of tin, however, showed a positive effect on the rate of methanol oxidation.<sup>57</sup>

Most of the studies have involved the alloying of a second metal to platinum. The second metal was generally chosen because of its ability to increase the concentration of oxygenated species on the electrode surface, but also for its corrosion resistance. Even if some discrepancies exist in the literature, Pt-Ru is now widely accepted as the most interesting one, and hence our analysis will focus on this alloy in the next subsection. Other alloys such as Pt-Ir, Pt-Os,<sup>58</sup> or Pt-Re<sup>59</sup> have also been reported to be good candidates, and Pt-Mo under specific conditions of preparation was claimed to have the desired properties.<sup>60</sup> The Pt-Sn alloy is still a subject

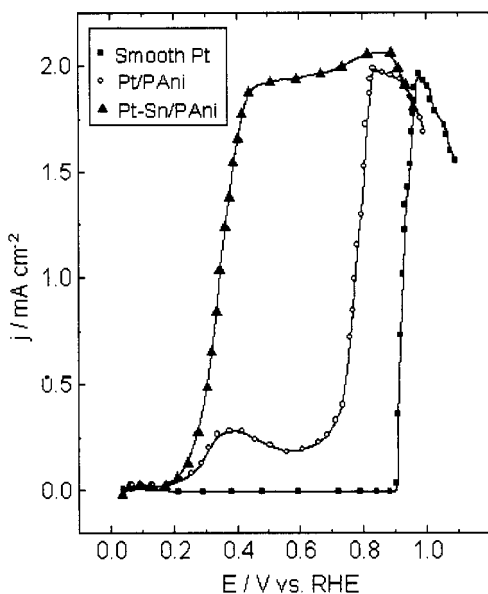


Figure 12. Electrocatalytic oxidation of CO (from a CO-saturated 0.1 M HClO<sub>4</sub> solution) on different Pt-based electrodes (sweep rate 5 mV/s, 25 °C): (■) smooth Pt, (O) 0.1 mg cm<sup>-2</sup> Pt dispersed in a polyaniline film, (▲) 0.1 mg cm<sup>-2</sup> Pt-Sn dispersed in a polyaniline film.

of discussion.<sup>23,24,61,62</sup> A rather small effect is observed for the oxidation of methanol by alloying tin to platinum. This is in contradiction to the very strong effect observed during the oxidation of CO or adsorbed CO on Pt-Sn (Fig. 12).<sup>63,64</sup> This result, which is quite surprising, shows that if methanol is dissociated mainly to adsorbed CO at platinum sites, the distribution of species on the surface is different from that encountered in the case of adsorption from dissolved CO. In the latter case, the surface of Pt-Sn is covered only by a single state of adsorbed CO species.<sup>63</sup> On pure Pt, different states of adsorbed CO exist, as proved by infrared reflectance spectroscopy, even for the case of CO from dissolved gaseous CO.

In addition to these different types of alloys, some studies were also devoted to alternatives to platinum as electrocatalysts. Unfortunately, it is clear that even if some catalytic activities were observed, they are far from those obtained with platinum.<sup>65,66</sup> Nickel tungsten carbides were investigated, but the electrocatalytic activity recorded for methanol oxidation was very low. Tungsten carbide was also considered as a possible alternative owing to its ability to catalyze the electrooxidation of hydrogen. However, it had no activity for the oxidation of methanol and recently some groups showed that a codeposit of Pt and  $\text{WO}_3$  led to an enhancement of the activity of platinum.<sup>67,68</sup>

(b) *The case of Pt-Ru*

Despite considerable efforts made over the past 20 years, the best alloying component known to enhance the electrooxidation of methanol on platinum is still ruthenium. It was first proposed in the 1960s during the pioneering investigations on methanol fuel cell electrocatalysts at Shell Research Laboratory.<sup>69</sup> The main advantage of using a Pt-Ru electrocatalyst is its ability to shift the potential of methanol oxidation in the negative direction, compared with Pt.<sup>23,24,32,70-74</sup> As a result, the current densities observed with a Pt-Ru electrode are higher than with pure platinum in the DMFC operating potential region. This can be explained by the following:

1. the presence of Ru increases the possibility of having adsorbed OH species on the electrode surface, which results in the oxidation of the adsorbed intermediate species (mainly CO) at a lower potential and/or;
2. the presence of Ru minimizes the formation of the CO poisoning species.

Evidence for the first reason was demonstrated in X-ray photoelectron spectroscopy (XPS)<sup>75</sup> or X-Ray Absorption Near Edge Structure (XANES) studies,<sup>76</sup> as well as by many voltammetric studies.<sup>23,24,70</sup>

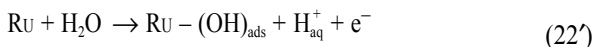
The different kinds of adsorbed CO were observed by *in situ* infrared reflectance spectroscopy.<sup>73,74</sup> The results showed that using bulk Pt-Ru alloys, the adsorbed CO species formed by dissociation of methanol, or from dissolved CO on the surface of the electrode, are different on Pt and on Ru.<sup>74</sup> The adsorption of CO occurs on pure Pt and Ru and on alloys of different compositions, but a shift detected in the wave number of the

linearly adsorbed CO shows that CO is more strongly bonded to the Pt than to the Ru surface. This can be interpreted as an electronic effect due to the formation of the alloy.<sup>33</sup>

Another very interesting result obtained from these FTIRS measurements is the difference between adsorbed CO obtained from dissolved CO and that from the dissociation of adsorbed methanol. The shift in wave number is more important with dissolved CO. These shifts may also be correlated with the superficial composition of the alloys, and it was observed that the optimized composition for the oxidation of CO (about 50 at.% Ru) is different from that for the oxidation of methanol (about 15 at.% Ru). FTIR spectra also revealed that the amount of adsorbed CO formed from methanol dissociation is considerably higher on Pt than on Pt-Ru. For a Pt<sub>0.9</sub>-Ru<sub>0.1</sub> alloy, the amount of linearly adsorbed CO is very small (Fig. 8), suggesting a low coverage in the poisoning species. Moreover, by observing the potentials at which the CO<sub>2</sub> IR absorption band appears, it is possible to conclude that the oxidation of both (CHO)<sub>ads</sub> and (CO)<sub>ads</sub> species occurs at much lower potentials on a Pt-Ru alloy electrode than on pure Pt.

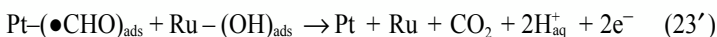
These conclusions from the infrared reflectance spectra recorded with Pt and Pt-Ru bulk alloys were confirmed in electrocatalysis studies on small bimetallic particles dispersed on high surface area carbon powders.<sup>32</sup> Concerning the structure of bimetallic Pt-Ru particles, *in situ* Extended X-Ray Absorption Fine Structure (EXAFS)-XANES experiments showed that the particle is a true alloy.<sup>77</sup> For practical application, it is very important to determine the optimum composition of the Pt-Ru alloys. Even if there are still some discrepancies, several recent studies<sup>71-74</sup> have concluded that an optimum composition about 15 to 20 at.% in ruthenium gives the best results for the oxidation of methanol. This composition is different from that for the oxidation of dissolved CO (about 50 at.% Ru), confirming a different spatial distribution of the adsorbed species.

By comparison with the mechanism discussed above for pure platinum, the promoting effect of ruthenium can result from a bifunctional mechanism as follows: The adsorbed OH is formed both at Pt sites [reaction (22)], and at Ru sites in a lower potential range according to:



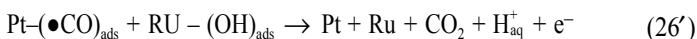
then the oxidation of formyl-like species can occur either by (23) or by:





The rate of reaction (23') is higher than that of reaction (23), mainly at lower potentials.

Since no oxidation of methanol was observed on pure Ru, it is probable that there is no  $-(\bullet\text{CHO})_{\text{ads}}$  on Ru. However, adsorption of CO was observed on an Ru electrode from solution containing dissolved CO. The adsorbed CO observed on a Pt-Ru electrode during the adsorption of methanol may arise mainly from the dissociation of methanol at Pt sites, followed by the migration of such CO species toward the neighboring Ru sites. The removal of adsorbed CO by oxidation with adsorbed OH may occur by one of two ways: (1) at Pt sites according to reactions (26) or (27) and (25), and (2) at Ru sites according to reaction (26'):



or reaction (27'):



followed by reaction (25). At a set potential, the rates of the intermediate step [Eqs. (26') and (27')] are higher than those of the corresponding steps as expressed by Eqs. (26) and (27).

## 5. Concluding Remarks on Mechanisms

The mechanism of electrooxidation of methanol is now nearly well understood. From the considerable effort made during the past 20 years, it is now possible to propose electrocatalysts with acceptable activities for DMFCs, even though further improvement is still necessary. Despite considerable research efforts, Pt-Ru alloys are the only acceptable catalysts for the electrooxidation of methanol at low anode potentials. Two questions still remain unanswered:

1. Is Pt-Ru really the best electrocatalyst? If so, how can its activity be improved?
2. What is the stability of such a bimetallic electrode, as well as that of other bimetallic and multimetallic electrodes, which exhibit high activity for methanol oxidation?

The extensive state of knowledge of the electrooxidation of methanol, as presented in this section, offers prospects of tailoring new multimetallic

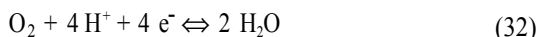
electrocatalysts with higher activities and stabilities. Such types of electrocatalysts should have several properties: (1) the capability of dissociating the methanol molecule, (2) the ability to encourage the presence of a sufficient concentration of adsorbed oxygenated species at its surface, and (3) the easy removal of poisoning species. All these conditions cannot be fulfilled by one and even two metals. It is for these reasons that tailoring of electrocatalysts with various components is necessary, i.e., platinum for the dissociation of methanol, ruthenium for the adsorption of (OH), and a third metal, the role of which could be to avoid or to limit the formation of adsorbed CO. Tin seems to have the properties for this last characteristic, since when it is associated with platinum, it is very efficient in electrooxidizing CO. The difficulty is to prepare such multimetallic electrocatalysts dispersed on a carbon powder and to maintain the different types of active sites close to each other at the atomic level. Some possible techniques for such a purpose are chemical reduction of metallic salts, electrodeposition, and use of colloidal alloys. Even if it appears possible to develop a multimetallic electrocatalyst with high activity, the problem of stability will also have to be resolved. The main problems connected with stability are the preferential dissolution of one component and a decrease in the active surface area by an increase in the size of the particles.

#### IV. OXYGEN ELECTROREDUCTION AND PROTON EXCHANGE MEMBRANE

In this section, we summarize the kinetic behavior of the oxygen reduction reaction (ORR), mainly on platinum electrodes since this metal is the most active electrocatalyst for this reaction in an acidic medium. The discussion will, however, be restricted to the characteristics of this reaction in DMFCs because of the possible presence in the cathode compartment of methanol, which can cross over the proton exchange membrane.

##### 1. The Oxygen Electroreduction Reaction<sup>40,78</sup>

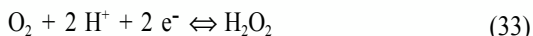
At the cathode, oxygen electroreduction occurs according to the overall reaction (in acid medium):



The kinetics of this reaction are relatively slow ( $i_0$  from  $10^{-6}$  to  $10^{-10}$  A  $\text{cm}^{-2}$ , referred to the geometric surface area, depending on the degree of dispersion of the platinum catalyst), which is the main cause of the high

overpotential  $\eta_c$  ( $\eta_c \approx$  about 400 mV for a hydrogen oxygen PEMFC, working at 500 mA cm<sup>-2</sup>). The deviation from the equilibrium potential, even at low current densities, is a consequence of some related processes:

1. The production of H<sub>2</sub>O<sub>2</sub>, either as an intermediate in the four-electron reduction of O<sub>2</sub> to water, or as a reaction product. In the latter case the thermodynamic equilibrium potential of the reaction, i.e.,



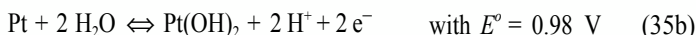
is 0.695 V/SHE, instead of 1.23 V/SHE for the overall oxygen reduction reaction. Usually in an acid medium, such as in a PEMFC, no H<sub>2</sub>O<sub>2</sub> is formed at a platinum electrode at an operating potential,  $E_c$ , of 0.9 to 0.7 V.

2. A slow rate-determining step, i.e.,

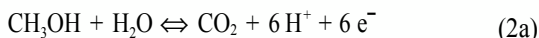


where the adsorbed intermediate (O<sub>2</sub>H<sub>ads</sub>) follows a Temkin isotherm at low overpotential, leading to a Tafel slope of  $-(RT/F)$  (low current densities). At high overvoltage (high current densities and low coverage), the adsorption isotherm becomes Langmuirian on the pure platinum surface, and the Tafel slope corresponds to  $-(2RT/F)$ , as normally observed.

3. Observance of a mixed potential of about 1.0 V (instead of the equilibrium thermodynamic reversible potential  $E_c^0 = 1.23$  V vs. SHE) due to the formation of surface oxides at the platinum electrode, according to different electrode reactions:



or even to the presence of minute traces of organic impurities undergoing an oxidation reaction, such as with methanol:



In all these cases, the electrode potential  $E_m$  will be determined by a mixed reaction resulting from the reduction of oxygen and the oxidation of the

platinum surface or of methanol at the same potential  $E_m$ . Since both reactions are quite irreversible, a Tafel behavior is practically always observed. Under these conditions, the current density ( $j_m$ ) and mixed potential ( $E_m$ ) are given by the equations:

$$j_m = j_{oa} e^{(E_m - E_a^o)/b_a} = j_{oc} e^{-(E_m - E_{oc})/b_c} \quad (36a)$$

and:

$$E_m = \frac{b_c E_a^o + b_a E_{oc}^o}{b_a + b_c} + \frac{b_a b_c}{b_a + b_c} \ln \frac{j_{oc}}{j_{oa}} \quad (36b)$$

where  $j_{oi}$  and  $b_i$  are the exchange current density and the Tafel slopes, respectively, for both half-cell reactions.

The exchange current density  $j_{oa}$  for methanol oxidation depends on the methanol concentration, i.e.:

$$j_{oa} = n F k_s^0 [\text{CH}_3\text{OH}]^{\alpha_a} \quad (37)$$

where the value of the charge transfer coefficient  $\alpha_a$  is very probably equal to 0.5. For the sake of simplicity, the standard rate constant  $k_s^0$  includes the concentration of the oxidized species (i.e.,  $\text{CO}_2$ ). Therefore a small crossover of methanol through the membrane, increasing, for example, the methanol concentration in the cathodic compartment by a factor of  $10^6$ , will result in a negative shift of the potential,  $\Delta E_m$ , at the oxygen cathode, which is expressed by the following equation:

$$\Delta E_m = \frac{b_a b_c}{b_a + b_c} \log \frac{j_{oa}}{j_{oa}'} \approx \frac{120}{2} \log 10^{-3} \approx -180 \text{ mV} \quad (38)$$

with  $j_{oa}' = 10^3 j_{oa}$  and  $b_a \approx b_c \approx 120 \text{ mV/decade}$  for both the oxygen reduction (at high current densities) and the methanol oxidation reactions.<sup>52</sup> For a higher membrane crossover rate, leading to a methanol concentration in the cathodic compartment on the order of  $10^{-2} \text{ M}$  for Nafion 117, after 5 hr of operation, as measured in our laboratory,<sup>22</sup> the shift of the oxygen electrode potential will be  $\Delta E_m \approx 120/2 \log 10^{-5} \approx -300 \text{ mV}$ . Such cathode potential shifts are effectively observed in a working DMFC-PEMFC (Fig. 13).

Therefore, one main drawback of the PEMFC configuration with a standard proton exchange membrane (such as Nafion) and a standard platinum gas diffusion cathode is the cathode depolarization caused by a mixed potential resulting from the methanol crossover through the mem-

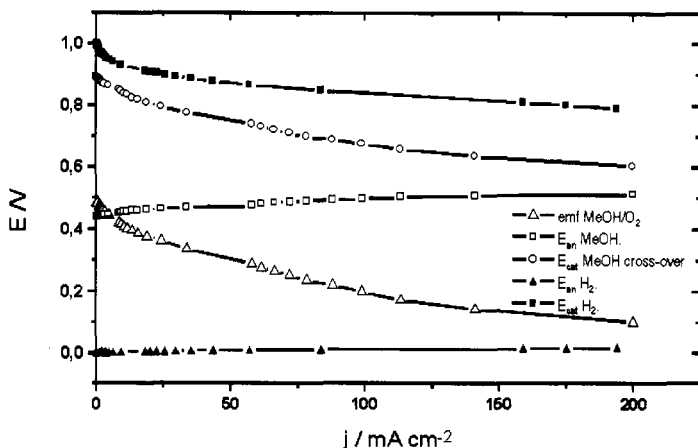


Figure 13. Comparison of oxygen electrode performance in H<sub>2</sub>-O<sub>2</sub> PEMFC and DMFC: (■) potential of the H<sub>2</sub>-O<sub>2</sub> PEMFC cathode, (○) potential of the DMFC cathode, (Δ) DMFC cell potential.

brane. There are two possibilities for overcoming these difficulties; the first is to conceive new electrocatalysts for oxygen reduction but which are highly inactive for methanol oxidation, and the second is to develop new membranes that are more methanol impermeable.

## 2. Concepts for New Oxygen Reduction Electrocatalysts

Among the non-noble metal electrocatalysts suitable for the ORR, organometallic macrocycles have often been considered as an alternative to platinum-based catalysts.<sup>79</sup> In particular, transition metal phthalocyanines and porphyrins, which have a similar square planar structure, were thoroughly examined for their activity toward oxygen electroreduction. Investigations of O<sub>2</sub> reduction electrocatalysts have usually been carried out on thin films of the organometallic complex supported on a carbon, a graphite, or a metal substrate, such as gold.<sup>80-84</sup> The nature of the central metal ion (Fe, Co, Mn, Ni)<sup>85</sup> or that of the substituents of the organic ligands has a strong influence on the catalytic activity.<sup>86</sup> The polymerization of the macrocyclic monomer, which is possible through the highly conjugated organic structures with delocalized  $\pi$  electrons, greatly improved the electrical conductivity of the film and therefore its electroactivity. Co and Fe porphyrins and/or phthalocyanines were found to be the best non-noble

metal electrocatalysts for oxygen electroreduction. It was found that the electrocatalytic activity is mainly associated with the metallic  $M^{II/III}$  redox couple. Many experiments carried out in our laboratory and in other laboratories showed a very beneficial effect in that these macrocyclic compounds are insensitive to methanol, i.e., no methanol oxidation is observed on these compounds, nor is the oxygen cathode depolarized in the presence of methanol.

For practical cathodes of a PEM fuel cell, the macrocyclic compounds are supported on a carbon powder (such as Vulcan XC72) and thermally treated (up to 800 °C), which substantially increases their electrocatalytic activities. After pyrolysis and dispersion of the macrocyclic catalysts on the carbon substrate, the nature and structure of the electrocatalytic sites are difficult to assign and correlate with their electroactivity for oxygen reduction. The pyrolysis treatment also destroys the molecular structure. A better approach is to disperse the electrocatalytic entity at the molecular level in a convenient substrate, such as an electron-conducting polymer (polyaniline PANi, or polypyrrole PPy). One of the first ideas was to incorporate a tetrasulfonated cobalt porphyrin (CoTSPP) or a tetrasulfonated iron phthalocyanine (FeTSPc) as a counter-ion during the electropolymerization of pyrrole.<sup>87,88</sup> These modified electrodes, particularly those containing FeTSPc, display an excellent electrocatalytic activity for the oxygen reduction reaction, somewhat similar to that of platinum electrodes, leading to a four-electron process in an acid medium.<sup>89,90</sup> However, the stability of these electrodes is poor due to degradation of the PPy film at the electrode potential of the oxygen cathode. A better stability is obtained when the macrocyclic catalyst is dispersed in a PANi film, and this may be due to a greater resistance to oxidation by small traces of hydrogen peroxide resulting from a two-electron reduction process.<sup>89</sup>

Since the macrocycle counter-ion can be expelled from the polymeric matrix at low potentials, an alternative is to directly electropolymerize a modified or substituted metal porphyrin or phthalocyanine containing an electropolymerizable functional group (e.g., an amino group). This approach was followed by Murray et al., who showed that a poly-tetra-(*o*-aminophenyl)porphyrin (poly-CoTAPP) film formed by electropolymerization of the corresponding monomer on a glassy carbon electrode displayed a good electrocatalytic activity for the oxygen reduction reaction.<sup>91,92</sup> Similarly, the electropolymerization in nonaqueous medium (acetonitrile containing 0.1 M tetraethylammonium perchlorate)

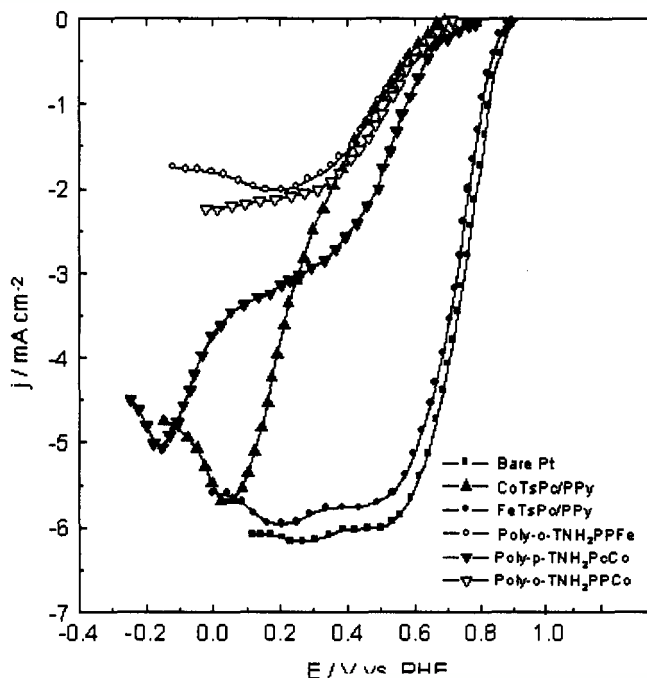


Figure 14. Oxygen electroreduction at different transition metal macrocyclic electrocatalysts. Comparison with the behavior of a Pt electrode (■).

of cobalt tetraaminophthalocyanine (CoTAPc) leads to electrocatalytically active oxygen cathodes,<sup>93</sup> which are more efficient for a four-electron reduction process than those prepared from the cobalt porphyrin monomer (CoTAPP).

The behavior of these modified electrodes toward oxygen electroreduction was compared with that of bare platinum (Fig. 14). This figure shows that the tetrasulfonated iron phthalocyanine dispersed in a polypyrrole film is the best nonmetallic electrocatalyst, displaying an electrocatalytic activity close to that of platinum. The presence of 0.1  $M$   $\text{CH}_3\text{OH}$  in the electrolytic solution (0.5  $M$   $\text{H}_2\text{SO}_4$ ) does not affect the oxygen reduction wave except for the Pt electrode, confirming the prospect of these macrocyclic transition metal electrocatalysts being methanol insensitive during oxygen electroreduction in a DMFC.

### 3. Development of New Proton Exchange Membranes

One way to avoid the depolarization of the oxygen cathode by the presence of methanol is to develop new membranes with a lower methanol crossover. This is extremely difficult because the proton exchange membranes must in addition have good ionic conductivities and good mechanical and chemical stabilities (in time and in temperature). These membranes must also be produced with relatively inexpensive starting materials and low-cost manufacturing processes. In order to evaluate the methanol crossover through the membranes, the concentration of methanol in the cathode compartment can be followed by high performance liquid chromatography (HPLC) as a function of time and for different electrode potentials. This experiment was carried out in our laboratory in a special two-compartment cell, the anode compartment containing 0.1 M CH<sub>3</sub>OH in 0.5 M H<sub>2</sub>SO<sub>4</sub>, and the cathode compartment containing the supporting electrolyte (0.5 M H<sub>2</sub>SO<sub>4</sub>). The two compartments were separated by the membrane under study. Comparative studies made in our laboratory with Nafion 117 as a reference membrane and some new membranes (Fig. 15) based on ethylene-tetrafluoroethylene films (ETFE), showed that methanol crossover through Nafion 117 is relatively high ( $6.7 \times 10^{-6}$  mol/min/cm<sup>2</sup>), but this can be decreased by a factor of 2 to 3 with a new proton exchange membrane containing a barrier film.<sup>94</sup>

Similar membranes, but using cross-linked poly(tetrafluoroethylene-hexafluoropropylene) copolymers (FEP) also gave good results, but at relatively low temperatures (60 °C).<sup>95</sup> Other types of membranes, such as sulfonated polyimides,<sup>96</sup> fluorinated poly(aryl ether sulfone), or sulfonated copolymer incorporating trifluorostyrene monomer,<sup>97</sup> were also developed, mainly for the H<sub>2</sub>-O<sub>2</sub> PEMFC. A new approach is to consider high temperature-resistant membranes, such as polybenzimidazole (PBI) and to impregnate them with phosphoric acid to increase the ionic conductivity.<sup>98</sup> Such membranes were tested in a DMFC working up to 200 °C. The methanol crossover was estimated to be ten times less than that observed with Nafion, and good performance characteristics were obtained in a DMFC working at 200 °C as a consequence of the improved kinetics at both electrodes, which was due to higher working temperatures.

All these attempts to improve the membrane characteristics by decreasing the methanol crossover and increasing their temperature resistance gave encouraging results. However, modification of the existing membranes (e.g., with barrier screens) without decreasing the electrical



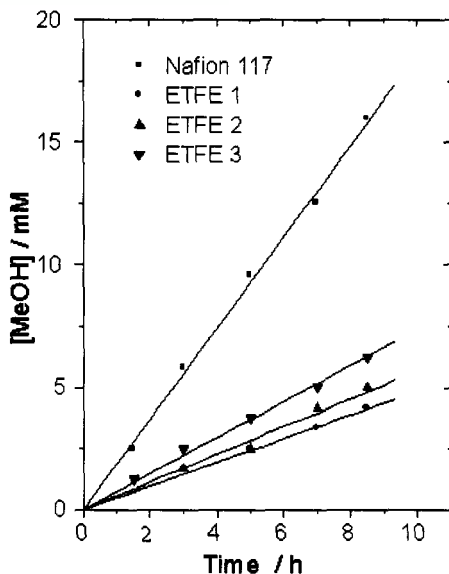


Figure 15. Extent of methanol crossover through different ETFE proton-conducting membranes. Comparison with the behavior of Nafion 117 (■).

conductivity seems to be a goal difficult to reach. Similarly, an increase in thermal stability without decreasing ionic conductivity, and a decrease in the membrane cost are other challenges to be resolved in accelerating the development of DMFCs.

## V. PROGRESS IN TECHNOLOGY

### 1. Single-Cell Investigations to Attain High Performance Levels

#### (i) *Synopsis of Achievements from the 1960s to 1990s*

The enthusiasm for developing DMFCs (the fuel cell researcher's dream) evolved in the 1960s, which was really the boom period for R&D activities on all types of fuel cell technologies, mainly because of NASA's vital need for fuel cell power plants for space vehicles. As early as the 1960s it was recognized that the major challenges in developing DMFCs

are to (1) significantly enhance the electrochemical reactivity of methanol [it is important to note that the exchange current density for methanol oxidation even on the best electrocatalyst (i.e., Pt-Ru) to date is about six orders of magnitude lower than that for hydrogen oxidation]; and (2) minimize the crossover of methanol from the anode to the cathode because it causes considerable decreases in the voltage and Coulombic efficiencies.

In spite of these challenges, there is still great enthusiasm for developing DMFCs because (1) methanol is a liquid fuel with a high energy content (gravimetrically and volumetrically; these values are about half of those for gasoline); and (2) it eliminates a bulky, heavy, and complex fuel processor, which is estimated to have about the same weight and volume as an electrochemical cell stack. Further, when one takes into consideration the efficiency of the fuel processor (about 70%), even at a lower efficiency of the electrochemical cell stack with  $\text{CH}_3\text{OH}$  than that obtained with  $\text{H}_2$ , the overall efficiencies of the direct and indirect DMFCs could have nearly the same values. An attempt is made in this subsection to present a synopsis of the progress in DMFC technology at the single-cell level in the past four decades. It is worth pointing out that R&D activities were highest in the 1960s and revitalized in the 1990s because of the “dream” of using DMFCs in electric vehicles.<sup>99</sup> Another attractive application of DMFCs, which has always been highlighted, is for portable or remote power sources (civilian and military).

During the previous decades, the active players engaged in the development of DMFCs were the researchers at Shell Thornton Research in England,<sup>17,21</sup> Exxon Research and Engineering in the United States,<sup>100</sup> Hitachi in Japan,<sup>18</sup> and Battelle Institute in Germany.<sup>85</sup> Single cells were developed in acid, alkaline, and buffered electrolytes. It was soon realized that the optimum choice was the acid electrolyte because of the problems of, (1) the carbonation of the alkaline electrolyte and deposition of a solid carbonate within the porous structure in this electrolyte, and (2) low ionic conductivity in the resulting buffered electrolytes. Platinum and a multitude of platinum-based alloys (Pt-Ru, Pt-Sn, Pt-Mo, etc.) were evaluated as the electrocatalysts for oxidation of methanol.<sup>22,54</sup> Even as early as these investigations (1960s and early 1970s), it was realized that an effective electrocatalyst for methanol oxidation must be bifunctional, i.e., the electrocatalyst must adsorb methanol and water at potentials close to the reversible potential. Platinum was the only metallic electrocatalyst that could perform these functions, but the drawback was that adsorption of

methanol occurs at low overpotentials, while water is adsorbed at higher overpotentials. As a consequence of the development of alloy catalysts for gas phase oxidation of low molecular weight hydrocarbons and alcohols, high surface-area alloy catalysts (Pt with Ru, Mo, Sn, Ti, Re) were tested for electrooxidation of methanol.<sup>21,22</sup> The incorporation of a second element, which provides nascent oxygen sites for oxidation of organic species (formed by chemisorption and surface reaction of methanol), was found to be beneficial in decreasing the overpotential for this reaction. There was a second advantage of the nascent oxygen, i.e., it is capable of oxidatively removing the organic intermediate species and hence of reducing the decay rate of the performance of the methanol electrode with time.

In most of the single-cell studies from the 1960s to the 1980s, sulfuric acid (1 to 3 M) was used as the electrolyte and methanol was dissolved in the electrolyte. The single cell contained an auxiliary for electrolyte circulation. In these cells, platinum was used as the electrocatalyst for oxygen reduction. Some alternatives attempted included metal organic complexes (phthalocyanines, porphyrins).<sup>21</sup> An interesting study was performed at Exxon, i.e., the use of a redox couple ( $\text{Mo}^{5+}$ - $\text{Mo}^{6+}$ ) for electrooxidation of methanol. In this case, the electron transfer of the reaction at the anode was the conversion of  $\text{Mo}^{5+}$  to  $\text{Mo}^{6+}$ , which then oxidizes methanol close to the electrode surface via a chemical reaction. Shell also carried out some single-cell studies with a super acid (trifluoromethane sulfonic acid) as the electrolyte<sup>21</sup>; the reason for this approach was that previous work had shown that the performance of a hydrogen-oxygen fuel cell in this acid was considerably higher than in phosphoric acid.<sup>101</sup> This result was attributed to the faster oxygen reduction kinetics in  $\text{CF}_3\text{SO}_3\text{H}$  than in  $\text{H}_3\text{PO}_4$ , mainly because of the lower adsorption of anions on platinum from the former acid. The noble metal loading in the electrode was high (about 4 mg/cm<sup>2</sup>). The presence of methanol in the electrolyte also caused the depolarization of the oxygen electrode. This was in spite of the considerably higher value of the interelectrode spacing in these single cells, compared with that in today's PEMFCs. The performances of the single cells were relatively low. At best, it was possible to attain a cell potential of 0.4 V at a current density of 50–100 mA/cm<sup>2</sup>.<sup>100</sup> There was also some decay in performance with time.

## ***(ii) Optimization of Structures and Compositions of Electrodes and Operating Conditions***

Recent studies (in the 1990s) focused on the optimization of structures and compositions of electrodes, membranes, and membrane electrode assemblies (MEA) and of operating conditions. The major accomplishments in these areas are summarized as follows:

1. The performance in single cells was considerably higher because of the use of perfluorosulfonic acid polymer electrolytes (e.g., Nafion). As stated earlier, these electrolytes have the advantages of minimal anion adsorption, which led to enhanced electrode kinetics. At the University of Newcastle in England, it was found that a Nafion-containing Pt-Ru electrode (Pt loading of  $3.0 \text{ mg/cm}^2$ ) exhibited current densities over  $300 \text{ mA/cm}^2$  at a cell potential of  $0.3 \text{ V}$  and  $80 \text{ }^\circ\text{C}$ .<sup>58</sup> At the CNR in Messina, Italy, raising the temperature to  $95 \text{ }^\circ\text{C}$  led to an increase in performance:  $300 \text{ mA/cm}^2$  at a cell potential of  $0.45 \text{ V}$  (with a Pt loading of  $0.8 \text{ mg/cm}^2$  at the anode and  $0.5 \text{ mg/cm}^2$  at the cathode).<sup>102</sup> The Jet Propulsion Laboratory in California, in conjunction with Giner, Inc. and the University of Southern California, has developed a DMFC with a Pt-Ru anode (Pt loading  $0.5 \text{ mg/cm}^2$ ), which has a cell potential of  $0.4 \text{ V}$  at a current density of  $100 \text{ mA/cm}^2$  at  $60 \text{ }^\circ\text{C}$ .<sup>103</sup> When the noble metal loading for the anode was increased to  $4 \text{ mg/cm}^2$  and the oxygen pressure to  $2.36 \text{ atm}$ , the cell potentials at a current density of  $400 \text{ mA/cm}^2$  were  $0.47 \text{ V}$  and  $0.36 \text{ V}$  with oxygen and air, respectively, as the cathodic reactant at a temperature of  $90 \text{ }^\circ\text{C}$ . Methanol ( $1 \text{ M}$ ) was fed as a liquid into the DMFC. The intrinsic electroactivity of Pt-Ru electrocatalysts for methanol oxidation has been improved at Johnson Matthey in England by electrodes fabricated with  $20 \text{ wt.}\%$  platinum and  $20 \text{ wt.}\%$  Pt,  $10 \text{ wt.}\%$  Ru on carbon black in a recast Nafion film between the Nafion 117 membrane and current collector.<sup>25</sup>

2. Investigations at Siemens in Erlangen, Germany, have used unsupported platinum-ruthenium anodes ( $4 \text{ mg/cm}^2$ ) and platinum black cathodes ( $4 \text{ mg/cm}^2$ ).<sup>19</sup> Their best performances were  $0.52 \text{ V}$  at  $400 \text{ mA/cm}^2$ . At Los Alamos National Laboratory in New Mexico,<sup>104</sup> the electrocatalyst was unsupported Pt-RuO<sub>x</sub> at the anode and unsupported Pt black at the cathode (Pt loading about  $2 \text{ mg/cm}^2$ ). In a subsequent study, the thinner Nafion 112 membrane was used to reduce the ohmic drop. Under pressure at  $400 \text{ mA/cm}^2$ , cell potentials of  $0.57 \text{ V}$  with O<sub>2</sub> and  $0.52$

V with air were attained. The group at the University of Newcastle also reported similar performances using electrodes with a Pt loading of about  $2 \text{ mg/cm}^2$ .<sup>58</sup>

3. The optimization of operating conditions is vital for attaining the highest level of performance in DMFCs. Methanol can be fed as a vapor or as a liquid into the DMFC. Vapor-fed systems have the advantage of better cell performance. However, such systems need auxiliaries for waste heat removal, and fuel preheating will also be necessary. Since waste heat removal is simplified in the liquid-fed DMFCs, most of the DMFC R&D activities are now using this mode of operation. With the liquid-fed system, another major problem in PEMFCs (i.e., drying out of membrane) is overcome. It may also be possible to operate the DMFC without humidification of the oxygen and under pressure, the operating temperature of the DMFC could be raised to  $130 \text{ }^\circ\text{C}$ .<sup>25</sup> The advantages of the high temperature–high pressure operation are the enhanced kinetics of the half-cell reactions and the reduced poisoning of the anode by adsorbed intermediates.

4. DMFCs operating under less severe conditions of temperature ( $60$  to  $100 \text{ }^\circ\text{C}$ ) and pressure (close to atmospheric air pressure) were recently demonstrated, particularly for portable power sources. At  $90 \text{ }^\circ\text{C}$  with  $20$  psig air pressure, the performance attained is  $0.44 \text{ V}$  at  $300 \text{ mA/cm}^2$ .<sup>105</sup> At a lower temperature ( $60 \text{ }^\circ\text{C}$ ) and  $1$  atm air pressure, a voltage of  $0.4 \text{ V}$  at  $150 \text{ mA/cm}^2$  was obtained by JPL, using electrodes of  $25\text{-cm}^2$  active surface area and containing  $4 \text{ mg/cm}^2$  of platinum-based catalysts. At LANL, a  $50\text{-cm}^2$ ,  $2\text{-mm}$ -thick DMFC single cell operating at  $60 \text{ }^\circ\text{C}$  with ambient air pressure gave good performance ( $0.4 \text{ V}$  at  $200 \text{ mA/cm}^2$ ) and was able to operate for more than  $2000$  hr at  $100 \text{ }^\circ\text{C}$  with more than  $90\%$  of fuel utilization and a power density of  $150 \text{ mW/cm}^2$  without loss of performance (Fig. 16).<sup>106</sup> This demonstrates the ability to achieve a peak power density of  $0.15 \text{ W/cm}^2$  near  $100 \text{ }^\circ\text{C}$  using  $30$  psig air and with an overall Pt loading of  $2.6 \text{ mg/cm}^2$  (Fig. 17).<sup>106</sup>

5. Researchers at Argonne National Laboratory in Illinois have investigated the prospects of developing DMFCs with ceramic electrolytes operating at  $450$  to  $550 \text{ }^\circ\text{C}$ .<sup>107</sup> The advantages of operating DMFCs at these temperatures are: (1) Methanol and perhaps even gasoline can be used directly as the fuel. (2) CO formed as an intermediate is not a poison, but a fuel. (3) The problem of methanol crossover is eliminated. (4) Product water formed as a vapor can easily be removed, which solves the

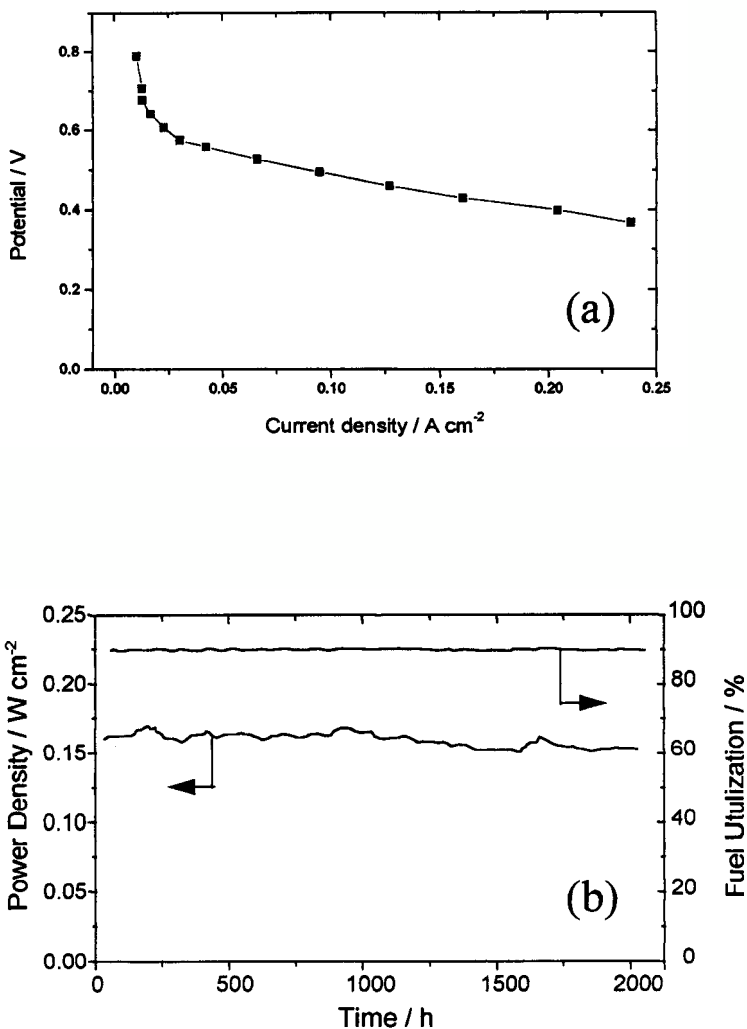


Figure 16. (a) Current voltage characteristic of a 50-cm<sup>2</sup>, 2-mm-thick, DMFC single cell operating under benign conditions: 60 °C, 1 M methanol feed, ambient air pressure, stoichiometric air flow of 2.5 at 150 mA/cm<sup>2</sup>. (b) Life test of power density and fuel utilization for the same DMFC single cell operating at 100 °C and 0.4 V with air feed at 30 psig. (After Ref. 106; reproduced with permission.)

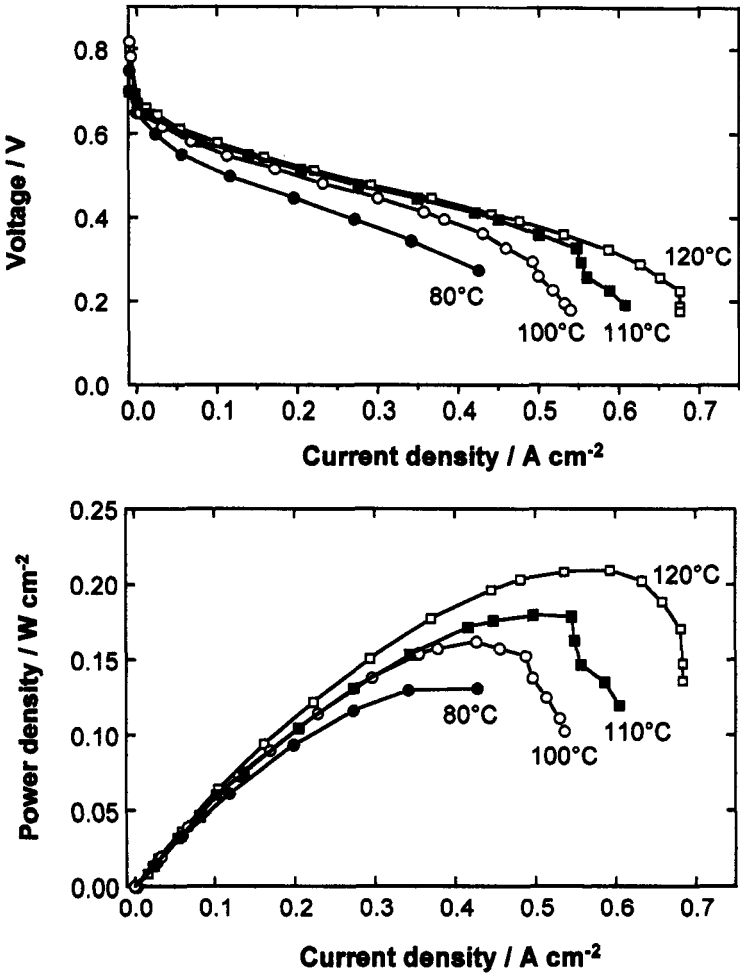


Figure 17. Voltage and power density as a function of current density for a DMFC single cell. Overall Pt loading of  $2.6 \text{ mg/cm}^2$ , anode feed of  $1 \text{ M}$  methanol, cathode feed of 30 psig air. (After Ref. 106; reproduced with permission.)

water management problem encountered in PEMFCs. (5) It offers the potential for a system with a greatly simplified configuration, compared with that of PEMFCs. Conversely, the disadvantages of a DMFC with a ceramic electrolyte are: (1) They have a relatively high operating tempera-

ture, because of which the startup time may be relatively long. However, on the positive side, such a DMFC can have applications as stationary power generation and power sources for heavy-duty transportation (fleet vehicles, buses, trucks, etc.). (2) Ceramic components require complex and expensive fabrication techniques. Preliminary investigations have been conducted in a single cell with a flat-plate design at 500 °C. The materials used in this cell were  $\text{Ce}_{0.9} \text{Gd}_{0.1} \text{O}_{1.95}$  for the electrolyte; the anode contained  $\text{Ni-Ce}_{0.9} \text{Gd}_{0.1}$ . This combination of materials was necessary to extend the three-dimensional reaction zone in order to have both electronic and ionic (oxide ions) conductivity in the active layer, which is akin to the impregnation of Nafion (a proton conductor) in the PEMFC fuel cell electrodes. One of the challenges in this technology is to develop methods (tape casting, vapor deposition) for the thin-layer formation of the individual components to form the thin-film structure. A promising method is tape casting of organic formulations, which include the dispersing agent, binder, and plasticizer. Initial studies were carried out with hydrogen gas mixtures (6 to 50%  $\text{H}_2$ ) and with methanol vapor. The performance of the SOFC with 50%  $\text{H}_2$ -air was good, reflecting a low IR drop in the cell. The performance of the SOFC using methanol (17 M) was comparable to that with 6%  $\text{H}_2$  as the fuel.

Table 4 and Fig. 18 illustrate the performance levels achieved by the active players in DMFC R&D.<sup>25</sup> The main goal in DMFC research in the U.S. and European programs is to achieve a stable performance level of 200 mW/cm<sup>2</sup> at a cell potential of 0.5 to 0.6 V. It is because of the relatively low activity of the electrocatalyst for methanol electrooxidation that this power level is less than half that of a PEMFC with  $\text{H}_2$  as a fuel. A higher power level of the DMFC is essential for a transportation application, but the present power level goal is quite adequate for small portable power sources.

### ***(iii) Minimization of Permeability to Methanol of Proton-Conducting Membranes***

Apart from the problems of low electrocatalytic activity of the methanol electrode and poisoning of the electrocatalyst by adsorbed intermediates, an overwhelming problem is the migration of the methanol from the anode to the cathode via the proton-conducting membrane. The perfluoro-sulfonic acid membrane contains about 30% of water by weight, which is essential for achieving the desired conductivity. The proton conduction occurs by a mechanism (proton hopping process) similar to what occurs



**Table 4**  
**Summary of DMFC Electrical Performances Currently Achieved (Single Cell)**

Research group (Country/year)	Esso (U.S. 1964)	Hitachi (Japan 1984)	Siemens (Germany 1994)	Univ. Newcastle (UK 1994)	JPL/Giner (US 1996)	LANL (US 1996)	IFC (U.S. 1997)
Reference	100	18	19	25	103	104	112
Electrolyte	3.7 M H <sub>2</sub> SO <sub>4</sub>	2.5 M H <sub>2</sub> SO <sub>4</sub>	Nafion 117	Nafion 117	Nafion 117	Nafion 112	Nafion 117
Pt-Ru anode catalyst loading/mg cm <sup>-2</sup>	Porous platinum	Pt-Ru/8	4	5	2.5	2.2	4
Pt cathode catalyst <sup>2</sup> load- ing/mg cm <sup>-2</sup>	Porous platinum	?	4	5	2.5	2.3	5
Methanol feed/concentra- tion	Liquid feed/0.5M	Liquid feed/1 M	Vapor feed	Vapor feed	Liquid feed/1 M	Liquid feed/1 M	Liquid feed/1 M
Pressure/bar (oxidant)	Ambient	Ambient (air)	4	5	1.4 (air)	3	1 (air)
Temperature (°C)	60	60	130	98	90	110	77
Cell performance (potential @ current)	0.4 V @ 100 mA cm <sup>-2</sup>	0.3 V @ 60 mA cm <sup>-2</sup>	0.52 V @ 400 mA cm <sup>-2</sup>	0.5 V @ 400mA cm <sup>-2</sup>	0.5 V @ 300 mA cm <sup>-2</sup>	0.57 V @ 400 mA cm <sup>-2</sup>	0.36 V @ 200 mA cm <sup>-2</sup>
Specific power (mW cm <sup>-2</sup> )	40	24	210	200	150	230	75
Power per g of platinum (wg <sup>-1</sup> )	?	3	30	20	30	50	10

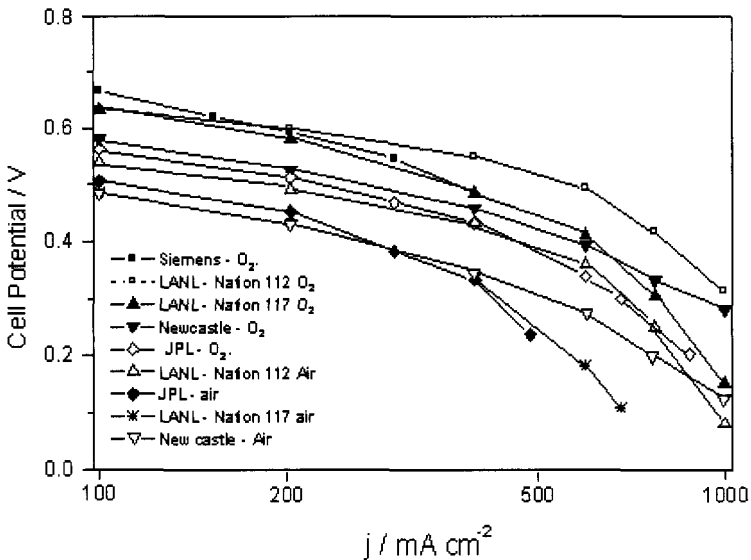


Figure 18. Tafel plots from single cell DMFC data from several research groups. (After Ref. 25; reproduced with permission.)

in an aqueous acid electrolyte (e.g.,  $\text{H}_2\text{SO}_4$ ,  $\text{HClO}_4$ ). Methanol is highly soluble in water over the entire range of composition from nearly 0% to nearly 100%. This is very much unlike the case of gaseous reactants such as  $\text{H}_2$  and  $\text{O}_2$ . Even in the latter case, the crossover current corresponds to about  $1 \text{ mA/cm}^2$  at 1 atm pressure, which is not too serious a problem when a fuel cell operates at about  $500 \text{ mA/cm}^2$ .

There are three very detrimental effects of the methanol crossover through the membrane: (1) The extent of crossover is so high (corresponding to a current density of  $100 \text{ mA/cm}^2$  for a methanol-oxygen or methanol-air fuel cell operating at  $300 \text{ mA/cm}^2$ ) that it can cause a loss of Coulombic efficiency by about 20 to 30%. (2) The methanol, which reaches the cathode, depolarizes the oxygen electrode, causing a decrease in the open circuit potential from 0.7–0.6 V to about 0.5 V. Thus the maximum possible efficiency of the cell (assuming no zero activations, ohmic and mass transport overpotentials) is only 65%. (3) The performance of the oxygen electrode is reduced, probably owing to the presence

of small amounts of organic adsorbed intermediates, at half-cell potentials less than 0.8 V.

A multitude of theoretical papers on modeling and experimental studies on the crossover problem and on methods to minimize it have appeared in the literature during the past 3–5 years and have also been presented at national and international meetings and conferences. Investigations at Los Alamos National Laboratory have reported that the crossover decreases with increasing current drawn from the cell.<sup>108</sup> An explanation for this result is not apparent because one can expect it only at current densities very close to the limiting current densities, which causes a diffusion gradient in the active layer of the fuel electrode. A second result from this group is that the crossover is decreased by increasing the operating temperature of the DMFC to about 130 °C, probably due to some vaporization of the CH<sub>3</sub>OH in the fuel, which is circulated, reducing the methanol concentration at the back of the electrode (Fig. 19).<sup>108</sup>

Methanol crossover was also investigated as a function of the ionomeric membrane thickness<sup>109,110</sup> and it was found to decrease with

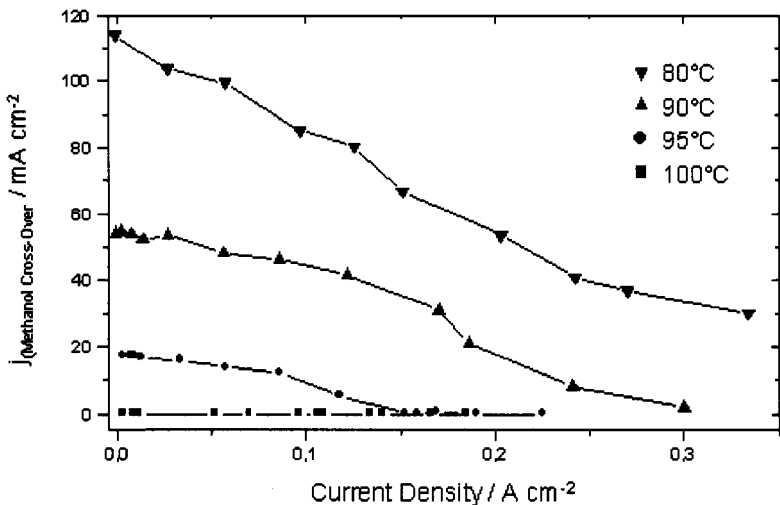


Figure 19. Extent of methanol crossover (expressed in current density) as functions of temperature and current density. (After Ref. 108; reproduced with permission.)

increasing thickness and current density.<sup>110</sup> However, the membrane resistance increases with thickness and there is an optimum thickness (7 to 10 mils) as a result of the combined effects of ionic conductivity and methanol crossover.<sup>110</sup>

A prototype DMFC using methanol and oxygen was developed at Case Western Reserve University in Ohio.<sup>111</sup> The electrolyte in this cell was a polymer electrolyte composed of phosphoric acid and polybenzimidazole. The ratio of the phosphoric acid to the imidazole group was about five to one. The main idea of using such an electrolyte was to operate the fuel cell at about 200 °C in order to (1) enhance the kinetics of the methanol oxidation and oxygen reduction reactions, (2) minimize CO poisoning, and (3) reduce methanol crossover. In this investigation, it was claimed that complete oxidation of methanol occurred in this fuel cell and methanol crossover was only 5 to 10%. However, in a previous study at International Fuel Cells, South Windsor, Connecticut, it was found that methanol crossover in a fuel cell with phosphoric acid embedded in a silicon carbide matrix was high and some methanol was consumed to form methyl phosphate and dimethyl ether.

One may conclude from all these studies that the loss in fuel utilization and Coulombic efficiency in a DMFC due to methanol crossover is still a major barrier in the development of such types of electrochemical power sources.

## 2. Cell Stack Development and Demonstration

The leading organizations in DMFC stack development are IFC in the United States<sup>112</sup> and Siemens in Germany.<sup>19</sup> The goals of the project at IFC were to develop a 150-W, 600-Whr, 24-V module; this project was sponsored by the Defense Advanced Research Project Agency for applications such as a backpack power source for military applications. IFC has also obtained financial support from the U.S. Department of Energy for component development. To date, a 10-cell stack (active surface area of electrodes  $\approx 37 \text{ cm}^2$ ) has been designed, built, and tested with liquid-fed methanol and air at ambient temperature.<sup>112</sup> The hydrophilic anode contained Pt-Ru ( $4 \text{ mg/cm}^2$ ) and Pt black ( $2 \text{ mg/cm}^2$ ) electrocatalysts. The hydrophobic cathode had  $5 \text{ mg/cm}^2$  of Pt black as the electrocatalyst. The anode flow field consisted of an inlet liquid feed to the bottom of the cell and a two-phase effluent from the top of the cell back to the center of the manifold. The performance of the 10-cell stack, as shown in Fig. 20, matched the performance predicted on the basis of the results in single

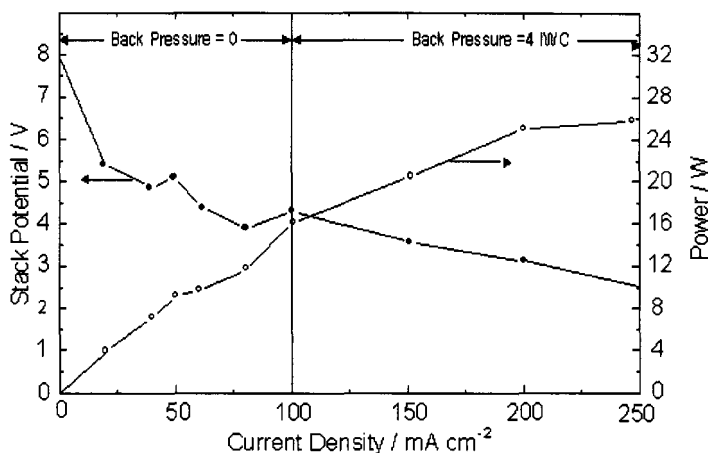


Figure 20. Performance characteristics of the International Fuel Cells 10-cell DMFC stack. (After Ref. 112; reproduced by permission of The Electrochemical Society, Inc.)

cells. The cell stack was capable of operation at 3.6 V and 200 mA/cm<sup>2</sup>. The cell temperature was set by the balance between heat loss, primarily by evaporative cooling, heat generation, and methanol crossover.

The Jet Propulsion Laboratory and Giner Inc. have an on-going collaboration to develop electrochemical DMFC stacks. A 5-cell stack (with an active area of the electrode of 25 cm<sup>2</sup>) was designed and constructed for operation with unpressurized air.<sup>103,105,113,114</sup> The performance characteristics of the stack at two operating temperatures (60 and 90 °C) and two 1 M methanol flow rates (5 and 2 liter/min), are rather good: 2 V at 250 mA/cm<sup>2</sup> at 90 °C. The variation in cell-to-cell performance was very small.<sup>103</sup> Efforts are being made at several other laboratories (e.g., LANL, H-Power) to design, construct, and test DMFC stacks.

In Europe, there are several programs under the support of the European Commission. The goal of the Joule III NEMECCEL Program (which involves four industrial companies—Thomson CSF and PSA in France, De Nora in Italy, Solvay in Belgium, one CNR laboratory in Italy and two Centre National de la Recherche Scientifique (CNRS) laboratories in France, including our laboratory) is to develop a stack with a power level of 200 mW/cm<sup>2</sup> at a cell potential of 0.5 to 0.6 V and a total power

of 1 kW at 130 °C. Another Joule III program involving Siemens and Johnson Matthey aims to evaluate and develop a DMFC stack in the kilowatt power range, based on a process allowing industrial manufacturing of large membrane-electrode assemblies. On the other hand, the state of Baden-Württemberg, in Germany, in January 1997 launched a two-phase 3-year program (total budget 7.2 million DM) on the DMFC, involving ten laboratories and research organizations (e.g., Zentrum für Sonnenenergie und Wasserstoff Forschung-ZS W, Deutsches Zentrum für Luft und Raumfahrt-DLR, Fraunhofer Institut für Solare Energiesysteme-ISE, University of Ulm, University of Stuttgart). The main objectives are to investigate some critical components of the DMFC (anode catalysts, ionomeric membranes), and to investigate the cell technology in order to achieve good performance (250 mW/cm<sup>2</sup> at 0.4 V for an elementary cell operating up to 150 °C).

In Japan, a 5-year MITV/NEDO program on DMFC under the leadership of the Japan Automobile Research Institute (JARI) was started at the end of 1998. This DMFC project involves different automobile companies (Nissan, Suzuki), industrial companies (Japan Storage Battery, Sumitomo Metal, Mitsubishi Gas Chemical) and twelve national and academic laboratories for a total budget of 20 million US\$. It is focused on the development of new catalysts and new protonic membranes allowing a DMFC to work up to 200 °C, leading to higher power densities (up to 500 mW/cm<sup>2</sup>). The system components (bipolar plates, air compressor, fuel and water treatment) will also be optimized. The technical targets are a fuel cell efficiency of 40%, a power density of fuel cell stack of 50 W/liter, a fuel cell system efficiency of 30%, and a vehicle efficiency of 24%. If this goal is reached, the JARI will be involved to develop 10-kW stacks for the electric vehicle.

## VI. PROGNOSIS—DMFCs FOR THE 21ST CENTURY

The DMFC is the most attractive type of fuel cell as a powerplant for electric vehicles and as a portable power source, because methanol is a liquid fuel with values for the specific energy and energy density being about equal to half those for liquid hydrocarbon fuels (gasoline and diesel fuel).

After petroleum resource are depleted, methanol is the logical liquid fuel for the above-mentioned and other applications, because it can be

synthesized on a large scale quite economically from the world-wide, abundant primary energy resources (natural gas, coal, or biomass).

Fundamental studies, carried out since the early seventies, using *in-situ* electrochemical-spectroscopic (or on-line gas chromatographic or mass spectrometry) techniques have provided great insight on the mechanistic and electrocatalytic aspects of the methanol oxidation reaction. The accomplishments in these investigations are at a peak level to tailor-make multifunctional, multimetallic electrocatalysts with the desired characteristics, i.e., (i) fast dissociative adsorption of methanol, (ii) removal of adsorbed, poisoning species by using electrocatalysts to provide nascent oxygen or redox sites to accelerate the rates of the intermediate steps and hence of the overall reaction.

Though there were only relatively short periods since the 1960s (Space Era—1960s, Energy Era—1970s, and Military and Environmental Eras—1980s and 1990s, respectively), with limited financial support, to develop DMFCs, a significant breakthrough in the 1990s was due to the high degree of success in the technology development of DMFCs by using a proton conducting membrane for the electrolyte. The PEMFC technology (using pure hydrogen or hydrogen produced by fuel-processing of methanol or gasoline) for electric vehicle applications is advancing so rapidly that its fringe benefit will be to accelerate DMFC technology development, in respect to optimization of the structure and composition of the membrane, electrodes and membrane electrode assembly, finding membranes for the operation of the fuel cell at 150 to 200°C, developing DMFCs with advanced bipolar plates, etc.

The challenging problems in DMFC technology development are to (i) enhance the electrocatalytic activities for methanol oxidation, (ii) speed up the oxidative removal of the poisoning adsorbed intermediate species which causes a degradation of the performance, and (iii) minimize the transport of methanol from the anode to the cathode and thereby achieve nearly 100% Coulombic efficiency and at least a 40% voltage efficiency at the desired power levels. Progress made in these directions shed light for the development and commercialization of DMFCs in the 21st century.

Our crystal-ball predictions are that DMFCs will first be commercialized as portable power sources for military and civilian applications before the year 2010 and that there will then be a quantum jump in the technology to be in a position to drive DMFC-powered electric vehicles 10 years thereafter.

## ACKNOWLEDGMENTS

The authors are grateful to several research agencies (DGXII at the European Commission and ADEME and the Provincial Council Poitou-Charentes in France) for their support in the investigation of the components of a DMFC, and to the National Science Foundation (U.S.)/CNRS (France) for their sponsorship in a 3-year cooperative research program on proton exchange membrane fuel cells and electrocatalysis of methanol oxidation.

## REFERENCES

- <sup>1</sup>W. Mitchell Jr. (ed.), *Fuel Cells*, Academic Press, New York, 1963.
- <sup>2</sup>H. Liebhafsky and E. J. Cairns, *Fuel Cells and Fuel Cell Batteries*, Wiley, New York, 1968.
- <sup>3</sup>K. R. Williams (ed.), *An Introduction to Fuel Cells*, Elsevier, Amsterdam, 1966.
- <sup>4</sup>J. O'M. Bockris and S. Srinivasan, *Fuel Cells: Their Electrochemistry*, McGraw-Hill, New York, 1969.
- <sup>5</sup>A. J. Appleby and E. R. Foulkes, *Fuel Cell Handbook*, Van Nostrand Reinhold, New York, 1989.
- <sup>6</sup>S. Srinivasan and R. Mosdale, *Bull. Electrochem. Soc.* **12** (1996) 170.
- <sup>7</sup>K. Kordesch and G. Simader, *Fuel Cells and Their Applications*, VCH, Weinheim, 1996.
- <sup>8</sup>K. B. Prater, *J. Power Sources* **37** (1992) 181.
- <sup>9</sup>L. J. M. J. Blömen and M. N. Mugerwa (eds.), *Fuel Cell Systems*, New York, 1993.
- <sup>10</sup>W. Dönitz, G. Gutman, and P. Urban, in *Proc. 2nd International Symposium on New Materials for Fuel Cell and Modern Battery Systems*, Ed. by O. Savadogo and P. R. Roberge, 1997, pp. 14–26.
- <sup>11</sup>C. Lamy and J. M. Léger, in *Proc. 2nd International Symposium on New Materials for Fuel Cell and Modern Battery Systems*, Ed. by O. Savadogo and P. R. Roberge, Ecole Polytechnique, Montreal, 1997, pp. 477–488.
- <sup>12</sup>T. O. Pavela, *Ann. Acad. Sci. Fennicae AII*, **59** (1954) 7.
- <sup>13</sup>E. W. Justi and A. W. Winsel, Brit. Patent 821,688 (1955).
- <sup>14</sup>J. E. Wynn, *Proc. Ann. Power Sources Conf.* **14** (1960) 52.
- <sup>15</sup>H. E. Hunger, *Proc. Ann. Power Sources Conf.* **14** (1960) 55.
- <sup>16</sup>J. N. Murray and P. G. Grimes, in *Fuel Cells*, American Institute of Chemical Engineers, New York, 1963, p. 57.
- <sup>17</sup>R. W. Glazebrook, *J. Power Sources* **7** (1982) 215.
- <sup>18</sup>K. Tamura, T. Tsukui, T. Kamo, and T. Kudo, *Hitachi Hyoron* **66** (1984) 49.
- <sup>19</sup>M. Waidhas, W. Drenckhahn, W. Preidel, and H. Landes, *J. Power Sources* **61** (1996) 91.
- <sup>20</sup>A. R. Landgrebe, R. K. Sen, and D. J. Wheeler, in *Proc. of the DOE Workshop on Direct Methanol Air Fuel Cells*, The Electrochem. Society, Pennington, NJ, **PV92-14**, 1992, pp. 111–129.
- <sup>21</sup>B. D. McNicol, in *Power Sources for Electric Vehicles: Studies in Electrical and Electronic Engineering*, Vol. 11, Ed. by B. D. McNicol and D. A. J. Rand, Elsevier, Amsterdam, 1984, pp. 807–838.
- <sup>22</sup>C. Lamy and J.-M. Léger, in *Proc. 1st International Symposium on New Materials for Fuel Cell Systems*, Ed. by O. Savadogo, P. R. Roberge, and T. N. Veziroglu, Ecole Polytechnique, Montreal, 1995, pp. 296–309.
- <sup>23</sup>R. Parsons and T. Vandernoot, *J. Electroanal. Chem.* **257** (1989) 9.



- <sup>24</sup> B. Beden, C. Lamy, and J.-M. Léger, Electrochemical Oxidation of Oxygenated Aliphatic Organic Compounds at Noble Metal Electrodes, in *Modern Aspects of Electrochemistry*, Vol. 22, Ed. by J. O'M. Bockris, B. E. Conway, and R. E. White, Plenum Press, New York, 1992, pp. 97–264.
- <sup>25</sup> M. P. Hogarth and G. A. Hards, *Platinum Metal Rev.* **40** (1996) 150.
- <sup>26</sup> C. Lamy and J.-M. Léger, *Proceedings of the DOE Workshop on Direct Methanol Air Fuel Cells*, Ed. by A. R. Landgrebe, R. K. Sen, and D. J. Wheeler, PV. 92-14, The Electrochemical Society, Pennington, NJ, 1992, pp. 111–129.
- <sup>27</sup> C. Lamy and J.-M. Léger, *J. Phys. N.*, C1,4 (1994) 253.
- <sup>28</sup> M. Shibata and S. Motoo, *J. Electroanal. Chem.* **209** (1986) 151.
- <sup>29</sup> E. M. Belgsir, H. Huser, J.-M. Léger, and C. Lamy, *J. Electroanal. Chem.* **225** (1987) 281.
- <sup>30</sup> T. Iwasita-Vielstich, in *Advances in Electrochemical Science and Engineering*, Vol. 1, Ed. by H. Gerischer and C. W. Tobias, VCH Verlag (Weinheim), 1990, p. 127.
- <sup>31</sup> B. Beden and C. Lamy, in *Spectroelectrochemistry, Theory and Practice*, Ed. by R. J. Gale, Plenum Press, New York, 1998, pp. 189–259.
- <sup>32</sup> C. Lamy, J.-M. Léger, F. Hahn, B. Beden, R. Durand, and A. Kabbabi, in *Electrode Process IV*, Ed. by A. Wieckowski and K. Itaya, The Electrochem. Society, Pennington, NJ, PV96-8, 1996, pp. 356–370.
- <sup>33</sup> A. Hamnett, *Catal. Today* **38** (1997) 445.
- <sup>34</sup> B. Beden, F. Hahn, S. Juanto, C. Lamy, and J.-M. Léger, *J. Electroanal. Chem.* **225** (1987) 215.
- <sup>35</sup> B. Beden, C. Lamy, A. Bewick, and K. Kunimatsu, *J. Electroanal. Chem.* **121** (1981) 343.
- <sup>36</sup> S. Juanto, B. Beden, F. Hahn, J.-M. Léger, and C. Lamy, *J. Electroanal. Chem.* **237** (1987) 119; *ibid.* **238** (1987) 323.
- <sup>37</sup> B. V. Tilak, B. E. Conway, and H. Angerstein-Kozłowska, *J. Electroanal. Chem.* **48** (1973) 1.
- <sup>38</sup> N. H. Li, S. G. Sun, and S. P. Chen, *J. Electroanal. Chem.* **430** (1997) 57.
- <sup>39</sup> S. Swathirajan and Y. M. Mickhail, *J. Electrochem. Soc.* **138** (1991) 1321.
- <sup>40</sup> J. O'M. Bockris and S. U. M. Khan, *Surface Electrochemistry, A Molecular Approach*, Plenum Press, New York, 1993.
- <sup>41</sup> P. S. Kauranen, E. Skou, and J. Munk, *J. Electroanal. Chem.* **404** (1996) 1.
- <sup>42</sup> E. Herrero, K. Franaszczuk, and A. Wieckowski, *J. Phys. Chem.* **98** (1994) 5074.
- <sup>43</sup> A. Papoutsis, J.-M. Léger, and C. Lamy, *J. Electroanal. Chem.* **359** (1993) 141.
- <sup>44</sup> K. Kinoshita, *J. Electrochem. Soc.* **137** (1990) 845.
- <sup>45</sup> A. Kabbabi, F. Gloaguen, F. Andolfatto, and R. Durand, *J. Electroanal. Chem.* **373** (1994) 251.
- <sup>46</sup> B. J. Kennedy and A. Hamnett, *J. Electroanal. Chem.* **283** (1990) 271.
- <sup>47</sup> M. Watanabe, S. Saegusa, and P. Stonehart, *J. Electroanal. Chem.* **271** (1989) 213.
- <sup>48</sup> T. Frelink, W. Visscher, and J. R. van Veen, *J. Electroanal. Chem.* **382** (1995) 65.
- <sup>49</sup> F. Gloaguen, J.-M. Léger, and C. Lamy, *J. Appl. Electrochem.* **27** (1997) 1052.
- <sup>50</sup> C. Lamy, J.-M. Léger, and F. Gamier, in *Handbook of Organic Conductive Molecules and Polymers*, Vol. 3, Ed. by H. S. Nalwa, Wiley, Chichester, 1997, pp. 471–496.
- <sup>51</sup> H. Laborde, J.-M. Léger, and C. Lamy, *J. Appl. Electrochem.* **24** (1994) 219.
- <sup>52</sup> E. Gloaguen, T. Nappom, M.-J. Croissant, S. Berthelot, J.-M. Léger, C. Lamy, and S. Srinivasan, in *Proc. of the Symposium on Electrode Materials and Process for Energy Conversion and Storage IV*, Ed. by J. McBreen, S. Mukerjee, and S. Srinivasan, The Electrochemical Society, Pennington, NJ, PV 97-13, 1997, pp. 131–138.
- <sup>53</sup> X. Ren, M. S. Wilson, and S. Gottesfeld, *J. Electrochem. Soc.* **143** (1996) L12.
- <sup>54</sup> M. M. P. Janssen and J. Moolhuysen, *Electrochim. Acta* **21** (1976) 869.
- <sup>55</sup> A. B. Anderson, E. Grantscharova, and S. Seong, *J. Electrochem. Soc.* **143** (1996) 2075.
- <sup>56</sup> C. Ma and A. D. Kowalak, *Mat. Res. Soc. Proc.* **368** (1995) 145.
- <sup>57</sup> M. Watanabe, Y. Furuuchi, and S. Motoo, *J. Electroanal. Chem.* **191** (1985) 367.
- <sup>58</sup> A. Hamnett and B. J. Kennedy, *Electrochim. Acta* **33** (1988) 1613.

- <sup>59</sup>K. J. Cathro, *Electrochem. Tech.* **5** (1967) 441.
- <sup>60</sup>A. J. Wang, H. Nakajima, and H. Kita, *J. Electroanal. Chem.* **250** (1988) 213.
- <sup>61</sup>A. Norton Haner and P. N. Ross, *J. Phys. Chem.* **95** (1991) 3740.
- <sup>62</sup>K. Wang, H. A. Gasteiger, N. M. Markovic, and P. N. Ross, *Electrochim. Acta* **41** (1996) 2587.
- <sup>63</sup>H. A. Gasteiger, N. Markovic, and P. N. Ross, *Catal. Lett.* **36** (1996) 1.
- <sup>64</sup>W. T. Napporn, J.-M. Léger, and C. Lamy, *J. Electroanal. Chem.* **408** (1996) 141.
- <sup>65</sup>G. T. Burstein, C. J. Barnett, A. R. J. Kucernak, and K. R. Williams, *J. Electrochem. Soc.* **143** (1996) L139.
- <sup>66</sup>G. T. Burstein, C. J. Barnett, A. R. J. Kucernak, and K. R. Williams, *Catal. Today* **38** (1997) 425.
- <sup>67</sup>P. Shen, K. Chen, and A. C. C. Tseung, *J. Chem. Soc. Faraday Trans.* **90** (1994) 3089.
- <sup>68</sup>A. K. Shukla, M. K. Ravikumar, A. S. Arico, G. Candiano, V. Antonucci, N. Giordano, and A. Hamnett, *J. Appl. Electrochem.* **25** (1995) 528.
- <sup>69</sup>B. D. McNicol, *J. Electroanal. Chem.* **118** (1981) 71.
- <sup>70</sup>M. Watanabe and S. Motoo, *J. Electroanal. Chem.* **60** (1975) 267.
- <sup>71</sup>H. A. Gasteiger, N. Markovic, P. N. Ross, and E. J. Cairns, *J. Phys. Chem.* **97** (1993) 12020.
- <sup>72</sup>H. A. Gasteiger, N. Markovic, P. N. Ross, and E. J. Cairns, *J. Electrochem. Soc.* **141** (1994) 1795.
- <sup>73</sup>R. Ianniello, V. M. Schmidt, U. Stimming, J. Stumper, and A. Wallau, *Electrochim. Acta* **39** (1994) 1863.
- <sup>74</sup>A. Kabbabi, R. Faure, R. Durand, B. Beden, F. Hahn, J.-M. Léger, and C. Lamy, *J. Electroanal. Chem.* **444** (1998) 41.
- <sup>75</sup>K. Franaszczuk and J. Sobkowski, *J. Electroanal. Chem.* **327** (1992) 235.
- <sup>76</sup>D. Aberdam, R. Durand, R. Faure, F. Gloaguen, J. L. Hazemann, E. Herrero, A. Kabbabi, and O. Ulrich, *J. Electroanal. Chem.* **398** (1995) 43.
- <sup>77</sup>J. McBreen, S. Mukerjee, S. Srinivasan, J.-M. Léger, W. T. Napporn, and C. Lamy, in *The 1997 Joint International Meeting* (192nd ECS and 48th ISE Meetings), 1997, abstract 1086.
- <sup>78</sup>M. R. Tarasevich, A. Sadkowsky, and E. Yeager, in *Comprehensive Treatise of Electrochemistry*, Vol. 7, Ed. by B. E. Conway, J. O'M. Bockris, E. Yeager, S. U. M. Khan, and R. E. White, Plenum Press, New York, 1983, pp. 301–398.
- <sup>79</sup>J. H. Zagal, *Coordination Chemistry Reviews* **119** (1992) 89.
- <sup>80</sup>R. Jasinski, *J. Electrochem. Soc.* **122** (1965) 526.
- <sup>81</sup>H. Alt, H. Binder, and G. Sandstede, *J. Catal.* **28** (1973) 8.
- <sup>82</sup>J. Zagal, R. K. Sen, and E. Yeager, *J. Electroanal. Chem.* **83** (1977) 207.
- <sup>83</sup>G. Magner, M. Savy, and G. Scarbeck, *J. Electrochem. Soc.* **127** (1980) 1076.
- <sup>84</sup>H. G. Jahnke, Ber. Bunsenges. *Phys. Chem.* **72** (1968) 1053.
- <sup>85</sup>H. Alt, H. Binder, W. Lindner, and G. Sandstede, *J. Electroanal. Chem.* **31** (1971) 19.
- <sup>86</sup>F. Beck, W. Zammert, J. Heiss, H. Miller, and R. Polster, *Z. Naturforsch.* **28A** (1973) 1009.
- <sup>87</sup>R. A. Bull, F. R. Fan, and A. J. Bard, *J. Electrochem. Soc.* **131** (1984) 687.
- <sup>88</sup>K. Okabayashi, O. Ikeda, and H. Tamura, *J. Chem. Soc., Chem. Commun.* (1983) 684.
- <sup>89</sup>A. El Hourch, S. Belcadi, P. Moisy, P. Crouigneau, J.-M. Léger, and C. Lamy, *J. Electroanal. Chem.* **339** (1992) 1.
- <sup>90</sup>A. Elzing, A. Van Der Putten, W. Visscher, and E. Barendrecht, *J. Electroanal. Chem.* **233** (1987) 113.
- <sup>91</sup>A. Bettelheim, B. A. White, S. A. Raybuck, and R. W. Murray, *Inorg. Chem.* **26** (1987) 1009.
- <sup>92</sup>A. Bettelheim, B. A. White, and R. W. Murray, *J. Electroanal. Chem.* **217** (1987) 271.
- <sup>93</sup>O. El Mouahid, C. Coutanceau, E. M. Belgsir, P. Crouigneau, J.-M. Léger, and C. Lamy, *J. Electroanal. Chem.* **426** (1997) 117.
- <sup>94</sup>C. Lamy, W. Vielstich, J. Lundsgaard, and J. Brunea, *Final Report*, Joule Contract JOU2-CT94-0310, 1996.

- <sup>95</sup>O. Haas, H. P. Brack, F. N. Büchi, B. Gupta, and G. G. Scherer, in *Proc. 2nd International Symposium on New Materials for Fuel Cell and Modern Battery Systems*, Ed. by O. Savadogo and P. R. Roberge, Ecole Polytechnique, Montreal, 1997, pp. 836–849.
- <sup>96</sup>S. Faure, N. Comet, G. Gebel, R. Mercier, M. Pineri, and B. Sillion, in *Proc. 2nd International Symposium on New Materials for Fuel Cell and Modern Battery Systems*, Ed. by O. Savadogo and P. R. Roberge, Ecole Polytechnique, Montreal, 1997, pp. 818–827.
- <sup>97</sup>A. E. Steck and C. Stone, in *Proc. 2nd International Symposium on New Materials for Fuel Cell and Modern Battery Systems*, Ed. by O. Savadogo and P. R. Roberge, Ecole Polytechnique, Montreal, 1997, pp. 792–807.
- <sup>98</sup>J. S. Wainright, R. F. Savinell, and M. H. Litt, in *Proc. 2nd International Symposium on New Materials for Fuel Cell and Modern Battery Systems*, Ed. by O. Savadogo and P. R. Roberge, Ecole Polytechnique, Montreal, 1997, pp. 808–817.
- <sup>99</sup>F. T. Bacon, *J. Electrochem. Soc.* **126** (1979) 7C.
- <sup>100</sup>C. E. Heath, *Proc. Ann. Power Sources Conf.* **18** (1964) 33.
- <sup>101</sup>A. J. Appleby and B. S. Baker, *J. Electrochem. Soc.* **125** (1978) 408.
- <sup>102</sup>A. S. Arico, P. Creti, H. Kim, R. Mantegna, N. Giordano, and V. Antonucci, *J. Electrochem. Soc.* **143** (1996) 3950.
- <sup>103</sup>S. R. Narayanan, G. Halpert, W. Chun, B. Jeffries-Nakamura, T. I. Valdez, H. Frank, and S. Surampudi, in *Proc. of the 37th Power Sources Conference*, June 1996, pp. 96–99.
- <sup>104</sup>S. Gottesfeld, S. J. C. Cleghorn, X. Ren, T. E. Springer, M. S. Wilson, and T. Zawodzinski, *Fuel Cell Seminar*, November 1996, Ed. by Courtesy Associates, Washington abstract pp. 521–524.
- <sup>105</sup>S. R. Narayanan, A. Kindler, B. Jeffries-Nakamura, W. Chun, H. Frank, M. Smart, S. Surampudi, and G. Halpert, in *Proc. of the First International Symposium on Proton Conducting Membrane Fuel Cells*, Ed. by S. Gottesfeld, G. Halpert, and A. R. Landgrebe, The Electrochemical Society, Pennington, NJ, PV 95-23, 1995, pp. 261–266.
- <sup>106</sup>X. Ren, S. C. Thomas, P. Zelenay, and S. Gottesfeld, *Fuel Cell Seminar*, November 1998, Ed. by Courtesy Associates, Washington abstract pp. 745–748.
- <sup>107</sup>R. Doshi and M. Krampelt, “Ceramic Direct Methanol Fuel Cells,” paper presented at DOE Fuel Cells for Transportation Program National Laboratory R&D Meeting, Washington DC, July 1997.
- <sup>108</sup>S. Gottesfeld, “Direct Methanol Fuel Cells,” paper presented at the DOE Fuel Cells for Transportation Program National Laboratory R&D Meeting, Washington DC, July 1997.
- <sup>109</sup>X. Ren, T. A. Zawodzinski Jr., F. Uribe, H. Dai, and S. Gottesfeld, in *Proc. of the First International Symposium on Proton Conducting Membrane Fuel Cells*, Ed. by S. Gottesfeld, G. Halpert, and A. R. Landgrebe, The Electrochemical Society, Pennington, NJ, PV95-23, 1995, pp. 284–298.
- <sup>110</sup>S. R. Narayanan, H. Frank, B. Jeffries-Nakamura, M. Smart, W. Chun, G. Halpert, J. Kosek, and C. Cropley, in *Proc. of the First International Symposium on Proton Conducting Membrane Fuel Cells*, Ed. by S. Gottesfeld, G. Halpert, and A. R. Landgrebe, The Electrochemical Society, Pennington, NJ, PV95-23, 1995, pp. 278–283.
- <sup>111</sup>J-T. Wang, J. S. Wainright, R. F. Savinell, and M. Litt, *J. Appl. Electrochem.* **26** (1996) 751.
- <sup>112</sup>T. F. Fuller, B. L. Murach, and D. L. Maricle, in *191th Meeting of the Electrochemical Society*, Vol. 97-1, abstract 620, The Electrochemical Society, Pennington, NJ, 1997, p. 812.
- <sup>113</sup>S. Surampudi, S. R. Narayanan, E. Vamos, H. Frank, G. Halpert, A. LaConti, J. Kosek, G. K. Surya Prakash, and G. A. Olah, *J. Power Sources* **47** (1994) 377.
- <sup>114</sup>S. R. Narayanan, T. Valdez, N. Rohatgi, W. Chun, and G. Halpert, in *Fuel Cell Seminar*, November 1998, Ed. by Courtesy Associates, Washington abstract pp. 707–709.

# Transport Properties of Molten Salts

Isao Okada

*Department of Chemistry, Sophia University, Tokyo, Japan*

## I. INTRODUCTION

In contrast to thermodynamic properties, transport properties are classified as irreversible processes because they are always associated with the creation of entropy. The most classical example concerns thermal conductance. As a consequence of the second principle of thermodynamics, heat spontaneously moves from higher to lower temperatures. Thus the transfer of  $\Delta H$  from temperature  $T_1$  to  $T_2$  creates a positive amount of entropy:

$$\Delta S = \Delta H(1/T_2 - 1/T_1) \quad (1)$$

The same property of entropy generation holds for other processes. In electrical conductance, charged particles move from higher to lower electrical potentials. In diffusion phenomena, all chemical entities are transferred from higher to lower chemical potentials.

It is empirically known that a linear relation exists between a potential gradient or the force  $X$  and the conjugate flux  $J$ , and the laws of Ohm, Fourier, and Fick's first law for electrical conduction, thermal conduction, and diffusion, respectively, within a range of suitably small gradients:

$$J = LX \quad (2)$$

where  $L$  is the proportionality constant or the transport coefficient.<sup>1</sup> More precisely

$$J_e = -\kappa(d\psi/dx) \quad (\text{Ohm's law}) \quad (3)$$

*Modern Aspects of Electrochemistry, Number 34*, edited by John O'M. Bockris *et al.*  
Kluwer Academic /Plenum Publishers, New York, 2001.

$$J_t = -\lambda(dT/dx) \quad (\text{Fourier's law}) \quad (4)$$

$$J_i = -D(dc_i/dx) \quad (\text{Fick's law}) \quad (5)$$

Here,  $\psi$  is the electric field,  $\kappa$  is the electrical conductivity or electrolytic conductivity in the Système International (SI) unit,  $\lambda$  the thermal conductivity, and  $D$  the diffusion coefficient.  $J_e$  is the electric current per unit area,  $J_t$  is the heat flow per unit area per unit time, and  $J_i$  is the flow of component  $i$  in units of mass, or mole, per unit area per unit time.

In the general case of  $n$  independent gradients the relation is

$$J_i = \sum_{k=1}^n L_{ik} X_k \quad (i=1, \dots, n) \quad (6)$$

The off-diagonal elements of  $L_{ik}$  represent the thermodynamic coupling of  $J_i$  and  $X_k$ .

Although the transport properties, conductivity, and viscosity can be obtained quantitatively from fluctuations in a system at equilibrium in the absence of any driving forces, it is most common to determine the values from experiments in which a flux is induced by an external stress. In the case of viscous flow, the shear viscosity  $\eta$  is the proportionality constant connecting the magnitude of shear stress  $S$  to the flux of matter relative to a stationary surface. If the flux is measured as a velocity gradient, then

$$S = \eta \, dv_x/dy \quad (7)$$

While the choice of a reference plane is usually simple for heat and electricity flow, this is not the case for diffusion in liquid mixtures.

All the transport properties derive from the thermal agitation of species at the atomic scale. In this respect, the simplest phenomenon is the diffusion process. In fact, as a consequence of thermal kinetic energy, all particles are subjected to a perfectly random movement, the velocity vector having exactly the same probability as orientation in any direction of the space. In these conditions, the net flux of matter in the direction of the concentration gradient is due only to the gradient of the population density.

Since thermal agitation is the common origin of transport properties, it gives rise to several relationships among them, for example, the Nernst-Einstein relation between diffusion and conductivity, or the Stokes-Einstein relation between diffusion and viscosity. Although transport

phenomena are irreversible processes, we can consider that the corresponding parameters are also properties of the matter in the equilibrium state. Indeed, the conductance value is the defined limit of  $i/E$  when the current density  $i$  tends to zero. The same extrapolation applies to diffusion or viscosity properties.

While electrical conductivity, diffusion coefficients, and shear viscosity are determined by weak perturbations of the fundamental diffusional motions, thermal conductivity is dominated by the vibrational motions of ions.<sup>2</sup> Heat can be transmitted through material substances without any bulk flow or long-range diffusion occurring, simply by the exchange of momentum via collisions of particles. It is for this reason that in liquids in which the rate constants for viscous flow and electrical conductivity are highly temperature dependent, the thermal conductivity remains essentially the same at lower as at much higher temperatures and more fluid conditions.

Finally, it must be recalled that the transport properties of any material are strongly dependent on the molecular or ionic interactions, and that the dynamics of each entity are narrowly correlated with the neighboring particles. This is the main reason why the theoretical treatment of these processes often shows similarities with models used for thermodynamic properties. The most classical example is the treatment of dilute electrolyte solutions by the Debye–Hückel equation for thermodynamics and by the Debye–Onsager equation for conductivity.

In the case of molten salts, no obvious model based on statistical mechanics is available because the absence of solvent results in very strong pair correlation effects. It will be shown that the fundamental properties of these liquids can be described by quasi-chemical models or, alternatively, by computer simulation of molecular dynamics (MD).

## II. DATABASE

The National Institute of Standards and Technology (NIST) molten salts database has been designed to provide engineers and scientists with rapid access to critically evaluated data for inorganic salts in the molten state. Properties include density, viscosity, electrical conductance, and surface tension. Properties for approximately 320 single salts and 4000 multicomponent systems are included, the latter being primarily binary. Data have been abstracted from the literature over the period 1890–1990. The primary data sources are the National Bureau of Standards–National

**Table 1**  
**NBS–NSRDS Molten Salt Publications**

Vol. no.	Pub. year	Subject <sup>a</sup>	Ref.
1	(1968)	Single salts ( $\rho$ , $\kappa$ , $\eta$ )	3
2	(1969)	Single salts ( $\gamma$ )	4
3	(1972)	Binary mixtures: nitrates and nitrites	5
4.1	(1974)	Binary mixtures: fluorides	6
4.2	(1976)	Binary mixtures: chlorides	7
4.3	(1977)	Binary mixtures: bromides and iodides	8
4.4	(1979)	Binary mixtures: mixed halides	9
5.1	(1980)	Additional mixtures other than nitrates, nitrites, and halides	10
5.2	(1983)	Additional mixtures: mixed anion systems	11
6	(1988)	Cumulative data to March 1988	12

<sup>a</sup> $\rho$ , density;  $\kappa$ , electrical conductance;  $\eta$ , viscosity;  $\gamma$ , surface tension.

Standard Reference Data System (NBS–NSRDS) publications on molten salts listed here.

A few more similar data compilations have been issued by Janz's group and also include diffusion coefficients.<sup>13–15</sup> They have regarded  $\text{KNO}_3$  and  $\text{NaCl}$  as the standard molten salts at “middle” and “high” temperature ranges, respectively, and compiled data on various properties, together with their recommended values, in one volume.<sup>16</sup>

The molten salt standard program<sup>17</sup> was initiated at Rensselaer Polytechnic Institute (RPI) in 1973 because of difficulties being encountered with accuracy estimates in the NBS–NSRDS molten salt series. The density, surface tension, electrical conductivity, and viscosity of  $\text{KNO}_3$  and  $\text{NaCl}$  were measured by seven laboratories over the world using samples distributed by RPI. The data from these “round-robin” measurements of raw properties were submitted to RPI for evaluation. Their recommendations are summarized in Table 2.

To extend the electrolytic conductivity reference database considerably above 1200 K,  $\text{CaF}_2$  has also been adopted as a standard by them, with extension of the temperature range for the electrolytic conductivities of  $\text{KNO}_3$  and  $\text{NaCl}$ . Their provisional recommendations as of 1991 are given in Table 3. New data recommended for molten alkali chlorides will be discussed in Section VI.

**Table 2**  
**Molten Salt Standards: Recommendations, 1978**

Property	System	Equation	T(K)	Accuracy (%)
Density		(g cm <sup>-3</sup> )		
	KNO <sub>3</sub>	$\rho = 2.3063 - 0.7235 \times 10^{-3} T$	620–730	±0.25
	NaCl	$\rho = 2.1389 - 0.5426 \times 10^{-3} T$	1080–1300	±1.0
Surface tension		(mN m <sup>-1</sup> )		
	KNO <sub>3</sub>	$\gamma = 154.715 - 71.7080 \times 10^{-3} T$	620–760	±0.5
	NaCl	$\gamma = 191,160 - 71.8800 \times 10^{-3} T$	1080–1240	±1.5
Electrolytic conductivity		(S cm <sup>-1</sup> )		
	KNO <sub>3</sub>	$\kappa = -2.125 + 5.7332 \times 10^{-3} T - 2.0301 \times 10^{-6} T^2$	615–790	±0.5
	NaCl	$\kappa = -5.6241 + 13.964 \times 10^{-3} T - 6.0245 \times 10^{-6} T^2$	1080–1250	±1.0
Viscosity		(mPa s)		
	KNO <sub>3</sub>	$\eta = 29.7085 - 71.1208 \times 10^{-3} T + 44.7023 \times 10^{-6} T^2$	615–760	±2.0
	NaCl	$\eta = 89.272 \times 10^{-3} \exp(2641.21/T)$	1080–1210	±0.2

**Table 3**  
**Molten Salts Standards: Provisional Recommendations, 1991**

Property	System	Equation	T(K)	Accuracy (%)
Electrolytic conductivity		(S cm <sup>-1</sup> )		
	CaF <sub>2</sub>	$\kappa = 16.89932 \exp(-1707.18/T)$	1690–1850	±1.5
Viscosity		(mPa s)		
	KNO <sub>3</sub>	$\eta = 8.541 \times 10^{-2} \exp(2156.12/T)$	615–790	±1.2
	NaCl	$\eta = 0.109184 \exp(2439.98/T)$	1083–1500	±2.4



Some 30 years ago, transport properties of molten salts were reviewed by Janz and Reeves,<sup>18,19</sup> who described classical experimental techniques for measuring density, electrical conductance, viscosity, transport number, and self-diffusion coefficient.

### III. ELECTRICAL CONDUCTANCE

#### 1. Electrolytic Conductivity

Good electrical conductance is one of the characteristics of many though not all molten salts. This characteristic has often been employed industrially. Various models have been proposed for the mechanism of electrical conductance. Electrolytic conductivity is related to the structure, although structure and thermodynamic properties are not the main subjects of this chapter. Electrolytic conductivities of various metal chlorides at the melting points are given in Table 4 together with some other related properties.<sup>20</sup>

**Table 4**  
**Properties of Some Metal Chlorides**

Salt	$\chi_M^a$	Structure <sup>b</sup>	$T_m$ (K)	$\Delta S$ (J K <sup>-1</sup> mol <sup>-1</sup> )	$\Delta V_m/V_m^c$	$\kappa$ (S cm <sup>-1</sup> )	$\eta$ (mPa s)
NaCl	0.40	NaCl	1074	6.30	0.28	3.6	1.0
CuCl	1.20	Wurtzite	696	2.43	0.16	3.7	4.1
MgCl <sub>2</sub>	1.28	CdCl <sub>2</sub>	980	9.74	0.28	1.0	2.2
CaCl <sub>2</sub>	0.60	CaCl <sub>2</sub>	1045	6.44	0.043	2.0	3.4
SrCl <sub>2</sub>	0.55	CaF <sub>2</sub>	1146	3.44	0.11	2.0	3.7
ZnCl <sub>2</sub>	1.44	ZnCl <sub>2</sub>	570	4.09	0.14	1×10 <sup>-3</sup>	4×10 <sup>3</sup>
HgCl <sub>2</sub>	1.32	HgCl <sub>2</sub>	554	9.11	0.21	3×10 <sup>-5</sup>	1.6
AlCl <sub>3</sub>	1.66	AlCl <sub>3</sub>	466	18.14	0.47	5×10 <sup>-7</sup>	0.36
GaCl <sub>3</sub>	1.68	GaCl <sub>3</sub>	351	7.84	0.17	2×10 <sup>-6</sup>	1.8
YCl <sub>3</sub>	0.66	AlCl <sub>3</sub>	994	7.56	0.0045	0.39	—
SbCl <sub>3</sub>	2.08	SbCl <sub>3</sub>	346	8.96	0.17	2×10 <sup>-4</sup>	—
LaCl <sub>3</sub>	0.705	UCl <sub>3</sub>	1131	11.49	0.16	1.3	6.7
BiCl <sub>3</sub>	2.08	BiCl <sub>3</sub>	507	11.20	0.18	0.38	41.0

Notes:  $T_m$ , melting point;  $\Delta S$ , entropy change on melting;  $\kappa$ , electrolytic conductivity;  $\eta$ , shear viscosity.

<sup>a</sup>Chemical scale of element proposed by Pettifor.<sup>21</sup>

<sup>b</sup>Structure of high-temperature crystal phase.

<sup>c</sup>Relative difference between molar volume of the melt at the melting point  $T_m$  and that at room temperature; the volume of the solid at  $T_m$  is unknown in some cases.

The terms “specific conductivity” and “equivalent conductivity” were previously used. However, these terms are not recommended for use as the SI units. They should be replaced by “molar conductivity” according to the SI recommendation, which states as follows, “When the mole is used, the elementary entities must be specified and may be atoms, molecules, ions, electrons, other particles, or specified groups of such particles.” Thus, when we previously used “equivalent conductivity,” we should now use “molar conductivity,” where we define the molar unit so that it is equal to the “equivalent” unit previously used. For example, we define  $(1/2)\text{Ca}^{2+}$ ,  $(1/3)\text{La}^{3+}$ ,  $(1/2)\text{CO}_3^{2-}$  and  $\text{Al}_{1/3}\text{F}$  as molar units.

Electrolytic conductivity has also been measured in many binary systems.<sup>5-11</sup> Although data on conductivities in binary mixtures are very useful for practical purposes, the information from such data alone is limited from the viewpoint of elucidation of the mechanism. For example, the empirical Markov rule<sup>22</sup> is well known for the electrical conductivity of binary mixtures. However, many examples have been presented where this rule does not hold well.

## 2. Methods of Measuring Transport Numbers in Mixtures

Internal or external mobilities in additive binary systems provide more heuristic information than in pure salts. For pure salts, the only parameter that can be obtained easily is the temperature, while detecting a change in pressure needs a difficult technique as well as specialized apparatus. However, in additive binary systems, where the composition can be easily varied, two mobilities can be compared under the same condition.

For obtaining internal or external mobilities, the corresponding transport numbers are usually measured. There are several methods for determining transport numbers in molten salts; that is, the Klemm method (countercurrent electromigration method or column method), the Hittorf method (disk method), the zone electromigration method (layer method), the emf method, and the moving boundary method. These are described in a comprehensive review.<sup>23</sup>

There is difficulty in defining the absolute mobilities of the constituent ions in a molten salt, since it does not contain fixed particles that could serve as a coordinate reference. Experimental means for measuring external transport numbers or external mobilities are scarce, although the zone electromigration method (layer method)<sup>24</sup> and the improved Hittorf method<sup>25</sup> may be used. In addition, external mobilities in molten salts cannot be easily calculated, even from molecular dynamics simulation.

Klemm<sup>23</sup> has proposed defining internal mobility by reference to one defined ion of the system, such as the anion. In the case of pure salt, the internal transport number of the cation is then unity. In the case of a mixture, the internal mobility  $u_j$  is related to the internal transport number  $t_j^i$  by

$$u_j = (t_j^i/x_j)(\kappa V_m/F) = (t_j^i/x_j)(\Lambda/F) \quad (8)$$

where  $\kappa$  is the conductivity;  $x$  the mole fraction,  $F$  the Faraday constant,  $V$ , the molar volume, and  $\Lambda$  the molar conductivity; the mole should be defined as the quantity previously called the "equivalent quantity."

The  $\epsilon_{12}$  is related to the internal transport number  $t_j^i$  and  $t_2^i$  by

$$\epsilon_{12} = (u_1 - u_2)/(x_1 u_1 + x_2 u_2) = \{(t_1^i/x_1) - (t_2^i/x_2)\} = (t_1^i - x_1)/x_1 - x_1 \quad (9)$$

Therefore,

$$t_1^i = x_1 + \epsilon_{12} x_1 x_2 \quad (10)$$

$$t_2^i = x_2 - \epsilon_{12} x_1 x_2 \quad (11)$$

The internal transport numbers may be measured most accurately and precisely by the Klemm method, which was developed for the purpose of isotope separation.<sup>26</sup> This method has the following merits: (1) It is insensitive to a small amount of impurities, such as water. (2) Even in the region of very small concentration of an ion of interest,  $\epsilon_{12}$  can be measured accurately. (3) It can be applied to additive ternary systems.<sup>27,28</sup> An apparatus for the Klemm method of measuring  $\epsilon_{12}$  in nitrate mixtures is shown in Fig. 1. This cell developed for nitrates by Okada's group<sup>29,30</sup> has the following advantages compared with other electromigration cells: (1) The gas ( $\text{NO}_2 + \text{O}_2$ ) does not need to be introduced into the cathode. (2) Even relatively expensive salts such as  $\text{RbNO}_3$  and  $\text{CsNO}_3$  can be used because only a small amount of the salt is needed for investigation. (3) The temperature of the molten salt under investigation can be kept constant by a molten salt bath.

It should be noted that when a mobility ratio is expressed in terms of the transport number, an experimental error, say, of  $\pm 0.01$ , is not small enough at small concentrations, as seen from Eq. (8). For example, at  $x_1 = 0.05$ , this error amounts to as much as  $\pm 20\%$  for  $u_1$ . It is thus preferable to express the ratio in terms of  $\epsilon_{12}$  rather than  $t^i$ .

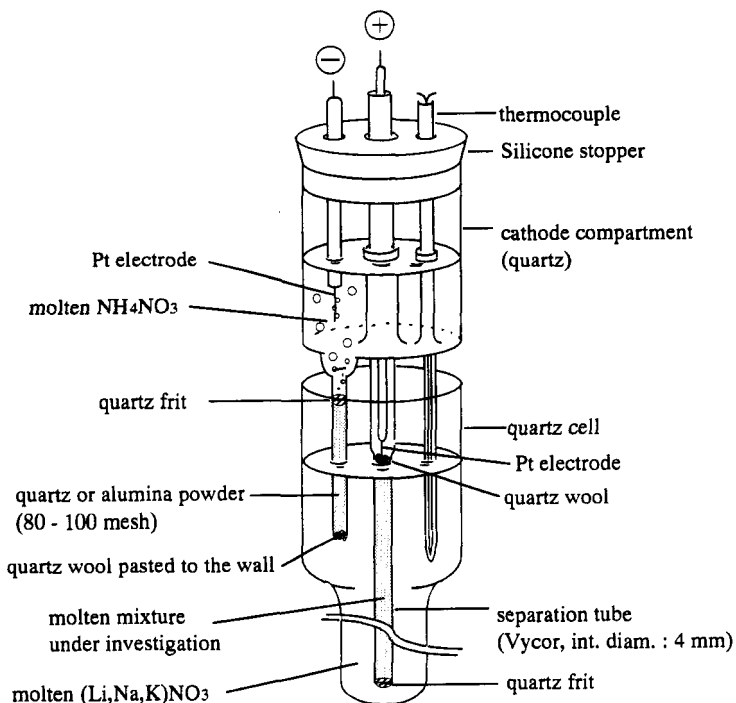


Figure 1. Electromigration cell for molten nitrates. (Reprinted from Ref. 30 with permission from *Z. Naturforschung*.)

### 3. Pattern of the Isotherms in Binary Monovalent Cation Systems

The patterns of isotherms of the internal mobilities in binary systems consisting of two monovalent cations and a common anion could provide useful insight into the mechanism of electric conductance. The patterns may be classified into two types.<sup>31</sup> In Fig. 2 the isotherms are schematically shown versus the mole fraction of the larger cation,  $x_2$ .

Type I is typical and is subclassified into five types (Ia, Ib, Ic, and Id), the isotherms of the smaller cation decrease with increasing  $x_2$ ; those of the larger ones also decrease except at high  $x_2$ , the slope being sharper in the former case. In some systems at very high  $x_1$ , the isotherms of the larger cation,  $u_2$ , decrease rather sharply with increasing  $x_1$ , particularly when the size difference between two cations is great and the temperature is low.

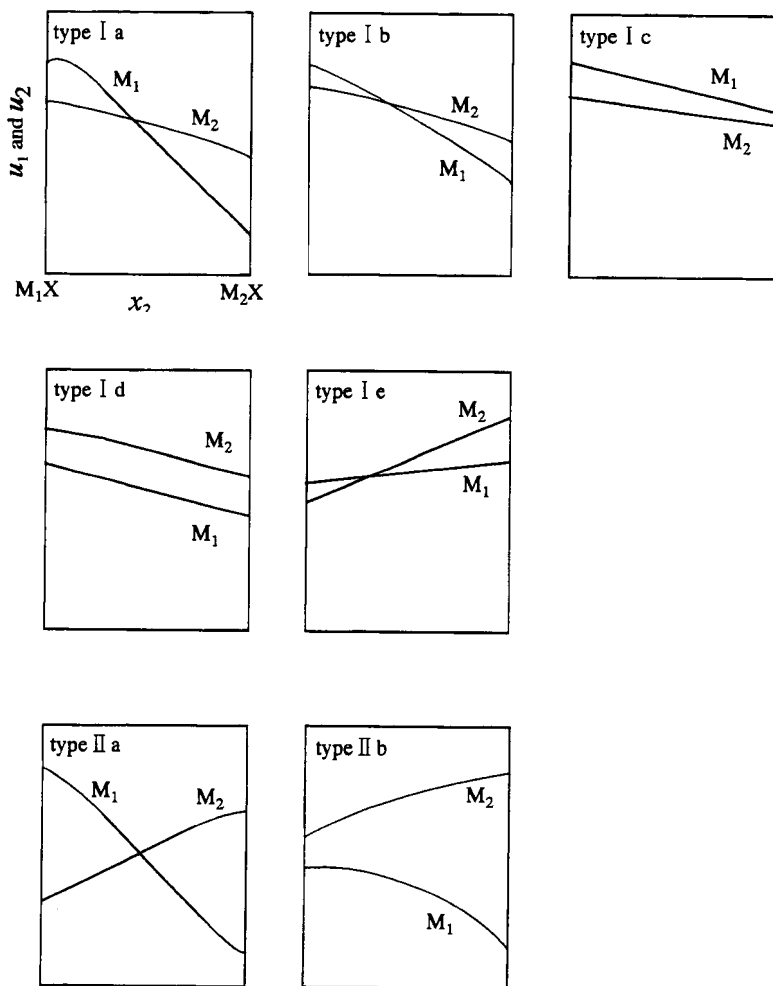


Figure 2. Isotherm patterns of internal mobilities vs. mole fraction of  $M_2X$  in  $(M_1, M_2)X$ , where  $M_1$  and  $M_2$  are the smaller and larger cations, respectively, and  $X$  is a common anion.

This sharp decrease is attributable to “the free space effect,” which is described in Section III.5(ii). When such a decrease does not occur, the system is classified as type Ib.

Type II refers to the case in which the isotherms for both cations increase with increasing concentration of the respective cations. Such isotherms have been found for  $(\text{Li}, \text{K})\text{F}_{.32}$ ,  $(\text{Li}, \text{K})(\text{SO}_4)_{1/2}$ ,<sup>33,34</sup>  $(\text{Na}, \text{K})\text{OH}$ ,<sup>35</sup>  $(\text{Ag}, \text{Cs})\text{Br}$ ,<sup>36,37</sup>  $(\text{Ag}, \text{Na})\text{I}$ ,<sup>37,38</sup>  $(\text{Ag}, \text{K})\text{I}$ ,<sup>37,38</sup> and  $(\text{Ag}, \text{CS})\text{I}$ .<sup>37</sup> In charge asymmetric systems such as  $(\text{K}, \text{Ca}_{1/2})\text{Cl}$ ,<sup>39</sup> such isotherms also usually appear. A common feature of these type II systems is the particularly strong interaction of one cation with the common anion compared with that of the second cation with the anion. The strongly interacting cation will retard the internal mobility of the second cation. This is called the “tranquilization effect,” and will be explained in Section III.5(iii).

The isotherms of some systems give particularly useful information, as with those for  $u_{\text{K}}$  in  $(\text{Li}, \text{K})(\text{CO}_3)_{1/2}$ <sup>40</sup> (Fig. 3) where the interaction between  $\text{Li}^+$  and  $\text{CO}_3^{2-}$  is particularly strong because of the divalency of the anion, when  $\text{Li}^+$  exerts a tranquilization effect on  $u_{\text{K}}$  as in  $(\text{Li}, \text{K})(\text{SO}_4)_{1/2}$ . Although  $u_{\text{K}}$  in the carbonate system decreases slightly with increasing  $x_{\text{K}}$  in the relatively high  $x_{\text{K}}$  region, the decrease is not as distinct as in the sulfate system. This is presumably because  $\text{CO}_3^{2-}$  is planar-triangular and the interaction with  $\text{Li}^+$  is not as strong as that for  $\text{SO}_4^{2-}$  where the positively charged central S atom is shielded by the tetrahedrally surrounding O atoms.

#### 4. The Chemla Effect

While trying to enrich lithium isotopes by the Klemm method in the late 1950s, Chemla employed a mixture of  $\text{LiBr}$  and  $\text{KBr}$  with the intention of reducing the operating temperature. Surprisingly, at the anode side, the ratio  $\text{Li}/\text{K}$  soon reached a constant value, although<sup>7</sup>  $\text{Li}$  continued to be enriched there.<sup>41,42</sup> It was found later that this occurred because the isotherms of the internal and external mobilities of  $\text{Li}^+$  and  $\text{K}^+$  have a crossing point, as shown in Fig. 2 (type IIb). Since then, several interpretations have been presented. This phenomenon was named the *Chemla effect* about 20 years after his discovery.<sup>30</sup> The Chemla effect is not limited to the system  $(\text{Li}, \text{K})\text{Br}$ , but is fairly common in binary systems consisting of two monovalent cations with a common anion.

Interpretation of this effect was considered to be a crucial key to a better understanding of the mechanism of electric conductance of molten

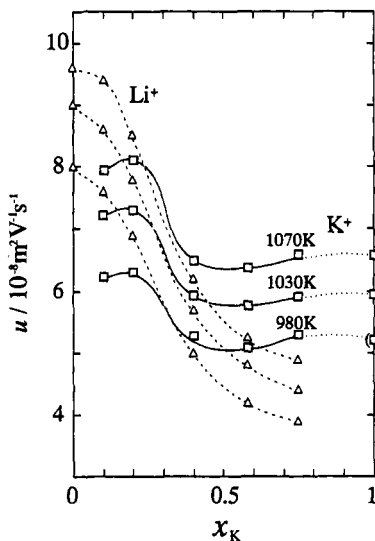


Figure 3. Isotherms of  $u_{\text{Li}}$  and  $u_{\text{K}}$  in  $(\text{Li}, \text{K})(\text{CO}_3)_{1/2}$ . The values of pure  $\text{K}(\text{CO}_3)_{1/2}$  are extrapolated with respect to temperature because the temperatures are less than the melting point (1164 K). (Reprinted from C. Yang, R. Takagi, K. Kawamura, and I. Okada, "Internal Cation Mobilities in the Molten Binary System  $\text{Li}_2\text{CO}_3\text{-K}_2\text{CO}_3$ ," *Electrochim. Acta* **32**: 1607–1611, Fig. 2, Copyright © 1987 with permission from Elsevier Science.)

salts. There is some evidence that the anion polarization model<sup>43,44</sup> is not suitable for interpretation of the Chemla effect. For example, in the fluoride system  $(\text{Li}, \text{K})\text{F}$  where anion polarization is smaller than in chlorides and bromides, crossing of mobilities occurs even more explicitly.<sup>32</sup> In a system with a common cation  $\text{Li}(\text{Cl}, \text{NO}_3)$  where the polarizability of the common cation is very small, an "anion Chemla effect" has been observed.<sup>45</sup> It is clear that this anion Chemla effect cannot be explained in terms of the cation polarization.

The self-exchange velocity (SEV),<sup>46</sup> which can be calculated from molecular dynamics simulation, has reproduced the Chemla effect. Fur-

ther, MD calculation based on linear response theory also describes this phenomenon in  $(\text{Li}, \text{Cs})\text{Cl}$ ,<sup>47</sup> where the polarization of the constituent ions has not been explicitly taken into account. This suggests that the anion polarization model could not interpret the effect. The MD prediction that the Li-Cl distance becomes smaller with increasing concentration of CsCl has been substantiated by a neutron diffraction study.<sup>48</sup>

The essence of the SEV may be understood as frequencies of cation-anion dissociation. Let us consider the separating motion of C from the reference anion A as shown in Fig. 4. When another cation of the same kind ( $A'$ ) reaches C, C can move away toward  $A'$  and leave A together with  $A'$ . For simplicity of explanation, these ions are collinearly arranged. The potentials felt by C from A and  $A'$  are depicted for different Cl-Cl distances in Fig. 5 for the cases of Cl-Li-Cl and Cl-K-Cl in  $(\text{Li}, \text{K})\text{Cl}$  mixtures,<sup>49</sup> and are obtained by superposition of the two pair potentials presented by Tosi and Fumi.<sup>50</sup> As the Cl-Cl distance,  $d$ , becomes longer, the potential barrier becomes higher. It should be noted that the potential barrier is very high compared with the magnitude of the kinetic energy, provided the Cl-Cl distance is long enough. As the mole fraction of KCl increases, the average  $d$  becomes longer; in other words, the A-C pair is more associated. Thus the SEV will decrease with increasing  $d$ , but the decreasing rate is smaller for Li than for K. Thus the SEVs of Li and K will have a crossing point, and the isotherms of the two internal mobilities have a Chemla crossing point.

The SEV has been calculated also in carbonate systems such as  $(\text{Li}, \text{K})(\text{CO}_3)_{1/2}$  and  $(\text{Li}, \text{Na})(\text{CO}_3)_{1/2}$ .<sup>51,52</sup> The Chemla effect in the SEV occurs in the former but not in the latter, which is consistent with the experimental results.

## 5. Empirical Equation for Internal Mobility

### (i) Alkali Ion Systems

Binary alkali nitrates have been systematically studied; the isotherms are shown in Fig. 6. The Chemla effect occurs in all systems except for  $(\text{Li}, \text{Na})\text{NO}_3$ . Figure 6 shows that with an increase in temperature the crossing point shifts toward higher concentrations of the smaller cation.

Okada et al.<sup>53</sup> found that the internal mobilities of  $\text{Li}^+$  in molten alkali nitrates are well expressed as a function of molar volume, independent of the kind of the second cation. This finding leads to a general empirical equation:



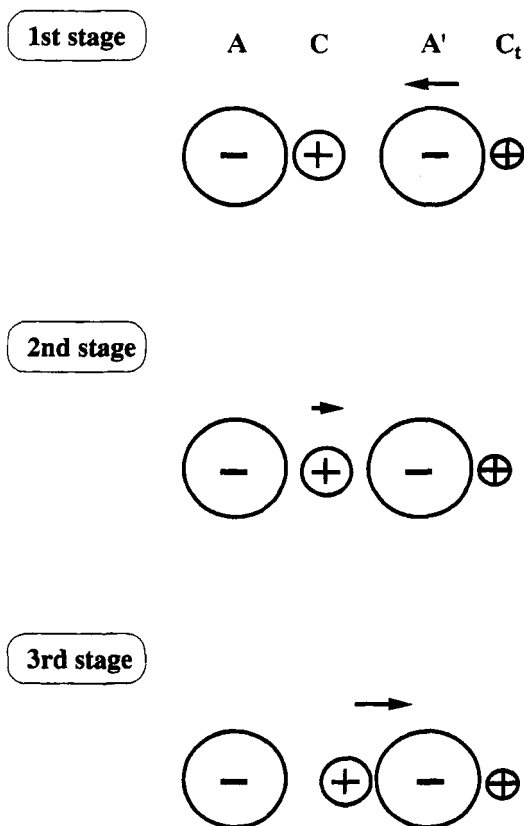


Figure 4. Schematic representation of separating motion of cation C from the reference ion A. A' is another anion of the same kind, and C, plays a role of tranquilizer if the interaction of A'-C<sub>t</sub> is much stronger than that of A'-C.

$$u = [A/(V_m - V_0)] \exp(-E/RT) \quad (12)$$

where  $V_m$  is the molar volume of the mixtures, and  $A$ ,  $V_0$ , and  $E$  are constants nearly independent of the second cation. In Fig. 7,  $u_{\text{Na}}$  is shown as a function of the molar volume; the data for mixtures with  $\text{AgNO}_3$  and  $\text{TlNO}_3$  are also included ( $u_{\text{Rb}}$  is shown in Fig. 12). Most of the cases where internal mobilities deviate from the empirical equation (12), which other-

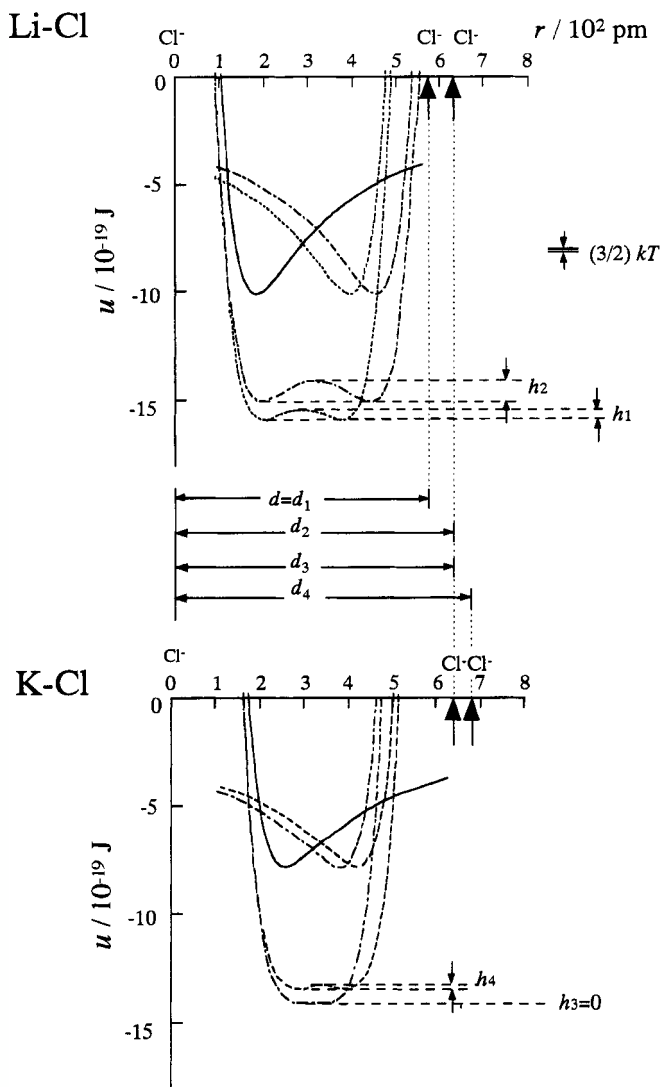


Figure 5. Potentials felt by a cation located between two  $\text{Cl}^-$  ions separated by distance  $d$  (top:  $\text{Li}^+$ , bottom:  $\text{K}^+$ ), ( $d_1 = 580 \text{ pm}$ ,  $d_2 = d_3 = 640 \text{ pm}$  and  $d_4 = 680 \text{ pm}$ ).<sup>49</sup> The relevant pair potentials taken from Ref. 50 are also shown. The magnitude of the kinetic energy  $(3/2) kT$  at 1000 K is shown for comparison. (Reprinted from Ref. 49 with permission from *Z. Naturforschung.*)

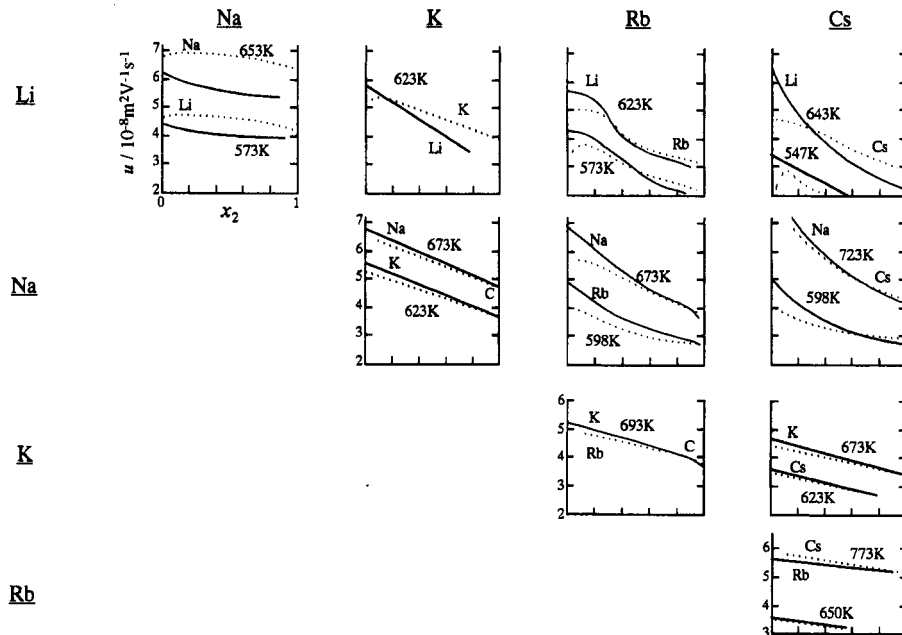


Figure 6. Isotherms of the internal mobilities in 10 binary alkali nitrates. C: Chemla crossing point marked only for the unclear cases. (Reprinted from M. Chemla and I. Okada, "Ionic Mobilities of Monovalent Cations in Molten Salt Mixtures," *Electrochim. Acta* **35**: 1761–1776, Fig. 5. Copyright © 1990 with permission from Elsevier Science.)

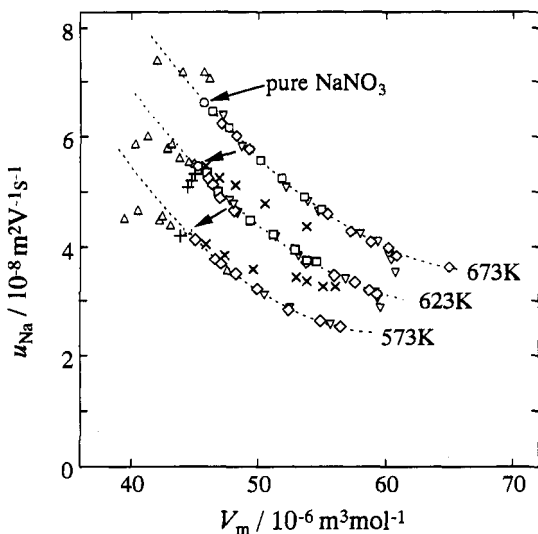


Figure 7. Isotherms of  $u_{Na}$  in various binary nitrates ( $M_1, M_2$ ) $\text{NO}_3$  as a function of molar volume.  $M_1 = \text{Na}^+$ ,  $\Delta$ ;  $M_2 = \text{Li}^+$ ,  $\circ$ ;  $\text{Na}^+$ ,  $\square$ ;  $\text{K}^+$ ,  $\nabla$ ;  $\text{Rb}^+$ ,  $\diamond$ ;  $\text{Cs}^+$ ,  $+$ ;  $\text{Ag}^+$ ,  $\times$ ;  $\text{Tl}^+$ . (Reprinted from M. Chemla and I. Okada, "Ionic Mobilities of Monovalent Cations in Molten Salt Mixtures," *Electrochim. Acta* **35**: 1761–1776, Fig. 7, Copyright © 1990 with permission from Elsevier Science.)

wise holds well, can be interpreted in terms of (1) the free space effect, (2) the tranquilization effect, and (3) the agitation effect. If the internal mobility of a cation of interest is appreciably greater than expected from Eq. (12), it is being influenced by the second cation because of the agitation effect. When the second cation is  $\text{Tl}^+$ , the agitation effect occurs, which will be discussed in Section III.5(iv) and (v). It should be noted that the internal mobilities decrease with increasing molar volume.

The internal mobilities of alkali halides have not yet been investigated systematically as with the alkali nitrates. However, it seems that an equation similar to Eq. (12) holds. To indicate this explicitly, the reciprocal values of the internal mobilities at 973 K in  $(\text{Li}, \text{CS})\text{Cl}^{54}$  are shown in Fig. 8. Figure 8 indicates that  $u^{-1}$  is a linear function of  $V_m$ , as Eq. (12) suggests; however, the parameters  $A$ ,  $V_0$ , and  $E$  are different at two different  $V_m$

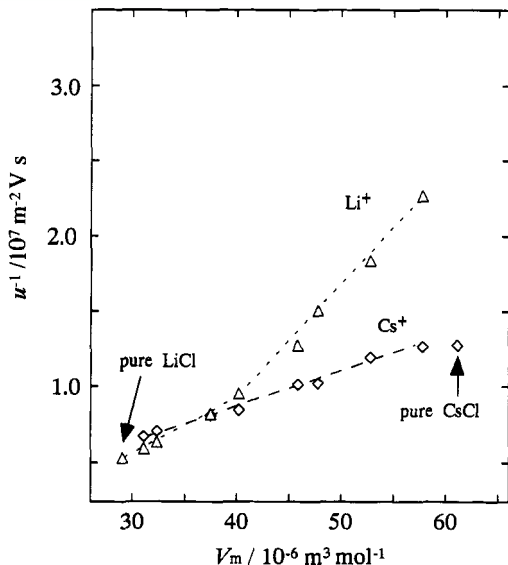


Figure 8. Isotherms of  $u_{\text{Li}^+}^{-1}$  and  $u_{\text{Cs}^+}^{-1}$  in (Li, Cs)Cl at 973 K. (Reprinted from I. Okada and H. Horinouchi, "The Chemla Effect in the Mobilities in the Molten Binary System of Lithium Chloride and Caesium Chloride," *J. Electroanal. Chem* **396**: 547, Fig. 4, Copyright © 1995 with permission of Elsevier Science.)

ranges, and furthermore, the borders of the two  $V_m$  ranges are different for  $\text{Li}^+$  and  $\text{Cs}^+$ . This is presumably due to structural changes around these cations.

### (ii) Free Space Effect

It can be easily imagined that if free space is very small, large ions in particular become less able to move. As seen from Fig. 6, mobilities such as  $u_{\text{Rb}}$  and  $u_{\text{Cs}}$  decrease at very high concentrations of  $\text{LiNO}_3$ . The free space seems to be caused at first by the restriction of the reorientational motion of polyatomic anions. To demonstrate this explicitly, the reciprocal values  $u^{-1}$  for several binary systems containing  $\text{Li}^+$  are plotted against the molar volume in Fig. 9; since data are not available yet for systems containing  $\text{LiOH}$ , the data for  $(\text{Na}, \text{K})\text{OH}^{35}$  are shown instead. A positive deviation from the straight lines, that is, a negative deviation of  $u$ , is observed

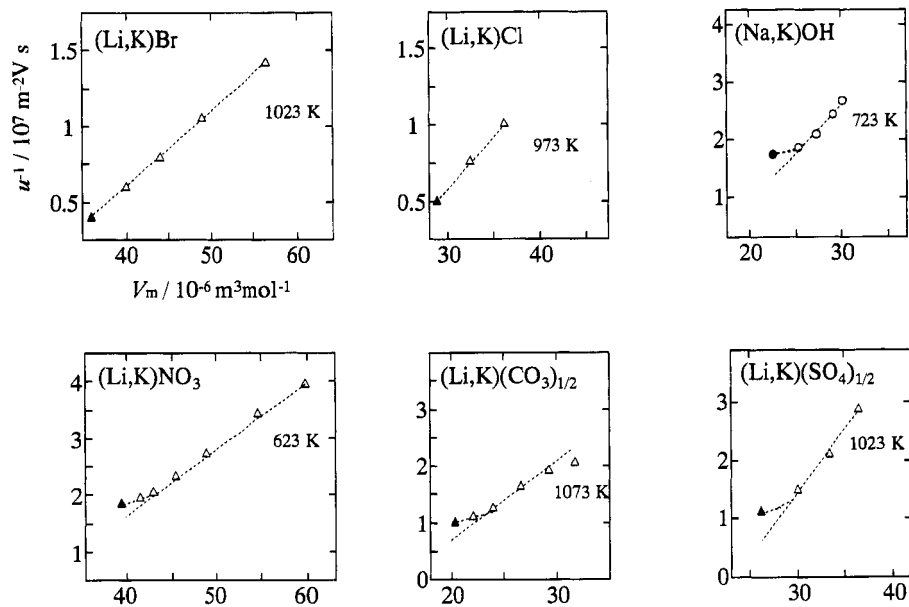


Figure 9. Reciprocal values of internal mobilities vs. molar volume in some binary systems: (Li, K)Br, (Li, K)Cl, (Na,K)OH, (Li, K)NO<sub>3</sub>, and (Li, K)(SO<sub>4</sub>)<sub>1/2</sub>, (Reprinted from M. Chemla and I. Okada, "Ionic Mobilities of Monovalent Cations in Molten Salt Mixtures," *Electrochim. Acta* **35**: 1761–1776, Fig. 10, Copyright © 1990 with permission from Elsevier Science.)

only for systems of polyatomic anions, which is due to the free space effect. Thus, it seems that for alkali halides, and in particular for alkali chlorides, the free space effect does not occur under ambient pressure.

### (iii) *Tranquilization Effect*

In such systems as  $(M_1, M_2)X$  ( $M_1$ , monovalent cation;  $M_2$ , divalent cation;  $X$ , common anion), the much stronger interaction of  $M_2$  with  $X$  leads to restricted internal mobility of  $M_1$ . This is called the *tranquilization effect* by  $M_2$  on the internal mobility of  $M_1$ . This effect is clear when  $M_2$  is a divalent or trivalent cation. However, it also occurs in binary alkali systems such as  $(Na, K)OH$ .<sup>55</sup> The isotherms belong to type II (Fig. 2);  $u_K$  decreases with increasing concentration of Na. Since the ionic radius of OH<sup>-</sup> is as small as  $F^-$ ,<sup>55</sup> the Coulombic attraction of Na-OH is considerably stronger than that of K-OH.

It is sometimes difficult to distinguish between the free space effect and the tranquilization effect; the former is usually more pronounced at lower temperatures. However, if the two effects are superimposed, for example, possibly for  $u_K$  at very low concentration in  $(Li, K)(CO_3)_{(1/2)}$ , it is nearly impossible to deconvolute them.

The tranquilization effect may be also explained in terms of the dynamic dissociation model (Fig. 4), where  $C_t$  interacts more strongly with  $A'$  than  $C$  does, when the separating motion of  $C$  from the reference ion  $A$  will be retarded. Thus,  $C_t$  plays the role of a tranquilizer ion.

### (iv) *Agitation Effect*

In such systems as  $(M_1, M_2)X$  mentioned above, the internal mobility of  $M_2$  becomes greater with higher  $M_1$  concentration, and the reverse when  $M_1$  is replaced by  $M_2$ . The reason may be a reverse of the tranquilization effect. Moreover, this effect does not occur in alkali nitrate or alkali chloride mixtures except for systems containing  $Tl^+$ , which clearly has an agitation effect on the internal mobilities of the second monovalent cations in binary nitrates, as is discussed in the next section.

### (v) *Anomalous Behavior of Ag(I) and Tl(I)*

The effect of highly polarizable cations on transport properties has scarcely been studied. Since the nitrate melts of  $Ag^+$  and  $Tl^+$  are stable and have high polarizabilities, as shown in Table 5, their internal mobilities in binary mixtures containing one or both of these cations have been measured frequently.<sup>57</sup> The isotherms are shown for  $u_{Ag}$  and  $u_{Tl}$  in Figs. 10 and 11,

**Table 5**  
**Some Fundamental Properties of Alkali Metal, Ag(I) and Tl(I) Ions and their Nitrate Melts**

Salt	LiNO <sub>3</sub>	NaNO <sub>3</sub>	KNO <sub>3</sub>	RbNO <sub>3</sub>	CsNO <sub>3</sub>	AgNO <sub>3</sub>	TlNO <sub>3</sub>
Cation							
Ionic radius <sup>a55</sup> (Pm)	59(IV)	102(VI)	138(VI)	152(VI)	167(VI)	115(VI)	150(VI)
Ionic mass (g mol <sup>-1</sup> )	6.941	22.98	39.09	85.46	132.9	107.8	204.3
Polarizability <sup>59</sup> (10 <sup>-30</sup> m <sup>3</sup> )	0.030	0.182	0.844	1.42	2.45	1.72	3.50
Polarizability/ionic radius <sup>3</sup>	0.146	0.172	0.321	0.404	0.526	1.13	1.04
Nitrate melt							
Melting point (°C)	261	308	333	316	414	212	206
Molar volume at 350 °C (10 <sup>-6</sup> m <sup>3</sup> mol <sup>-1</sup> )	39.64	44.95	54.24	59.34	67.48 <sup>b</sup>	44.49	57.28
Internal mobility at 350 °C (Ref. 3) (10 <sup>-8</sup> m <sup>2</sup> V <sup>-1</sup> s <sup>-1</sup> )	5.482 (350 °C)	5.427 (350 °C)	3.715 (350 °C)	2.995 (350 °C)	2.882 <sup>b</sup> (350 °C)	5.707 (350 °C)	4.201 (350 °C)
External transport number of cation <sup>23</sup>	0.84 (350 °C)	0.71 (350 °C)	0.57 (350 °C)	0.59 (350 °C)	0.37 (450 °C)	0.78 (250 °C)	0.31 (220 °C)

<sup>a</sup>The Roman numerals in the parentheses indicate coordination numbers for which the ionic radii are given here.

<sup>b</sup>This is the extrapolated value for a temperature less than the melting pint.



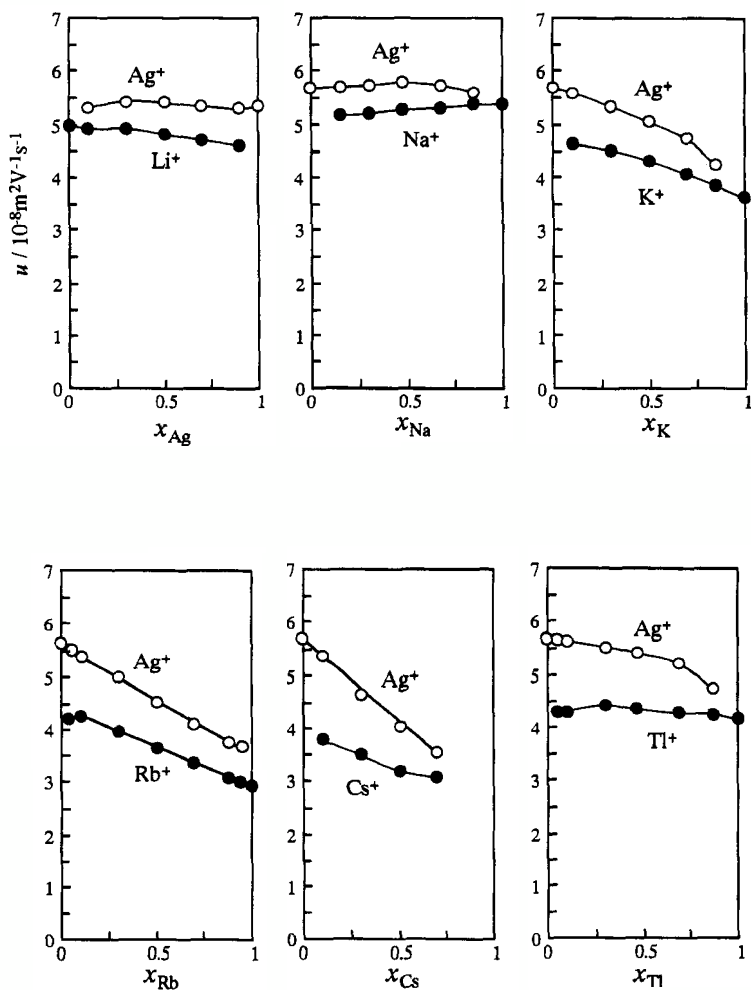


Figure 10. Isotherms of internal mobilities in various binary nitrates containing  $\text{Ag}^+$  as one cation. (Reprinted from I. Okada and P.-H. Chou, "Anomalous Behavior of Internal Mobilities for  $\text{Ag}(\text{I})$  and  $\text{Tl}(\text{I})$  Ions in Molten Nitrates," *J. Electrochem. Soc.* **144** (4): 1333, 1997, Fig.2. Reproduced by permission of the Electrochemical Society, Inc.)

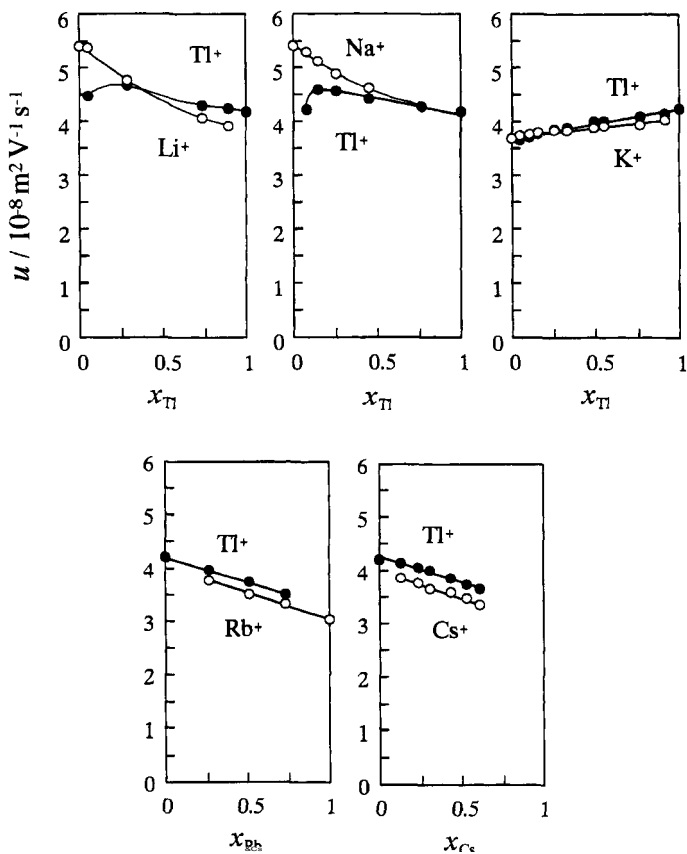


Figure 11. Isotherms of internal mobilities in various binary nitrates containing  $\text{Tl}^+$  as one cation. (Reprinted from I. Okada and P.-H. Chou, "Anomalous Behavior of Internal Mobilities for  $\text{Ag}(\text{I})$  and  $\text{Tl}(\text{I})$  Ions in Molten Nitrates," *J. Electrochem. Soc.* **144**(4): 1333, 1997, Fig.2. Reproduced by permission of the Electrochemical Society, Inc.)

respectively. The mobilities of  $\text{Ag}^+$  are greater than those of any other cations in the ranges of concentration and temperature investigated. This fact also supports the suggestion that the non-Coulombic interaction in  $\text{AgCl}$  and  $\text{AgBr}$  is mainly due to van der Waals interaction and is not due to covalency.<sup>57</sup> For  $\text{Tl}^+$ , the Chemla effect occurs in  $(\text{Li}, \text{Tl})\text{NO}_3$ ,  $(\text{Na}, \text{Tl})\text{NO}_3$ , and  $(\text{K}, \text{Tl})\text{NO}_3$ . The isotherms of  $(\text{K}, \text{Tl})\text{NO}_3$  are anomalous in that both  $u_{\text{K}}$  and  $u_{\text{Tl}}$  increase with increasing molar volume, as shown in Fig. 12.

When internal mobilities of  $\text{Ag}^+$  are plotted against the molar volume of the mixtures, Eq. (12) seems to be applicable to  $\text{Ag}^+$ . The internal mobilities of  $\text{Tl}^+$  are plotted against molar volume in Fig. 12 as a comparison-

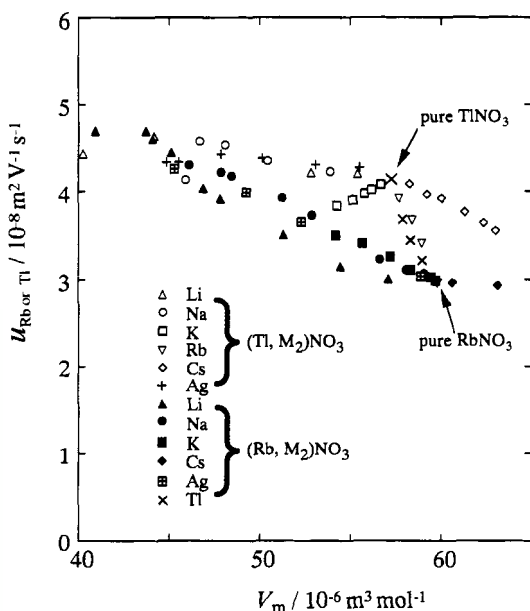


Figure 12. Isotherms of  $u_{\text{Tl}}$  compared with  $u_{\text{Rb}}$  in various binary nitrates as a function of molar volume. (Reprinted from I. Okada and P.-H. Chou, "Anomalous Behavior of Internal Mobilities for  $\text{Ag}(\text{I})$  and  $\text{Tl}(\text{I})$  Ions in Molten Nitrates," *J. Electrochem. Soc.* **144**(4): 1333, 1997, Fig. 13. Reproduced by permission of the Electrochemical Society, Inc.)

son with  $u_{\text{Rb}}$  since the ionic radii of  $\text{Tl}^+$  and  $\text{Rb}^+$  are similar, but the internal mobilities of  $\text{Tl}^+$  are greater than those of  $\text{Rb}^+$ . The values  $u_{\text{Tl}}$  do not follow an equation similar to Eq. (12), but mostly depart from such a curve at pure  $\text{TlNO}_3$ . The effect of these cations on the internal mobilities of the second cation is that  $\text{Ag}^+$  has a slight tranquilization effect, except for  $u_{\text{Li}}$ , whereas  $\text{Tl}^+$  has an agitation effect, i.e., these highly polarizable cations have opposite effects on the internal mobilities of the second cations and are listed in Table 6. The tranquilization effect of  $\text{Ag}^+$  can be easily understood from Fig. 4 if  $C_i$  is  $\text{Ag}^+$ . This explanation also shows that  $\text{Ag}^+$  does not have an appreciable tranquilization effect for  $u_{\text{Li}}$ . In the case of  $\text{Tl}^+$ , the Coulombic interaction with  $A'$  may not be so strong because of the large size of  $\text{Tl}^+$ . Instead, the  $\text{Tl}^+\text{-Tl}^+$  nearest distance may become shorter than that of  $\text{K}^+\text{-K}^+$  in their pure nitrates, which is supported by X-ray diffraction data for these melts.<sup>58</sup> Thus, in the melts containing  $\text{Tl}^+$ , the  $\text{Tl}^+\text{-Tl}^+$  nearest distance is rather short, as schematically depicted in Fig. 13, and therefore the anion (which is  $\text{NO}_3^-$  in this case) can readily move from one  $\text{Tl}^+$  toward another  $\text{Tl}^+$ . This assumption is also supported by the experimental finding that the external transport number of  $\text{Tl}^+$  is small in  $\text{TlNO}_3$  (Table 5).

#### (vi) Multivalent Charge Symmetric Binary Mixture

Multivalent cation mixtures have not been studied as extensively as monovalent cation mixtures. The following systems have been studied so far:  $(\text{Ca}, \text{Ba})_{1/2}\text{Cl}$ ,<sup>60</sup>  $(\text{Y}, \text{La})_{1/3}\text{Cl}$ ,<sup>61</sup> and  $(\text{Y}, \text{Dy})_{1/3}\text{Cl}$ .<sup>61</sup> The isotherms of  $(\text{Y}, \text{La})_{1/3}\text{Cl}$  are shown in Fig. 14. In these three systems the mobility decreases with increasing molar volume. This trend is similar to that in monovalent cation systems. An equation such as Eq. (12) seems to hold. The larger cation is more mobile than the smaller one in the former two

**Table 6**  
The Effect of Highly Polarizable Cations on the Internal Mobility of the Second Cation in  $(\text{M}_1, \text{M}_2)\text{NO}_3$

$\text{M}_1$	$\text{M}_2$	Li	Na	K	Rb	Cs	Ag	Tl
Ag		No effect	Tranq	Tranq	Tranq	Tranq	—	Tranq
Tl		Agit	Agit	Agit	Agit	Agit	Agit	Self-agit

Notes: tranq. tranquilization effect; agit, agitation effect; self-agit, self-agitation effect.

Separating motion of  $\text{NO}_3^-$  from  $\text{K}^+$



Separating motion of  $\text{NO}_3^-$  from  $\text{Tl}^+$



Figure 13. Schematic picture of separating motion of  $\text{NO}_3^-$  from reference cation ( $\text{Tl}^+$  or  $\text{K}^+$ ).

cases. The ionic radii of  $\text{Y}^{3+}$  and  $\text{Dy}^{3+}$  are much the same, while the mass of the former ion is much less than that of the latter, as given in Table 7. Thus the mass plays a role in this case and the mobility of Y is slightly larger than that of Dy. Although the examples are very limited, it may be concluded that the mobility of a larger cation is generally greater than that of a smaller one because the dissociation occurs more easily.

#### (vii) Charge Asymmetric Binary Mixture

In the alkali and alkaline earth nitrate mixtures, the internal mobilities have been systematically investigated,<sup>70</sup> the isotherms being shown in Fig. 15. The internal mobilities of the alkali ions as a function of the molar volume are much smaller than expressed by an equation such as Eq. (12). This means that the internal mobilities of the alkali ions,  $u_{\text{alk}}$ , are modified by the tranquilization effect caused by the divalent cations. The  $u_{\text{alk}}$  is assumed to be expressed by

$$u_{\text{alk}} = u^*(1 - \Delta_{\text{TE}}) \quad (13)$$

where  $u^*$  is the value expressed by Eq. (12) and  $\Delta_{\text{TE}}$  is a factor representing the magnitude of the tranquilization effect. Consider the potential felt by

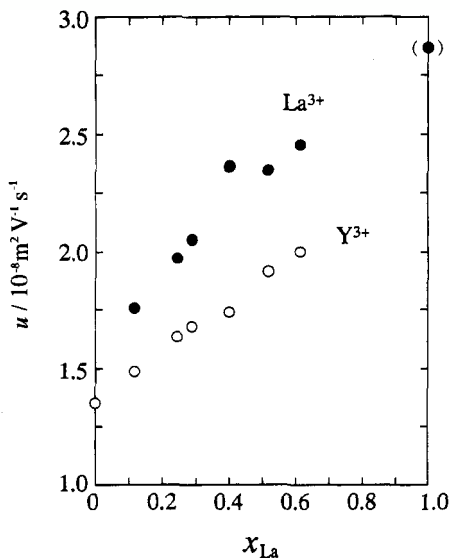


Figure 14. Isotherms of  $u_Y$  and  $u_{La}$  in  $(Y, La)_{1/3}Cl$ . (Reprinted from H. Matsuura, I. Okada, Y. Iwada, and J. Mochinaga, "Internal Cation Mobilities in the Molten Binary Systems  $(Y, La)Cl_3$  and  $(Y, Dy)Cl_3$ , *J. Electrochem. Soc.* **143**(1): 336, 1996, Fig. 4. Reproduced by permission of the Electrochemical Society, Inc.)

$A'$  from  $C$  and  $C_t$  in Fig. 4. The values of  $\Delta_{TE}$  are found to be related to the difference in the Coulombic potentials of the cation of interest and the tranquilizer cation.<sup>70</sup>

As for chloride systems,  $(K, Ca_{1/2})Cl^{39}$  and  $(K, Dy_{1/3})Cl^{71}$  have been studied. The isotherms for the latter are shown in Fig. 16, where  $u_K$  decreases with increasing concentration of Dy, which is due to the tranquilization effect of  $Dy^{3+}$ . However,  $u_{Dy}$  does not change as much while  $x_{Dy}$  is high, but at high  $x_K$ ,  $u_{Dy}$  decreases, which may be due to an increase in the species  $[DyCl_6]^{3-}$ . However, it has not been ascertained that this species actually becomes the electrolytic conducting species since this depends on the lifetime of this species.

**Table 7**  
**Some Properties of pure  $Y_{(1/3)}Cl$ ,  $La_{(1/3)}Cl$ , and  $Dy_{(1/3)}Cl$**

	$Y_{(1/3)}Cl$	$La_{(1/3)}Cl$	$Dy_{(1/3)}Cl$
Atomic number of cation	39	57	66
Atomic weight of cation	88.9095	138.9055	162.50
Cationic radius (pm)	90.0 <sup>a</sup>	103.2 <sup>a</sup>	91.2 <sup>a</sup>
Crystal structure type	$AlCl_3^b$	$UCl_3^b$	$AlCl_3^b$
Coordination number of cation in the crystal	6	9	6
Coordination number of cation in the melt	$\sim 6^c$	$\sim 6^d$	$\sim 6^e$
Melting point (K)	987 <sup>f</sup>	1150 <sup>f</sup>	928 <sup>f</sup>
Change in molar volume on melting (%)	0.45 <sup>f</sup>	19.4 <sup>f</sup>	0.32 <sup>f</sup>
Molar volume at 1073 K ( $10^{-6}m^3mol^{-1}$ )	25.46	25.00 <sup>f</sup>	25.36 <sup>f</sup>
Conductivity at 1073 K ( $S m^{-1}$ )	51.2	110.7 <sup>g</sup>	56.2

<sup>a</sup>Ref. 55.

<sup>b</sup>Ref. 62.

<sup>c</sup>Refs. 63, 64.

<sup>d</sup>Ref. 65.

<sup>e</sup>Refs. 66,67.

<sup>f</sup>Ref. 68.

<sup>g</sup>Ref. 69.

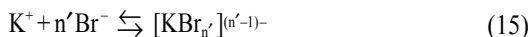
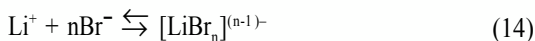
## 6. Electrically Conducting Species

It is not as easy as it appears to know which are the electrically conducting species in molten salts. It seems to be nearly impossible to determine the electrically conducting species by experiment alone.<sup>72</sup>

It is still controversial whether these species are associated or non-associated. Three models in this respect are introduced here.

### (i) *Associated Species Model*

Chemla's group proposed an associated model more than 30 years ago for the purpose of interpreting the Chemla effect soon after its discovery.<sup>73,74</sup> For example, the following chemical equilibria were considered:



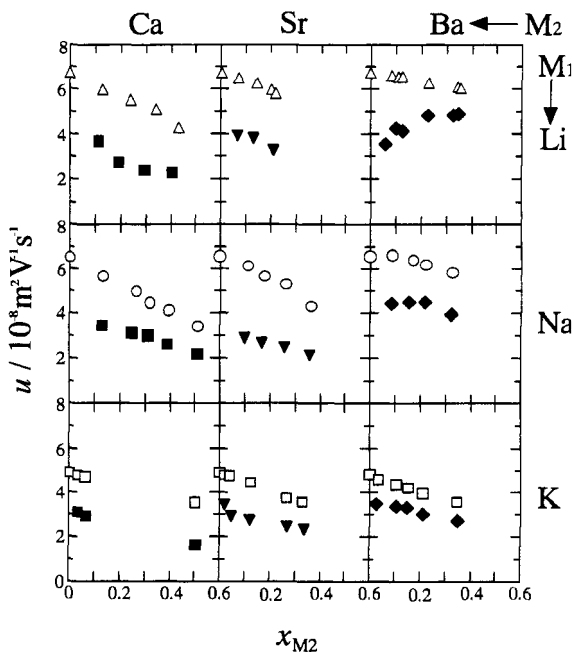


Figure 15. Isotherms of internal mobilities in alkali-alkaline earth nitrate mixtures. The mobility of the alkali ion is always greater than that of the alkaline earth ion. (Reprinted from T. Koura, H. Matsuura, and I. Okada, "A Dynamic Dissociation Model for Internal Mobilities in Molten Alkali and Alkaline Earth Nitrate Mixtures," *J. Mol. Liq.* **73-75**: 195, Fig. 4, Copyright © 1997 with permission from Elsevier Science.)

Based on quite similar equilibria for the nitrate system  $(\text{Li}, \text{K})\text{NO}_3$ , Lantelme and Chemla quantitatively estimated the existing species so that the experimental mobilities and self-diffusion coefficients could be obtained consistently. This could be successfully done. However, no direct evidence has been obtained yet that such species as  $[\text{LiBr}_n]^{(n-1)-}$  and  $[\text{KBr}_n]^{(n-1)-}$  are really electrically conducting species.

### (ii) Association (or Dissociation) Model

According to the model proposed by Klemm and Schäfer,<sup>75,76</sup> the Chemla effect is explained qualitatively. Although molten  $\text{LiBr}$  has a



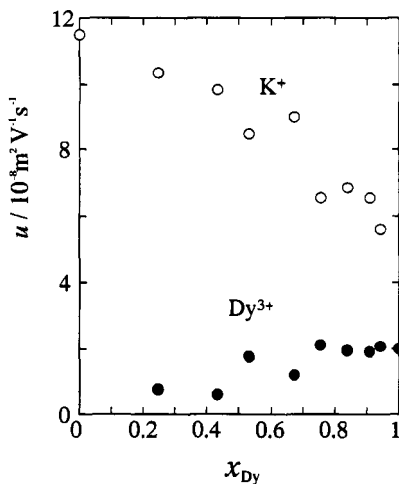
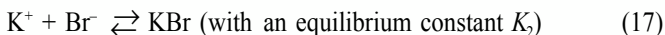
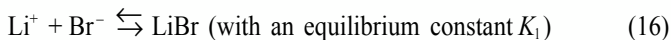


Figure 16. Isotherms of  $u_K$  and  $u_{Dy}$  in  $(K, Dy)_{1/3}Cl$ . (Reprinted from Ref. 71 with permission from *Z. Naturforschung*.)

larger conductivity than molten KBr, more ions are associated with a neutral molecule in the former than in the latter because  $Li^+$  is smaller than  $K^+$ . In the mixtures,  $Li^+$  and  $K^+$  compete in the formation of molecules  $LiBr$  and  $KBr$ , respectively, the smaller  $Li^+$  being more successful. Therefore, as  $x_K$  increases in the mixtures,  $u_{Li}$  decreases more sharply than  $u_K$ , and thus the mobility isotherms may cross. Here, the following chemical equilibria are assumed:



They assumed that the mobilities of the dissociated species  $Li^+$  and  $K^+$ ,  $u_1^d$  and  $u_2^d$  respectively, are independent of composition. They have applied this model to  $(Li, Cs)Cl$  using three experimental values,<sup>54</sup> which are  $u_1(0)$ ,  $u_2(1)$ , and  $u_1(x_2) = u_2(x_2)$  at the Chemla crossing point. Since the calculated isotherms deviate considerably from the experimental ones, they suppose that the dependence of  $K_1$  and  $K_2$  on the mixing ratio must be assumed.

Danek and his group have independently proposed a quite similar model, which they call the *dissociation model*.<sup>77,78</sup> For this model Olteanu and Pavel have presented a versatile numerical method and its computing program.<sup>79</sup> However, they calculated only the electrical conductivity or the molar conductivity of the mixtures, and the deviation of the internal mobilities of the constituting cations from the experimental data is consequently vague.

This model is similar to the associated species model in that a chemical equilibrium is assumed between existing species, and it is different in that in the latter only a nonassociated ionic species is assumed to be the electrically conducting species.

### (iii) *Dynamic Dissociation Model*

Okada et al.<sup>46,70</sup> have presented a dynamic dissociation model, which is schematically shown in one dimension in Fig. 4. They assumed that the separating motion of a cation (or anion) of interest from the reference anion (cation), which is called the *self-exchange velocity*,<sup>46</sup> is the electrically conducting process, which will be considered in Section III.7(iii) in more detail. The Chemla effect can also be reproduced by the SEV.

In a possible hypothesis, Smirnov et al.<sup>80</sup> have proposed that a transient process such as  $[\text{MX}_4]^{3-} + [\text{MX}_3]^{2-} \rightarrow [\text{MX}_3]^{2-} + [\text{MX}_4]^{3-}$  is the electrically conducting process. Their concept may be similar to the dynamic dissociation model.

The dynamic dissociation model resembles the association (or dissociation) model in that electrically conducting species are assumed to be nonassociated species, and it differs from the association model in that in the dynamic dissociation model the dissociation process itself is the electrically conducting process, while in the association model, the amount of the dissociated species is constant according to the chemical equilibrium.

## 7. Molecular Dynamics Simulation

Molecular dynamics and Monte Carlo simulations have been extensively applied to molten salts since 1968 to study structure, thermodynamic properties, and dynamic properties from a microscopic viewpoint. Several review papers have been published on computer simulation of molten salts.<sup>81-86</sup> Since the Monte Carlo method cannot yield dynamic properties, MD methods have been used to calculate dynamic properties.

**(i) Current Autocorrelation Method**

When the linear response theory<sup>87</sup> is applied to electric conductivity in an ionic melt, the total charge current  $J(t)$  can be defined as

$$A(t) = J(t) = \sum_i q_i r_i \quad (18)$$

If a time-dependent electric field,

$$E(t) = E_0 \exp(-i\omega t) \quad (19)$$

is applied to a system of ions, the real part of the linear response of the current can be written as

$$\langle \Delta J(t) \rangle = \text{Re} (1/3kT) \int_{-\infty}^t \langle J(t-s)J(0) \rangle E(s) ds = \text{Re} \sigma(\omega) E_0 \exp(-i\omega t) \quad (20)$$

where

$$\sigma(\omega) = (1/3kT) \int_0^{\infty} \langle J(t)J(0) \rangle \exp(i\omega t) dt \quad (21)$$

The electric conductivity  $\kappa$  at  $\omega \rightarrow 0$  can be identified as

$$\kappa = \lim_{\omega \rightarrow 0} \sigma(\omega) / V' = (1/3kTV') \int_0^{\infty} \langle J(t)J(0) \rangle dt \quad (22)$$

where  $V'$  is the volume of a basic cell of MD simulation.

Extending this to a system consisting of two kinds of cations (1 and 2) and one kind of anion, Klemm<sup>88</sup> has derived equations for calculating internal cation mobilities. The internal mobility  $u_{\alpha\beta}$  of an  $\alpha$  ion with reference to a  $\beta$  ion is directly related to the velocity change in the relevant two ions caused by the perturbation field:

$$u_{\alpha\beta} = \lim_{\omega \rightarrow 0} \langle \Delta \{v_{\alpha}(t) - v_{\beta}(t)\} \rangle / E_0 \exp(-i\omega t) = (e/3kT) \int_0^{\infty} L_{\alpha\beta}(t) dt \quad (23)$$

where  $E_0$  is the constant electric field,  $V_{\alpha}(t)$  is the collective velocity, and  $L_{\alpha\beta}(t)$  is the correlation function.

$$V_{\alpha}(t) = \sum_i^{\alpha} r_i(t)/N_{\alpha}$$

$$L_{\alpha\beta}(t) = -C_{\alpha-} + C_{\beta-} + x_1 C_{\alpha 1} + x_2 C_{\alpha} - x_1 C_{\beta 1} - x_2 C_{\beta 2}$$
(24)

(25)

Here,  $x$  is the mole fraction and

$$C_{\alpha\beta} = |z_{-}|N_{-} \langle v_{\alpha}(t)v_{\beta}(0) \rangle$$
(26)

Thus,  $u_{1-}$ ,  $u_{2-}$ , and  $\kappa$  can be evaluated from the velocity group correlation functions  $C_{\alpha\beta}$ :

$$u_{1-} = (1/3kT) \int_0^{\infty} L_{1-}(t) ds$$
(27)

$$u_{2-} = (1/3kT) \int_0^{\infty} L_{2-}(t) ds$$
(28)

$$K = (F/V)(x_1 u_{1-} + x_2 u_{2-})$$
(29)

Internal mobilities were calculated for molten LiCl and (Li, Cs)Cl ( $x_{Cs} = 0.90$ ).<sup>47</sup> The values are given in Table 8, which shows that the calculated  $u_{Li}$  is much smaller than  $u_{Cs}$ ; that is, the Chemla effect can be reproduced by MD simulation.

**Table 8**  
**Calculated Internal Mobilities of Pure LiCl and (Li, Cs)Cl ( $x_{Cs} = 0.90$ )**  
**Compared with Experimental<sup>47</sup>**

Salt	Cation	Li-Li	Li-Cs	Li-Cl	Cs-Cs	Cs-Cl	Cl-Cl	$u_{calc.}$	$u_{exp.}$
		(10 <sup>-7</sup> m <sup>2</sup> V <sup>-1</sup> s <sup>-1</sup> )							
LiCl	Li <sup>+</sup>	1.28	—	0.50	—	—	0.050	1.82	1.82
(Li, Cs)Cl	Li <sup>+</sup>	0.37	-0.13	-0.44	—	0.12	0.44	0.36	0.44
(x <sub>Cs</sub> = 0.90)	Cs <sup>+</sup>	—	-0.014	-0.040	0.036	0.25	0.44	0.67	0.79

Note: The contribution from each pair is also given.

For MD where the Tosi–Fumi potentials<sup>50</sup> were used, the pressure was 240 MPa and 110 MPa for pure LiCl and the mixture, respectively. The calculated temperatures were 957 K and 955 K for pure LiCl and the mixture, respectively. The experimental temperature was 973 K.

### (ii) Response Function Method

The ensemble average of the response  $\langle \Delta J \rangle$  can be calculated directly from MD simulation in the presence and absence of an external field:

$$\langle \Delta J(t) \rangle = \langle J(t) \rangle_H - J(t)_{H_0} \quad (30)$$

where  $H$  and  $H_0$  represent the perturbed and unperturbed systems, respectively. To avoid the large disturbance caused by thermal fluctuation, Ciccotti et al.<sup>89</sup> proposed an MD procedure in which the noise in calculating  $\Delta J(t)$  can be drastically reduced. If two MD calculations for the perturbed and unperturbed systems start from the same initial conditions, the current due to the thermal fluctuation must be nearly the same within a certain period. The external field applied only in the  $x$  direction is a step function  $\phi(t)$  at  $t = 0$ ,

$$E(t) = E_0 \phi(t) \quad (31)$$

where  $x$  is a unit vector and  $\phi(t)$  is the step function:

$$\begin{aligned} \phi(t) &= 0 & t < 0 \\ &= 1 & t \geq 0 \end{aligned} \quad (32)$$

The electric current induced in the same direction ( $x$ -direction) is calculated directly:

$$\Delta J_x(t) = J_x^h(t) - J_x^{h_0}(t) \quad (33)$$

The steady-state conductivity is given by

$$\kappa = \langle \Delta J_x(\infty) \rangle / E_0 V \cong \langle \Delta J_x \text{ (at a plateau)} \rangle / E_0 V \quad (34)$$

The electrolytic conductivities calculated by this method are given in Table 9 together with the self-diffusion coefficients. The calculated conductivities agree surprisingly well with the experimental ones when a small perturbation on an order of 1 V cm<sup>-1</sup> is applied.

**Table 9**  
**Results of MD Calculations**

Salt	$V_m$ ( $10^{-6} \text{ m}^3 \text{ mol}^{-1}$ )	$T$ (K)	$D_+$ ( $10^{-9} \text{ m}^2 \text{ s}^{-1}$ )	$D_-$	$\kappa$ ( $10^2 \text{ s m}^{-1}$ )	$\Delta_d$
LiF	15.00	1287	13.6	11.3	12.1 (9.3)	0.16
NaCl	39.10	1262	10.6 (14.0)	9.9 (10.1)	4.2 (4.2)	0.09 (0.18)
NaI	57.46	1081	9.4 (10.5)	6.8 (5.9)	2.5 (2.7)	0.14 (0.08)
KI	68.97	989	4.5	3.7	1.42 (1.38)	-0.06
RbCl	56.48	1119	5.0(6.6)	5.2(5.8)	1.81 (1.81)	-0.01 (0.15)
RbI	75.75	1086	4.3	3.5	1.09 (1.09)	-0.03

Note: The values in the parentheses are experimental results.  $\Delta_d$  is the deviation from the Nernst-Einstein equation expressed by  $\kappa = (F^2/V_m RT)(z_+ D_+ - z_- D_-) / (1 - \Delta_d)$ .

### (iii) Self-Exchange Velocity

Okada et al.<sup>46</sup> have found that internal mobilities are strongly related to the separating motion of unlike ion pairs defined by the self-exchange velocity, which can be easily calculated from MD simulation:

$$V_s = (R_2 - \langle R_2 \rangle) / \tau \quad (35)$$

where  $R_2$  is the distance at which the partial distribution function  $g_{ij}(r)$  for the pair of interest reaches unity after the first peak, and  $\langle R_2 \rangle$  is the average distance of unlike ion pairs within  $R_2$ ;  $\tau$  is the time in which the ion moves from  $\langle R_2 \rangle$  to  $R_2$ .

For (Li, Cs)Cl, the internal mobilities have been calculated from Eqs. (27) and (28), and are given in Table 8. The SEVs were calculated from the same MD runs and are plotted against the calculated internal mobilities in Fig. 17 with excellent correlation between these calculated quantities. The good correlation of the SEV with the calculated and experimental internal mobilities suggests that relatively short-range cation-anion interaction plays a role in internal mobilities and the separating motion of pairs, that is dissociation, is related to the internal mobilities. In other words, the result of the SEV supports the dynamic dissociation model.

Thus the SEV can reproduce apparently anomalous phenomena in electrical conductance such as the Chemla effect,<sup>46,49</sup> a maximum of electrolytic conductivity of some salts containing  $\text{Li}^+$  as a function of pressure,<sup>90</sup> an expected maximum in electrolytic conductivity as a func-

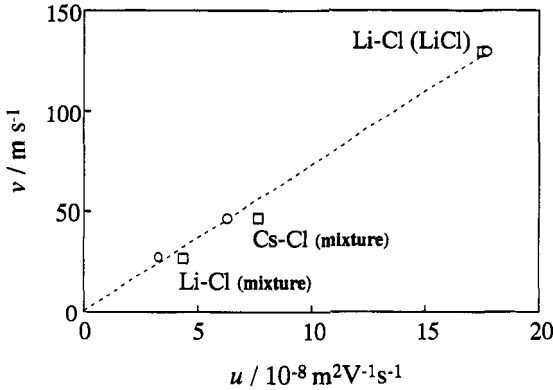


Figure 17. Self-exchange velocities vs. internal mobilities calculated from the same MD runs for pure LiCl and (Li, Cs)Cl mixture ( $x_{\text{Cs}} = 0.90$ ).<sup>47</sup>  $\square$ : experimental for  $u$ . (Reprinted from Ref. 47 with permission of Trans Tech Publications.)

tion of temperature<sup>91</sup> and an increase in the isotope effect of mobilities with temperature.<sup>92</sup>

## IV. DIFFUSION

### 1. Macroscopic Description

For diffusion in liquid electrolytes such as molten salts, two forces acting on an ion of interest should be taken into account: the gradient of the chemical potential and the charge neutrality. Thus the electrochemical potential rather than the chemical potential should be the driving force for diffusion.

According to irreversible thermodynamics, the entropy production per unit volume  $\dot{S}$  for an isothermal system can be written

$$T \dot{S} = \sum_i J_i X_i \quad (36)$$

For an isothermal system without velocity gradients and chemical reactions, Eq. (36) reduces to

$$T \dot{S} = - \sum_{k=1}^n (J_k)_{MF} \cdot [\text{grad}(\mu_k + z_k F \phi)] \quad (37)$$

where  $\phi$  is the electrical potential and  $(J_k)_{MF}$  is the mass fixed flow of a component defined as

$$(J_k)_{MF} = c_k(v_k - v) \quad (38)$$

Here  $v$  is the barycentric velocity. For a system in mechanical equilibrium,  $v$  can be replaced by any arbitrary velocity and therefore it is replaced here by the velocity of the volume fixed reference:  $w (=0)$ . Then Eq. (37) becomes

$$T \dot{S} = - \sum_{k=1}^n c_k v_k \cdot [\text{grad}(\mu_k + z_k F \phi)] \quad (39)$$

In molten salts, owing to the charge neutrality,

$$\sum_k c_k Z_k = 0 \quad (40)$$

For a system of constant pressure and temperature, the Gibbs–Duhem relation holds:

$$\sum_{k=1}^n c_k \{\text{grad}(\mu_k + z_k F \phi)\} = 0 \quad (41)$$

From this relation, the force on particle  $n$  can be eliminated:

$$T \dot{S} = - \sum_{k=1}^{n-1} c_k (v_k - v_n) \cdot [\text{grad}(\mu_k + z_k F \phi)] \quad (42)$$

If we choose component  $n$  as the velocity reference, the relative fluxes of remaining  $(n-1)$  components are independent. For this case,

$$J_i = c_i (v_i - v_n) = - \sum_{k=1}^{n-1} L_{ik} [\text{grad}(\mu_k + Z_k F \phi)] \quad (43)$$

For the case of independent forces and fluxes, the Onsager reciprocal relation holds:



$$L_{ki} = L_{ik} \quad (44)$$

The phenomenological constants can be expressed in terms of experimental quantities.<sup>93</sup> The  $L_{ij}$  represents the interaction of component  $i$  with other particles of component  $j$ . In molten salts no component seems particularly suitable for serving as a solvent. The use of a volume fixed frame of reference for defining the fluxes gives a more symmetrical representation. The equations for the phenomenological constants are given by Sundheim.<sup>94</sup>

When there are  $n$  ionic species, there are  $(n-1)$  neutral components. For example, for  $\text{Li}^+$ ,  $\text{Na}^+$ ,  $\text{Cl}^-$ , and  $\text{Br}^-$ , the components might be any three of  $\text{LiCl}$ ,  $\text{LiBr}$ ,  $\text{KCl}$ , and  $\text{KBr}$ . If  $\text{LiCl}$ ,  $\text{LiBr}$ , and  $\text{KCl}$  were the components used,  $c$  mol  $\text{cm}^{-3}$  of  $\text{KBr}$  may be represented as  $c$  mol  $\text{cm}^{-3}$  of  $\text{KCl}$ ,  $c$  mol  $\text{cm}^{-3}$  of  $\text{LiBr}$  -  $c$  mol  $\text{cm}^{-3}$  of  $\text{LiCl}$ . In general, we may write the flows  $J_k$  in terms of the flows  $J_{km}$  of the neutral component formed from species  $k$  and  $m$  as

$$J_k = \sum_m z_m J_{km} \quad (45)$$

where the summation is taken for the  $(n-1)$  components of formulas  $\text{K}_z^+ \text{L}_{z+}^-$  and  $z_m$  is the valence number.

The conventional description of diffusion in a two-component liquid system is given with Fick's first law:

$$J_A = -D_A \text{grad } c_A \quad (46)$$

$$J_B = -D_B \text{grad } c_B \quad (47)$$

By selecting the reference properly, the diffusion coefficients  $D_A$  and  $D_B$  can be made equal to each other. This value is termed the mutual diffusion (or interdiffusion) coefficient  $D_{AB}$ . The reference frame is one across which no change in volume occurs (fixed volume):

$$J_A^{(v)} \bar{v}_A + J_B^{(v)} \bar{v}_B = 0 \quad (48)$$

Since  $\bar{v}_A c_A + \bar{v}_B c_B = 1$ ,

$$D_A(v) = D_B(v) = D_{AB}(v) \quad (49)$$

and

$$J_A^{(v)} = -D_{AB}^{(v)} \text{grad } c_A \quad (50)$$

$$J_B^{(v)} = -D_{AB}^{(v)} \text{grad } c_B \quad (51)$$

The fixed mass (M) and fixed number (N) reference frames can also be defined. The mutual diffusion is equally well described in any of these three coordinate systems:

$$D_{AB}^{(v)} = D_{AB}^{(M)} = D_{AB}^{(N)} \quad (52)$$

If species 1 is a tracer for species 2,  $D_{12}$  is termed the "tracer diffusion" (or self-diffusion) coefficient of species 2,  $D_2^*$ . Thus, for three ionic species the tracer diffusion coefficients can be obtained from consideration of a three-component (four-species) system in which one species is a tracer for another.

## 2. Measurement Methods

In the data compiled by Janz and Bansal,<sup>13</sup> various methods for measuring diffusion coefficients in molten salts are mentioned. The methods may be broadly classified as electrochemical and analytical. However, some other methods have occasionally been employed. Various electrochemical methods were reviewed by Lesko.<sup>95</sup> Tracer diffusion in molten salts was reviewed by Spedding in 1971,<sup>96</sup> where some other methods were also mentioned.

Of the electrical methods, only two representative methods will be considered here. Other electrical methods have been discussed previously, e.g., in Refs. 11 and 96. Capillary methods have been used often and discussed for their sources of errors<sup>97</sup> and are therefore not particularly considered here.

The precision stated in Table 10<sup>97</sup> is given by the standard deviations obtained from a statistical analysis of the experimental data of one run and of a number of runs. These parameters give an indication of the internal consistency of the data of one run of measurements and of the reproducibility between runs. The systematic error is far more difficult to discern and to evaluate, which causes an uncertainty in the resulting values. Such an estimate of systematic errors or uncertainties can be obtained if the measuring method can also be applied under circumstances where a more exact or a "true" value of the property to be determined is known from other sources.

**Table 10**  
**Methods Used to Measure Diffusion Coefficients in Molten Salts<sup>97</sup>**

Method	Precision (%)	Uncertainty (%)	Inter-diffusion	Self-diffusion	Deviation from theory	Remarks
Electrochemical methods						
Chronopotentiometry	3	10	Yes	No		Only ions different from those of solvent
Chronoamperometry						
Linear sweep						
Polarography						
Rotating disk electrode						
Faradaic impedance						
Analytical transport-coupled methods						
Interferometric method	5	30	Yes	No		Large refractive index difference necessary

Capillary method						
Capillary in	3	10	Yes <sup>a</sup>	Yes	Immersion and $\Delta I$ effect	
Capillary out	2	15	Yes <sup>a</sup>	Yes		
Porous frit technique tracer	4	20	Yes <sup>a</sup>	Yes		
Diffusion-coupled method	4	20	Yes	Yes	Initial and final conditions	
Diaphragm cell	3	10	Yes	No		
Gravimetric technique					Calibration	
Conventional	3	10	Yes	No		
Improved	1	5	Yes	No		
Chromatographic method						Nonvolatile salts
Paper strip	4	15	Yes <sup>a</sup>	Yes		
Cylindrical thin-layer method						
Other						
Nuclear magnetic resonance (NMR) line-width technique	10	30	Yes <sup>a</sup>	Yes	Correlation effect not chemical diffusion coefficient	
Conductance method						

<sup>a</sup>Only in the high dilution case.

### (i) Chronopotentiometry

Chronopotentiometry has been widely used to determine diffusion coefficients in molten salts. Chronopotentiometry is an experimental procedure in which the potential of an electrode is observed as a function of time during the passage of a constant current sufficiently large to produce concentration polarization with respect to the species undergoing electrochemical reaction.

The transition time  $\tau$  is related to the diffusion coefficient by the Sand equation:

$$D = [4\tau I^2 / (\pi z^2 F^2 A^2 C_0^2)] \quad (53)$$

where  $I$  is the constant electrolysis current in amperes,  $z$  is the number of electrons involved in the electron transfer step,  $A$  is the area of the indicator electrode, and  $C_0$  is the concentration of the species of interest in the bulk of the solution. The transition time is the time required for the species to be removed at the electrode surface by electrolysis. It has been shown by Laity and McIntyre<sup>95</sup> that when sufficiently small concentrations are employed, the chronopotentiometric diffusion coefficients defined by Eq. (53) become substantially identical with ordinary diffusion coefficients. As long as the initial concentration  $C_0$  is low (less than 0.04 mol dm<sup>-3</sup>), the migration current can be neglected.

A typical chronopotentiogram is shown in Fig. 18. When the slopes corresponding to the intervals shown in Fig. 18 are designated  $S_0$ ,  $S_1$ , and  $S_2$ , the diffusion coefficient is calculated from<sup>99</sup>

$$z F C_0 \sqrt{\pi D} / 2i_T = \{1 - (S_1/S_0)\} \sqrt{\tau_1 + \tau_2} - \{(S_2/S_0) - (S_1/S_0)\} \sqrt{\tau_2} \quad (54)$$

where  $i_T$  is the total current density. For example, diffusion coefficients of the alkaline earth metal ions Ca<sup>2+</sup>, Sr<sup>2+</sup>, and Ba<sup>2+</sup> in an equimolar mixture (Na, K)Cl have been measured.<sup>100</sup>

### (ii) Linear Sweep Voltammetry

In linear sweep voltammetry, a rapidly changing ramp potential is applied to the indicator electrode. The current increases to a maximum and then decays. The peak current,  $i_p$ , is given by the Randles-Sevcik equation:

$$i_p = 0.446(nF)^{3/2} A C_0 D^{1/2} V_s^{1/2} / (RT)^{1/2} \quad (55)$$

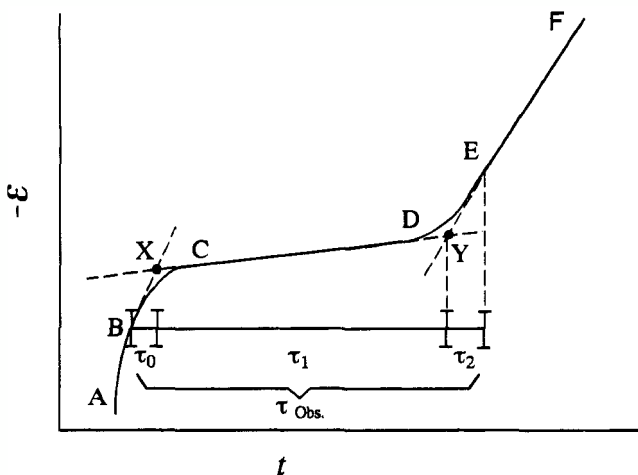


Figure 18. A typical chronopotentiogram; variation of potential with time.

where  $V_s$  is the voltage sweep rate ( $V\ s^{-1}$ ) and  $A$  and  $C_0$  have the same meanings as in Eq. (53).  $i_p/V^{1/2}C_0$  should be constant.  $D$  is calculated from Eq. (55).

### (iii) Wave-Front Shearing Interferometry

Wave-front shearing interferometry has been applied to transparent molten salt systems by Gustafsson et al.<sup>101</sup> The optical path of a light beam traversing the cell at an arbitrary level  $x$  is expressed by

$$R(x, t) = \int_0^L \mu dx \quad (56)$$

where  $\mu$  is the refractive index and  $L$  is the cell length in the  $z$ -direction of the optical axis. If the time  $t_0$  at which the injected material has dissolved and spread perpendicular to the optical axis is small compared with the time  $t$  at which the optical path is recorded, one has

$$R(x, t) = \mu_0 L + (\partial\mu/\partial c) M(\pi Dt)^{-1/2} \exp(-x^2/4Dt) \quad (57)$$

where  $\mu$  is taken to be

$$\mu = \mu_0 + (\partial\mu/\partial c)c \quad (58)$$

with a constant concentration dependence  $(\partial\mu/\partial c)$ . Here,  $M$  is the total amount of solute supplied to the bottom divided by the cell width. If  $b$  is the shear of the wave fronts in the cell plane, the path difference is given by

$$\begin{aligned} \Delta R(x, t) &= R(x + b/2, t) - R(x - b/2, t) \\ &= (\partial\mu/\partial c)M(\pi Dt)^{-1/2}[\exp\{-(x + b/2)^2/4 Dt\} \\ &\quad - \exp\{-(x - b/2)^2/4 Dt\}] \end{aligned} \quad (59)$$

When calculating the diffusion coefficient, we use the fact that  $\Delta R$  has the same value for two fringes, which are symmetrically located relative to the minimum (see Fig. 19). This gives

$$\begin{aligned} Dt[\log_{10} \sinh(bx_i/4 Dt) - \log_{10} \sinh(bx_j/4 Dt)] \\ - \{1/(4 \log_e 10)\}(x_i^2 - x_j^2) = 0 \end{aligned} \quad (60)$$

Using the same fringes as above, we obtain

$$D = 0.10857(x_i^2 - x_j^2)/[t \log_{10}(x_i/x_j)] \quad (61)$$

Interdiffusion coefficients of somenitrates have been measured by this method<sup>101-105</sup>

#### (iv) Spin Echo Method

While the nuclear magnetic resonance (NMR) technique has widely been used to study diffusion processes of normal liquids, solids, or colloidal systems, there are only a few applications to molten salts. The spin echo self-diffusion method with pulsed field gradients was applied to molten salts by Herdlicka et al.<sup>106</sup> There is no need to set up or maintain a concentration gradient.

The spin echo amplitude  $M(2\tau, g)$  in the presence of a magnetic field gradient of strength  $g$  and duration  $\delta$  is given, as schematically shown in Fig. 20, by

$$M(2\tau, g) = M(2\tau, 0) \exp\{-\gamma^2 D g^2 \delta^2 (\Delta - \delta/3)\} \quad (62)$$

where  $M(2\tau, 0)$  refers to the amplitude of the NMR signal, including relaxation effects obtained in the absence of the field-gradient pulses, and

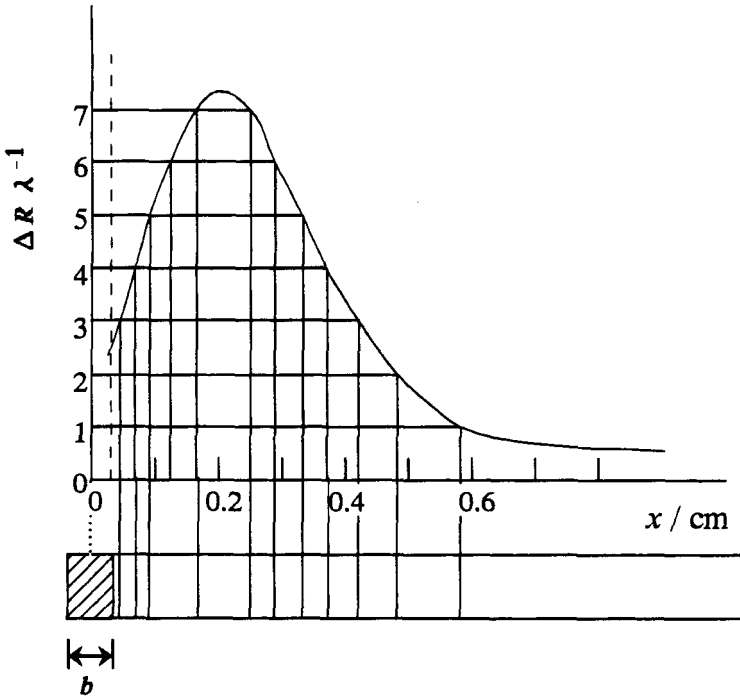


Figure 19. The optical path difference  $\Delta R$  as a function of the  $x$ -coordinate with the interferogram shown below. The shear  $b$  is taken to be 0.07 cm and  $D \times t$  to be  $2 \times 10^{-2}$  cm<sup>2</sup>. (Reprinted from Ref. 101 with permission from *Z. Naturforschung*.)

$\gamma$  is the gyromagnetic ratio of the nucleus to be measured. The echo maximum is measured at time  $2\tau$  for various applied linear magnetic field gradients by keeping time intervals  $\tau$  between the radiofrequency pulses and  $\Delta$  between gradient pulses at constant values. Each experiment was performed with  $\Delta$  fixed to 20 ms and  $\delta$  varying from 0.5 to 8 ms. The  $\tau$  was set to 20 ms and it coincided practically with  $\Delta$  since the radiofrequency pulses were negligible compared with the other time intervals. The value of  $M(2\tau, g)$  was measured for about 30 different values of  $\delta$  at a given  $g$ . The results were fitted to Eq. (62) and  $D$  was calculated.

Table II shows self-diffusion coefficients obtained by various methods.



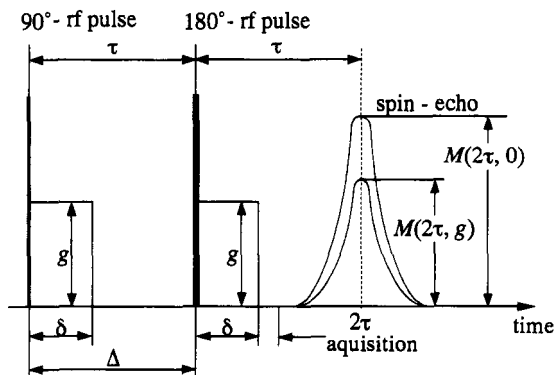


Figure 20. Pulse sequence for spin echo measurements of self-diffusion coefficients. (Reprinted from Ref. 106 with permission from *Z. Naturforschung*.)

Table 11  
Self-diffusion Coefficients of  $\text{Na}^+$  in Molten  $\text{NaNO}_3$  Obtained by Various Methods  $D = D_0 \exp(-E/kT)$

Method	$D$ ( $10^{-9}\text{m}^2\text{s}^{-1}$ )	$D_0$ ( $10^{-7}\text{m}^2\text{s}^{-1}$ )	$E$ ( $\text{kJ mol}^{-1}$ )	Ref.		
Diffusion out of capillary	2.33	1.89	20.79	108, 109		
	2.27			109–111		
Diffusion into capillary	2.10	0.55	17.99	112		
	2.13			113		
	2.14			17.99	114	
	2.48			0.80	18.07	115
	2.38			0.80	18.20	116
Impregnated paper strip	2.49	0.63	16.99	117		
	2.30			22.18	118	
	2.73			22.18	119	
Porous frit	2.32			120		
NMR spin echo	2.30	0.662	17.43	107		

In Fig. 11, the value of  $D$  of  $\text{Na}^+$  in molten  $\text{NaNO}_3$  measured at 623 K by the spin-echo method is compared with those measured by some other methods.<sup>106</sup>

### 3. Molecular Dynamics Simulation

#### (i) Mean-Square Displacement

Self-diffusion coefficients are dynamic properties that can be easily obtained by molecular dynamics simulation. The properties are obtained from mean-square displacement by the Einstein equation:

$$D = (1/6) \lim_{t \rightarrow \infty} [r(t) - r(0)]^2 \quad (63)$$

This can be obtained also from the velocity autocorrelation function according to the Green-Kubo relation<sup>87</sup>:

$$D = (1/3) \int_0^{\infty} \langle \mathbf{v}(0) \cdot \mathbf{v}(t) \rangle dt \quad (64)$$

This equation, called the Kubo equation, is equivalent to the Einstein equation. However, it is easier to estimate self-diffusion coefficients from the slope of the mean-square displacements.

#### (ii) Fractal Behavior

If the diffusion trajectory of an ion is divided into sections of length  $\epsilon$  and the number of divisions is denoted as  $N(\epsilon)$ ,

$$N(\epsilon) \propto \epsilon^{-D_f} \quad (65)$$

where  $D_f$  is the fractal dimension.<sup>121,122</sup> The fractal dimension shows a measure of self-similarity in a geometric pattern. For Brownian motion in ordinary fluids, the value of  $D$  is expected to be 2.

The coordinate function  $x(t) - x(0)$  was plotted at an interval of  $12 \Delta t$ . A gap  $G$  is a time interval for which  $x(t) - x(0) = 0$ . Gaps between successive values of  $\tau$  are characterized by a probability function  $\text{Pr}(G > g)$  for finding a gap of duration  $G$  greater than a given value  $g$  as

$$P(g) \equiv \text{Pr}(G > g) \quad (66)$$

If there is self-similarity in zero sets, the probability function is expressed by

$$P(g) \propto g^{\bar{D}} \quad (67)$$

where  $\bar{D}$  is the fractal dimension of the zero set. The relation between  $D_f$  and  $\bar{D}$  is

$$D_f = 1/(1-\bar{D}) \quad (68)$$

The fractal behavior of diffusion trajectories of ions has been studied in the molten phase of AgI as well as in the  $\alpha$ -phase.<sup>123</sup> The  $D_f$  values for an MD system with 250  $\text{Ag}^+$  and 250  $\Gamma^-$  at 900 K were calculated from Fig. 21 to be 2 and 2.17, respectively. The mean-square displacements are shown in Fig. 22 in comparison with those of the  $\alpha$ -phase at 670 K. As results of supplementary MD simulations, these authors obtained  $D_f=2$  for  $\text{Ag}^+$  and  $\bar{D}=2.17$  at 1000 K and  $D_f=2$  for both ions at 2000 K. Thus, they have concluded that: (1) at an extremely high temperature above the melting point, the system is in a completely liquid state, which leads to a

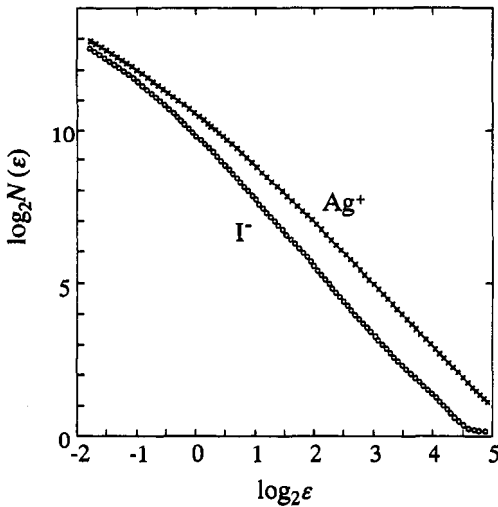


Figure 21. The division number  $N(\epsilon)$  for the trajectories of  $\text{Ag}^+$  and  $\Gamma^-$  at 900 K. (Reprinted from M. Kubayashi and F. Shimojo, "Molecular Dynamics Studies of Molten AgI.II. Fractal Behavior of Diffusion Trajectory," *J. Phys. Soc. Jpn.* **60**: 4076–4080, 1991, Fig. 6, with permission of the Physical Society of Japan.

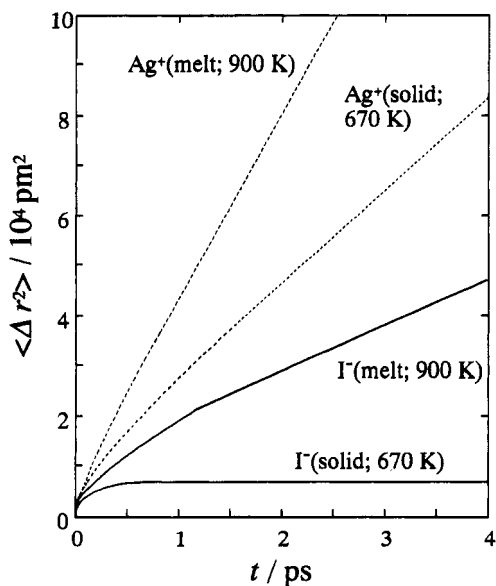


Figure 22. Mean-square displacements of  $\text{Ag}^+$  and  $\text{I}^-$  at 670 K and 900 K. (Reprinted from M. Kobayashi and F. Shimojo, "Molecular Dynamics Studies of Molten AgI. II. Fractal Behavior of Diffusion Trajectory," *J. Phys. Soc. Jpn.* **60**: 4076-4080, 1991, Fig. 8, with permission of the Physical Society of Japan.)

value of  $D_f = 2$ , and (2) at a temperature near the melting point, the local structure may be similar to that in the solid state.

## V. VISCOSITY

Shear viscosity is a measure of the ability of one layer of molecules to move over an adjacent layer. Bulk viscosity will be mentioned in Section V.2. Since viscosity usually refers to shear viscosity, the term will be used in this way unless otherwise stated. Recommended techniques for measuring the viscosity of high-temperature melt are given below. Experimental data are available from the database mentioned in Section I.2. Data on viscosities of slags (7 single component systems, 35 two-component

systems, 62 three-component systems, 19 four-component systems, 4 five-component systems, and 7 six-component systems) are available in a report by the National Physical Laboratory, UK.<sup>124</sup>

## 1. Measurement Methods

### (i) Oscillating Cylinder

A body of a cylindrical or spherical shape is suspended in a melt and oscillating rotational motion is fed to it. A schematic drawing of a viscometer is shown in Fig. 23. This initial oscillation is gradually attenuated by the viscosity resistance. The viscosity is obtained as an absolute value from the logarithmic decrement of the swings of the pendulum's oscillation. Since the sample melt can be completely closed in this method, this is the best method for a melt of high temperature.

Tørklep and Øye<sup>125</sup> measured the viscosity of NaCl by this method, which has been adopted as the standard (see Section 1.2). The accuracy of the working equation is better than 0.1% for the cylinder geometry, liquid densities, and liquid viscosities used by these authors. They claim that the remarkable theoretical analysis of oscillating-body viscometers given by Kestin and Newell<sup>126</sup> supersedes all former, less accurate theories. All the results were once suspect owing to possible solid impurities in the liquid,

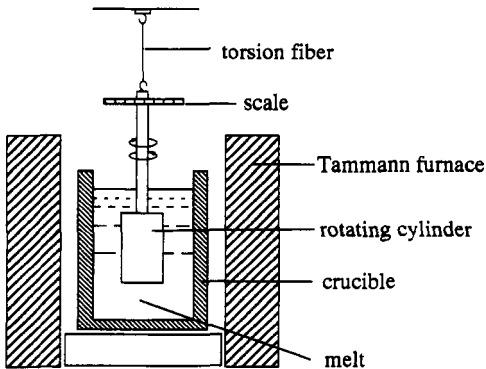


Figure 23. Schematic drawing of oscillating cylinder viscometer. (Reprinted from Ref. 124. Crown Copyright © 1992. Reproduced by permission of the Controller of Her Majesty's Stationary Office.)

gas bubbles adhering to the cylinder, insufficient mixing, or strong convection, even if the damping viscosity might still appear to be normal. The data have been fitted to

$$\eta(\text{mPa s}) = 89.272 \times 10^{-3} \exp(2641.2/T) \quad (1080-1210 \text{ K})$$

(error:  $\pm 0.2\%$ ) (69)

The standard deviation of  $\eta$  (mPa s) in the fit is 0.05%.

This method yields an absolute value. When a melt is near the melting point, the viscosity is so high that non-Newtonian behavior occurs.

### (ii) *Oscillating Cup*

The logarithmic decrement of the oscillations of a pendulum consisting of a crucible containing a test liquid is measured by the oscillating cup method. A schematic drawing of the oscillating cup (vessel) viscometer is shown in Fig. 24.

This method has the advantages<sup>127</sup> that (1) only a small amount of specimen is required; (2) the desired temperature can be easily maintained; (3) the cup can be made from noncorrosive material; (4) the cylindrical shape allows precise machine working. In contrast to the inherent advan-

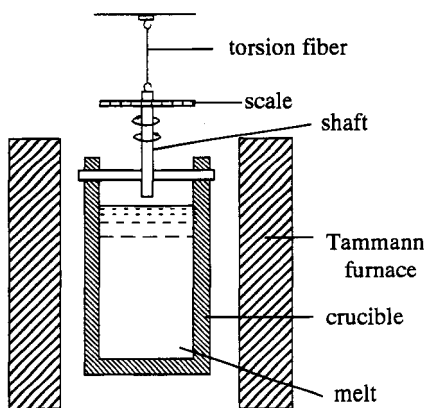


Figure 24. Schematic drawing of oscillating cup viscometer. (Reprinted from Ref. 124. Crown Copyright © 1992. Reproduced by permission of the Controller of Her Majesty's Stationary Office.)

tages of this method over other methods, its mathematical complexity has restricted its extensive application. Several efforts have been made to derive a rigorous solution, and one type of equation depends on the characteristic dimensions of the cup and the kinematic viscosity of the fluid under investigation. Another type of solution<sup>127</sup> was derived by introducing the Laplace transform to facilitate the complicated evaluation. A working equation is given by Brockner et al.,<sup>128</sup> in which the viscosity of an NaCl-AlCl<sub>3</sub> melt mixture was determined. Nagashima's group<sup>127</sup> measured the viscosity of KNO<sub>3</sub> by this method, and Shvidkovskii's method is a variant of the oscillating cup method.<sup>129</sup>

Sato et al.<sup>130</sup> measured the viscosities of some binary and ternary alkali carbonates. Since melt creep must be prevented, a highly sintered alumina crucible was used instead of a gold-plated nickel crucible. Homogeneity of a mixture sample was achieved by gas bubbling. A laser beam is combined with a computer-assisted time counter to obtain the logarithmic decrement. Roscoe's equation<sup>131</sup> has been used for calculation of the viscosity, while it has been claimed by Abe et al.<sup>127</sup> that the viscosities calculated from Roscoe's equation are 0.6–1.5% lower than those from more rigorous equations.

### (iii) *Rotating Cylinder*

Rotating cylinder viscometers consist of two concentric cylinders, corresponding to the bob and the crucible, one cylinder of which is rotated at a constant speed. The viscosity is determined from measurement of the torque generated. A schematic drawing is shown in Fig. 25. This method is most popular for measuring viscosity at high temperatures and is suitable for melts with high viscosity. The viscosity is calculated from

$$\eta = (M/8\pi^2 nh)(1/r_i^2 - 1/r_o^2) \quad (70)$$

where  $M$  is the torque,  $n$  the number of revolutions per second,  $h$  and  $r$  the height and radius of the inner cylinder, and  $r_o$  the radius of the outer cylinder. Equation (70) applies to infinitely long cylinders, and viscometers of this type are usually calibrated with reference samples both at room and at high temperatures.

A concentric cylinder method in which the outer cylinder is rotated has been presented by Bockris and Lowe<sup>132</sup> for measuring the viscosity of silicates up to 1800 °C.

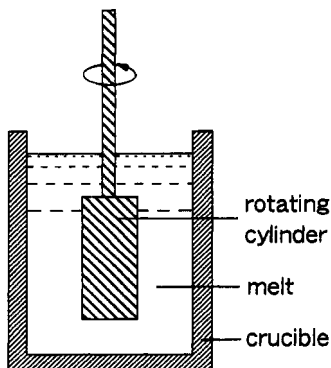


Figure 25. Schematic drawing of rotating cylinder viscometer. (Reprinted from Ref. 124. Crown Copyright © 1992. Reproduced by permission of the Controller of Her Majesty's Stationary Office.)

The viscosity of molten  $\text{BeF}_2$ <sup>133</sup> and  $\text{LiF-BeF}_2$  mixture<sup>134</sup> has been measured with this method. In this experiment, cylindrical spindles of Inconel, varying in radius between 0.158 and 1.65 cm, were rotated in nickel vessels of 2.05 cm internal radius.

#### (iv) Capillary

In the capillary method, the time required for a liquid to flow through a capillary tube is determined. The melt under investigation flows with a constant rate through a tube with a small, definite cross-sectional area, such as a cylindrical capillary. The viscosity can be measured in an absolute way from the pressure drop. This method can yield the most reliable absolute data, the viscosity being given by a modified Hagen-Poiseuille equation:

$$\eta = \pi r^4 \rho g h t / 8(L + nr) V - m \rho V / 8\pi(L + nr)t \quad (71)$$

where  $\rho$  is the density of the melt;  $r$  and  $L$  are the diameter and the length of the capillary, respectively;  $h$  is the effective height of the melt;  $V$  is the eluted volume;  $g$  is acceleration of gravity;  $n$  and  $m$  are constants for correction; and  $t$  is the time for elution. The second term of the right-hand



side is reduced because a certain amount of kinetic energy remains in the liquid after it has left the capillary and that has not been expended in overcoming friction. With one viscometer, all the coefficients of the right-hand side of Eq. (71) except  $\rho$  and  $t$  are constants and therefore the kinematic viscosity is

$$v = \eta / \rho = C_1 t - C_2 / t \quad (72)$$

By using a liquid with a known kinematic viscosity such as distilled water, the values of  $C_1$  and  $C_2$  can be determined. Ejima et al.<sup>135</sup> have measured the viscosity of alkali chloride melts. The equations obtained, both the quadratic temperature equation and the Arrhenius equation, are given in Table 12, which shows that the equation of the Arrhenius type fits better than the quadratic equation.

The experimental procedure employed a capillary viscometer made of quartz<sup>135</sup> as shown in Fig. 26. A solid sample was put in the filtration chamber and the top of the chamber was sealed under a vacuum. Then the sample was heated to melting and filtered into the viscometer and the connecting tube sealed at the middle. The viscometer was settled inside a transparent electric furnace and after the temperature of the melt was stabilized, the furnace containing the viscometer was turned upside down, which transferred the melt into the funnel. Then the tube was turned

**Table 12**  
**Viscosity Equations as a Function of Temperature**

Substance	Viscosity equation (mPa s)	Temp. range (K)	Std. dev.
LiCl	$\eta = 8.9119 - 1.2847 \times 10^{-2} T + 5.0585 \times 10^{-6} T^2$ $\eta = 0.108696 \exp(19375/RT)$	886–1169	0.007 <sub>6</sub> 0.002 <sub>9</sub>
NaCl	$\eta = 7.2226 - 9.2588 \times 10^{-3} T + 3.2635 \times 10^{-6} T^2$ $\eta = 0.09463 \exp(21439/RT)$	1078–1180	0.000 <sub>8</sub> 0.000 <sub>8</sub>
KCl	$\eta = 8.8090 - 1.1936 \times 10^{-2} T + 4.3709 \times 10^{-6} T^2$ $\eta = 0.07084 \exp(2391/RT)$	1051–1191	0.001 <sub>1</sub> 0.001 <sub>1</sub>
RbCl	$\eta = 11.3651 - 1.6147 \times 10^{-2} T + 6.1632 \times 10^{-6} T^2$ $\eta = 0.07676 \exp(24031/RT)$	1000–1182	0.002 <sub>5</sub> 0.002 <sub>1</sub>
CsCl	$\eta = 11.2141 - 1.6325 \times 10^{-2} T + 6.3386 \times 10^{-6} T^2$ $\eta = 0.06078 \exp(24942/RT)$	933–1183	0.005 <sub>9</sub> 0.002 <sub>5</sub>

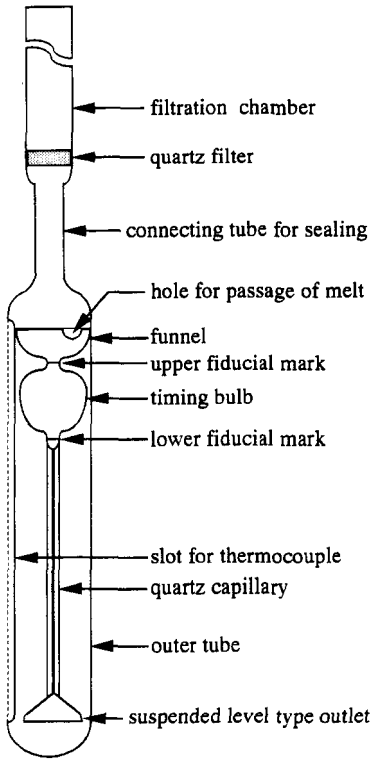


Figure 26. Capillary viscometer. (Reprinted from Ref. 135 with permission of the Chemical Society of Japan.)

around by 180°, when the melt in the timing bulb descended through the capillary. The falling time was measured with the naked eye.

**(v) Falling Ball**

When a ball falls (or ascends) in a melt under gravity, the velocity follows the Stokes equation, from which the viscosity can be calculated:

$$\eta = \frac{2gr^2(\rho_k - \rho_{liq})}{9v} \tag{73}$$

where  $r$  is the radius of the ball,  $\rho_k$  and  $\rho_{liq}$  are the densities of the ball and liquid, respectively, and  $v$  is the velocity of descent (or ascent) of the ball.

It is necessary to measure the viscosity under the condition of a small Reynolds number, and experiments with high precision can be expected for viscosities over 0.1 Pa s. This method has also been used to measure the viscosity of slag melts,<sup>124</sup> when the time taken to pull a ball out of the melt with constant force was measured.

### (vi) Industrial Viscometers

Several simple viscometers have been developed for "in plant" determinations of slag viscosities<sup>124</sup> they include a Herty viscometer<sup>136,137</sup> and a Krabiell immersion viscometer.<sup>138</sup>

## 2. Bulk Viscosity

Bulk viscosity refers to the ability to generate a pressure,  $\Delta p$ , resistant to a change in volume of a liquid:

$$\Delta p = -\eta_b \, dv/dt \quad (74)$$

where  $\eta_b$  is the bulk viscosity and  $v$  the relative volume change.

Bulk viscosity,  $\eta_b$ , is evaluated from the ultrasonic absorption coefficient  $\alpha$  and shear viscosity  $\eta_s$  by<sup>139</sup>

$$\eta_b = \eta_{eff} - \eta_{cl} = (\alpha/f^2)(\rho U^3/2\pi^2) - [(4/3)\eta_s + (\gamma - 1)\lambda/c_p] \quad (75)$$

where  $\eta_{eff} = (\alpha/f^2)(\rho U^3/2\pi^2)$  is the effective viscosity, which determines the total dissipation of the energy of sound waves during a unit period per unit volume;  $\eta_{cl}$  is called the classical viscosity, which contributes to energy absorption of the sound waves on account of the dynamic viscosity and to the thermal conductivity;  $U$  is the sound velocity,  $\gamma = c_p/c_v$  ( $c_p$  and  $c_v$  are isopiestic and isovolumic specific heat capacities, respectively); and  $\lambda$  is the thermal conductivity. In the case of molten salts, absorption due to thermal conductivity is small compared with that due to the viscosities, and therefore the third term on the right-hand side is neglected.

The bulk viscosities of molten alkali nitrates measured by Ejima's group<sup>140</sup> are shown in Fig. 27, where the bulk viscosity decreases with increasing temperature. The ratios of  $\eta_b/\eta_s$  are approximately constant over the temperature range investigated. This suggests that the activation energies of the bulk viscosity and the shear viscosity are much the same.

Minchenko and Smirnov<sup>141,142</sup> have measured the absorption coefficients of sound in binary molten salts (Na, Cs)Cl, (Na, Cs)Br, (Na, Cs)I, K(Cl, Br), K(Br, I), K(Cl, I), Cs(Cl, Br), Cs(Br, I), and Cs(Cl, I) and

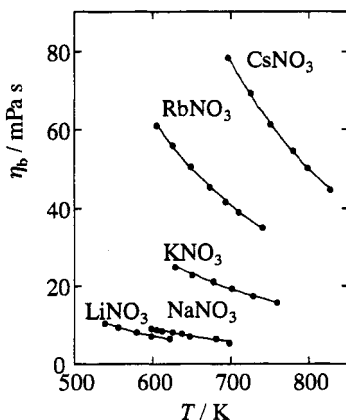


Figure 27. Bulk viscosity of alkali nitrates. (Reprinted from Ref. 140 with permission of the Japan Institute of Metals.)

calculated the bulk viscosities. The variations in the bulk viscosity and its components with temperature are well approximated by

$$\eta_b = a_1 - b_1 T \quad (76)$$

$$\ln \eta_{\text{eff}} = a_2 + (b_2/T) \quad (77)$$

$$\ln \eta_{\text{cl}} = a_3 + (b_3/T) \quad (78)$$

where  $a$  and  $b$  are constants.

A linear relation exists between the sound-absorption coefficients in the melts and their volumes ( $V$ ,  $\text{cm}^3$ ) as a function of temperature:

$$\text{chlorides: } 10^{15} \alpha/f^2 = 3.84 - 5.19 \times 10^{-3} T + (0.513 - 0.198 \times 10^{-3} T)V \quad (79)$$

$$\text{bromides: } 10^{15} \alpha/f^2 = 9.49 - 6.29 \times 10^{-3} T + (0.396 - 0.114 \times 10^{-3} T)V \quad (80)$$

$$\text{iodides: } 10^{15} \alpha/f^2 = -2.85 - 3.86 \times 10^{-3} T + (0.611 - 0.187 \times 10^{-3} T)V \quad (81)$$

These equations may be used by interpolation to estimate, with ~10% error, sound absorption in melts.

It is claimed by Minchenko and Smirnov<sup>141,142</sup> that a correlation should exist between bulk viscosity and the bonding energy between the associated species and the ions of the second coordination sphere.

For the origin of the bulk viscosity, there are two relaxation mechanisms. One is the thermal relaxation that arises from the slow interchange of energy between the external and internal degrees of freedom and is typical for nonassociated liquids. The other is the structural rearrangement, which is caused by the time lag in responding to the change in the external variables and which is found in associated liquids. Zhu et al.<sup>143</sup> consider that the bulk viscosity of molten alkali carbonates is due to structural relaxation because  $d\eta_b/dT$  is negative and  $\eta_b/\eta_s$  is nearly independent of temperature and is the same order of magnitude as those of associated liquids.

### 3. Recommended Values

#### (i) *Experimental Uncertainties in Viscosity Measurements*

The recommended techniques for measuring the viscosity of high-temperature melts given above have the main difficulties listed in Table 13.

#### (ii) *Standard Salts*

The recommended viscosity data for NaCl and KNO<sub>3</sub> melts are available for calibration, as mentioned in Section II. There still exists appreciable, though small, disagreement between the data obtained by the two groups, that is, Øye's group and Nagashima's group.<sup>144</sup> Ejima et al.<sup>135</sup>

**Table 13**  
**Main Difficulties Involved in Typical Methods for Measuring Viscosity**

Technique	Difficulties
Oscillating cylinder	Difficult for high-vapor pressure fluid
Oscillating cup	Meniscus effect
Rotating cylinder	Difficult for low-viscosity fluid
Capillary flow	Limited capillary materials
Falling ball	Difficult for nontransparent fluids and for low-viscosity fluids

performed their second series of measurements on NaCl by a capillary method, which is in agreement with the data by Øye's group.<sup>125</sup> For other salts, there are no well-established recommendations and further measurements are needed.

Mills<sup>124</sup> has concluded in his review article on molten slags that (1) most viscosity measurements were subject to experimental uncertainties of  $\pm 25\%$ ; (2) in some cases experimental uncertainties could be  $> \pm 50\%$ ; and (3) experimental uncertainties as low as  $\pm 10\%$  could be achieved by careful calibration of viscometers with high and low temperature reference materials.

#### 4. Factors Determining Viscosity

Although the viscosity of a mixture is determined by many factors, the main factors are considered to be the specific volume and the cohesive force between ions, which are related to each other. In Fig. 28, isotherms of the viscosity are shown for various compositions of  $(\text{Li}, \text{Na})_2\text{CO}_3$  mixtures. At high concentrations of  $\text{Li}_2\text{CO}_3$ ,  $\text{Li}^+$  is coordinated by  $\text{CO}_3^{2-}$  ions. Thus the system is more "polymerized," and therefore the viscosity is high. As the concentration of  $\text{Li}^+$  decreases, the  $\text{CO}_3^{2-}$  ion coordinates more strongly to  $\text{Li}^+$  and less strongly to the second cation, and therefore the system becomes less polymerized and the viscosity decreases. However, at a high concentration of the second cation, the concentration of  $\text{Li}^+$  becomes weak, which leads to coordination of a  $\text{CO}_3^{2-}$  ion to the neighboring second cations, and the viscosity increases slightly.

##### (i) Stokes–Einstein–Debye Relation

It is important from a practical viewpoint to predict the shear viscosity of mixtures from those of pure melts. For alkali nitrate melts, a linear dependence has been found between the reorientational line width obtained by Raman measurements and the ratio of temperature divided by shear viscosity.<sup>145</sup> For  $\text{NO}_3^-$  ions, the depolarized Raman scattering from  $\sim 1050 \text{ cm}^{-1}$  total stretching vibrational mode ( $A_1$ ) has a contribution to the line width  $L_r$ , which is caused by the reorientational relaxation time of the  $C_{3v}$  axis of this ion. The Stokes–Einstein–Debye (SED) relation establishes a relation between the shear viscosity  $\eta$  of a melt and the relaxation time  $\tau_r$  for the reorientation of a particle immersed in it:

$$\tau_r = V\eta_s / kT \quad (82)$$

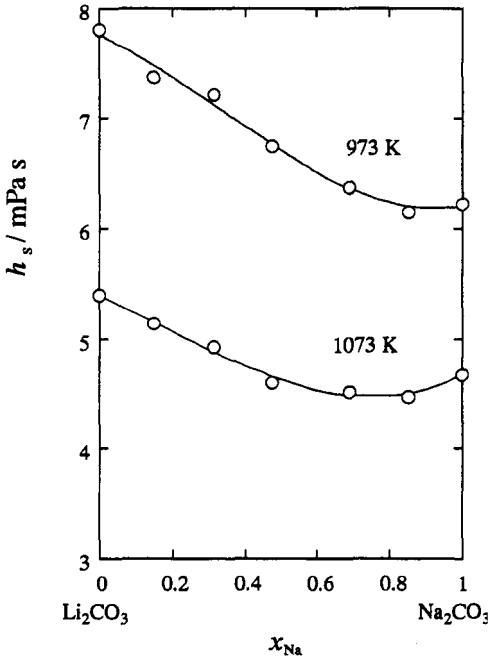


Figure 28. Isotherms of the shear viscosities of (Li, Na)<sub>2</sub>CO<sub>3</sub>. (Reprinted from Y. Sato, T. Yamamura, H. Zhu, M. Endo, T. Yamazaki, H. Kato, and T. Ejima, "Viscosities of Alkali Carbonate Melts for MCFC," in *Carbonate Fuel Cell Technology*, D. Shores, H. Maru, I. Uchida, and J. R. Selman, eds., p. 427, Fig. 9, 1993. Reproduced by permission of the Electrochemical Society, Inc.)

where  $V$  is an effective volume of the particle. Although Eq. (82) was derived originally for a macroscopic particle, it may be successfully applied to microscopic particles. For molten NaNO<sub>3</sub>, (Na, K)NO<sub>3</sub> (50–50 mol%), and Ca<sub>2</sub>K<sub>3</sub>(NO<sub>3</sub>)<sub>7</sub>, a plot of  $\Gamma_r$ , vs.  $T/h$  shows that the linear relation holds well:

$$\Gamma_r = \Gamma_0 + BT/\eta_s \quad (83)$$

The occurrence of a term  $\Gamma_0$  besides the term is analogous to that in Eq. (83) implies that there are at least two different types of elementary

relaxation processes. For an aqueous solution of  $\text{NaNO}_3$  of various concentration at 303 K, a relation with the same slope as in the molten salt case is observed. From the slope  $B$  the volume  $V$  is estimated as  $25 \times 10^3 \text{ nm}^3$ , which is close to the effective rigid volume of an  $\text{NO}_3^-$  ion,  $24.8 \times 10^3 \text{ nm}^3$ .<sup>19</sup> For the well-known glass-forming substance  $\text{Ca}_2\text{K}_3(\text{NO}_3)_7$ , the deviation from linearity is found at extremely high viscosity, which may be due to the glass-forming behavior. The slopes of plots for  $(\text{Li}, \text{Rb})\text{NO}_3$  mixtures<sup>146</sup> are in qualitative agreement with the other nitrate data. Thus one can conclude that the  $\text{NO}_3^-$  ion determines the  $\tau$  and  $\eta$ , while the cations play only a secondary role. However, the cations seem to determine the bulk viscosity. Figure 29 shows that Eq. (83) provides reliable values for slow relaxation over about six orders of magnitude of time.

A review article has been published on depolarized Raman spectroscopy in molten salts,<sup>147</sup> and it is discussed briefly here for the case of molten nitrates. Polarized (VV) and depolarized (HV) Raman scattering of the  $1050 \text{ cm}^{-1}$  line was used. The intensity of the isotropic part of the

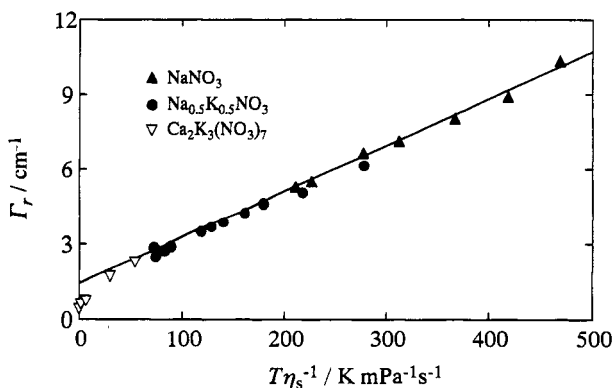


Figure 29. Reorientational line width  $\Gamma_r$  from Raman spectra plotted against  $T/\eta$  for  $\text{NaNO}_3$ ,  $\text{Na}_{0.5}\text{K}_{0.5}\text{NO}_3$ , and  $\text{K}_3\text{Ca}_2(\text{NO}_3)_7$ . The straight line is drawn according to Eq. (90):  $\Gamma_r = 1.5 \text{ cm}^{-1} + 0.184 (T/\eta_s)$ . (Reprinted from A. Kisluk, S. Loheider, A. Sokolov, M. Soltwisch, Q. Quitmann, E. Shasha and A. Voronel, "Relaxation and Shear Viscosity in Mixed Ionic Melts," *Phys. Rev.* **52B**: R13083–R13086, Fig. 3, 1995. Copyright © 1995 by the American Physical Society.)



scattering,  $I_{\text{iso}}$ , can be obtained from the polarized and depolarized intensity by

$$I_{\text{iso}}(\omega) = I_{\text{VV}}(\omega) - (4/3)I_{\text{HV}}(\omega) \quad (84)$$

The shapes of both  $I_{\text{VV}}$  and  $I_{\text{HV}}$  lines are assumed to be represented by simple Lorentzians. For a totally symmetric vibration with a low polarization ratio as in the present case, the vibrational and reorientational relaxation times  $\tau_v$  and  $\tau_r$  can be determined from the half-widths of the isotropic and anisotropic spectra. Since the value of  $I_{\text{HV}}$  is much smaller than that of  $I_{\text{VV}}$  for the  $1050 \text{ cm}^{-1}$  line, the contribution of  $I_{\text{HV}}$  to the isotropic intensity can be neglected:

$$\Gamma_{\text{iso}} = \Gamma_v = \Gamma_{\text{VV}} \quad (85)$$

$$\Gamma_{\text{aniso}} = \Gamma_{\text{HV}} = \Gamma_v + \Gamma_r \quad (86)$$

and

$$\Gamma_v = 1/(\pi c \tau_v) \quad (87)$$

$$\Gamma_r = 1/(\pi c \tau_r) = \Gamma_{\text{HV}} - \Gamma_{\text{VV}} \quad (88)$$

## 5. Molecular Dynamics Simulation

For liquids, few simple and widely accepted theories have been developed. The shear viscosity can be related to the way in which spontaneous fluctuations relax in an equilibrium system, leading to the time correlation function expression<sup>148,149</sup>:

$$\eta_s = (1/VkT) \int_0^{\infty} \langle J^{xy}(0)J^{xy}(t) \rangle dt \quad (89)$$

where  $J^{xy}$  are the Cartesian components of the stress tensor:

$$J^{xy} = \sum_{i=1}^N [(P_{ix} P_{iy}/m) - (1/2) \sum_{j=1, j \neq i}^N r_{ijz} (d\phi/dr_{ijx})] \quad (90)$$

The bulk viscosity  $\eta_b$  is calculated from the relation:

$$\eta_b + (4/3)\eta_s = (1/VkT) \int_0^{\infty} \langle (J^{xx}(t) - PV)(J^{xx}(0) - PV) \rangle dt \quad (91)$$

where  $P$  is the equilibrium pressure.

Equilibrium molecular dynamics simulations have been performed to obtain the solution of the time correlation function (Table 14).<sup>150</sup>

Ciccotti et al.<sup>90</sup> have evaluated shear viscosity by applying a shearing force that is periodic in space and has by necessity a finite wave vector:

$$\mathbf{F}(\mathbf{r}_i, t) = \text{Re} F_x \exp(i\mathbf{k} \cdot \mathbf{r}_i) \theta(t) \mathbf{x} \quad (92)$$

It is assumed that the force  $\mathbf{F}$ , which by construction is orthogonal to  $\mathbf{k}$ , is directed along the  $x$ -axis.  $\theta(t) = 0$  at  $t < 0$  and  $=1$  at  $t > 0$ . The response for the  $k$ th Fourier component of the drift velocity  $\langle \hat{u}_x(\mathbf{k}, t) \rangle$  was calculated. The limiting value of this quantity is related to the shear viscosity by

$$\eta = \lim_{k \rightarrow 0} [\rho F_x / k^2 \langle \hat{u}_x(\mathbf{k}, \infty) \rangle] \quad (93)$$

where  $\rho$  is the number density. The mean response to a perturbation of the form in Eq. (93) is very different from that obtained in the calculation of conductivity [Eq. (34)], the plateau value being reached asymptotically. The calculated shear viscosity is given in Table 15.

Nonequilibrium molecular dynamics simulations provide another approach for viscosity predictions. This approach as well as equilibrium molecular dynamics was reviewed.<sup>153</sup>

For the most part these approaches have been applied and tested on spherically symmetric monoatomic or other simple molecules. Even for

**Table 14**  
**Simulation Results for Shear and Bulk Viscosities of Molten NaCl and KCl**

	T (K)	V (cm <sup>3</sup> mol <sup>-1</sup> )	N	n (10 <sup>4</sup> )	$\eta_b$	$\eta_s$ (mPa s)	$\eta_s(\text{exp})$
NaCl	1100	38.01	64	14	2.2 ± 0.7	1.05 ± 0.05	1.24 <sup>a,b</sup>
			216	3.8	1.6	1.16	
KCl	1096	49.88	64	14	2.1 ± 0.7	1.24	1.03 <sup>a,c</sup>

<sup>a</sup>Ref. 151.

<sup>b</sup>Ref. 125.

<sup>c</sup>Ref. 152.

**Table 15**  
**Shear Viscosity Calculated from MD Simulation<sup>90</sup>**

Salt	$V_m(\text{cm}^3\text{mol}^{-1})$	$T(\text{K})$	$\eta(\text{mPa s})$
LiF	15.00	1287	1.14
NaCl	39.10	1262	0.87(0.83)
NaI	51.46	1081	1.08(1.01)
KI	68.97	899	1.06(1.40)
RbCl	56.48	1119	0.99(0.90)
RbI	75.75	1086	1.12(0.96)

Note: Values in parentheses are experimental results.

such molecules, in most cases predicted viscosities were only within an order of magnitude of experimental values. Although these approaches are impractical at present, they may be promising in the future. The main problems are the accuracy of the intermolecular potential functions and the need for a huge computation time, which will be progressively improved.

## VI. THERMAL CONDUCTIVITY

During the past half century, the measurement of thermal properties has changed from being one of mainly academic interest to a vital necessity. This is due to the phenomenal increase in materials and related developments associated with all of the new and emerging technologies.<sup>154</sup> Despite the technological importance of molten salts and electrolyte solutions in, e.g., metallurgy and batteries, transport properties other than electric conductivity are still relatively unexplored by experimental and theoretical methods compared with those of nonionic liquids. There is, however, an increasing interest in thermal transport data in design methods for electrochemical process units.<sup>155</sup> There has been a change in emphasis from the classical steady-state methods to more novel transient techniques. Several years ago thermal conductivity and diffusivity measurements in molten salts were reviewed by Waseda and Ohta.<sup>156,157</sup>

In an isotropic medium, as for normal liquids, the Fourier equation holds:

$$J = -\lambda \nabla T \tag{94}$$

where  $J$  is the heat flow in unit time through unit area,  $\lambda$  the thermal conductivity, and  $\Delta T$  the temperature gradient. For the transient condition, Eq. (94) becomes

$$\nabla J = -C_p \rho (\partial T / \partial t) \tag{95}$$

where  $C_p$  is the specific heat capacity and  $\rho$  the density.

In the case that  $\lambda$ ,  $C_p$ , and  $\rho$  are independent of position and temperature, it follows from Eqs. (94) and (95) that

$$\nabla^2 T = (\rho C_p / \lambda) (\partial T / \partial t) \tag{96}$$

A thermal diffusion equation is expressed, as in Fick's second law of diffusion, by

$$\partial T(x, t) / \partial t = D_T \nabla^2 T \tag{97}$$

where  $D_T$  is the thermal diffusivity. From Eqs. (96) and (97),

$$\lambda = D_T \rho C_p \tag{98}$$

Therefore, if the three quantities are obtained,  $\lambda$  can be calculated.

Data on high-temperature melts are still limited. Conventional methods are difficult to apply because of the high values of thermal conductivity. Other difficulties in measuring molten salts are their corrosiveness, high electrical conductivities, and the necessity of careful preparation. Special care should be taken to exclude convection errors, which are usually the most serious source of errors, even at room temperature.

At temperatures above ca. 1000 K, heat transfer via radiation becomes significant, that is, the heat transfer can occur by optical energy waves (photons) as well as conduction (phonons), with the heat transfer equation expressed by

$$\rho C_p (\partial T / \partial t) = \lambda \nabla^2 T - \nabla F \tag{99}$$

where  $F$  is the heat flux due to radiation.  $\nabla F$  is negligible for transparent or optically very thin liquids, but not for opaque liquids; the energy flux  $q$  may be expressed by a combination of conduction and radiation:

$$q = J + F = -\lambda T - \lambda_r \nabla T \tag{100}$$

where  $\lambda_r$  is the radiative (photon) conductivity:

$$\lambda_r = 16n^2\sigma T^3/3k_R \quad (101)$$

Here  $\sigma$  is the Stefan–Boltzmann constant,  $n$  the refractive index, and  $k_R$  the absorption coefficient.

A steady-state method is disadvantageous in measurements on a mixture because for a long time the temperature gradient is likely to generate separation of the mixture due to thermal diffusion. Accurate measurement itself seems to be still one of the most pressing concerns for thermal diffusion of high-temperature melts.

## 1. Measurement Methods

### (i) Variable Gap

The variable gap method is a steady-state method, with the merit that transport of heat by radiation can be separated from the total heat flow:

$$\Delta\theta/Q = \{1/(\lambda + F \cdot \Delta x)\} \Delta x + K \quad (102)$$

where  $F$  is a coefficient related to the mean refractive index of the melt, the average absorption, and the average temperature.  $K$  is a constant of the cell;  $\Delta x$  which is variable, is the width of the melt of interest;  $\Delta\theta$  is the difference in temperature between the two ends of the melt;  $Q$  is the total flux of heat;  $\lambda$  is the thermal conductivity. Values of  $\Delta\theta/Q$  are obtained at various  $\Delta x$  and  $\lambda$  can be obtained from the value extrapolated to  $\Delta x \rightarrow 0$ . When  $\Delta x$  is small, it contains large errors, and therefore the measurement should be performed at various  $\Delta x$ . Cooke measured the thermal conductivities of fuel melts of a molten salt reactor experiment using this technique.<sup>158</sup>

### (ii) Hot-Wire

The hot-wire method is a transient method and can yield an absolute value. A long, thin wire, through which electric current is passed stepwise, is placed in a melt, when

$$\lambda = (Q/4\pi)d(\ln t)/d\theta \quad (103)$$

where  $Q$  is a caloric value per length and per time. From the relation between  $Q$  and  $\ln t/\theta$ , the value of  $\lambda$  is obtained. If the electric conductivity of melts is small,  $Q$  can be estimated accurately from the power supplied. However, since the electric conductivity of melts is usually high, the

surface of the wire has to be covered with an insulating material such as glasses and ceramic<sup>159-161</sup>

A number of variations of the transient hot-wire method have been devised, and an optical method to detect the temperature rise has been used.<sup>144</sup> A modified transient hot-wire technique using a mercury-in-capillary probe was introduced by Nagashima et al.,<sup>162,163</sup> in which a thin mercury thread was used as a heater-thermometer and the capillary wall as an insulator. Using this method, they measured the thermal conductivity in mixture systems such as (Na, K)NO<sub>3</sub>,<sup>163</sup> (Li, Na)NO<sub>3</sub>,<sup>164</sup> and HTS(KNO<sub>3</sub>-NaNO<sub>3</sub>-NaNO<sub>2</sub>, 44-7-49 mol.%).<sup>164</sup>

DiGiulio and Teja<sup>165</sup> have developed a two-wire technique to obtain absolute values of thermal conductivity. Quartz capillaries filled with liquid gallium served as insulated hot wires. They measured the thermal conductivity of the NaNO<sub>3</sub>-KNO<sub>3</sub> eutectic in the range 525–590 K with 1% accuracy. Radiation by the fluid was also accounted for.

### (iii) Stepwise Heating

Kato et al.<sup>166,167</sup> have used electric stepwise heating of a thin metal layer to measure thermal diffusivity of molten salts. The ratio of the temperatures with time  $t_1$  and  $2t_1$  at distance  $x$  below the heating plate was evaluated as a function of the Fourier number:

$$F_0 = D_T t_1 / x^2 \quad (104)$$

where  $D_T$  is the thermal diffusivity of the molten salt. When the opposite surface of the planar source is heated at a constant rate,  $D_T$  can be determined by measuring the temperature rise at a distance  $x$  in the molten salt. The amount of heat generated in the source can be calculated from the current. The sample salt is heated from the surface downward to avoid the onset of convection flow. The cell must satisfy the following requirements: (1) The thin planar heat source heated by an electric current should maintain its flatness at all times. (2) The temperature sensor should be thin enough not to affect the temperature response with its heat capacity. (3) The heat source and the temperature sensor should be insulated from the sample salt to avoid electric current leakage. Using this method, these authors have measured the thermal diffusivity of molten LiNO<sub>3</sub>,<sup>167</sup> NaNO<sub>3</sub>,<sup>166,167</sup> KNO<sub>3</sub>,<sup>167</sup> (Li, Na, K)F,<sup>167</sup> and some LiF-BeF<sub>2</sub> mixtures.<sup>166,167</sup>

**(iv) Parallel-Plate**

In the parallel-plate method, the heat flux downward is measured by a “fluxmeter” under which the thermal bond material and the molten salt of interest are located.<sup>168</sup> Because the thermal transfer is only conductive if the thermal contacts are perfect, the balance of heat flow through the layers is

$$\lambda_F \Delta T_F / \ell_F = \lambda \Delta T / \ell + h(\delta T + \delta T_F) \quad (105)$$

where  $\ell$  is the thickness of the layer and  $h$  is the heat transfer coefficient; the index F refers to the fluxmeter. In practice, the apparatus is regulated so that the horizontal temperature differences are nil and  $\lambda$  is easily obtained from the measurement of  $\Delta T, \Delta T_F, \ell, \ell_F$  and from the known value of  $\lambda_F$ .

Measurements on  $\text{NaNO}_3$  and  $\text{KNO}_3$  using this method by Santini et al.<sup>168</sup> have been criticized by Nagasaka and Nagashima<sup>169</sup> because this type of steady-state method is only suited for solid materials because of the considerable errors due to convection and other heat losses.

**(v) Laser Flash**

In the laser flash method, the heat is put in by laser flash instead of electric current in the stepwise heating method mentioned above. Thus this method may be classified as a stepwise heating method. A two-layered laser flash method was developed by Tada et al.<sup>170,171</sup> The experimental method and the data analysis, including a case involving radiative heat flow, are described in detail in the review article by Waseda and Ohta.<sup>156,157</sup> A thin metal plate is placed at the surface of a melt. A laser pulse is irradiated onto a metal plate of thickness  $\ell$  having high thermal conductivity. The sample liquid under the metal plate and the inert gas above the plate are designated as the third and first layers, respectively. The temperature of the second layer becomes uniform in a short time<sup>172</sup> and the response thereafter is expressed by

$$T_2(t)/T_0 = \exp(h^2 t) \operatorname{erfc}(h t^{1/2}) \quad (106)$$

$$h = h_a + h_b \quad (107)$$

where

$$h_a = (\rho_s \lambda_s C_{ps})^{1/2} / (\rho_d C_{pd} \ell) \quad (108)$$

$$h_b = (\rho_g \lambda_g C_{pg})^{1/2} / (\rho_d C_{pd} \ell) \tag{109}$$

$$T_0 = Q / (\rho_d C_{pd} \ell) \tag{110}$$

Here,  $Q$  is the heat energy input per area;  $\rho$  and  $C_p$  are the density and specific heat capacity, respectively; and indices  $g$ ,  $d$ , and  $s$  refer to the gas, metal, and liquid sample layers, respectively. With Eq. (106), the thermal conductivity of the sample liquid is obtained from the measured temperature response of the metal without knowing the thermal conductivity of the metal disk and the thickness of the sample liquid. There is no constant characteristic of the apparatus used. Thus, absolute measurement of thermal conductivity is possible, and the thermal conductivities of molten sodium and potassium nitrates have been measured.<sup>171</sup>

The two-layered laser flash method has been applied to some molten systems above 1000 K.<sup>172</sup> In Fig. 30 an example of curve fitting is shown for molten calcium aluminosilicate at 1723 K.<sup>156</sup> An analysis in which the radiative component is taken into account gives a good fit. The thermal conductivity and the radiative component parameter can be determined simultaneously by a curve-fitting procedure.

**(vi) Laser Flash Method—Three-Layer Technique**

In the laser flash method, a melt of interest is placed between two parallel plates. The upper plate is heated stepwise and the thermal diffusivity is measured from the rise in temperature. The specific design for molten materials and especially slags employed by Ohta et al.<sup>173</sup> is based on the differential three-layer technique utilizing a special cell that can be accommodated in the system. A schematic diagram of the principle of the measurement section is shown in Fig. 31. A laser pulse irradiates the upper (platinum) crucible and the temperature response of the surface of the lower platinum crucible is observed, a liquid specimen being sandwiched between the two.

The temperature rise  $\theta$  at the initial time  $t$  for a three-layer system can be given by

$$\partial \ln(\theta t^{1/2}) / \partial(1/t) = -(\alpha_1 + \alpha_2 + \alpha_3)^2 / 4 \tag{111}$$

where  $\alpha_i = \ell_i / D_{Ti}^{1/2}$ . Plotting  $\ln(\theta t^{1/2})$  against  $1/t$  gives a straight line having a slope of  $-(\alpha_1 + \alpha_2 + \alpha_3)^2 / 4$ . Thus, if  $\alpha_1 + \alpha_3$  and  $\ell_2$  are known, the thermal diffusivity of the sample liquid can be determined. This



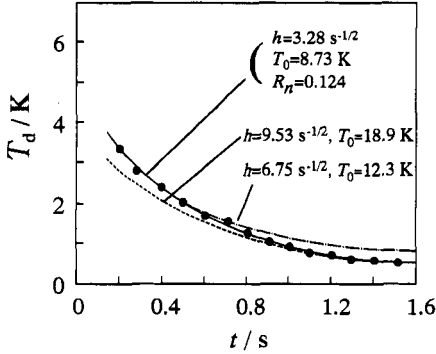


Figure 30. Temperature response curve of CaO-Al<sub>2</sub>O<sub>3</sub>-SiO<sub>2</sub>: 39-14-47 mol.% at 1723 K. (●): experimental values. (—): curve fitting including the radiative component  $R_n = 0.124$ ,  $h = 3.28 \text{ s}^{-1/2}$ , and  $T_0 = 8.73 \text{ K}$ ; (-----) and (- - - - -): curve fitting without thermal radiation effect  $R_n$ . (Reprinted from Y. Waseda and H. Ota, "Current Views on Thermal Conductivity and Diffusivity Measurements of Oxide Melts at High Temperature," *Solid State Ionics* **22**: 263–284, Fig. 21, Copyright © 1987 with permission of Elsevier Science.)

method has been further developed by these authors.<sup>175</sup> For the purpose of accurate measurement of specimen thickness, two runs were performed in which the thicknesses were both  $\ell$  and  $\ell + \Delta\ell$ , where, even if the absolute value of  $\ell$  is not known,  $\Delta\ell$  can be determined accurately with a built-in micrometer. The thermal diffusivity is obtained through curve fitting using a three-layer analysis.

### (vii) Forced Rayleigh Scattering

The force Rayleigh scattering method was developed by Nagashima's group.<sup>175,176</sup> Thermal diffusivity can be measured in a contact-free manner within a time interval of 1 ms, with a small temperature rise of 0.1 K and with a small volume of about 10 mm<sup>3</sup>. The sample needs to be colored by an admixture of a "dye" for suitable absorption of a heating laser beam. The principle is schematically shown in Fig. 32. Two beams of equal intensity divided by means of a beam splitter cross in the sample to create

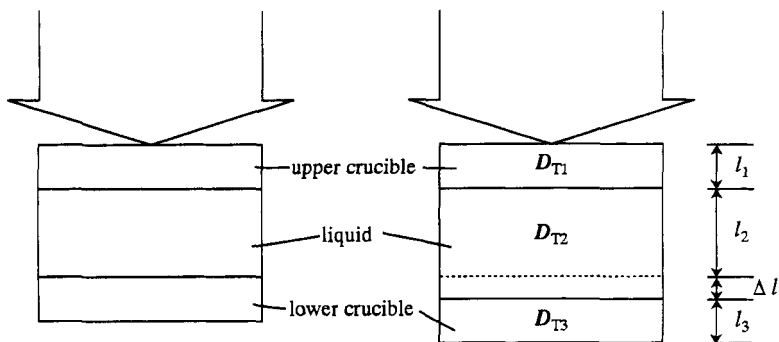


Figure 31. Principle of a devised three-layer technique. (Reprinted from Ref. 175 of Kluwer Academic/Plenum Publishers.)

the interference pattern. The interference pattern induces a corresponding spatially sinusoidal temperature distribution, which acts as an optical phase grating for a low-power probing laser beam. The grating period  $\Lambda$ , sample thickness  $d$ , and absorption coefficient  $\alpha$  can be chosen so that the assumption of one-dimensional heat conduction in the direction of  $x$  is permissible. The decaying temperature profile can be expressed by

$$T(x, t) = T_0 + \Delta T_0 [1 + \cos qx \exp(-t/\tau)] \quad (112)$$

where  $T_0$  is the initial temperature,  $\Delta T_0$  the initial spatial temperature amplitude,  $t$  the elapsed time after heating, and  $q (= 2\pi/\Lambda)$  the wave number of the interference pattern. Equation (112) shows that the spatial temperature amplitude decays exponentially with the relaxation time of heat conduction  $\tau$ ,

$$\tau = (1/D_T)(\Lambda/2\pi)^2 \quad (113)$$

The spatially periodic temperature distribution produces the corresponding refractive index distribution, which acts as an optical phase grating for the low-power probing laser beam of the nonabsorbed wavelength in the sample. The thermal diffusivity is determined by detecting the temporal decay of the first-order diffracted probing beam  $I_1$  [ $\propto \exp(-2t/\tau)$ ] expressed by

$$DT = -(1/2)(\Lambda/2\pi)^2 [d \ln I_1(t)/dt] \quad (114)$$

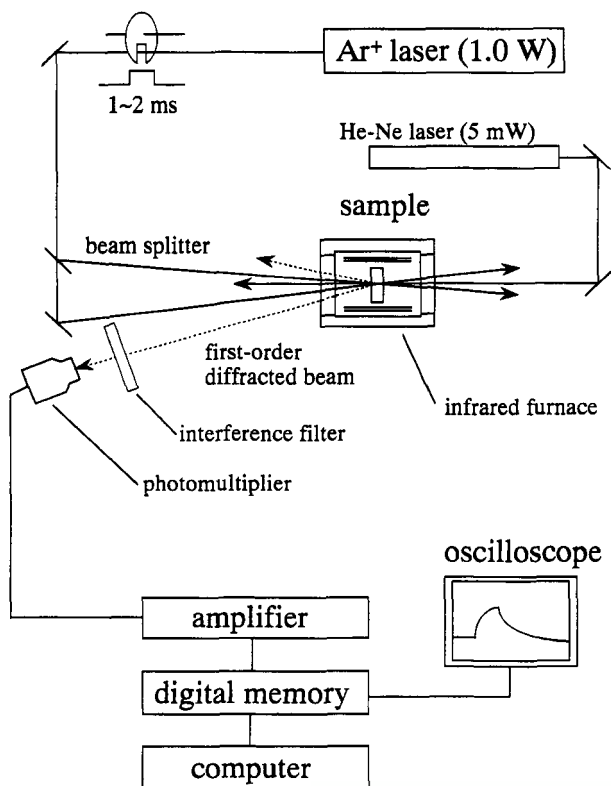


Figure 32. Schematic diagram of the forced Rayleigh scattering method. (Reprinted from Ref. 175 with permission of the American Institute of Physics.)

Nagashima et al. have measured the thermal diffusivity of alkali chlorides<sup>177</sup> bromides,<sup>178</sup> and iodides<sup>179</sup> by this method.

### (viii) Wave-Front Shearing Interferometry

The wave-front shearing interferometric method can be applied to transparent melts which do not attack cell windows made of silicate glass. The principle of this method has been given by Gustafsson.<sup>180</sup> A thin foil is placed vertically, a laser beam passing in the  $y$ -direction along the plane. The heat is transferred in a melt in the direction of  $x$ . The slope of the

temperature  $T(x, y, t) - T(0)$  is related to the refractive index by  $n = n_0 + [T(x, y, t) - T(0)](\partial n/\partial T)$ . The optical length  $R$  for passing the melt of  $2L$  is  $R = \int_{-L}^L n \, dy$ . Solution of the equation of thermal conductivity gives

$$R(x, t) = (2Qd)/\lambda \sqrt{\pi} (\partial n/\partial T) \{ \sqrt{D_T t} \exp(-x^2/4D_T t) - (\sqrt{\pi} x) \operatorname{erfc}(x/2\sqrt{D_T t}) \} \tag{115}$$

where  $\lambda$  is the thermal conductivity,  $D_T$  the thermal diffusivity,  $Q$  the generated heat, and  $d$  the width of the foil. The difference in the optical paths between two beams divided by a distance  $b$  with an optical divider called the *Savart plate* is  $\Delta R = b \, dR/dx$ . The dark interference fringes appear at the positions  $\Delta R = n' \lambda_w$  ( $n'$  being integers) in the  $x$ -direction.

Gustafsson et al.<sup>181</sup> measured the thermal conductivity and thermal diffusivity of molten  $\text{NaNO}_3$  and  $\text{KNO}_3$ . The approximate dimension of the foil used for  $\text{NaNO}_3$  was platinum measuring  $0.010 \times 40 \times 86 \text{ mm}^3$ . The foil was heated by a constant electric current and the measurements were completed within 10 s. Errors due to radiation were considered to be negligible. The accuracy was claimed to be +2.6% for thermal conductivity and  $\pm 3\%$  for thermal diffusivity, but the effect of current leak from the metallic foil to the molten salts was neglected.

If we designate the distances between a pair of fringes appearing at both sides of the foil images as  $x_1, x_2, x_3, \dots$  in ascending order of magnitude, it follows theoretically that  $(x_i/\sqrt{D_T t})$  should be constant, that is

$$\begin{aligned} & \operatorname{erfc}(x_1/2\sqrt{D_T t}) - \operatorname{erfc}(x_2/2\sqrt{D_T t}) \\ & = \operatorname{erfc}(x_2/2\sqrt{D_T t}) - \operatorname{erfc}(x_3/2\sqrt{D_T t}) = \dots \end{aligned} \tag{116}$$

The interference fringes for  $\text{KNO}_3\text{-NaNO}_2$  (0.244-0.756) are shown in Fig. 33.<sup>182</sup> Plots of  $x^2$  as a function of time for a typical experiment using heat transfer salt ( $\text{NaNO}_3\text{-KNO}_3\text{-NaNO}_2$ ; 7-44-49 mol%) are shown in Fig. 34.<sup>183</sup> When convection is not negligible, the plots start to deviate from a straight line. Thus the effect of the convection can be eliminated from the calculation, which is one of the advantages of this method.

This method provides thermal conductivity as well as thermal diffusivity:

$$\lambda = bQd(\partial n/\partial T) \{ \operatorname{erfc}(x_2/4\sqrt{D_T t}) - \operatorname{erfc}(x_1/4\sqrt{D_T t}) \} / \lambda_w \tag{117}$$

Alternatively,  $\lambda$  can be calculated from Eq. (98).

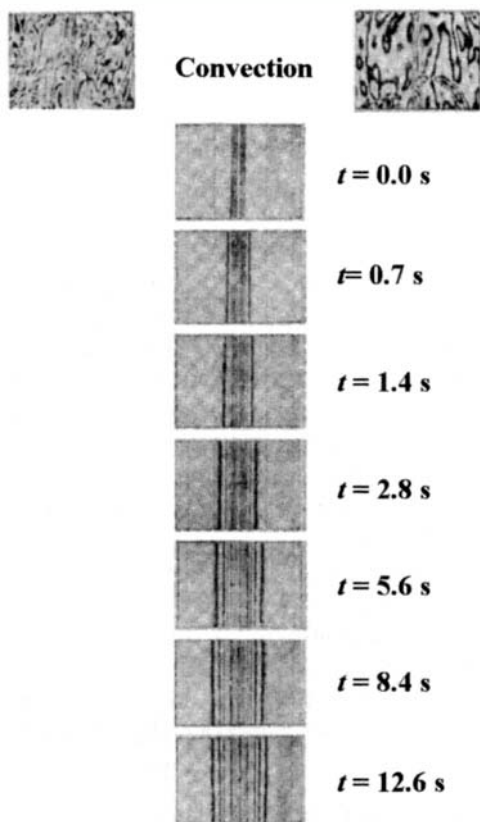


Figure 33. Interference fringes. (Reprinted from Ref. 182 with permission of the Chemical Society of Japan.)

## 2. Evaluation of Experimental Data

Nagasaka and Nagashima<sup>169</sup> have assessed the accuracy of the measurements for molten  $\text{NaNO}_3$  and  $\text{KNO}_3$ , which are stable in a molten state over a rather wide range of temperatures. The general criteria are described in Ref.<sup>184</sup>. Because of the difficulties associated with molten salts, the following factors should also be considered in the assessment: (1) appropriateness of the technique to high-temperature molten salts, (2) the possibility of radiative and convective heat losses, (3) heat losses and any

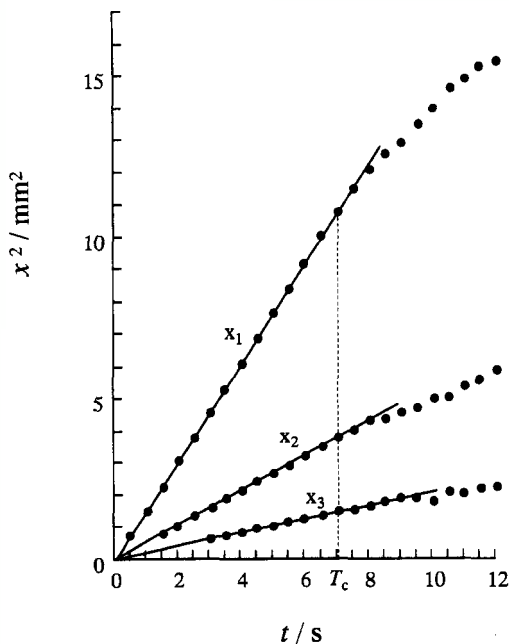


Figure 34. Plots of  $x^2$  as a function of time for a typical experiment in heat-transfer salts at 168°C. (Reprinted from O. Odawara, I. Okada, and K. Kawamura, "Measurement of Thermal Diffusivity of HTS by Optical Interferometry," *J. Chem. Eng. Data* **22**: 222–225, Copyright © 1977 American Chemical Society.)

correction made, (4) whether it is an absolute or a relative method, (5) consistency of data, and (6) purity and treatment of samples.

The data on molten  $\text{NaNO}_3$  are summarized in Table 16. Nagasaka and Nagashima<sup>169</sup> recommended the following empirical relation obtained by the transient hot-wire method with ceramic-coated probes:

$$\lambda = 0.620(3) - 1.8 \times 10^{-4} T, \quad 584 \text{ K} < T < 662 \text{ K} \quad (118)$$

where  $\lambda$  is in  $\text{W m}^{-1}\text{K}^{-1}$ .

In some methods thermal diffusivity rather than thermal conductivity is primarily obtained. No appreciable temperature dependence was found for the thermal diffusivity of molten  $\text{NaNO}_3$ .<sup>166,181,183</sup>

**Table 16**  
**Summary of Thermal Conductivity Measurements of Molten NaNO<sub>3</sub>**

Year	Method	Temperature range (K)	Temperature dependency	Claimed accuracy (%)	Data points	Grade <sup>a</sup>	Ref.
1961	Transient hot wire (without insulation)	582	—	±2.8	1	B	185
1964	Transient hot wire	586–738	—		13	B	186
1965	Concentric cylinder (gap: 0.9 mm)	602–695	—	±5	6	C	187
1967	Concentric cylinder	613–693	$0.288_7 + 4.77_1 \times 10^{-4}T$	±3–5	—	C	188
1968	Optical interferometry	588–727	$0.255_9 + 4.4 \times 10^{-4}T$	±2.6	9	C	181
1970	Concentric cylinder	583–727	$0.402_3 + 2.6_8 \times 10^{-4}T$	±5	—	C	189
1977	Optical interferometry	581–691	—		9		190
1981	Laser flash	593–643	—	±3.8			171
1982	Transient hot wire	588	—	±3	1	A	163
1984	Parallel plate	583–783	$0.28 + 5.0 \times 10^{-4}T$		—	C	168
1985	Concentric cylinder	593–673	—	±4	10	A	191
1989	Transient hot wire (ceramic-coated probe)	584–662	$0.6203 - 1.8 \times 10^{-4}T$	±3	28	A	161
1991	Laser flash (three-layered)						173

<sup>a</sup>The reponed data have been classified into three grades by Nagasaka and Nagashirna<sup>169</sup> grade A, accurate within ±3–4%; grade B, accurate within ±10–15%; and grade C, accurate to less than ±15%. Where a grade is not given here, the work was not cited in Ref. 169.

#### 4. Molecular Dynamics Simulation

The Einstein relation for thermal conductivity is given by<sup>153</sup>

$$\lambda = \lim_{t \rightarrow \infty} (1/6VkT^2t) \left\langle \sum_{i=1}^N [\mathbf{r}_i(t) \bar{E}_i(t) - \mathbf{r}_i(0) \bar{E}_i(0)]^2 \right\rangle \quad (119)$$

where  $\bar{E}_i$  is the instantaneous excess energy of molecule  $i$ :

$$\bar{E}_i = E_i - (1/N) \sum_{j=1}^N E_j \quad (120)$$

where  $E_i$  is the internal energy (kinetic plus potential) of molecule  $i$ . The corresponding Green-Kubo relation is

$$\lambda = (1/3VkT^2) \int_0^{\infty} \langle \mathbf{S}(t) \cdot \mathbf{S}(0) \rangle dt \quad (121)$$

where

$$\mathbf{S}(t) = d \left[ \sum_{i=1}^N \mathbf{r}_i(t) \bar{E}_i(t) \right] / dt \quad (122)$$

Sindzinger and Gillan<sup>150</sup> have calculated the thermal conductivity for NaCl and KCl melts as well as for solids on the basis of MD simulations in full thermal equilibrium using the Green-Kubo relations (Table 17).<sup>87</sup> In a single molten salt system, the local fluxes  $j_z$  and  $j_e$  of charge and energy

**Table 17**  
Simulation Results for the Thermal Conductivity of  
Molten NaCl and KCl<sup>150</sup>

Salt	$T(\text{K})$	$V(\text{cm}^3\text{mol}^{-1})$	$N$	$n(10^4)$	$\lambda(\text{W m}^{-1}\text{K}^{-1})$	$\lambda(\text{W m}^{-1}\text{K}^{-1});$ exp
NaCl	1100	38.01	64	14	0.65±0.06	0.41 <sup>a</sup> , 0.51 <sup>b</sup>
			216	3.8	0.67	
KCl	1096	49.88	64	14	0.41±0.04	0.37 <sup>c</sup> , 0.39 <sup>b</sup>

<sup>a</sup>Ref. 192.

<sup>b</sup>Ref. 177.

<sup>c</sup>Ref. 193; for other data, see Ref. 194.



flux, respectively, are described by the phenomenological transport equations:

$$j_z = -L_{zz} \nabla(\mu_z/kT) - L_{ze} \nabla(-1/kT) \quad (123)$$

$$j_e = -L_{ez} \nabla(\mu_z/kT) - L_{ee} \nabla(-1/kT) \quad (124)$$

where  $\mu_z$  is the electrochemical potential and  $L_s$  are the phenomenological coefficients. The coefficients  $L_{\alpha\beta}$  ( $\alpha, \beta = z, e$ ) can be expressed by

$$L_{\alpha\beta} = (1/3V) \int_0^{\infty} \langle J_{\alpha}(t) \cdot J_{\beta}(0) \rangle dt \quad (125)$$

where  $J_{\alpha}$  represents the total fluxes of charge and energy in the system, and angle brackets indicate the average in full thermal equilibrium. The thermal conductivity is given by

$$\lambda = (L_{ee} - L_{ze}^2/L_{zz})/T^2 \quad (126)$$

Sindzinger and Gillan<sup>150</sup> have made simulations at constant volume and constant temperature on systems containing 64 and 216 ions using the Tosi-Fumi potentials.<sup>50</sup>

Bresme et al.<sup>195</sup> have calculated the thermal diffusivity and thermal conductivity of a model system using nonequilibrium molecular dynamics simulations. The interatomic potentials of the model system are of a Lennard-Jones/spline function with an ionic tail of variable range and magnitude. The range was varied by selecting either a Coulomb or a Yukawa tail, and the magnitude was varied with the ionic charge strength. The thermal conductivity appears to be insensitive to the potential range for ionic systems, but seems to follow a simple law of corresponding states.

## VII. CONCLUSION

Because of the inherent technical difficulties, investigations of transport properties in molten salts are much less common than those of aqueous solutions. However, interpretation of the phenomena seems to be even simpler in molten salts where water is not involved. Molten salt systems are considered to be the simplest liquid electrolytes. Data have been compiled largely due to the great efforts of the Janz group.<sup>3-19</sup>

The studies of the transport properties dealt with in this chapter are in rather different stages of research development. Electrolytic conductivity can be understood on a molecular level for such simple molten salts as alkali halides. Experimentally, electrolytic conductivity can be measured very accurately, and internal mobilities in binary mixtures, which provide useful information, may also be measured accurately. For self-diffusion coefficients, which may be the most fundamental transport coefficients, experimental data are not as abundant nor have they increased much during the past two decades. The study of diffusion coefficients by molecular dynamics simulation is promising in the future. The accuracy of the data calculated in molecular dynamics simulation depends on the quality of the potentials used. Viscosity data are also limited except for slags, where it is needed industrially. Thermal conductivities have not been measured for many systems and the data often seem to involve appreciable errors. At present, a theoretical approach to viscosities and thermal conductivities has not advanced enough. However, these transport coefficients can be calculated and therefore predicted by equilibrium or nonequilibrium molecular dynamics simulation, although the computation time needed is huge except for self-diffusion coefficients. As the computation time is progressively reduced, theoretical aspects of this field will soon likely show progress. On the other hand, a steady improvement is badly needed in the experimental techniques.

### ACKNOWLEDGMENT

We are much indebted to Professor M. Chemla at Université Pierre et Marie Curie for his invaluable suggestions and encouragement.

### REFERENCES

- <sup>1</sup>H. J. V. Tyrrell and K. R. Harris, *Diffusion in Liquids*, Butterworths, London, 1984.
- <sup>2</sup>C. A. Angell, in *Molten Salt Chemistry*, Ed. by G. Marnantov and R. Marassi, NATO ASI Series Vol. 202, 1986, p. 123.
- <sup>3</sup>G. J. Janz, F. W. Dampier, and P. K. Lorenz, *Molten Salts, Vol. 1: Electrical Conductance, Density, and Viscosity Data*, U.S. Dept. of Commerce, National Bureau of Standards, NBS-NSRDS-15, Washington, DC, 1968.
- <sup>4</sup>G. J. Janz, Chr. G. M. Dijkhuis, G. R. Lakshminarayanan, R. P. T. Tomkins, and J. Wong, *Molten Salts Handbook, Vol. 2: Thermodynamics and Surface Tensions*, U.S. Dept. of Commerce, National Bureau of Standards, NBS-NSRDS-28, Washington, DC, 1969.
- <sup>5</sup>G. J. Janz, U. Krebs, H. Siegenthaler, and R. P. T. Tomkins, *J. Phys. Chem. Ref. Data* **1** (1972) 581; *Molten Salts, Vol. 2: Physical Properties of Nitrates, Nitrites and Mixtures*,

- American Chemical Society-American Institute of Physics-National Bureau of Standards, Washington, DC, 1972.
- <sup>6</sup>G. J. Janz, G. Gardener, U. Krebs, and R. P. T. Tomkins, *J. Phys. Chem. Ref: Data* **3** (1974) 115; *Molten Salts*, Vol. 4, Part 1: *Fluorides: Electrical Conductance, Density, viscosity and Surface Tension Data*, American Chemical Society-American Institute of Physics-National Bureau of Standards, Washington, DC, 1974.
- <sup>7</sup>G. J. Janz, R. P. T. Tomkins, C. B. Allen, J. R. Downey, Jr., G. L. Gardener, U. Krebs, and K. Singer, *J. Phys. Chem. Ref: Data* **4** (1975) 871; *Molten Salts*, Vol. 4, Part 2: *Chloride Mixtures*, American Chemical Society-American Institute of Physics-National Bureau of Standards, Washington, DC, 1975.
- <sup>8</sup>G. J. Janz, R. P. T. Tomkins, C. B. Allen, J. R. Downey, Jr., and K. Singer, *J. Phys. Chem. Ref: Data* **6** (1977) 409; *Molten Salts*, Vol. 4, Part 3: *Bromides and Mixtures: Iodides and Mixtures*, American Chemical Society-American Institute of Physics-National Bureau of Standards, Washington, DC, 1977.
- <sup>9</sup>G. J. Janz, R. P. T. Tomkins, and C. B. Allen, *J. Phys. Chem. Ref: Data* **8** (1979) 125; *Molten Salts*, Vol. 4, Part 4: *Mixed Halide Melts*, American Chemical Society-American Institute of Physics-National Bureau of Standards, Washington, DC, 1979.
- <sup>10</sup>G. J. Janz and R. P. T. Tomkins, *J. Phys. Chem. Ref: Data* **9** (1980) 831; *Molten Salts*, Vol. 5, Part 1: *Additional Single and Multi-Component Salt Systems*, American Chemical Society-American Institute of Physics-National Bureau of Standards, Washington, DC, 1980.
- <sup>11</sup>G. J. Janz and R. P. T. Tomkins, *J. Phys. Chem. Ref: Data* **12** (1983) 591; *Molten Salts*, Vol. 5, Part 2: *Additional Multi-Component Salt Systems*, American Chemical Society-American Institute of Physics-National Bureau of Standards, Washington, DC, 1980.
- <sup>12</sup>G. J. Janz, *J. Phys. Chem. Ref: Data* **17**, Supplement (1988); *Thermodynamic and Transport Properties for Molten Salts: Correlation Equations for Critically Evaluated Density, Surface Tension, Electrical Conductance and Viscosity Data*, American Chemical Society-American Institute of Physics-National Bureau of Standards, Washington, DC, 1988.
- <sup>13</sup>G. J. Janz and N. P. Bansal, *J. Phys. Chem. Ref.* **11** (1982) 505; *Molten Salts Diffusion Coefficients in Single and Multi-Component Salt Systems*, American Chemical Society-American Institute of Physics-National Bureau of Standards, Washington, DC, 1982.
- <sup>14</sup>G. J. Janz, C. B. Allen, N. P. Bansal, R. M. Murphy, and R. P. T. Tomkins, *Physical Properties Data Compilations Relevant to Energy Storage, Molten Salts: Data on Single and Multi-Component Salt Systems*, U.S. Dept. of Commerce, National Bureau of Standards, NBS-NSRDS-61, Washington, DC, 1979.
- <sup>15</sup>G. J. Janz and R. P. T. Tomkins, *Physical Properties Data Compilations Relevant to Energy Storage, Molten Salts: Data on Additional Single and Multi-Component Salt Systems*, U.S. Dept. of Commerce, National Bureau of Standards, NBS-NSRDS-61, Washington, DC, 1981.
- <sup>16</sup>G. J. Janz, *J. Phys. Chem. Ref: Data* **9** (1980) 791; *Molten Salts Data as Reference Standards for Density, Surface Tension, viscosity and Electrical Conductance: KNO<sub>3</sub> and NaCl*, American Chemical Society-American Institute of Physics-National Bureau of Standards, Washington, DC, 1980.
- <sup>17</sup>G. J. Janz, *Mater: Sci. Forum* **73-75** (1991) 707.
- <sup>18</sup>G. J. Janz and R. D. Reeves, in *Advances in Electrochemistry and Electrical Engineering* Vol. 5, Ed. by P. Delahay and C. W. Tobias, Interscience, New York, 1967.
- <sup>19</sup>G. J. Janz, *Molten Salts Handbook*, Academic Press, New York, 1967.
- <sup>20</sup>M. P. Tosi, *Z. Phys. Chem. (München)* **184** (1994) 139.
- <sup>21</sup>D. G. Pettifor, *Solid State Commun.* **51** (1984) 31; *J. Phys. C: Solid State Phys.* **19** (1986) 285.
- <sup>22</sup>B. E. Markov, *Dokl. Akad. Nauk SSSR* **110** (1956) 441.

- <sup>23</sup>A. Klemm, in *Advances in Molten Salt Chemistry*, Vol. 6, Ed. by G. Marnantov, C. B. Mamantov and J. Braunstein, Elsevier, Amsterdam, 1987, p. 1.
- <sup>24</sup>M. Chemla and A. Bonnin, *C. R. Acad. Sci.* **241** (1955) 1288.
- <sup>25</sup>F. Lantelme and M. Chemla, *Bull. Soc. Chim. Fr.* (1963) 2200.
- <sup>26</sup>A. Klemm, H. Hintenberger, and P. Hoerness, *Z. Naturforsch.* **2a** (1947) 245.
- <sup>27</sup>J. Habasaki and I. Okada, *Z. Naturforsch.* **40a** (1985) 906.
- <sup>28</sup>A. Endoh and I. Okada, *Z. Naturforsch.* **43a** (1988) 638.
- <sup>29</sup>I. Okada, *Z. Naturforsch.* **33a** (1978) 498.
- <sup>30</sup>I. Okada, R. Takagi, and K. Kawamura, *Z. Naturforsch.* **34a** (1979) 498.
- <sup>31</sup>M. Chemla and I. Okada, *Electrochim. Acta* **35** (1990) 1761.
- <sup>32</sup>R. Takagi, I. Okada, and K. Kawamura, unpublished.
- <sup>33</sup>A. Kvist, *Z. Naturforsch.* **21a** (1966) 1221.
- <sup>34</sup>V. Ljubimov and A. Lundén, *Z. Naturforsch.* **21a** (1966) 1592.
- <sup>35</sup>C. Yang, O. Odawara, and I. Okada, *J. Electrochem. Soc.* **136** (1989) 120.
- <sup>36</sup>G. Poillerat and J. Brenet, *J. Chim. Phys.* **76** (1979) 67.
- <sup>37</sup>J. Richter and A. Seifert, *Z. Naturforsch.* **41a** (1986) 545.
- <sup>38</sup>H.-P. Bossmann, A. Hildebrandt, and J. Richter, *Z. Naturforsch.* **41a** (1986) 1192.
- <sup>39</sup>H. Matsuura and I. Okada, *Denki Kagaku* **61** (1993) 732.
- <sup>40</sup>C. Yang, R. Takagi, K. Kawamura, and I. Okada, *Electrochim. Acta* **32** (1987) 1607.
- <sup>41</sup>M. Chemla, Commissariat à l'Énergie Atomique, Brevet D'Invention, France No. 1216418 (1960).
- <sup>42</sup>J. Périé and M. Chemla, *C. R. Acad. Sci.* **250** (1960) 3986.
- <sup>43</sup>C. T. Moynihan, *Ionic Interactions*, Vol. 1, Ed. by S. Petrucci, Academic Press, New York, 1971, p. 261.
- <sup>44</sup>S. I. Smedley, *The Interpretation of Ionic Conductivity in Liquids*, Plenum Press, New York, 1980, p. 171.
- <sup>45</sup>A. Endoh and I. Okada, *J. Electrochem. Soc.* **137** (1990) 933.
- <sup>46</sup>I. Okada, R. Takagi, and K. Kawamura, *Z. Naturforsch.* **35a** (1980) 493.
- <sup>47</sup>I. Okada, S. Okazaki, H. Horinouchi, and Y. Miyamoto, *Mater. Sci. Forum* **73-75** (1991) 175.
- <sup>48</sup>Y. Miyamoto, S. Okazaki, O. Odawara, I. Okada, M. Misawa, and T. Fukunaga, *Mol. Phys.* **82** (1994) 887.
- <sup>49</sup>I. Okada, *Z. Naturforsch.* **42a** (1987) 21.
- <sup>50</sup>M. P. Tosi and F. G. Fumi, *J. Phys. Chem. Solids* **25** (1964) 45.
- <sup>51</sup>J. T. W. M. Tissen, G. J. M. Janssen, and J. P. van der Erden, *Mol. Phys.* **82** (1994) 101.
- <sup>52</sup>J. T. W. M. Tissen, Thesis, University of Utrecht, 1992.
- <sup>53</sup>I. Okada, R. Takagi, and K. Kawamura, *Z. Naturforsch.* **36a** (1981) 381.
- <sup>54</sup>I. Okada and H. Horinouchi, *J. Electroanal. Chem.* **396** (1995) 547.
- <sup>55</sup>R. D. Shannon, *Acta Cryst.* **A32** (1976) 751.
- <sup>56</sup>I. Okada and P.-H. Chou, *J. Electrochem. Soc.* **144** (1997) 1332.
- <sup>57</sup>M. Bucher, *Phys. Rev.* **30B** (1984) 947.
- <sup>58</sup>H. Ohno, K. Igarashi, N. Umesaki, and K. Furukawa, *X-Ray Diffraction Analysis of Ionic Liquids*, Trans. Tech. Publications, Aedemansdorf, Switzerland, 1994.
- <sup>59</sup>M. Blander, *Molten Salt Chemistry*, Ed. by M. Blander, Interscience, New York, 1964, p. 127.
- <sup>60</sup>H. Matsuura and I. Okada, *Z. Naturforsch.* **49a** (1994) 690.
- <sup>61</sup>H. Matsuura, I. Okada, Y. Iwadate, and J. Mochinaga, *J. Electrochem. Soc.* **143** (1996) 334.
- <sup>62</sup>R. W. G. Wyckoff, *Crystal Structure*, Vol. 2, Interscience, New York, 1964, pp. 57 and 78.
- <sup>63</sup>M.-L. Saboungi, D. L. Price, C. Scamehorn, and M. P. Tosi, *Europhys. Lett.* **15** (1991) 283.
- <sup>64</sup>G. N. Papatheodorou, *J. Chem. Phys.* **66** (1977) 2893.

- <sup>65</sup>G. N. Papatheodorou, *Inorg. Nucl. Chem. Lett.* **11** (1975) 483.
- <sup>66</sup>J. Mochinaga, Y. Iwadate, and K. Fukushima, *Mater. Sci. Forum* **73-75** (1991) 147.
- <sup>67</sup>J. Mochinaga, Y. Miyagi, K. Igarashi, K. Fukushima, and Y. Iwadate, *Nippon Kagaku Kaishi* (1993) 459.
- <sup>68</sup>K. Igarashi and J. Mochinaga, *Z. Naturforsch.* **42a** (1987) 777.
- <sup>69</sup>K. Fukushima, Y. Iwadate, Y. Andou, T. Kawashima, and J. Mochinaga, *Z. Naturforsch.* **46a** (1991) 1055.
- <sup>70</sup>T. Koura, H. Matsuura, and I. Okada, *J. Mol. Liq.* **73-74** (1997) 195.
- <sup>71</sup>H. Matsuura, I. Okada, R. Takagi, and Y. Iwadate, *Z. Naturforsch.* **53a** (1998) 45.
- <sup>72</sup>J. L. Copeland, *Transport Properties of Ionic Liquids*, Gordon and Breach, New York, 1974.
- <sup>73</sup>J. Périć, M. Chemla, and M. Gignoux, *Bull. Soc. Chim. Fr.* (1961) 1249.
- <sup>74</sup>F. Lantelme, Thesis, University of Paris, 1965.
- <sup>75</sup>A. Klemm, *Z. Naturforsch.* **39a** (1984) 471.
- <sup>76</sup>A. Klemm and L. Schäfer, *Z. Naturforsch.* **51a** (1996) 1229.
- <sup>77</sup>V. Danek, *Chem. Papers* **43** (1989) 25.
- <sup>78</sup>M. Chrenkova and V. Danek, *Chem. Papers* **44** (1990) 329.
- <sup>79</sup>M. Olteanu and P. M. Pavel, *Rev. Roum. Chim.* **40** (1995) 927.
- <sup>80</sup>M. V. Smirnov, K. A. Aleksandrov, and V. A. Khokhlov, *Electrochim. Acta* **22** (1977) 543.
- <sup>81</sup>L. V. Woodcock, *Advances in Molten Salt Chemistry*, Vol. 3, Ed. by J. Braunstein, G. Mamantov, and G. P. Smith, Plenum Press, New York, 1975, p. 1.
- <sup>82</sup>K. Singer, *Computational Methods in Classical and Quantum Physics, The Many-Body Problem in Statistical Mechanics*, Ed. by M. B. Hooper, Advance Pub., London, 1976, p. 289.
- <sup>83</sup>K. Kawamura and I. Okada, *Atomic Energy Rev.* **16** (1978) 209.
- <sup>84</sup>D. Adams and G. Hills, *Ionic Liquids*, Ed. by D. Inman and D. G. Lovering, Plenum Press, New York and London, 1981, p. 27.
- <sup>85</sup>N. H. March and M. P. Tosi, *Coulomb Liquids*, Academic Press, London, 1984.
- <sup>86</sup>M. Rovere and M. P. Tosi, *Rep. Prog. Phys.* **49** (1986) 1001.
- <sup>87</sup>R. Kubo, *J. Phys. Soc. Jpn.* **12** (1957) 570.
- <sup>88</sup>A. Klemm, *Z. Naturforsch.* **32a** (1977) 927.
- <sup>89</sup>G. Ciccotti, G. Jacucci, and I. R. McDonald, *Phys. Rev.* **13A** (1976) 426.
- <sup>90</sup>I. Okada, A. Endoh, and S. Baluja, *Z. Naturforsch.* **46a** (1991) 148.
- <sup>91</sup>I. Okada and R. Takagi, *Z. Naturforsch.* **36a** (1981) 378.
- <sup>92</sup>I. Okada, *Z. Naturforsch.* **39a** (1984) 880.
- <sup>93</sup>D. G. Miller, *J. Phys. Chem.* **70** (1966) 2639.
- <sup>94</sup>B. R. Sundheim, *Fused Salts*, Ed. by B. R. Sundheim, McGraw-Hill, New York, 1964, p. 165.
- <sup>95</sup>J. Lesko, *Chem. Listy* **69** (1975) 956.
- <sup>96</sup>P. L. Spedding, *Rev. Pure Appl. Chem.* **21** (1971) 1.
- <sup>97</sup>F. van der Graaf, Thesis, Amsterdam, 1981.
- <sup>98</sup>R. W. Laity and J. D. E. McIntyre, *J. Am. Chem. Soc.* **17** (1965) 3806.
- <sup>99</sup>A. Testa and W. Reinmuth, *Anal. Chem.* **33** (1961) 485.
- <sup>100</sup>A. V. Volkovich, *Melts* **7** (1993) 106.
- <sup>101</sup>S. E. Gustafsson, L.-E. Wallin, and T. E. G. Arvidsson, *Z. Naturforsch.* **23a** (1968) 1261.
- <sup>102</sup>T. E. G. Arvidsson, S.-Å. Afsenius, and S. E. Gustafsson, *J. Chem. Phys.* **53** (1970) 2621.
- <sup>103</sup>T. E. G. Arvidsson, S.-Å. Afsenius, and S. E. Gustafsson, *Z. Naturforsch.* **26a** (1971) 752.
- <sup>104</sup>I. Okada and S. E. Gustafsson, *Electrochim. Acta* **18** (1973) 275.
- <sup>105</sup>O. Odawara, I. Okada, and K. Kawamura, *Z. Naturforsch.* **34a** (1979) 504.
- <sup>106</sup>C. Herdlicka, J. Richter, and M. D. Zaidler, *Z. Naturforsch.* **43a** (1988) 1075.
- <sup>107</sup>A. S. Dworkin, R. B. Escue, and E. R. Van Artsdalen, *J. Phys. Chem.* **64** (1960) 872.
- <sup>108</sup>R. Mills, *J. Phys. Chem.* **77** (1973) 685.

- <sup>109</sup>E. R. van Artsdalen, D. Brown, A. S. Dworkin, and F. J. Miller, *J. Am. Chem. Soc.* **78** (1956) 1772.
- <sup>110</sup>F. Lantelme and M. Chemla, *Bull. Soc. Chim. Fr.* (1963) 969.
- <sup>111</sup>C. A. Angell and J. W. Tomlinson, *Disc. Faraday Soc.* **32** (1961) 237.
- <sup>112</sup>A. Bogacz and T. Niewodniczanski, *Pr: Nauk. Inst. Nevg. Metal. Pierw. Pzad. Polit. Wroclaw* **31** (1976) 153.
- <sup>113</sup>S. B. Tricklebank, L. Nanis, and J. O'M. Bockris, *Rev. Sci. Instrum.* **35** (1964) 807.
- <sup>114</sup>M. K. Nagarajan, L. Nanis, and J. O'M. Bockris, *J. Phys. Chem.* **68** (1964) 2726.
- <sup>115</sup>M. K. Nagarajan and J. O. M. Bockris, *J. Phys. Chem.* **70** (1966) 1845.
- <sup>116</sup>H. H. Emons, G. Braeutigam, and A. Winger, *Chem. Zvesti* **32** (1978) 776; *Z. Chem.* **16** (1976) 164.
- <sup>117</sup>S. Zuca and M. Constantinescu, *Rev. Roum. Chim.* **17** (1972) 385.
- <sup>118</sup>J. A. A. Ketelaar and E. P. Honig, *J. Phys. Chem.* **68** (1964) 1596; *Trans. Faraday Soc.* **62** (1966) 190.
- <sup>119</sup>J. C. T. Kwak and J. A. A. Ketelaar, *J. Phys. Chem.* **73** (1969) 94.
- <sup>120</sup>S. Forcheri and V. Wagner, *Z. Naturforsch.* **22a** (1967) 1171.
- <sup>121</sup>B. B. Mandelbrot, *The Fractal Geometry of Nature*, Freeman, New York, 1977.
- <sup>122</sup>A. Bunde and S. Havlin, *Fractals and Disordered Systems*, 2nd ed., Springer Verlag, Berlin, 1996.
- <sup>123</sup>M. Kobayashi and F. Shimojo, *J. Phys. Soc. Jpn.* **60** (1991) 4076.
- <sup>124</sup>K. C. Mills, Viscosities of Molten Slags, National Physical Laboratory, Teddington, (A)55, 1992.
- <sup>125</sup>K. Tørklep and H. A. Øye, *J. Phys. E: Sci. Instrum.* **12** (1979) 875.
- <sup>126</sup>J. Kestin and G. E. Newell, *Z. Angew. Math. Phys.* **8** (1957) 433.
- <sup>127</sup>Y. Abe, O. Kosugiyama, H. Miyajima, and A. Nagashima, *J. Chem. Soc. Faraday I*, **76** (1980) 2531.
- <sup>128</sup>W. Brockner, K. Tørklep, and H. A. Dye, *Ber: Bunsenges. Phys. Chem.* **83** (1979) 1.
- <sup>129</sup>V. P. Beskachko, G. P. Vyatkin, E. A. Utkin, and A. I. Shcheka, *Metals* **5** (1991) 114.
- <sup>130</sup>Y. Sato, T. Yamamura, H. Zhu, M. Endo, T. Yamazaki, H. Kato, T. Ejima and G. J. Janz, *Proceedings of the Third International Symposium on Carbonate Fuel Cell Technology*, Ed. by D. Shores, H. Maru, I. Uchida, and J. R. Selman, The Electrochemical Society, Pennington, NJ, 1993, p. 416.
- <sup>131</sup>R. Roscoe, *Proc. Phys. Soc.* **72** (1958) 576.
- <sup>132</sup>J. O'M. Bockris and D. C. Lowe, *J. Sci. Inst.* **30** (1953) 403.
- <sup>133</sup>C. T. Moynihan and S. Cantor, *J. Chem. Phys.* **48** (1968) 115.
- <sup>134</sup>S. Cantor, W. T. Ward, and C. T. Moynihan, *J. Chem. Phys.* **50** (1968) 2874.
- <sup>135</sup>T. Ejima, K. Shimakage, Y. Sato, H. Okuda, N. Kumada, and A. Ishigaki, *Nippon Kagaku Kaishi* 1982, p. 961.
- <sup>136</sup>C. H. Herty, *Stahl u Eisen* **54** (1934) 610.
- <sup>137</sup>C. H. Herty, *Stahl u Eisen* **56** (1936) 165.
- <sup>138</sup>H. J. Krabiell, *Stahl u Eisen* **64** (1944) 399.
- <sup>139</sup>K. E. Herzfeld and T. R. Litovitz, *Absorption and Dispersion of Ultrasonic Waves*, Academic Press, New York, 1959.
- <sup>140</sup>H.-M. Zhu, T. Saito, Y. Sato, T. Yamamura, K. Shimakage, and T. Ejima, *J. Jpn Inst. Metals* **55** (1991) 937.
- <sup>141</sup>V. I. Minchenko and M. V. Smirnov, *Rasplavy* (1991) 58.
- <sup>142</sup>V. I. Minchenko and M. V. Smirnov, *Rasplavy* (1992) 54.
- <sup>143</sup>H.-M. Zhu, T. Saito, Y. Sato, T. Yamamura, and T. Ejima, *Proc. 2nd. Asian Thermophysical Prop. Conf* 1989, p. 555.
- <sup>144</sup>A. Nagashima, *Appl. Mech. Rev.* **41** (1988) 113.
- <sup>145</sup>A. Kisluk, S. Loheider, A. Sokolov, M. Soltwisch, D. Quitmann, E. Shasha, and A. Voronel, *Phys. Rev.* **52** (1995) R13083.

- <sup>146</sup>T. Kato and T. Takenaka, *J. Chem. Phys.* **84** (1986) 3405.
- <sup>147</sup>M. H. Brooker and G. N. Papatheodorou, *Advances in Molten Salt Chemistry*, Vol. 5, Ed. by G. Mamantov and C. B. Mamantov, Elsevier, New York, 1983, p. 26.
- <sup>148</sup>M. P. Allen and D. J. Tildesley, *Computer Simulation of Liquids*, Oxford-Clarendon, Oxford, 1987.
- <sup>149</sup>W. D. Monnery, W. Y. Svrcek, and A. K. Mehrotra, *Can. J. Chem. Eng.* **73** (1995) 3.
- <sup>150</sup>P. Sindzinger and M. J. Gillan, *J. Phys.: Condens. Matter* **2** (1990) 7033.
- <sup>151</sup>R. E. Young and J. O'Connell, *Ind. Eng. Chem. Fundam.* **10** (1971) 418.
- <sup>151</sup>J. F. Jal, J. Dupuy, G. Chaussemy, A. Kaddoun, and J. Fornazero, *J. Physique Coll.* **41** (1980) C8 367.
- <sup>153</sup>P. T. Cummings and D. J. Evans, *Ind. Eng. Chem. Res.* **31** (1992) 1237.
- <sup>154</sup>R. P. Tye, *High Temp. High Press.* **24** (1992) 597.
- <sup>155</sup>S. K. Ratkje, *Electrochim. Acta* **36** (1991) 661.
- <sup>156</sup>Y. Waseda and H. Ohta, *Solid State Ionics* **22** (1987) 263.
- <sup>157</sup>H. Ohta and Y. Waseda, in *Molten Salt Techniques* Vol. 4, Ed. by R. J. Gale and D. G. Lovering, Plenum Press, New York, 1991, p. 83.
- <sup>158</sup>J. W. Cooke, *ORNL-4831* (1973).
- <sup>159</sup>Y. Nagasaka and A. Nagashima, *J. Phys. E: Sci. Instrum.* **14** (1981) 1435.
- <sup>160</sup>T. Karasawa, Y. Nagasaka, and A. Nagashima, *Trans. Japan Soc. Mech. Eng.* **B52** (1986) 940.
- <sup>161</sup>S. Kitade, Y. Kobayashi, Y. Nagasaka, and A. Nagashima, *High Temp. High Press.* **21** (1989) 219.
- <sup>162</sup>M. Hoshi, T. Omotani, and A. Nagashima, *Rev. Sci. Instrum.* **52** (1981) 755.
- <sup>163</sup>T. Omotani, Y. Nagasaka, and A. Nagashima, *Int. J. Thermophys.* **3** (1982) 17.
- <sup>164</sup>T. Omotani and A. Nagashima, *J. Chem. Eng. Data* **29** (1984) 1.
- <sup>165</sup>R. M. DiGiulio and A. S. Teja, *Int. J. Thermophys.* **13** (1992) 575.
- <sup>166</sup>Y. Kato, K. Kobayashi, N. Araki, and K. Furukawa, *J. Phys.* **E10** (1977) 921.
- <sup>167</sup>Y. Kato, K. Kobayashi, N. Araki, and K. Furukawa, *High Temp. High Press.* **15** (1983) 191.
- <sup>168</sup>R. Santini, L. Tadrst, J. Pantaloni, and P. Cerisier, *Int. J. Heat Mass Transfer*, **27** (1984) 623.
- <sup>169</sup>Y. Nagasaka and A. Nagashima, *Int. J. Thermophys.* **12** (1991) 769.
- <sup>170</sup>Y. Tada, M. Harada, M. Taniguchi, and W. Eguchi, *Rev. Sci. Instrum.* **49** (1978) 1305.
- <sup>178</sup>Y. Tada, M. Harada, M. Tanigaki, and W. Eguchi, *Ind. Eng. Chem. Fundam.* **20** (1981) 333.
- <sup>178</sup>T. Sakuraya, T. Emi, H. Ohta, and Y. Waseda, *Jpn. Inst. Metals* **46** (1982) 1131.
- <sup>173</sup>H. Ohta, G. Ogura, Y. Waseda, and M. Suzuki, *Rev. Sci. Instrum.* **61** (1990) 2645.
- <sup>174</sup>Y. Maeda, H. Sagara, R. P. Tye, M. Masuda, H. Ohta, and Y. Waseda, *Int. J. Thermophys.* **17** (1996) 253.
- <sup>175</sup>Y. Nagasaka, T. Hatakeyama, M. Okuda, and A. Nagashima, *Rev. Sci. Instrum.* **59** (1988) 1156.
- <sup>176</sup>Y. Nagasaka and A. Nagashima, *Int. J. Thermophys.* **9** (1988) 923.
- <sup>177</sup>Y. Nagasaka, N. Nakazawa, and A. Nagashima, *Int. J. Thermophys.* **13** (1992) 555.
- <sup>178</sup>N. Nakazawa, Y. Nagasaka, and A. Nagashima, *Int. J. Thermophys.* **13** (1992) 753.
- <sup>178</sup>N. Nakazawa, Y. Nagasaka, and A. Nagashima, *Int. J. Thermophys.* **13** (1992) 763.
- <sup>180</sup>S. E. Gustafsson, *Z. Naturforsch.* **22a** (1967) 1005.
- <sup>181</sup>S. E. Gustafsson, N. O. Halling, and R. A. E. Kjellander, *Z. Naturforsch.* **23a** (1968) 44.
- <sup>182</sup>Y. Iwadata, I. Okada, and K. Kawamura, *Nippon Kagaku Kaishi* (1992) 969.
- <sup>183</sup>O. Odawara, I. Okada, and K. Kawamura, *J. Chem. Eng. Data* **22** (1977) 222.
- <sup>184</sup>C. A. Nieto de Castro, S. F. Y. Li, A. Nagashima, R. D. Trengove, and W. A. Wakeham, *J. Phys. Chem. Ref Data* **15** (1986) 1073.
- <sup>185</sup>A. G. Turnbull, *Aust. J. Appl. Sci.* **12** (1961) 30,324.
- <sup>186</sup>E. McLaughlin, *Chem. Rev.* **64** (1964) 389.

- <sup>187</sup>H. Bloom, A. Doroszowski, and S. B. Tricklebank, *Aust. J. Chem.* **18** (1965) 1171.
- <sup>188</sup>L. R. White and H. T. Davis, *J. Chem. Phys.* **47** (1967) 5433.
- <sup>189</sup>J. McDonald and H. T. Davis, *J. Phys. Chem.* **74** (1970) 725.
- <sup>190</sup>O. Owadara, I. Okada, and K. Kawamura, *J. Chem. Eng. Data* **22** (1977) 222.
- <sup>191</sup>R. Tufeu, J. P. Petite, L. Denielou, and B. Le Neindre, *Int. J. Thermophys.* **6** (1985) 315.
- <sup>192</sup>V. D. Golyshev, M. A. Gonik, V. A. Petrov, and Yu M. Putlin, *Teplofiz. Vys. Temp.* **21** (1983) 899; Engl. Transl. *High Temp.* **21** (1983) 684.
- <sup>193</sup>J. McDonald and H. T. Davis, *Phys. Chem. Liq.* **2** (1971) 119.
- <sup>194</sup>Y. Nagasaka and A. Nagashima, *Int. J. Thermophys.* **14** (1993) 923.
- <sup>195</sup>F. Bresme, B. Hafskjold, and I. Wold, *J. Phys. Chem.* **100** (1996) 1879.



*This page intentionally left blank.*

# **Application of Electrochemical Techniques to the Study of Microbiologically Influenced Corrosion**

Brenda J. Little and Patricia A. Wagner

*Naval Research Laboratory, Stennis Space Center Mississippi*

## **I. INTRODUCTION**

Microbiologically influenced corrosion (MIC) caused by the presence and activities of microorganisms on metal surfaces leads to changes in rates and types of electrochemical reactions involved in corrosion processes. Microorganisms on metal surfaces produce highly localized changes in concentration of electrolytes, pH, and oxygen, leading to differential pitting cells, underdeposit, or crevice corrosion of passive metals. MIC can also result in selective dealloying, enhanced erosion, and enhanced galvanic corrosion. Electrochemical techniques, including measurements of redox potential, polarization resistance, corrosion potential, electrochemical impedance, electrochemical noise, and polarization curves have been applied to the study of metals exposed to seawater, fresh water, demineralized water, process chemicals, foodstuffs, soils, crude and distillate fuels, human plasma, and sewage. This chapter reviews biofilm formation, MIC mechanisms, and modern electrochemical techniques used for mechanistic studies and monitoring.

### **1. Biofilm Formation**

In aquatic environments, microbial cells attach to solids, including metals. Immobilized cells grow, reproduce, and produce extracellular polymers,

*Modern Aspects of Electrochemistry, Number 34*, edited by John O'M. Bockris *et al.*  
Kluwer Academic /Plenum Publishers, New York, 2001.

forming a matrix termed a *biofilm*. Biofilm formation consists of a sequence of steps and begins with adsorption of macromolecules (proteins, polysaccharides, and humic acids) and smaller molecules (fatty acids, lipids) at surfaces. Adsorbed molecules form conditioning films that alter physicochemical characteristics of the interface, including surface hydrophobicity and electrical charge. The amount of organic material adsorbed is a function of ionic strength and can be enhanced on metal surfaces by polarization.

During initial stages of biofilm formation, the major factor controlling the rate of colonization is hydrodynamics. Microbial colonization begins with transport of microorganisms to the interface and is mediated by at least three mechanisms: (1) diffusive transport due to Brownian motion, (2) convective transport due to the liquid flow, and (3) active movement of motile bacteria near the interface. The influence of convective transport exceeds the other two by several orders of magnitude. Once the microbial cell is in contact with a surface, it may or may not adhere. The ratio of cells adhering to a surface to the cells transported to the surface depends on surface properties, the physiological state of the organisms, and hydrodynamics near the surface.

Microbial cells transported with the stream of fluid above the surface interact with conditioning films. Immediately after attachment, microorganisms initiate production of slimy adhesive substances, predominantly exopolysaccharides (EPS) that assist the formation of microcolonies and microbial films. EPS create bridges for microbial cells to the substratum and permit negatively charged bacteria to adhere to both negatively and positively charged surfaces. EPS may also control interfacial chemistry at the mineral/biofilm interface.

Biofilm accumulation at surfaces is an autocatalytic process. Initial colonization increases surface irregularity and promotes further biofilm formation. Increased surface irregularity due to biofilm formation can influence particle transport and attachment rate by (1) increasing convective mass transport near the surface, (2) providing shelter from shear forces, and (3) increasing the surface area for attachment. Biofilm accumulation is the net result of attachment, growth, decay, and detachment. Attachment is due to microbial transport and subsequent binding to surfaces. Growth is due to microbial replication, and the growth rate is traditionally described by Monod kinetics:

$$\mu = \frac{\mu_{\max} * S}{K_s + S}$$

where  $\mu_{\max}$  is the maximum specific growth rate ( $t^{-1}$ ),  $K_s$  is the half-saturation coefficient (mol liters $^{-1}$ ), and  $S$  is the substrate concentration (mol liters $^{-1}$ ). Each species in the biofilm has its own growth parameters and there appear to be spatial distributions of these parameters.

Detachment includes two processes: erosion and sloughing. Sloughing is a process in which large pieces of biofilm are rapidly removed, frequently exposing the surface. The causes are not well understood. Biofilm erosion is defined as continuous removal of single cells or small groups of cells from the biofilm surface and is related to shear stress at the biofilm/fluid interface. An increase in shear stress increases the erosion rate and decreases the biofilm accumulation rate. Empirical observations indicate that the erosion rate is related to biofilm thickness and density.

Biofilms form compliant surfaces that actively interact with the hydrodynamic boundary layer. Microorganisms in biofilms are aggregated in cell clusters or microcolonies separated by interstitial voids. Microorganisms within biofilms are capable of maintaining environments at biofilm/surface interfaces that are radically different from the bulk in terms of pH, dissolved oxygen, and other organic and inorganic species. In some cases, these interfacial conditions could not be maintained in the bulk medium at room temperature near atmospheric pressure. As a consequence, microorganisms within biofilms produce reactions that are not predicted by thermodynamic arguments based on the chemistry of the bulk medium.

## 2. MIC Mechanisms

Biofilm formation on metal surfaces can be expected to have a wide variety of effects on corrosion and electrochemical parameters, ranging from little or no impact to aggressive accelerated corrosion or corrosion inhibition. The principal effect of biofilm formation under aerobic conditions is to increase the probability that localized corrosion will be initiated, rather than to affect the rate of corrosion once it has begun. That is, microorganisms can set up the proper conditions for pitting or crevice corrosion. Once localized corrosion has been initiated, they can maintain proper conditions (e.g., low oxygen) for continued pit or crevice growth. Under anaerobic, reducing conditions, aggressive MIC is observed when there is some mechanism for the removal or transformation of corrosion

products (i.e., there are switches from stagnation to flow or from anaerobic to aerobic conditions).

The most devastating MIC takes place in the presence of microbial consortia in which many physiological types of bacteria, including sulfate-reducing bacteria (SRB), acid-producing bacteria, metal-oxidizing bacteria, and metal-reducing bacteria (MRB), interact in complex ways within the structure of biofilms. MIC does not produce a unique form of localized corrosion. Instead, it can result in pitting, crevice corrosion, and underdeposit corrosion, in addition to enhanced galvanic and erosion corrosion. The following discussion is a brief description of microbial activities recognized to cause MIC.

Manganese and iron oxidation are coupled to cell growth and metabolism of organic carbon. Microbially deposited manganese oxide on stainless and mild steel alters electrochemical properties related to the potential for corrosion. Iron-oxidizing bacteria produce tubercles of iron oxides and hydroxides, creating oxygen-concentration cells that initiate a series of events that individually or collectively are very corrosive.

SRB, a diverse group of anaerobic bacteria isolated from a variety of environments, use sulfate in the absence of oxygen as the terminal electron acceptor in respiration. During biofilm formation, if the aerobic respiration rate within a biofilm is greater than the oxygen diffusion rate, the metal/biofilm interface can become anaerobic and provide a niche for sulfide production by SRB. The critical thickness of the biofilm required to produce anaerobic conditions depends on the availability of oxygen and the rate of respiration. The corrosion rate of iron and copper alloys in the presence of hydrogen sulfide is accelerated by the formation of iron sulfide minerals that stimulate the cathodic reaction.

Bacteria and fungi can produce a wide variety of organic acids (e.g., formic, acetic, or succinic), which may initiate or accelerate corrosion. Some bacteria produce mineral acids, which are extremely corrosive.

## II. TECHNIQUES

### 1. Redox Potential

A prepassivated platinum electrode and an electrode of the metal of interest have been used to follow the development of a biofilm to determine its effects on the corrosion behavior of structural materials.<sup>1</sup> The time dependence of the open circuit potential ( $E_{\text{corr}}$ ) of several stainless steels

and titanium was compared with that of the prepassivated platinum electrode. Figure 1(a) shows the time dependence of  $E_{\text{corr}}$  for 304L stainless steel in solutions with and without bacteria, while Fig. 1 (b) shows corresponding data for platinum. Zhang et al.<sup>1</sup> concluded that the data reflect bacterial growth (i.e., changes in the local environment induced by metabolic activities of the bacteria) and the resulting corrosion of the metal. The role of the platinum electrode was to indicate changes in the local oxygen concentration which were assumed to be the same as those on the stainless steel under investigation. The potential of platinum changes in the positive direction when the oxygen concentration is increased or pH decreased.

## 2. Polarization Resistance

Polarization resistance ( $R_p$ ) techniques can be used to continuously monitor the instantaneous corrosion rate of a metal. Mansfeld<sup>2</sup> provided a thorough review of the use of the polarization resistance technique for the measurement of corrosion currents.  $R_p$  is defined as:

$$R_p = (dE/di) \quad (1)$$

where  $R_p$  is the slope of a potential ( $E$ )–current density ( $i$ ) curve at  $E_{\text{corr}}$ , where  $i = 0$ . Corrosion current density ( $i_{\text{corr}}$ ) is calculated from  $R_p$  by:

$$i_{\text{corr}} = B/R_p \quad (2)$$

where

$$B = b_a b_c / 2.303 (b_a + b_c) \quad (3)$$

The exact calculation of  $i_{\text{corr}}$  for a given time requires simultaneous measurements of  $R_p$  and anodic and cathodic Tafel slopes ( $b_a$  and  $b_c$ ). Computer programs have been developed for the determination of precise values of  $i_{\text{corr}}$  according to Eqs. (2) and (3). Experimental values of  $R_p$  ( $R'_p$ ) contain a contribution from the uncompensated solution resistance ( $R_u$ ).<sup>2</sup>

$$R'_p = R_p + R_u \quad (4)$$

Significant errors in the calculation of corrosion rates can occur for electrolytes of low conductivity or systems with very high corrosion rates (low  $R_p$ ) if a correction for  $R_u$  is not applied. Corrosion rates will be underestimated in these cases. Additional problems can arise from the effects of the sweep rate used to determine  $R_p$  according to Eq. (1). If the

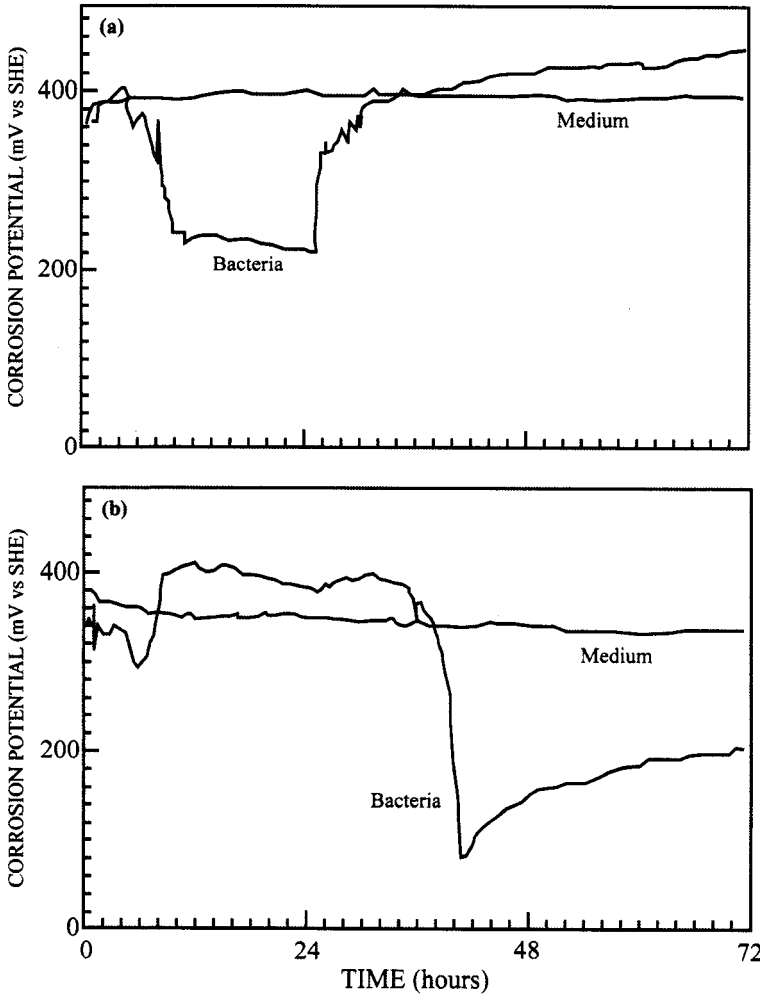


Figure 1. Open circuit potential vs. time in sterile medium and in medium with bacteria: (a) platinum, (b) 304L stainless steel. (Reprinted from Ref. 1 with permission from NACE International.)

sweep rate is too high, the experimental value of  $R_p$  will be too low and the calculated corrosion rate will be too high. For localized corrosion, experimental  $R_p$  data should be used only as a qualitative indication that rapid corrosion is occurring. Large fluctuations of  $R_p$  with time are often observed for systems undergoing pitting or crevice corrosion.

Applications of  $R_p$  techniques have been reported by King et al.<sup>3</sup> in a study of the corrosion behavior of iron pipes in environments containing SRB. In a similar study, Kasahara and Kajiyama<sup>4</sup> used  $R_p$  measurements with compensation of the ohmic drop and reported results for active and inactive SRB. Nivens et al.<sup>5</sup> calculated the corrosion current density from experimental  $R_p$  data and Tafel slopes for 304 stainless steel exposed to a seawater medium containing the non-SRB *Vibrio natriegens*.

A simplification of the polarization resistance technique is the linear polarization technique in which it is assumed that the relationship between  $E$  and  $i$  is linear in a narrow range around  $E_{\text{corr}}$ . Usually only two points ( $E$ ,  $i$ ) are measured and  $B$  is assumed to have a constant value of about 20 mV. This approach is used in field tests and forms the basis of commercial corrosion rate monitors.  $R_p$  can also be determined as the dc limit of the electrochemical impedance. Mansfeld et al.<sup>6</sup> used the linear polarization technique to determine  $R_p$  for mild steel sensors embedded in concrete exposed to a sewer environment for about 9 months. One sensor was periodically flushed with sewage in an attempt to remove the sulfuric acid produced by sulfur-oxidizing bacteria within a biofilm; another sensor was used as a control. A data logging system collected  $R_p$  at 10-min intervals simultaneously for the two corrosion sensors and two pH electrodes placed at the concrete surface. Figure 2 shows the cumulative corrosion loss ( $\Sigma INT$ ) obtained by integration of the  $1/R_p$  time curves as:

$$\Sigma INT = \int dt/R_p \quad (5)$$

A qualitative measure of the corrosion rate can be obtained from the slope of the curves in Fig. 2.  $\Sigma INT$  is given in units of s ohm<sup>-1</sup>. Owing to the presence of the uncompensated ohmic resistance and lack of values for Tafel slopes [Eq. (2)], data in Fig. 2 should be viewed as indicative of significant changes in corrosion rates. Corrosion loss remained low during the first 2 months, followed by a large increase for both flushed samples and controls. The corrosion rate increased when the surface pH reached values of 1 or less. Total corrosion loss as determined from integrated  $R_p$  data was less for the control than for the flushed sample.



$R_p$  data are meaningful for general or uniform corrosion but less so for localized corrosion, including MIC. In addition, the use of the Stern-Geary theory where the corrosion rate is inversely proportional to  $R_p$  at potentials close to  $E_{\text{corr}}$  is valid for conditions controlled by electron transfer, but not for the diffusion-controlled systems frequently found in MIC.

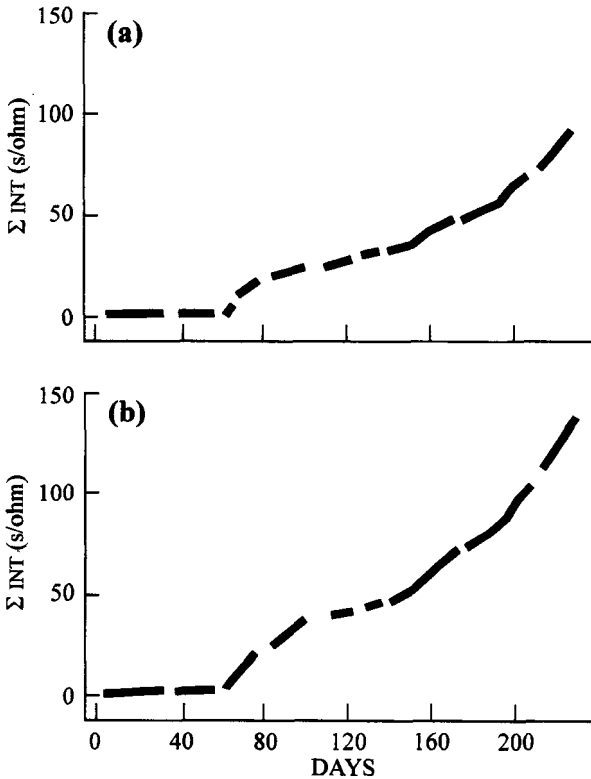


Figure 2. Cumulative corrosion loss  $\Sigma INT$  for mild steel sensors embedded in concrete and exposed to a sewer bypass: (a) control sample, (b) flushed sample. (Reprinted from Ref. 6 with permission from NACE International.)

### 3. Open Circuit Potential

The corrosion potential or open circuit potential ( $E_{\text{corr}}$ ) is easy to measure but difficult to interpret, especially when related to MIC. The time dependence of  $E_{\text{corr}}$  has been monitored for metals in natural and artificial media. Most published  $E_{\text{corr}}$  data for stainless steels in natural seawater show a rapid ennoblement during the first days of exposure. Figure 3 shows potential–time curves as reported by Johnsen and Bardal<sup>7</sup> for several stainless steels in flowing (0.5 ms<sup>-1</sup>) natural seawater.  $E_{\text{corr}}$  changed from  $-200$  mV to  $-250$  mV vs. a saturated calomel reference electrode (SCE) at the beginning of the test to  $-50$  mV for two of the alloys and to  $+200$  mV for the remaining four alloys after 28 days. The authors attributed ennoblement of  $E_{\text{corr}}$  to a change in cathodic properties of stainless steels as a result of microbiological activity on the surface.

Based on cathodic polarization curves, Dexter and Gao<sup>8</sup> concluded that the increase of  $E_{\text{corr}}$  for 316 stainless steel exposed to natural seawater was due to an increased rate of the cathodic reduction of oxygen at a given potential. It is not possible from  $E_{\text{corr}}$  or polarization curves to decide whether the increase in  $E_{\text{corr}}$  is due to thermodynamic effects, kinetic

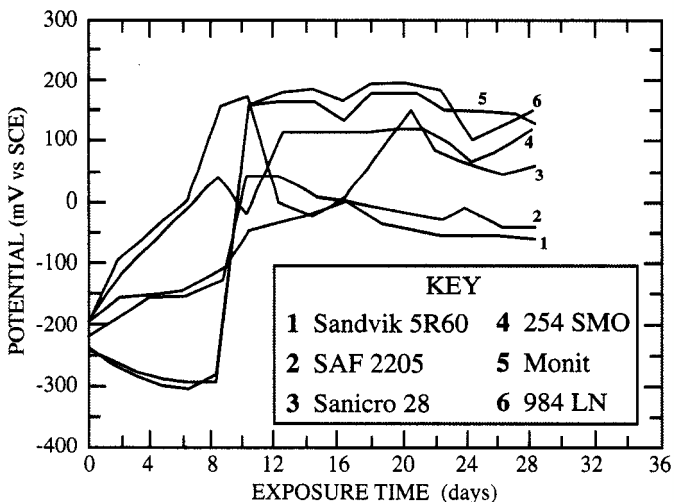


Figure 3. Open circuit potential vs time for six stainless steels exposed to flowing natural seawater. (Reprinted from Ref. 7 with permission from NACE International.)

effects, or both. The reversible potential of the oxygen reduction reaction can increase due to a local increase in the oxygen concentration or a decrease in pH. The complexity of this situation is illustrated by the fact that naturally occurring microorganisms within a marine biofilm can decrease or increase the local oxygen concentration and pH. An increase in the exchange current density for the oxygen reduction reaction would also lead to an increase in  $E_{\text{corr}}$ . Since  $E_{\text{corr}}$  is a mixed potential, its value can also change in response to changes in the passive current density of the stainless steel. Given that the kinetics were constant for the oxygen reduction reaction,  $E_{\text{corr}}$  would become more noble if the passive current density decreased with exposure time. Chandrasekaran and Dexter<sup>9</sup> concluded that a combination of pH reduction and hydrogen peroxide ( $\text{H}_2\text{O}_2$ ) production within marine biofilms contributed to ennoblement.

Both Linhardt<sup>10</sup> and Dickinson et al.<sup>11</sup> demonstrated that microbiologically deposited manganese oxide on stainless and mild steel coupons in fresh water (Fig. 4) caused an increase in  $E_{\text{corr}}$  and increased cathodic current density at potentials above  $-200 \text{ mV}_{\text{SCE}}$ .<sup>11</sup> Biomineralization of

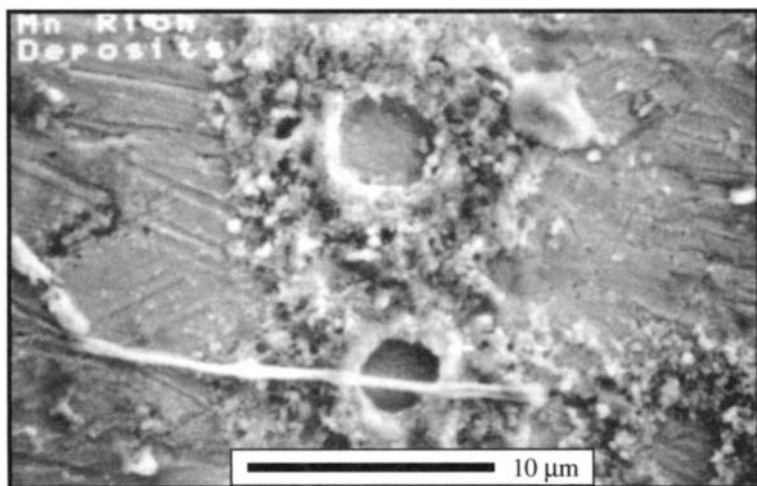


Figure 4. Annular deposits on 316L stainless steel after 13 days of exposure to fresh water (Reprinted from W. Dickinson, F. Caccavo and Z. Lewandowski, "The Ennoblement of Stainless Steel by Manganic Oxide Biofouling," *Corros. Sci.* **38** (8) p. 1413, fig. 4, Copyright 1996, with permission from Elsevier Science).

manganese oxides occurs widely in natural waters, and is a dominant control in geochemical cycling of the element.<sup>10</sup> Manganese oxidation is coupled to cell growth and metabolism of heterotrophic substrates. Manganese oxide deposits are formed on submerged materials, including metal, stone, glass, and plastic, and can occur in natural waters with manganese levels as low as 10–20 ppb. Microbially deposited manganese oxides have an amorphous structure as  $\text{MnO}_2$  (vernadite) and sometimes form a black precipitate of  $\text{MnO}_2$  (birnessite).

Dickinson et al.<sup>12</sup> monitored  $E_{\text{corr}}$  (SCE) for 316L stainless steel coupons for up to 120 days of exposure in fresh river water.  $E_{\text{corr}}$  was measured hourly by computer using a high-impedance ( $>10^{11} \Omega$ ), multiplexed, analog-to-digital converter. Polarization measurements were made initially using a computer-controlled potentiostat/galvanostat. High-density graphite counter-electrodes were used for all polarization measurements. The authors observed that the minimum  $E_{\text{corr}}$  required for ennoblement of the 316L stainless steel was  $-110 \text{ mV}_{\text{SCE}}$  at 10 hr of exposure. Ennobled potentials  $>300 \text{ mV}_{\text{SCE}}$  resulted from the formation of biofouling 2–40  $\mu\text{m}$  thick and at least 3–5% coupon coverage.  $E_{\text{corr}}$  measurements after removal of the biofilm from the ennobled metal surface and then after subsequent reformation established that adherent fouling was necessary for initiation and retention of ennoblement.

For mild steel corrosion under anodic control, manganese oxides can elevate corrosion current, but will cause little positive shift in  $E_{\text{corr}}$ . The increase in corrosion current may be significant, particularly for mild steel covered with biomineralized oxides and corrosion product tubercles that provide large mineral surface areas. Given sufficient conductivity in the tubercle (e.g., by magnetite), much of this material may serve as an oxide cathode to support corrosion at the oxygen-depleted anode within the tubercle. Continued biomineralization within the large tubercle may sustain a significant amount of the cathodic current.

In summary, ennobled  $E_{\text{corr}}$  can reach pitting potentials for low-molybdenum alloys. Passive metal corrosion currents on the order  $10 \text{ nA cm}^{-2}$  allow biomineralized material to accumulate.  $E_{\text{corr}}$  then shifts in the noble direction as increasing areal coverage anodically polarizes the metal.  $E_{\text{corr}}$  may reach the pitting potential for low-molybdenum alloys in dilute chloride media, increasing the risk of pit nucleation. Once nucleation occurs, cathodic current sustained by the  $\text{MnO}_2$  cathode impedes repassivation by holding the corrosion potential above the protection potential. More available cathode material will support a greater number

of pitting sites. Localized corrosion currents that exceed the biomineralization rate will discharge the oxide cathode so that eventually the corrosion rate becomes limited by the oxide biomineralization rate and by the availability of other cathodic reactants (typically dissolved oxygen). Biomineralized manganic oxides are efficient cathodes and increase cathodic current density on stainless steel by several decades at potentials between roughly  $-200$  and  $+400$  mV<sub>SCE</sub>. The extent to which the elevated current density can be maintained is controlled by the electrical capacity of the mineral, reflecting both total accumulation and conductivity of the mineral-biopolymer assemblage (only material in electrical contact with the metal will be cathodically active). Oxide accumulation is controlled by the biomineralization rate and the corrosion current, in that high corrosion currents will discharge the oxide as rapidly as it is formed. This variation in accumulation causes the oxides to exert different modes of influence on the corrosion behavior of active metals compared with passive metals. Potentiodynamic polarization measurements before and after exposures suggested changes in oxide mineralogy, enhancing oxygen reduction and shifting  $E_{\text{corr}}$  in a noble direction.

#### 4. Capacitance

The following paragraphs are from Dickinson et al.<sup>12</sup> They monitored capacitance ( $C$ ) and  $E_{\text{corr}}$  values over 50 days of exposure of 316L stainless steel to river water as a broad measure of near-surface changes that may reflect changes in surface oxides. Capacitance data were determined using the galvanostatic transient method. A 25-s, constant-current pulse in the range 2 to 10  $\mu\text{A cm}^{-2}$  was applied to stainless steel coupons to produce an overvoltage-time response. Applied current ( $I_{\text{app}}$ ) was chosen to generate  $< -10$  mV cathodic overvoltage ( $\eta$ ). Typical  $\eta$  was in the range  $-2$  to  $-8$  mV. After amplification through a high-impedance differential amplifier, signals were recorded at 10-ms intervals by computer.  $C$  was determined by nonlinear fitting as:

$$\eta = I_{\text{app}} R_p [1 - \exp(-t/R_p C)] \quad (6)$$

where  $t$  is time, assuming a simple parallel combination of  $R_p$  and  $C$  as the model for the electrode/solution interface. In most cases, this produced an acceptable fit, although introduction of a second time constant was required for some measurements to fit the data accurately. Close proximity

of working and reference electrodes and the small  $I_{app}$  made corrections for uncompensated resistance unnecessary.

Figure 5 shows the evolution of cathodic response to a  $10 \mu\text{A cm}^{-2}$ , 25-s galvanostatic pulse for a representative sample as  $E_{corr}$  increased during the river water exposures. The overvoltage-time response fit to Eq. (6) by nonlinear regression was used to determine  $R_p$  and  $C$ . The 10-ms sampling interval during the measurements was reflected by the continuous data curves, while filled circles indicated individual points generated from the computed  $R_p$  and  $C$  values. Data were fit by the simple parallel resistance-capacitance (RC) model used to generate Eq. (6). Initial values of  $R_p$  and  $C$  were in the ranges  $0.5 \text{ M}\Omega \text{ cm}^2$  to  $1.5 \text{ M}\Omega \text{ cm}^2$  and  $35 \mu\text{F cm}^{-2}$  to  $55 \mu\text{F cm}^{-2}$ , respectively, which is in good agreement with results obtained for stainless steel by Mansfeld et al.<sup>13</sup> using electrochemical impedance spectroscopy techniques. The steady decrease in final  $\eta$  with increasing  $E_{corr}$  shown in Fig. 5 may reflect the development of an increasing cathodic Tafel slope during ennoblement and appeared as an increase in the value of  $R_p$ . A corresponding decrease in  $C$  for data from

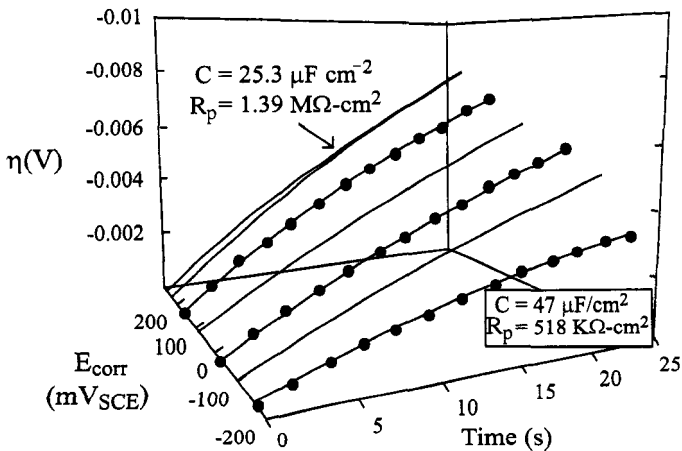


Figure 5. Evolution of cathodic response to  $10 \mu\text{A cm}^{-2}$  galvanostatic pulse as  $E_{corr}$  increases during biofouling of 316L stainless steel in fresh river water. Data shown by solid lines and circles indicate points generated from curve fit to Eq. (6). (Reprinted from Ref. 12 with permission from NACE International.)

Fig. 5 is shown in Fig. 6(a). In contrast, Fig. 6(b) shows constant  $C$ - $t$  behavior for a coupon that exhibited little change in  $E_{\text{corr}}$  during exposure.

To determine if the difference in  $C$  behavior for coupons in Figs. 6(a) and (b) was due to a difference in biofouling accumulation, extent of coverage and morphology of biofouling. Microscopic examination was used. Biofouling on the two coupons was indistinguishable. In summary, neither duration of exposure nor the mere presence of biofouling could account for the decrease in  $C$  shown in Fig. 6(a).

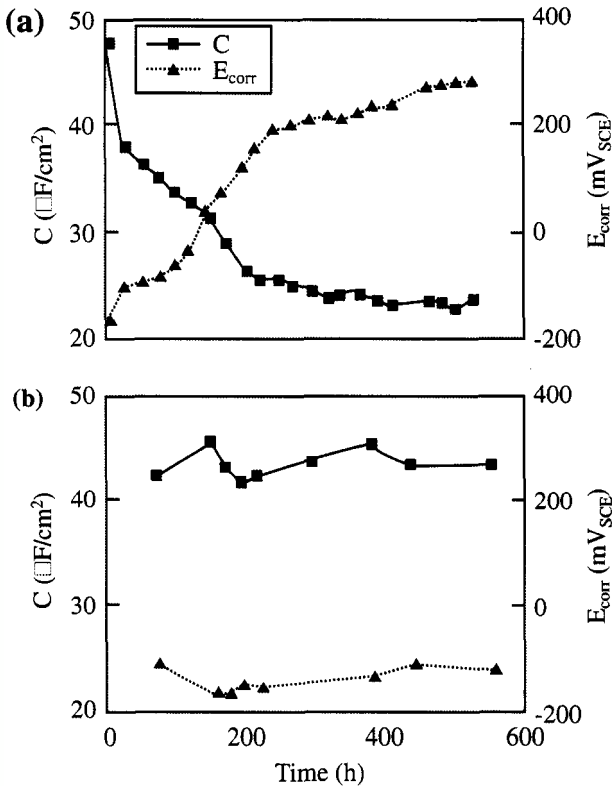


Figure 6.  $C$  and  $E_{\text{corr}}$  for two 316L stainless steel coupons during biofouling in fresh river water: (a)  $E_{\text{corr}}$  ennobled during exposure and (b)  $E_{\text{corr}}$  nearly constant during exposure. (Reprinted from Ref. 12 with permission from NACE International.)

$C$  values for a nonexposed coupon prepared in a manner identical to the exposed coupons were measured while the coupon was polarized by constant anodic current to determine if changes in  $C$  resulted solely from increased potential. For each potential, polarizing current was applied for  $\approx 1$  hr until the potential drift was  $< 2$  mV hr $^{-1}$  before making  $C$  measurements. Data given by the open squares in Fig. 7 show  $C$  was independent of potential over the range  $-100$  mV $_{SCE}$  to  $200$  mV $_{SCE}$ . This finding was in agreement with the results of Popat and Hackerman<sup>14</sup> for stainless steel in  $0.1$  M Na $_2$ SO $_4$  at neutral pH.

The strong correlation between  $C$  and ennobled  $E_{corr}$  is shown in Fig. 7. Capacitance is expressed as a fraction of initial capacitance ( $C_{init}$ ) to account for variation in the surface area of the coupons. Data were expressed satisfactorily by the relationship:

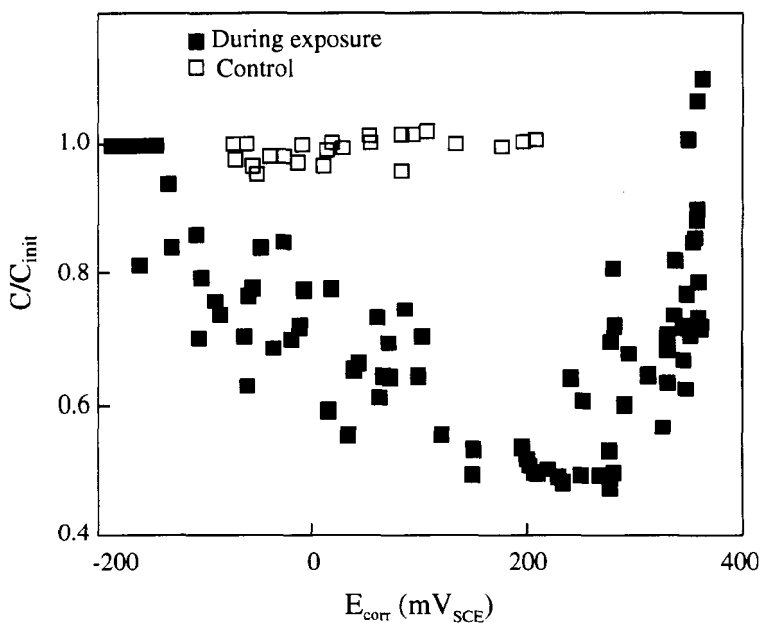


Figure 7.  $C/C_{init}$  ratio vs  $E_{corr}$  for six 316L stainless steel coupons during biofouling in fresh river water and for control coupon. (Reprinted from Ref. 12 with permission from NACE International.)



$$dC/dE_{\text{corr}} = -0.05 \pm -0.009 (\mu\text{F cm}^{-2})/\text{mV} \quad (7)$$

obtained by linear regression of the data between  $-100 \text{ mV}_{\text{SCE}}$  and  $200 \text{ mV}_{\text{SCE}}$  for each of six coupons.

The origin of the observed correlation was not established, and the relation was not interpreted as causal. It could be argued that a sustained elevated potential due to as-yet unknown microbial processes altered the passive film characteristics, as is known to occur for metals polarized at anodic potentials. If these conditions thickened the oxide film or decreased the dielectric constant to the point where passive film capacitance was on the order of double-layer capacitance ( $C_{\text{dl}}$ ), the series equivalent oxide  $C_{\text{dl}}$  would have begun to reflect the contribution from the oxide. In this scenario, decreased  $C$  would have appeared as a consequence of sustained elevated potential.

In a reverse sense, microbial processes may have influenced  $C$  by directly altering the oxide surface. Reported  $C$  values for  $\text{Fe}_3\text{O}_4$  in acidic and alkaline media range between  $50 \mu\text{F cm}^{-2}$  and  $300 \mu\text{F cm}^{-2}$ , while  $C$  for  $\gamma\text{-FeOOH}$  at neutral pH is reported as  $11 \mu\text{F cm}^{-2}$ .<sup>15</sup> Decreased  $C$  during ennoblement was consistent with transformation of  $\text{Fe}^{3+}$  to  $\gamma\text{-FeOOH}$  at the inner layer of a duplex passive film and may have reflected the formation of other  $3^+$  iron oxides. Vago et al.<sup>15</sup> showed oxygen reduction at  $-200 \text{ mV}_{\text{SCE}}$ , pH 10, to be five times more rapid on  $\gamma\text{-FeOOH}$  than on  $\text{Fe}_3\text{O}_4$ . This difference in rate closely matched that at  $-200 \text{ mV}_{\text{SCE}}$  in Fig. 8 of stainless steel before and after ennoblement. These considerations suggested that changes in  $C$  and cathodic current density may be due to changes in surface oxide properties.

The nature of the increase in  $C$  as the potential approached  $300 \text{ mV}_{\text{SCE}}$  (Fig. 7) was not explained. However, the shape of the galvanostatic curves used to determine  $C$  in this potential region showed increasing curvature for times  $< 5 \text{ s}$ . The curvature increased with increasing exposure. The authors incorporated an additional time constant in the model circuit by placing a second parallel RC pair in series with the first, to fit galvanostatic data for times  $< 5 \text{ s}$  at potentials  $> 300 \text{ mV}_{\text{SCE}}$ . With this model, the analytical solution for constant  $I_{\text{app}}$  was:

$$\eta = I_{\text{app}} \{R_p [1 - \exp(-t/R_p C_{\text{dl}})] + R_f [1 - \exp(-t/R_f C_f)]\} \quad (8)$$

where  $R_f$  and  $C_f$  are the resistance and capacitance associated with the oxide layer. While the physical significance of the circuit model is equivocal, it is invoked commonly for defect-free coatings and provided a

satisfactory fit to data. Applying Eq. (8) to data from a coupon at 330  $mV_{SCE}$  and 24 days later for that same coupon at 360  $mV_{SCE}$  produced a decrease in apparent oxide film  $C$  from 50  $\mu F cm^{-2}$  to 28  $\mu F cm^{-2}$  and an increase in  $C_{dl}$  from 66  $\mu F cm^{-2}$  to 212  $\mu F cm^{-2}$ . This corresponded to a slight increase in series equivalent  $C$  and suggested that the oxide film  $C$  continued to decrease with time at potentials  $> 300 mV_{SCE}$ . In light of the increasing curvature of galvanostatic measurements at these potentials, however, data for the region above 300  $mV_{SCE}$  in Fig. 7 should be taken as provisional. As shown in Fig. 5, data for potentials  $< \approx 300 mV_{SCE}$  were fit by Eq. (6).

$R_p$  and  $E_{corr}$  vs. time for the data in Fig. 5 are shown in Fig. 8. As noted, steeper cathodic polarization slopes characteristic of ennoblement would have caused  $R_p$  to increase if  $i_{corr}$  and the slope ( $b_a$ ) of the anodic polarization curve near  $E_{corr}$  remained constant. Figure 9 shows that  $i_{corr}$  increased only slightly if at all during ennoblement, while  $b_a$  was expected to have changed little in the passive region. Consequently, it was likely that  $R_p$  reflected changes in the cathodic polarization slope. These changes

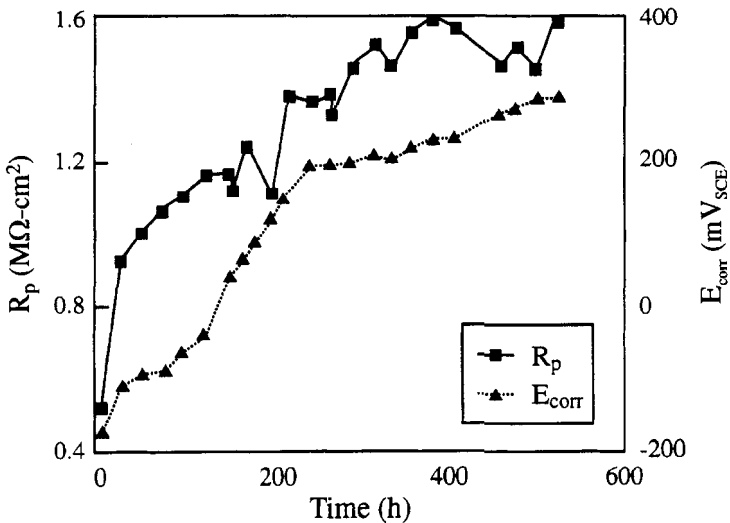


Figure 8.  $R_p$  and  $E_{corr}$  vs. time for 316L stainless steel during biofouling in fresh river water. (Reprinted from Ref. 12 with permission from NACE International.)

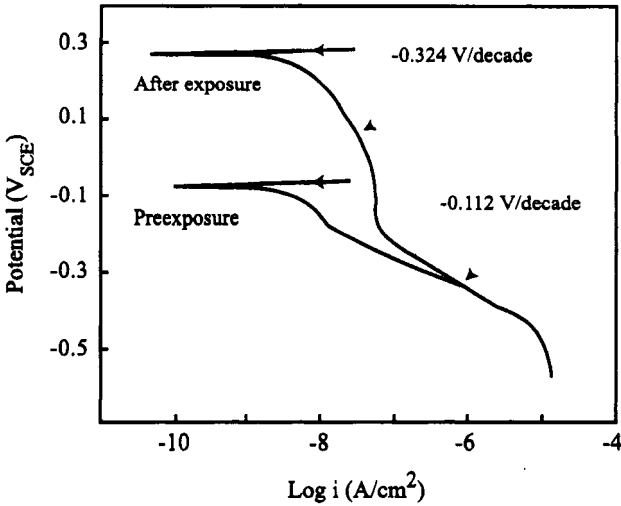


Figure 9. Potentiodynamic polarization curves for 316L stainless steel before and after biofouling during 20-day exposure to fresh river water. (Reprinted from Ref. 12 with permission from NACE International.)

may be related to electrical conductivity in the oxide, which would limit the cathodic rate if the increasing oxygen reduction rate approached the rate of electron conduction. The effect is analogous to a series reaction mechanism. The influence of oxide conductivity on net cathodic rate would have been even greater if conductivity decreased during ennoblement, as would have occurred with transformation of conductive  $\text{Fe}_3\text{O}_4$  to a semiconducting, ferric oxide ( $\text{Fe}_2\text{O}_3$ ) phase. The latter consideration suggested that cathodic polarization behavior for ennobled stainless steel was consistent with a  $\text{Fe}_3\text{O}_4/\text{Fe}_2\text{O}_3$  transformation.

An increase in reducible surface-bound material during ennoblement was demonstrated using galvanostatic reduction<sup>16</sup> techniques to monitor potential as a stainless steel coupon was cathodically polarized. Coulombs of reducible material were calculated from the duration of regions of polarization rate lag that indicated reduction of surface-bound material. Longer exposure times and thicker biofouling were not sufficient to increase the abundance of reducible surface-bound material. The increase seemed to be associated with increased  $E_{\text{corr}}$ .

## 5. Microsensors

Dickinson et al.<sup>12</sup> also used microelectrodes to measure dissolved oxygen (DO),  $\text{H}_2\text{O}_2$ , and local  $E_{\text{corr}}$  within biofouling deposits on stainless steel surfaces exposed to river water to further resolve the interfacial chemistry that resulted in ennoblement. Data were then compared with those from similar measurements as close as possible to the environment of a non-fouled substratum.

Lee and de Beer<sup>17</sup> describe the ideal microsensors as having small tip diameters to prevent distortion of the local environment, small sensor surfaces for optimal spatial resolution, low noise levels, stable signal, high selectivity, and strength to resist breakage. The DO microelectrode design has been described previously.<sup>18</sup>  $\text{H}_2\text{O}_2$  microelectrodes were prepared by sheathing tapered platinum wire within glass in a fashion identical to that used to construct the DO probes. The sensing tip was coated by dipping it in a solution of 1 g cellulose acetate (molecular weight = 60,000) dissolved in 20 ml acetone and air dried. Tip diameters were in the range of 5 to 15  $\mu\text{m}$ . DO and  $\text{H}_2\text{O}_2$  microelectrodes were polarized to  $-0.8 \text{ V}_{\text{SCE}}$  and  $0.8 \text{ V}_{\text{SCE}}$ , respectively, and current proportional to analyte concentration was measured using a picoammeter. For DO, air-saturated and nitrogen-purged volumes of reactor water were used to give a two-point calibration. The  $\text{H}_2\text{O}_2$  electrode was calibrated by adding known volumes of 30%  $\text{H}_2\text{O}_2$  (previously standardized by permanganate [ $\text{MnO}_4^-$ ] titration) to water from the reactor influent carboy. Separate calibrations performed over the pH range 2.2 to 9.6 showed an  $\text{H}_2\text{O}_2$  detection limit  $<2 \mu\text{M}$  at all PH.

Stainless steel microelectrodes were prepared by sheathing 100- $\mu\text{m}$  diameter stainless steel wire in glass. Tips were polished on a precision diamond wheel. Electrode response to variation in cathodic depolarizer concentration was confirmed by exposure to solution containing up to 6 mM  $\text{H}_2\text{O}_2$ . The increase in  $E_{\text{corr}}$  for the electrode was comparable to the change observed for sample coupons exposed to the same  $\text{H}_2\text{O}_2$  concentrations. The electrode was conditioned by exposure to the influent reactor solution for several hours before measuring  $E_{\text{corr}}$  within the biofouling deposits.

Profiles of DO and  $\text{H}_2\text{O}_2$  concentrations and microelectrode  $E_{\text{corr}}$  were measured within biofouling deposits on coupons. The microelectrodes, mounted in a commercial three-axis micromanipulator, were positioned above a deposit by adjusting the X-Y micromanipulator controls

manually. Vertical positioning was executed in 10- or 20- $\mu\text{m}$  increments, starting with the probe tip just above the deposit and continuing until the tip was within  $\sim 10\ \mu\text{m}$  of the metal substratum. Vertical movement was controlled by a computer-driven stepper motor attached to the micromanipulator  $z$ -axis. Probe position was determined by viewing the tip at  $70\times$  magnification through a stereo microscope. Positioning accuracy from bulk solution to the substratum was  $5\ \mu\text{m}$ . Measurements were usually stable within 30 s after the probe was positioned.

Microsensors have been used to develop profiles in mixed species biofilms. Figure 10 shows concentration profiles of sulfide, oxygen, and pH in a biofilm accumulated on the surface of a mild steel corrosion coupon.<sup>19</sup> The concentration of sulfide is highest near the metal surface, where iron sulfide forms quickly and covers the steel surface if both ferrous and sulfide ions are available. At low ferrous ion concentrations, adherent and temporarily protective films of iron sulfides are formed on the steel surface, with a consequent reduction in corrosion rate. High rates of SRB-induced corrosion of mild steel are maintained only in high concentrations of ferrous ion.

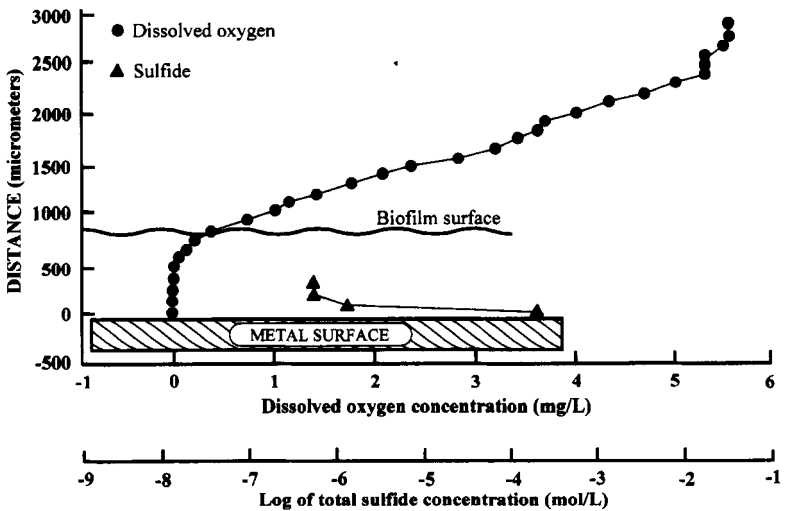


Figure 10. Concentration profiles of sulfide, oxygen, and pH in a biofilm on mild steel. (Reprinted from Ref. 19 with permission of Harwood Academic Publishers, Lausanne, Switzerland.)

In the Dickinson et al.<sup>12</sup> studies, the results of microelectrode measurements indicated that ennoblement was not caused by elevated levels of dissolved oxidants. Measurements at various heights above the substratum and at numerous sites over the coupon surface showed  $\text{H}_2\text{O}_2$  concentrations  $< 2 \mu\text{M}$  and no significant variation in  $E_{\text{corr}}$  for the stainless steel microelectrode at any site. DO profiles in the same regions showed saturation levels at all sites. Representative profiles are shown in Fig. 11.

The influence of  $\text{H}_2\text{O}_2$  concentration on stainless steel potential was determined by exposing a coupon to known concentrations of  $\text{H}_2\text{O}_2$  in aerated river water and measuring  $E_{\text{corr}}$  and pH. After correcting for a  $-60 \text{ mV/pH}$  unit change due to slight acidification from the added  $\text{H}_2\text{O}_2$ ,  $E_{\text{corr}}$  followed the relationship:

$$E_{\text{corr}} (\text{mV}) = 283.1 + 91.8 \log [\text{H}_2\text{O}_2] \quad (9)$$

over the  $\text{H}_2\text{O}_2$  concentration range from 0.1 to 100 mM. For  $\text{H}_2\text{O}_2$  concentrations  $< 30 \mu\text{M}$ ,  $E_{\text{corr}}$  was constant at  $-110 \text{ mV}_{\text{SCE}}$ . Equation (9) shows that  $\text{H}_2\text{O}_2$  must reach nearly molar concentrations to account for ennoblement. While microelectrodes cannot measure concentrations at

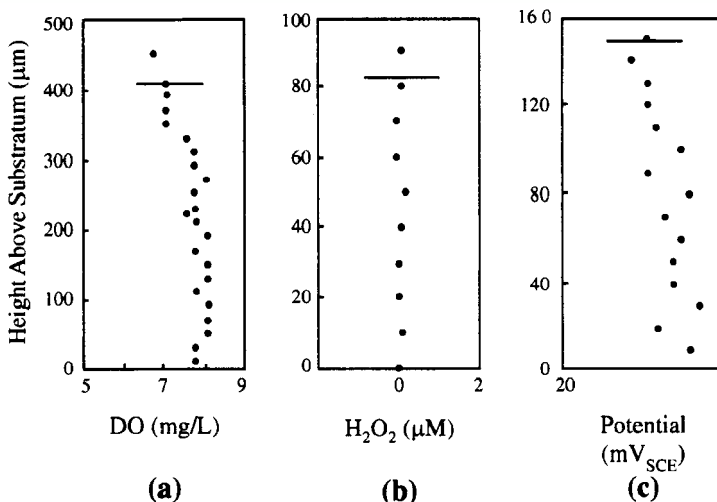


Figure 11. Microelectrode profiles in biofouling deposits on ennobled 316L stainless steel coupons. Horizontal line indicates biofouling/solution interface. (Reprinted from Ref. 12 with permission from NACE International.)

the metal surface directly, simple mass-transfer calculations based upon linear diffusion put an upper limit on these concentrations. Specifically,  $\text{H}_2\text{O}_2$  concentrations  $< 2 \mu\text{M}$  at a distance just a few micrometers from the surface could not have coexisted with steady-state surface concentrations as great as  $30 \mu\text{M}$ . Thus,  $\text{H}_2\text{O}_2$  neither caused nor contributed to ennoblement under the conditions studied.

$E_{\text{corr}}$  for the stainless steel microelectrode reflected concentrations of dissolved oxidants. The purpose in using the stainless steel microelectrode was to see how  $E_{\text{corr}}$  in the biofouling deposits compared with  $E_{\text{corr}}$  for the substratum. The fact that the probe  $E_{\text{corr}}$  did not change was evidence that  $E_{\text{corr}}$  for the substratum was influenced by near-surface conditions and not by general accumulation of dissolved oxidants within the biofouling. These surface conditions did not appear to involve near-surface accumulation of dissolved oxidants, since such accumulation would have been expected to cause a potential gradient near the surface, which was not observed.

Saturation DO level throughout the biofouling indicated low net respiration rates. The authors concluded that it is unlikely that bacteria were factors in ennoblement. Evidence that aerobic conditions were necessary for ennoblement was obtained by adding excess glucose to reactor influent media, causing the DO within the biofouling to decrease rapidly to  $< 0.1$  ppm. Within 48 hr after glucose addition,  $E_{\text{corr}}$  for ennobled coupons decreased from  $225 \text{ mV}_{\text{SCE}}$  to  $-400 \text{ mV}_{\text{SCE}}$ . Sixty hours after reestablishing aerated conditions,  $E_{\text{corr}}$  had regained values  $> 200 \text{ mV}_{\text{SCE}}$ .

## 6. Dual-Cell Technique

The dual cell, split cell, or biological battery allows continuous monitoring of changes in corrosion rates caused by the presence of a biofilm. Two identical electrochemical cells are biologically separated by a semipermeable membrane. The two working electrodes are connected to a zero resistance ammeter or a potentiostat set to an applied potential of 0 mV. Bacteria are added to one of the two cells and the sign and magnitude of the resulting galvanic current is monitored to determine details of the corrosive action of the bacteria. The dual-cell technique does not provide a means to calculate corrosion rates, but rather changes that are due to the presence of a biofilm.<sup>20</sup>

## 7. Electrochemical Noise Analysis

Electrochemical noise analysis (ENA) follows the fluctuations of potential or current as a function of time or experimental conditions. No externally applied signal is needed. In some cases, the potential of a test electrode is measured against a stable reference electrode (potential noise). In others, noise data are recorded for two electrodes of the same material connected to a zero resistance ammeter (current noise). No external signals are applied that may influence biofilm properties. Higher noise levels and greater fluctuations indicate the onset of localized corrosion. Spectral analysis of the structure of electrochemical noise can provide information on the nature of corrosion processes and the magnitude of the corrosion rate. This analysis determines spectral noise resistance, which is related to  $R_p$ . Figure 12(a) presents potential and current noise plots for mild steel in two cooling waters of different salt concentrations.<sup>21</sup> Cooling water No. 2 contained higher concentrations of chlorides and sulfates, producing very different fluctuation patterns. Figure 12(b) shows corresponding power-spectral density analyses for the same cooling waters. A higher slope for the spectral curves was obtained in the locally corroding No. 2 water than in the uniformly corroding No. 1 water. King et al.<sup>3</sup> interpreted noise measurements for steel pipes in environments containing SRB as being indicative of film formation and breakdown. Iverson et al.<sup>22,23</sup> used ENA to monitor corrosion of mild steel in a seawater culture of marine SRB and concluded that breakdown of the iron sulfide film was accompanied by generation of electrochemical noise. Moosavi et al.<sup>24</sup> presented data collected at  $E_{\text{corr}}$  for a reinforced concrete block exposed to a marine medium containing active SRB in two noise plots: a time record and a potential distribution chart showing the population and the magnitude of the potential fluctuations. Fluctuation in the noise record for 218 days was interpreted as due to the sudden rupture of the protective oxide film followed by immediate repassivation. The events recorded for an exposed rebar showed fluctuations lower than those observed with a covered rebar by a factor of 10. King et al.<sup>3</sup> interpreted noise measurements for steel pipes in environments containing SRB as being indicative of film formation and breakdown as the probable mechanism of corrosion. The magnitude of noise fluctuations depends on the total impedance of the system. A corroding metal undergoing uniform corrosion with fairly high corrosion rates might be less noisy than a passive metal showing occasional



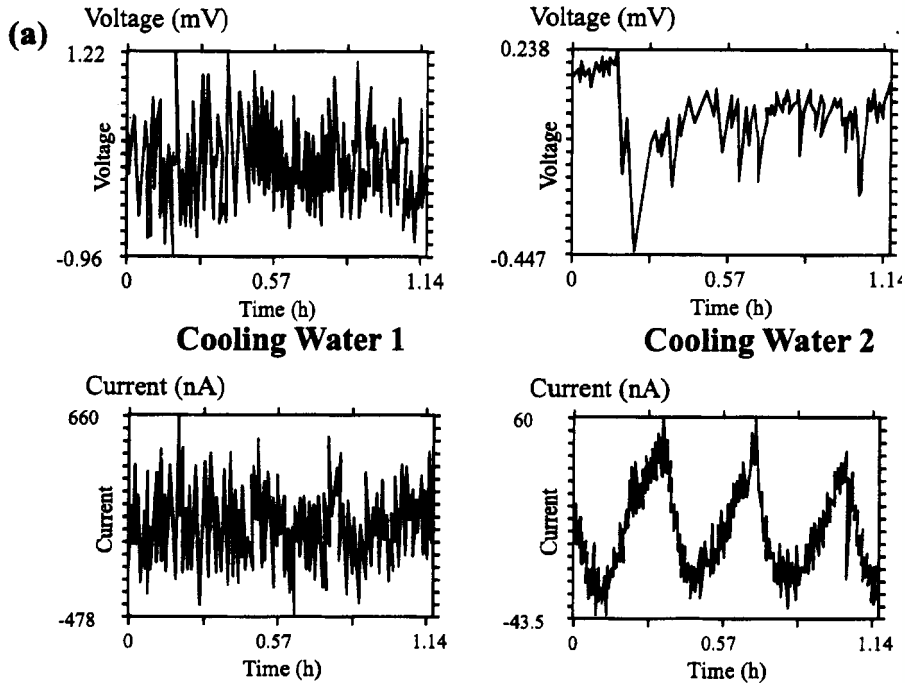


Figure 12. (a) Potential and current noise at mild steel in different cooling waters. (b) Power density (PSD) for potential and current noise at mild steel in different cooling waters. (Reprinted from Ref. 21 with permission from NACE International.)

(b)

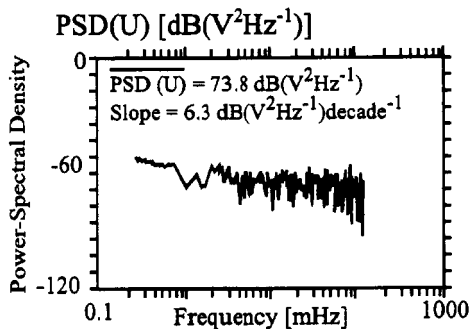
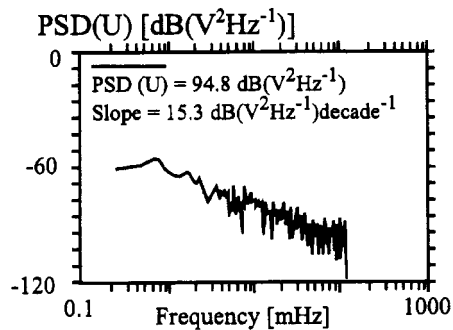
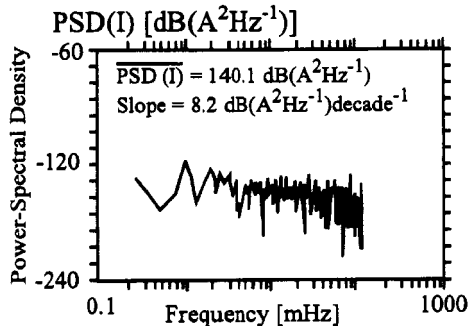
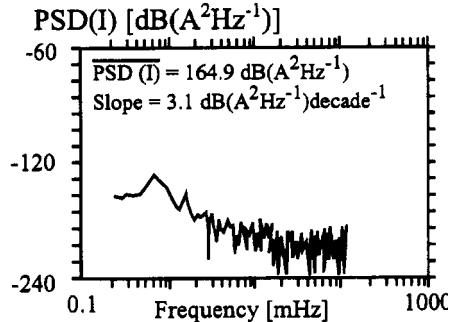
**Cooling Water 1****Cooling Water 2**

Figure 12. Continued.

bursts of noise due to localized breakdown of the film followed by rapid repassivation.

ENA was recently used for remote on-line corrosion monitoring of carbon steel electrodes in a test loop of a surge water tank at a gas storage field. An experimental design and system for remote ENA and collection of electrochemical impedance spectroscopy (EIS) data (Fig. 13) have been presented elsewhere.<sup>25</sup> In the gas storage field, noise measurements were compared with electrode weight loss measurements. Noise resistance ( $R_n$ ) was defined as

$$\sigma\{V(t)\}/\sigma\{I(t)\} \quad (10)$$

where  $\sigma\{V(t)\}$  is the standard deviation of potential fluctuations and  $\sigma\{I(t)\}$  is the standard deviation of current fluctuations. If one assumes that  $R_n$  is close to  $R_p$ , then the instant corrosion current ( $i_c$ ) can be obtained from the  $R_n$  data as follows:

$$i_c = B/R_n \quad (11)$$

where  $B = b_a b_c / 2.3(b_a + b_c)$ ,  $b_a$  and  $b_e$  are the anodic and cathodic Tafel slopes.  $\sum INT$  in grams can be calculated by integration of  $i_c$  over the exposure period:

$$\sum INT = C_g \int i_c dt_f \quad (12)$$

where  $t_f$  is the total exposure time, and  $C_g = 4.7 \times 10^5 \text{ g C}^{-1}$  is used for the conversion of  $\mu\text{A hr}^{-1}$  for electrodes with a  $5.5 \text{ cm}^2$  exposed area. Representative noise data for  $\sigma\{V(t)\}$ ,  $\sigma\{Z(t)\}$ ,  $R_n$ , and  $\sum INT$  are presented in Fig. 14. The slope of the  $\sum INT$ -time curve was steep during the initial exposure, indicating a high corrosion rate that decreased significantly. The average corrosion rate ( $CR_{\text{int}}$ ) in  $\mu\text{m yr}^{-1}$  during the exposure period was calculated as follows:

$$C_R = (\sum INT/t_f) C_p \quad (13)$$

where  $C_p$ , a conversion constant, is  $8.4 \times 10^4 \mu\text{m g}^{-1}$ .

$\sum INT$  and  $t_f$  are given in grams and years, respectively.  $CR_{\text{int}}$  values for 19 noise electrodes were compared with the mean corrosion rates determined from weight loss data (Fig. 15). The 19 points were fitted to a straight line through the origin using least-squares analysis. The results indicated that the slope of the curve was 0.84, with the regression coeffi-

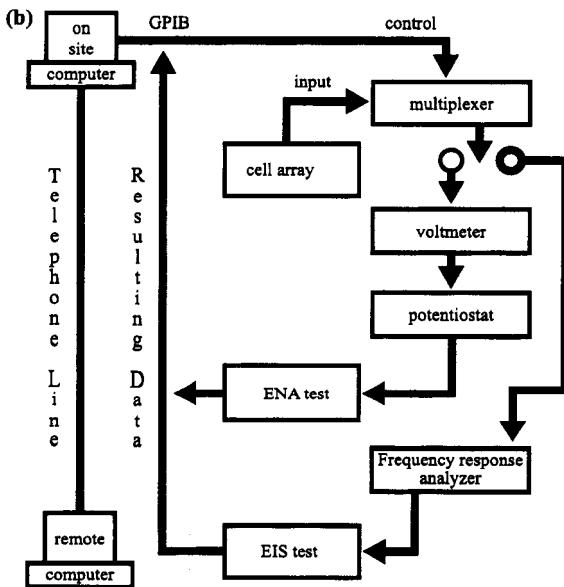
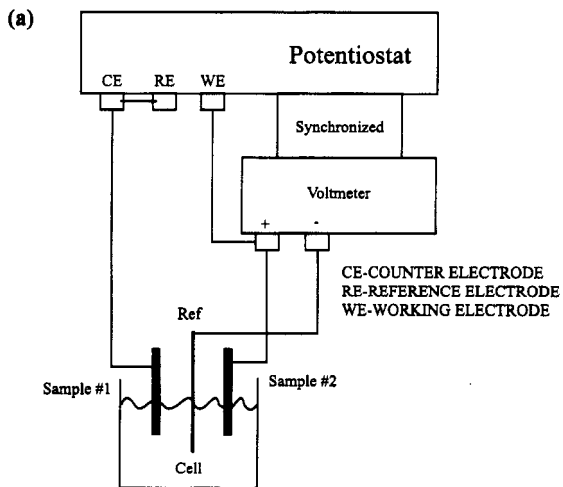


Figure 13. (a) Experimental approach for simultaneous collection of potential and current noise. (b) Schematic for remotely controlled impedance and noise multichannel data collection system. (Reprinted from F. Mansfield, C. Chen, C. C. Lee, and H. Xiao, "The Effect of Asymmetric Electrodes on the Analysis of Electrochemical Impedance and Noise Data," *Corros. Sci.* **38** (3): 497, Fig. 1. Copyright © 1996 with permission of Elsevier Science.)

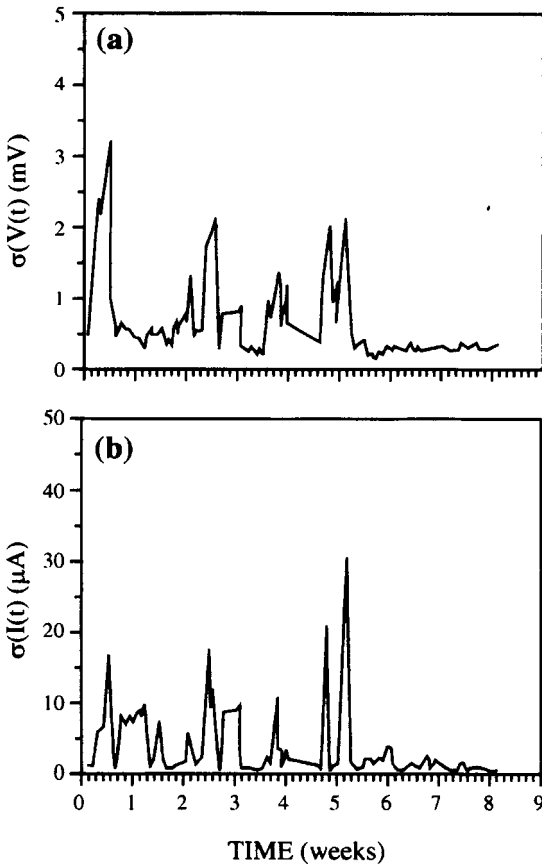


Figure 14. Representative noise data as monitored for steel electrodes exposed in a test loop at a gas storage field: (a)  $\sigma\{V(t)\}$ , (b)  $\sigma\{I(t)\}$ , (c)  $R_n$ , and (d)  $INT_{corr}$ .

cient ( $R^2$ ) equal to 0.86. The line with slope = 1 is for the ideal case where results obtained using the electrochemical noise data and weight loss measurements are identical. Good agreement between  $CR_{int}$  and weight loss measurements suggest that ENA is a promising tool in monitoring corrosion.

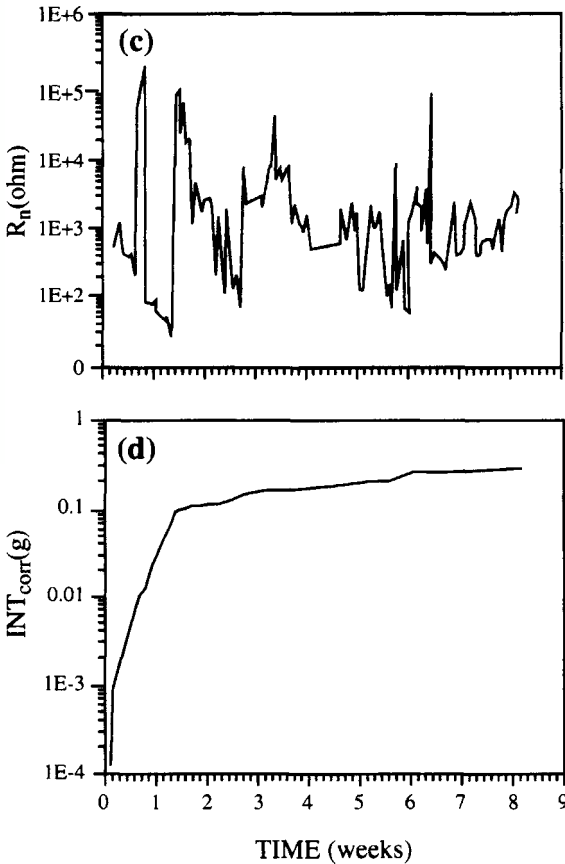


Figure 14. Continued.

## 8. Electrochemical Impedance Spectroscopy

Electrochemical impedance spectroscopy techniques record impedance data as a function of the frequency of an applied signal at a fixed potential. A large frequency range (65 kHz–1 mHz) must be investigated to obtain a complete impedance spectrum. Dowling et al.<sup>26</sup> and Franklin et al.<sup>27</sup> demonstrated that the small signals required for EIS do not adversely affect the numbers, viability, and activity of microorganisms within a biofilm. EIS data may be used to determine  $R_p$ , the inverse of the corrosion

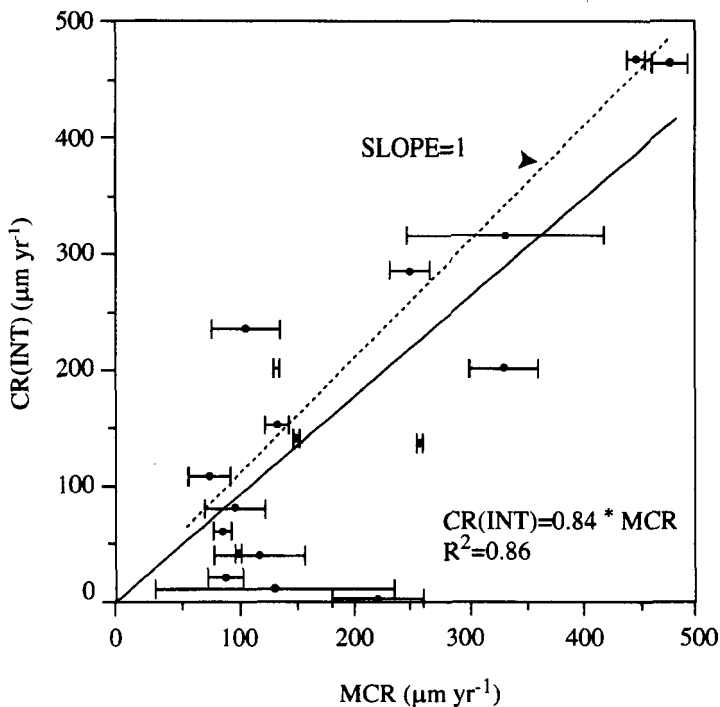


Figure 15.  $CR_{\text{int}}$  values for 19 noise probes compared with mean corrosion rates (MCR) determined from weight loss.

rate. EIS is commonly used for steady-state conditions (uniform corrosion); however, sophisticated models have been developed for localized corrosion.<sup>28,29</sup> Several reports have been published in which EIS has been used to study the role of SRB in corrosion of buried pipes and reinforced concrete.<sup>3,4,30</sup> The formation of biofilms and calcareous deposits on three stainless steels and titanium during exposure to natural seawater was monitored using EIS and surface analysis (Fig. 16).<sup>31</sup> Dowling et al.<sup>32</sup> studied the effects of MIC on stainless steel weldments in artificial seawater using EIS and small-amplitude cyclic voltammetry. They concluded from the frequency dependence of the impedance data that two relaxations were associated with the as-welded inoculated surface, while only one time constant was detected in the Bode plots for the as-welded

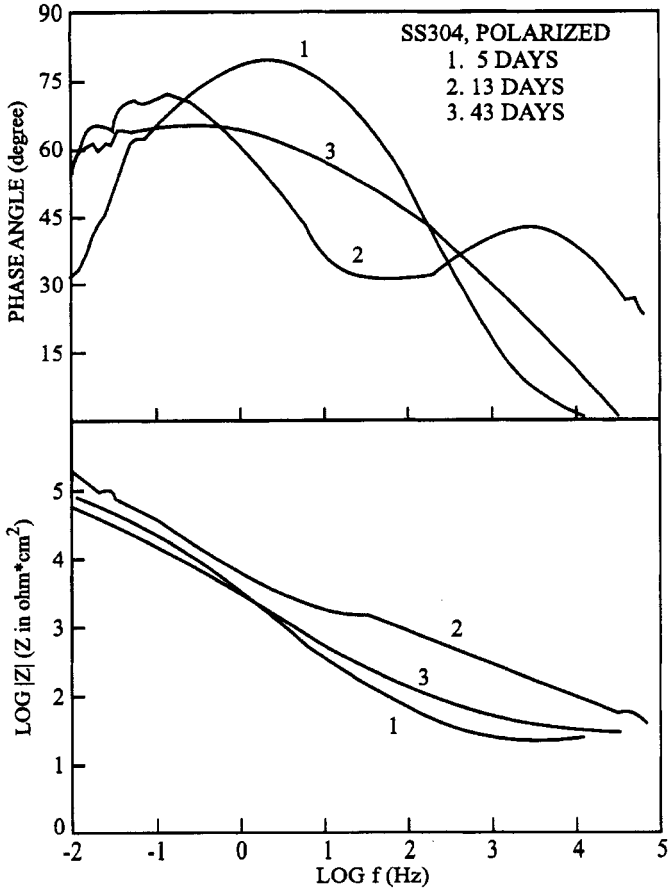


Figure 16. Impedance spectra for polarized 304 stainless steel after exposure periods of 5, 13, and 43 days. EIS data taken at  $E_{\text{corr}}$ .

sterile surface polished surfaces, speculating that the occurrence of a second time constant was due to the development of pits. Dowling et al.<sup>33</sup> used EIS to study the corrosion behavior of carbon steels affected by bacteria and attempted to determine  $R_p$  from the EIS data. Ferrante and Feron<sup>34</sup> used EIS data to conclude that the material composition of steels was more important for MIC resistance than bacterial population, incuba-



tion time, sulfide content, and other products of bacterial growth. Jones et al.<sup>35</sup> used EIS to determine the effects of several mixed microbiological communities on the protective properties of epoxy top coatings over zinc-primed steel. Spectra for the control remained capacitive, indicating intact coatings, while spectra for five samples exposed to mixed cultures of bacteria indicated corrosion and delamination (Fig. 17). Figure 18 shows EIS Bode plots for mild steel immersed in natural oilfield-produced water with [18(b)] and without [18(a)] added nutrients to support SRB growth.<sup>36</sup> Few changes resulted in the supplemented waters, while significant alterations were observed in those without supplements. Figure 18(a) shows a greater increase in the phase angle at lowest frequencies, suggesting the formation of a thicker biofilm.

The system for remote ENA and EIS data collection (Fig. 13) has been used to monitor polymer coating degradation over a 2-year period for coatings exposed to artificial and natural seawater.<sup>25</sup> After exposure periods of about 1 year, the polyurethane topcoat became susceptible to biodegradation, especially for coatings with zinc and aluminum primers. Most other coatings tested were not susceptible to biodegradation. Epoxy polyamide coatings had excellent water and chemical resistance, strong

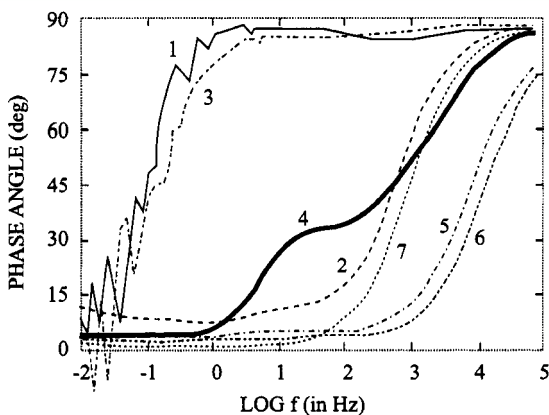


Figure 17. EIS Bode plot for epoxy coating over zinc-primed steel exposed for 2 months to uninoculated medium (curve 1) and six mixed cultures of facultative anaerobes (curves 2–7). (Reprinted from Ref. 35 with permission from NACE International.)

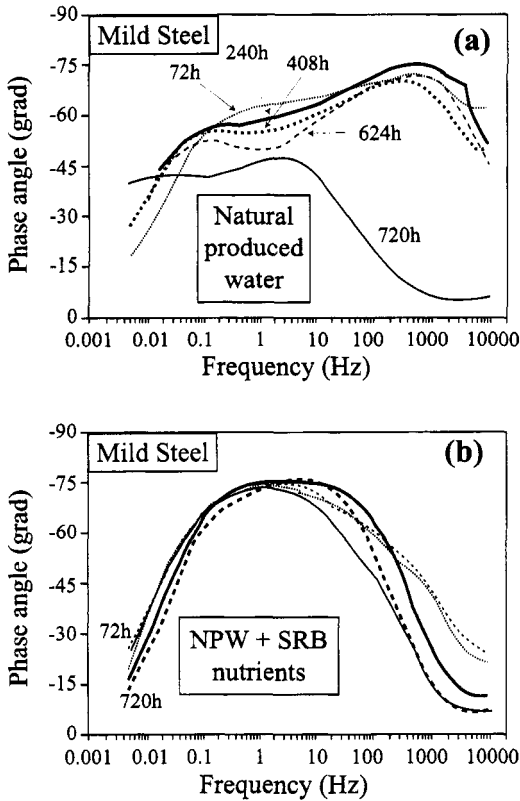


Figure 18. Phase angle vs. frequency plots from mild steel at different immersion times in (a) natural oilfield-produced water and (b) the same water with added SRB nutrients. (Reprinted from Ref. 36 with permission from NACE International.)

adhesion, and provided the most effective corrosion protection. Both epoxy polyamide and polyurethane were more protective than a latex topcoat. Silicone alkyd coatings, which are usually used for high-temperature applications, did not provide good corrosion protection because of adhesion loss during immersion.

The effects of different primers (metallic zinc, aluminum, and phosphate) over steel and an additional polyurethane topcoat over an epoxy

polyamide midcoat on coating performance in general and attack by microorganisms in particular were studied using a combination of ENA and EIS.<sup>25</sup> Spectra for a zinc primer and polyurethane topcoat had complicated shapes, with lower impedance values for coupons exposed to natural seawater (Fig. 19). Breakpoint frequencies ( $f_b$ ) for coupons in artificial seawater increased from 10 Hz in 2 years, but were much higher for coupons in natural seawater, where they increased significantly in the first 2 months, suggesting that the coating degraded more in natural than in artificial seawater [Fig. 20(a)]. Since both the  $R_p$  of the anodic reaction ( $R_a$ ) and the cathodic reaction ( $R_c$ ) have the same relationship to a delaminated area, only  $R_a$  is shown in Fig. 20(b).  $R_a$  decreased continuously in both media, with lower values in natural seawater, indicating increased coating degradation. The Warburg coefficient, an indicator of the influence of diffusion control in a system, decreases as a delaminated area increases. The coefficient showed a significant decrease in the first 2 months of the coated sample exposures and then remained more or less constant, with lower values in natural than in artificial seawater during the entire exposure period [Fig. 20(c)]. A damage function was defined that

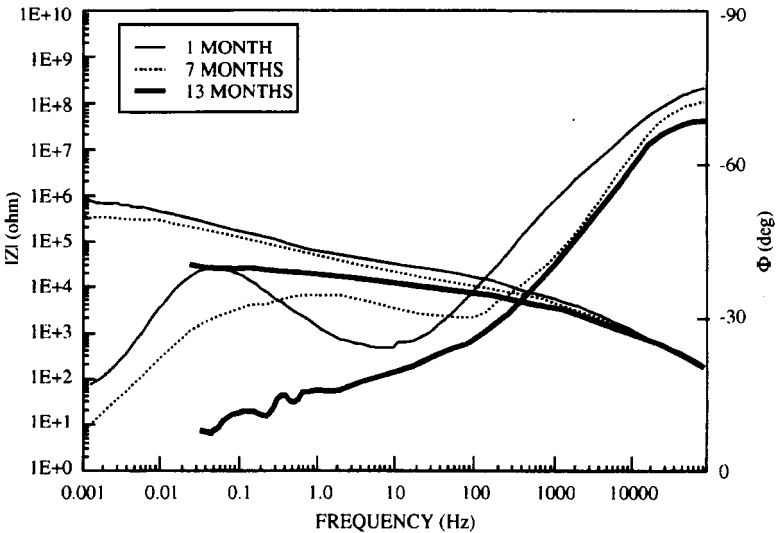


Figure 19. EIS spectra for zinc-coated steel with polyurethane topcoat exposed to natural seawater for 1, 7, and 13 months.

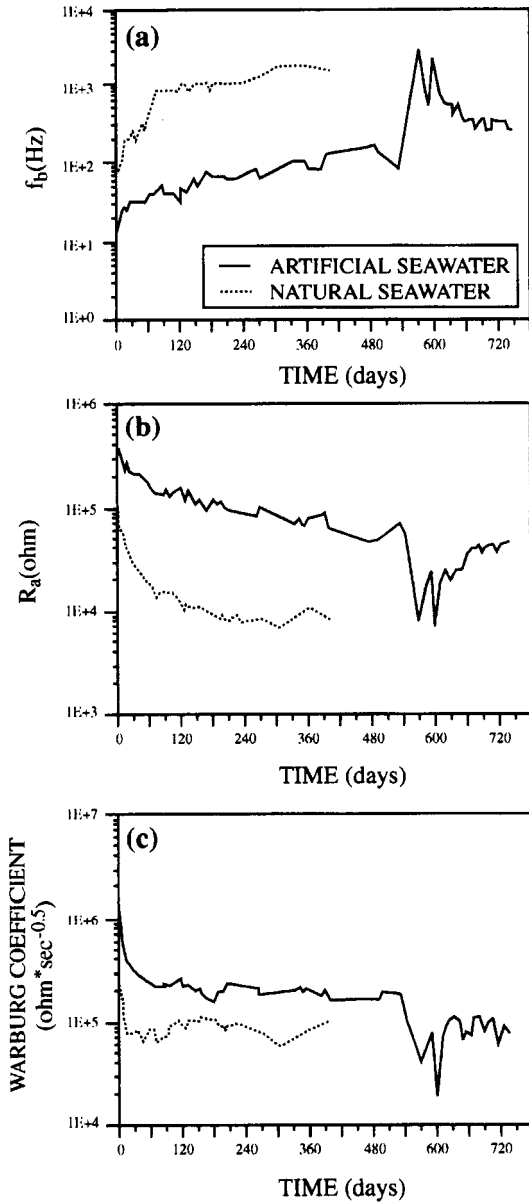


Figure 20. Time dependence of EIS parameters for zinc-coated steel with polyurethane topcoat after exposure to artificial and natural seawater: (a)  $f_b$ , (b)  $R_a$ , and (c) Warburg coefficient.

allowed qualitative assessment of coating deterioration due to MIC. Surfaces were examined using environmental scanning electron microscopy to confirm that remotely collected EIS damage functions were accurate. In all cases of delamination and localized corrosion, bacteria were enmeshed in the corrosion products. Mansfeld<sup>37</sup> determined  $C$  and  $R_p$  for ennobled 316L stainless steel samples exposed in natural seawater in Key West, Florida. Neither changed with time [Fig. 21(a), (b)], indicating that passive film properties did not change as a result of ennoblement in a marine environment.

### 9. Scanning Vibrating Electrode Techniques

Scanning vibrating electrode techniques (SVET) provide a sensitive means of locating local anodic and cathodic currents (vibrating microreference electrode) and potential distributions (Kelvin probe) associated with corrosion. SVET are nondestructive to biofilms and their components and can provide qualitative and quantitative data. Franklin et al.<sup>38</sup> used autoradiography of bacterial incorporated <sup>14</sup>C-acetate to locate bacterial metabolic activity and a scanning vibrating electrode to define anodic and cathodic currents on colonized steel surfaces (Fig. 22). Their results showed a correlation between the location of anodic activity of the steel and the location of incorporated label, suggesting that actively metabolizing bacteria may colonize active anodic sites. SVET are successfully used to monitor early phases of MIC, but are usually complemented by other investigative methods for an overview of corrosion processes.

### 10. Large Signal Polarization Techniques

In the electrochemical techniques described previously, measurements are carried out without the application of an external signal ( $E_{\text{corr}}$ , ENA) or with the application of only a very small perturbation ( $R_p$ , EIS). Large signal polarization techniques require potential scans ranging from several hundred millivolts to several volts. The choice of scan rate is important in MIC studies to reduce effects on biofilm structure and character. The faster the scan rate, the less the impact on microbial activities. Recording polarization curves provides an overview of reactions for a given corrosion system—charge-transfer or diffusion-controlled reactions, passivity, transpassivity, and localized corrosion phenomena. The effects of alloying or the addition of inhibitors can be recognized in the changes in the polarization curves. Quantitative information obtained from polarization curves includes the values of  $b_a$  and  $b_c$ ,  $i_{\text{corr}}$ , the values of the diffusion-

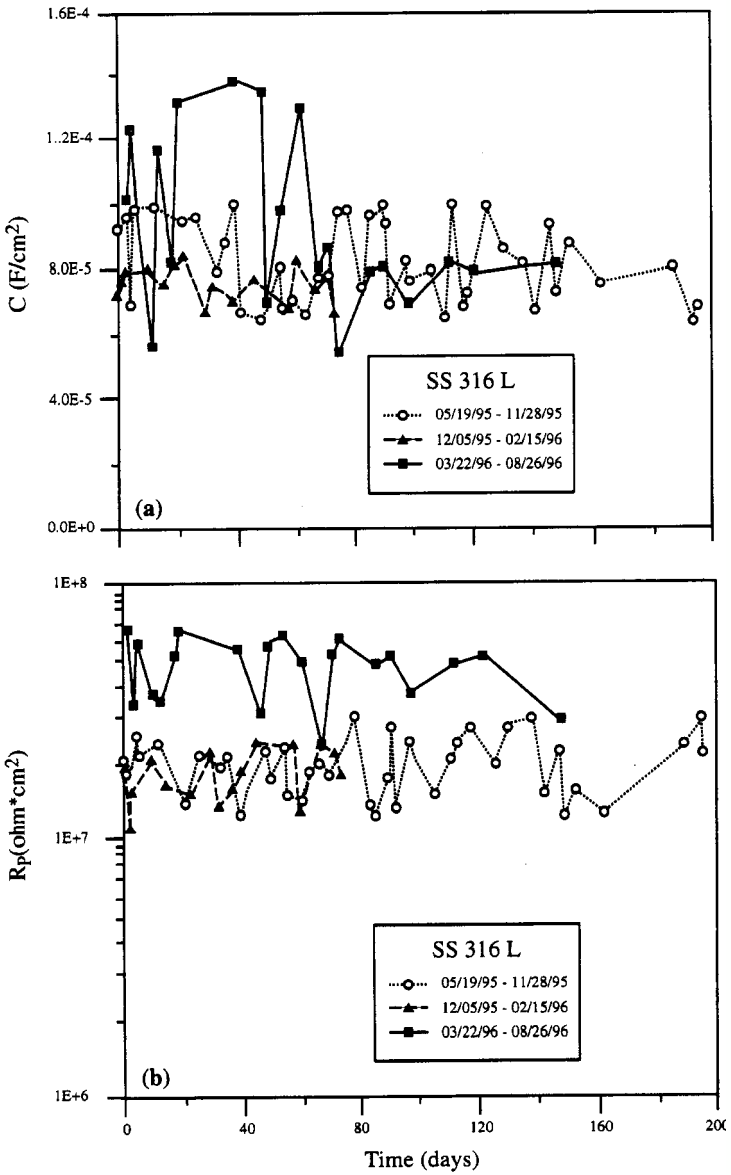


Figure 21. Data for ennobled 316L stainless steel exposed in Key West, Florida, seawater: (a)  $C$ , (b)  $R_p$ . (Reprinted from F. Mansfield, unpublished data.)

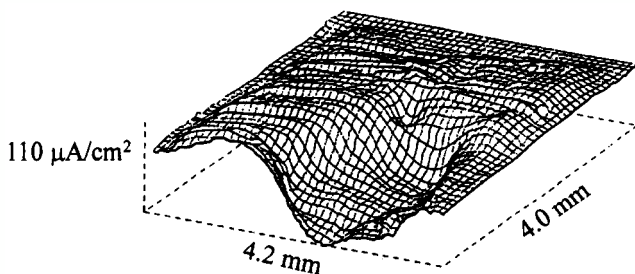


Figure 22. SVET current density map over carbon steel after 23 hr of exposure to aerobic bacteria. (Reprinted from Ref. 39 with permission from NACE International.)

limited current density for hydrogen reduction  $i_{l,h}$  and oxygen reduction  $i_{l,O_2}$  and parameters related to passivity such as the critical potential ( $E_{\text{crit}}$ ), critical current density ( $i_{\text{crit}}$ ) for passivation, and passive current density ( $i_{\text{pass}}$ ). Additional parameters such as pitting potential ( $E_{\text{pit}}$ ) and protection potential ( $E_{\text{prot}}$ ) are related to the susceptibility of a metal for localized corrosion.

Numerous investigators have used polarization curves to determine the effects of microorganisms on the electrochemical properties of metal surfaces and the resulting corrosion behavior. In most of these studies, polarization curves obtained in sterile media have been compared with those obtained in the presence of bacteria and fungi. Figure 23 shows current density vs. potential curves for corrosion systems with and without bacteria.<sup>40</sup> The complexity of the naval brass/polluted seawater interface was demonstrated by Deshmukh et al.<sup>41</sup> who discussed the influence of sulfide pollutants based on results obtained with potentiodynamic polarization curves. In the presence of sulfides or SRB,  $E_{\text{corr}}$  became substantially more negative. An active-passive transition and hysteresis in the reverse scan were observed. De Mele<sup>42</sup> used polarization techniques to evaluate biodeterioration of implant materials, including aluminum in human plasma and silver in saline solution containing  $\text{Na}_2\text{S}$ .

Polarization techniques have also been used to determine mechanisms by which microorganisms induce localized corrosion in the forms of pitting or crevice corrosion. In most cases  $E_{\text{pit}}$  was determined in the presence and absence of bacteria.  $E_{\text{pit}}$  provides data as to the tendency for pitting, but not the rate for pit propagation. Salvarezza et al.<sup>43</sup> and De Mele

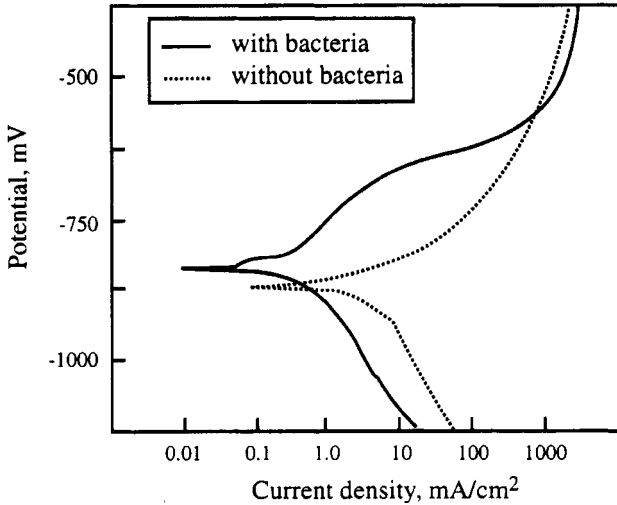


Figure 23. Current density vs. potential curves of a corrosion system with and without bacteria obtained by large signal polarization. (Reprinted from Ref. 40 with permission of Wiley-VCH, Weinheim, Germany.)

et al.<sup>44</sup> used several isolates obtained from jet fuel storage tank sludges to determine the influence of microorganisms on aluminum alloys in fuel-water systems. They concluded that  $E_{\text{pit}}$  could be used to determine biological attack. Other researchers<sup>45,46</sup> determined the influence of microbial contaminants in aircraft fuel, alloying elements, and surface heterogeneities on initiation and propagation of pitting in Al 7075 and concluded that electrochemical tests reproduced the corrosion problems observed in service conditions. Videla<sup>47</sup> used an  $E_{\text{pit}}$  technique in a study of the action of *Cladosporium resinae* growth on the electrochemical behavior of aluminum. Current transients at different potentials were compared for Al 2024 in 0.01 M NaCl and in 0.01 M NaCl + 0.05 M citric acid (pH 2.5). These data suggest that  $E_{\text{pit}}$  in 0.01 M NaCl was between -0.55 V and -0.50 VSCE and was more positive than -0.55 V in the solution of pH 2.5.

Ringas and Robinson<sup>48</sup> performed electrochemical tests on stainless steels and mild steels in three cultures of SRB. In all cases pitting resistance was lower in cultures of SRB. Potentiodynamic polarization



curves with a reverse scan were used for studies of 316 stainless steel in sterile media and in cultures of SRB. In sterile media, the alloy was passive and displayed a large passive range. The reverse scan showed that active pits did not form. The shape of the anodic polarization curve was very different in the bacterial culture.  $E_{\text{corr}}$  was more active; an active-passive transition was observed and the passive current density was higher, suggesting that the passive film formed in the bacterial culture was less protective. The reverse scan showed that active pits had been formed and did not repassivate. Similar results were shown for 409 and 430 stainless steels. The authors concluded that sulfide-induced pits were initiated at more negative potentials than those initiated by chlorides.

### III. CONCLUSIONS

As indicated by the data presented in this chapter, modern electrochemical techniques are useful for MIC investigations. However, the nature of MIC makes it extremely difficult to use electrochemical techniques for detection, quantification, mechanistic studies, or monitoring. MIC is often the result of viable microorganisms within a viscoelastic, nonconducting biofilm. Techniques that do not require application of an external signal ( $E_{\text{corr}}$ , dual-cell measurements, and ENA) permit electrochemical measurements without disruption of the causative processes. Most corrosion reactions in MIC are of a very localized nature. This makes use of electrochemical techniques, which in general produce an average signal over the entire surface, difficult. As with all studies of localized corrosion phenomena, more detailed and reliable information can be obtained when a number of different electrochemical techniques are combined. MIC does not produce a unique form of corrosion, so any analytical technique must be accompanied by differentiation between biological and abiological processes. Resolution requires the use of microbiological, surface analytical, and surface imaging techniques.

### ACKNOWLEDGMENTS

This work was supported by the Office of Naval Research, Program Element 601153N through the Defense Research Sciences Program, NRL Contribution Number NRL/BN7333-98-0003. The authors thank Dr. Paul Natishan, Naval Research Laboratory, Washington, DC for careful reading of this manuscript and insightful suggestions.

## REFERENCES

- <sup>1</sup>X. Zhang, R. A. Buchanan, E. E. Stansbury, and N. J. E. Dowling, in *CORROSION/89*, paper no. 512, NACE International, Houston, TX, 1989.
- <sup>2</sup>F. Mansfeld, in *Advances in Corrosion Science and Technology*, Vol. 6, Ed. by M. G. Fontana and R. W. Staehle, Plenum Press, New York, 1976, pp. 163–262.
- <sup>3</sup>R. A. King, B. S. Skerry, D. C. A. Moore, J. F. D. Stott, and J. L. Dawson, in *Biologically Induced Corrosion*, Ed. by S. C. Dexter, NACE International, Houston, TX, 1986, pp. 83–91.
- <sup>4</sup>K. Kasahara and E. Kajiyama, in *Biologically Induced Corrosion*, Ed. by S. C. Dexter, NACE International, Houston, TX, 1986, pp. 172–183.
- <sup>5</sup>D. E. Nivens, J. Q. Chambers, and D. C. White, in *Microbially Influenced Corrosion and Biodeterioration*, Ed. by N. J. Dowling, M. W. Mittelman, and J. C. Danko, University of Tennessee, Knoxville, TN, 1991, pp. 5–47–5–56.
- <sup>6</sup>F. Mansfeld, H. Shih, A. Postyn, J. Deviny, R. Islander, and C. L. Chen, *Corrosion* **47** (5) (1991) 369.
- <sup>7</sup>R. Johnsen and E. Bardal, *Corrosion* **41** (5) (1985) 296.
- <sup>8</sup>S. C. Dexter and G. Y. Gao, *Corrosion* **44** 10 (1988) 717.
- <sup>9</sup>P. Chandrasekaran and S. C. Dexter, *CORROSION/93*, paper no. 493, NACE International, Houston, TX, 1990.
- <sup>10</sup>P. Linhardt, *DECHEMA Monographs* **133** (1996) 77.
- <sup>11</sup>W. H. Dickinson, F. Caccavo, and Z. Lewandowski, *Corros. Sci.* **38** (8) (1996) 1407.
- <sup>12</sup>W. H. Dickinson, Z. Lewandowski, and R. D. Geer, *Corrosion* **52** (12) (1996) 910.
- <sup>13</sup>F. Mansfeld, R. Tsai, H. Shih, B. Little, R. Ray, and P. Wagner, *Corros. Sci.* **33** (3) (1992) 445.
- <sup>14</sup>P. V. Popat and N. Hackerman, *J. Phys. Chem.*, **65** (1961) 1201.
- <sup>15</sup>E. R. Vago, E. J. Calvo, and M. Stratmann, *Electrochim. Acta* **39** (1994) 1655.
- <sup>16</sup>N. Ramasubramanian, N. Preocanin, and R. D. Davidson, *J. Electrochem. Soc.* **132** (4) (1985) 793.
- <sup>17</sup>W. Lee and D. deBeer, *Biofouling* **8** (1995) 273.
- <sup>18</sup>Z. Lewandowski, W. C. Lee, W. G. Characklis, and B. Little, in *CORROSION/88*, paper no. 93, NACE International, Houston, TX, 1988.
- <sup>19</sup>W. Lee, Z. Lewandowski, M. Morrison, W. G. Characklis, R. Avci, and P. Nielsen, *Biofouling* **7** (1993) 217.
- <sup>20</sup>S. M. Gerchakov, B. J. Little, and P. Wagner, *Probing Microbiologically Induced Corrosion* **42** (1986) 689.
- A. Legat, in *12th International Corrosion Congress*, NACE International, Houston, TX, 1993.
- <sup>22</sup>W. P. Iverson, *J. Electrochem. Soc.* **115** (1968) 617.
- <sup>23</sup>W. P. Iverson, G. J. Olson, and L. E. Heverly, in *Biologically Induced Corrosion*, Ed. by S. C. Dexter, NACE International, Houston, TX, 1986, pp. 154–161.
- <sup>24</sup>A. N. Moosavi, J. L. Dawson, C. J. Houghton, and R. A. King, in *Biologically Induced Corrosion*, Ed. by S. C. Dexter, NACE International, Houston, TX, 1986, pp. 291–308.
- <sup>25</sup>F. Mansfeld, C. Chen, C. C. Lee, and H. Xiao, in *Corros. Sci.* **38** (3) (1996) 497.
- <sup>26</sup>N. J. E. Dowling, M. Franklin, D. C. White, C. H. Lee, and C. Lundin, in *CORROSION/89*, paper no. 187, NACE International, Houston, TX, 1989.
- <sup>27</sup>M. J. Franklin, D. E. Nivens, J. B. Guckert, and D. C. White, *Corrosion* **47** (7) (1991) 519.
- <sup>28</sup>M. Kendig, F. Mansfeld, and S. Tsai, *Corros. Sci.* **23** (4) (1983) 317.
- <sup>29</sup>F. Mansfeld, M. Kendig, and S. Tsai, *Corrosion* **38** (1982) 478.
- <sup>30</sup>K. Kasahara and E. Kajiyama, in *Microbially Influenced Corrosion and Biodeterioration*, Ed. by N. J. Dowling, M. W. Mittelman, and J. C. Danko, University of Tennessee, Knoxville, TN, 1991, pp. 2-33–2-39.

- <sup>31</sup>F. Mansfeld, R. Tsai, H. Shih, B. Little, R. Ray, P. Wagner, in *CORROSION/90*, paper no. 109, NACE International, Houston, TX, 1990.
- <sup>32</sup>N. J. E. Dowling, M. Franklin, D. C. White, C. H. Lee, and C. Lundin, in *CORROSION/89*, paper no. 187, NACE International, Houston, TX, 1989.
- <sup>33</sup>N. J. E. Dowling, J. Guezenec, M. L. Lemoine, A. Tunlid, and D. C. White, *Corrosion* **44** (12) (1988) 869.
- <sup>34</sup>V. Ferrante and D. Feron, in *Microbially Influenced Corrosion and Biodeterioration*, Ed. by N. J. Dowling, M. W. Mittleman, and J. C. Danko, University of Tennessee, Knoxville, TN, 1991, pp. 3-55-3-63.
- <sup>35</sup>J. Jones, M. Walch, and F. Mansfeld, in *CORROSION/91*, paper no. 108, NACE International, Houston, TX, 1991.
- <sup>36</sup>J. S. Luo, P. Angell, D. C. White, and I. Vance, in *CORROSION/94*, paper no. 265, NACE International, Houston, TX, 1994.
- <sup>37</sup>F. Mansfeld, unpublished data.
- <sup>38</sup>M. J. Franklin, D. C. White, and H. S. Isaacs, *Corros. Sci.* **32** (9) (1991) 945.
- <sup>39</sup>M. J. Franklin, D. C. White, and H. S. Isaacs, in *CORROSION/90*, paper no. 104, NACE International, Houston, TX, 1990.
- <sup>40</sup>G. Schmitt, *Mat. and Corros.* **48** (1997) 586.
- <sup>41</sup>M. B. Deshmukh, I. Akhtar, and C. P. De, in *2nd International Symposium on Industrial and Oriented Basic Electrochemistry*, Saest, India, IBH Publishing, Oxford, 1988.
- <sup>42</sup>M. F. L. de Mele, in *Argentine/USA Workshop on Biodeterioration (CONICET-NSF)*, Aquatec Quimica, LaPlata, Argentina (1986) 119.
- <sup>43</sup>R. C. Salvarezza, M. F. L. de Mele, and H. A. Videla, *Int. Biodeterior. Bull.* **15** (4) (1979) 125.
- <sup>44</sup>M. F. L. de Mele, R. C. Salvarezza, and H. A. Videla, *Int. Biodeterior. Bull.* **15** (2) (1979) 39.
- <sup>45</sup>H. A. Videla, P. S. Guimet, S. DoValle, and E. H. Reinoso, in *CORROSION/88*, paper no. 91, NACE International, Houston, TX, 1988.
- <sup>46</sup>B. M. Rosales, A. Puebla, and D. Cabral, in *12th International Corrosion Congress*, NACE International, Houston, TX, 1993, p. 3773.
- <sup>47</sup>H. Videla, in *Biologically Induced Corrosion*, Ed. by S. C. Dexter, NACE International, Houston, TX, 1986, pp. 215-222.
- <sup>48</sup>C. Ringas and F. P. A. Robinson, *Corrosion* **44** (6) (1988) 386.

## Cumulative Author Index for Numbers 1–34

Author	Title	Number
Abrūna, H. D.	X Rays as Probes of Electrochemical Interfaces	20
Adžić, R.	Reaction Kinetics and Mechanisms on Metal Single Crystal Electrode Surfaces	21
Agarwal, H. P.	Recent Developments in Faradaic Rectification Studies	20
Albella, J. M.	Electric Breakdown in Anodic Oxide Films	23
Allongue, P.	Physics and Applications of Semiconductor Electrodes Covered with Metal Clusters	23
Amokrane, S.	Analysis of the Capacitance of the Metal-Solution Interface. Role of the Metal and the Metal-Solvent Coupling	22
Andersen, J. E. T.	Automated Methods of Corrosion Measurement	31
Andersen, H. C.	Improvements upon the Debye Huckel Theory of Ionic Solutions	11
Andersen, T. N.	The Manganese Dioxide Electrode in Aqueous Solution	30
Andersen, T. N.	Potentials of Zero Charge of Electrodes	5
Aogaki, R.	Nonequilibrium Fluctuations in the Corrosion Process	33
Appleby, A. J.	Electrocatalysis	9
Aramata, A.	Underpotential Deposition on Single Crystal Metals	31
Arvia, A. J.	Transport Phenomena in Electrochemical Kinetics	6
Arvia, A. J.	A Modern Approach to Surface Roughness Applied to Electrochemical Systems	28
Augustynski, J.	Application of Auger and Photoelectron Spectroscopy of Electrochemical Problems	13
Badawy, W.A.	Photovoltaic and Photoelectrochemical Cells Based on Schottky Barrier Heterojunctions	30

Author	Title	Number
Badiali, J. P.	Analysis of the Capacitance of the Metal-Solution Interface. Role of the Metal and the Metal-Solvent Coupling	22
Baker, B. G.	Surface Analysis by Electron Spectroscopy	10
Balsene, L.	Application of Auger and Photoelectron Spectroscopy to Electrochemical Problems	13
Barthel, J.	Temperature Dependence of Conductance of Electrolytes in Nonaqueous Solutions	13
Batchelor, R. A.	Surface States on Semiconductors	22
Bauer, G. L.	Improvements in Fluorine Generation	33
Bauer, H. H.	Critical Observations on the Measurement of Adsorption at Electrodes	7
Bebelis, S. I.	The Electrochemical Activation of Catalytic Reactions	29
Bech-Nielsen, G.	Automated Methods of Corrosion Measurement	31
Becker, R. O.	Electrochemical Mechanisms and the Control of Biological Growth Processes	10
Beden, B.	Electrocatalytic Oxidation of Oxygenated Aliphatic Organic Compounds at Noble Metal Electrodes	22
Benderskii, V. A.	Phase Transitions in the Double Layer at Electrodes	26
Benjamin, I.	Molecular Dynamic Simulations in Interfacial Electrochemistry	31
Berg, H.	Bioelectrochemical Field Effects: Electrostimulation of Biological Cells by Low Frequencies	24
Berwick, A.	The Study of Simple Consecutive Processes in Electrochemical Reactions	5
Bisgård, A. D.	Automated Methods of Corrosion Measurement	31
Blank, M.	Electrochemistry in Nerve Excitation	24
Bloom, H.	Models for Molten Salts	9
Bloom, H.	Molten Electrolytes	2
Blyholder, G.	Quantum Chemical Treatment of Adsorbed Species	8
Bockris, J. O'M.	Electrode Kinetics	1
Bockris, J. O'M.	Ionic Solvation	1
Bockris, J. O'M.	The Mechanism of Charge Transfer from Metal Electrodes to Ions in Solution	6

Author	Title	Number
Bockris, J. O'M.	The Mechanism of the Electrode Position of Metals	3
Bockris, J. O'M.	Molten Electrolytes	2
Bockris, J. O'M.	Photoelectrochemical Kinetics and Related Devices	14
Boguslavsky, L. I.	Electron Transfer Effects and the Mechanism of the Membrane Potential	18
Breiter, M. W.	Adsorption of Organic Species on Platinum Metal Electrodes	10
Breiter, M. W.	Low-Temperature Electrochemistry at High-T <sub>2</sub> Superconductor/Ionic Conductor Interfaces	28
Brodskii, A. N.	Phase Transitions in the Double Layer at Electrodes	26
Burke, L. D.	Electrochemistry of Hydrous Oxide Films	18
Burney, H. S.	Membrane Chlor-Alkali Process	24
Charle, K. P.	Spin-Dependent Kinetics in Dye-Sensitized Charge-Carrier Injection into Organic Crystal Electrodes	19
Cheh, H. Y.	Theory and Applications of Periodic Electrolysis	19
Childs, W. V.	Improvements in Fluorine Generation	33
Christov, S. G.	Quantum Theory of Charge-Transfer Processes in Condensed Media	28
Conway, B. E.	The Behavior of Intermediates in Electrochemical Catalysis	3
Conway, B. E.	Fundamental and Applied Aspects of Anodic Chlorine Production	14
Conway, B. E.	Ionic Solvation	1
Conway, B. E.	Proton Solvation and Proton Transfer Processes in Solution	3
Conway, B. E.	Solvated Electrons in Field- and Photo-assisted Processes at Electrodes	7
Conway, B. E.	The Temperature and Potential Dependence of Electrochemical Reaction Rates, and the Real Form of the Tafel Equation	16
Conway, B. E.	Electroanalytical Methods for Determination of Al <sub>2</sub> O <sub>3</sub> in Molten Cryolite	26
Covington, A. K.	NMR Studies of the Structure of Electrolyte Solutions	12

Author	Title	Number
Daikhin, L. I.	Phase Transitions in the Double Layer at Electrodes	26
Damaskin, B. B.	Adsorption of Organic Compounds at Electrodes	3
Damjanovic, A.	The Mechanism of the Electrodeposition of Metals	3
Damjanovic, A.	Mechanistic Analysis of Oxygen Electrode Reactions	5
Desnoyers, J. B.	Hydration Effects and Thermodynamic Properties of Ions	5
Despić, A.	Electrochemistry of Aluminum in Aqueous Solutions and Physics of Its Anodic Oxide	20
Despić, A. R.	Transport-Controlled Deposition and Dissolution of Metals	7
Despić, A. R.	Electrochemical Deposition and Dissolution of Alloys and Metal Components—Fundamental Aspects	27
Djokić, S. S.	Electrodeposition of Nickel-Iron Alloys	22
Djokić, S. S.	Electroanalytical Methods for Determination of $Al_2O_3$ in Molten Cryolite	26
Drazic, D. M.	Iron and Its Electrochemistry in an Active State	19
Efrima, S.	Surface-Enhanced Raman Scattering (SERS)	16
Eisenberg, H.	Physical Chemistry of Synthetic Polyelectrolytes	1
Elving, P. J.	Critical Observations on the Measurement of Adsorption at Electrodes	7
Enyo, M.	Mechanism of the Hydrogen Electrode Reaction as Studied by Means of Deuterium as a Tracer	11
Enyo, M.	Sorption of Hydrogen on and in Hydrogen-Absorbing Metals in Electrochemical Environments	30
Erdey-Grúz, T.	Proton Transfer in Solution	12
Fahidy, T. Z.	Recent Advance in the Study of the Dynamics of Electrode Processes	27
Fahidy, T. Z.	The Effect of Magnetic Fields on Electrochemical Processes	32
Falkenhagen, H.	The Present State of the Theory of Electrolytic Solutions	2

Author	Title	Number
Farges, J.-P.	Charge-Transfer Complexes in Electrochemistry	12
Farges, J.-P.	An Introduction to the Electrochemistry of Charge Transfer Complexes II	13
Findl, E.	Bioelectrochemistry-Electrophysiology-Electrobiology	14
Floyd, W. F.	Electrochemical Properties of Nerve and Muscle	1
Foley, J. K.	Interfacial Infrared Vibrational Spectroscopy	17
Friedman, H. L.	Computed Thermodynamic Properties and Distribution Functions for Simple Models of Ionic Solutions	6
Frumkin, A. A. N.	Adsorption of Organic Compounds at Electrodes	3
Fuller, T. F.	Metal Hydride Electrodes	27
Fuoss, R. M.	Physical Chemistry of Synthetic Polyelectrolytes	1
Galvele, I. R.	Electrochemical Aspects of Stress Corrosion Cracking	27
German, E. D.	The Role of the Electronic Factor in the Kinetics of Charge-Transfer Reactions	24
Gileadi, E.	The Behavior of Intermediates in Electrochemical Catalysis	3
Gileadi, E.	The Mechanism of Oxidation of Organic Fuels	4
Girault, H. H.	Charge Transfer across Liquid-Liquid Interfaces	25
Goddard, E. D.	Electrochemical Aspects of Adsorption on Mineral Solids	13
Goodisman, J.	Theories for the Metal in the Metal-Electrolyte Interface	20
Gores, H.-J.	Temperature Dependence of Conductance of Electrolytes in Nonaqueous Solutions	13
Goruk, W. S.	Anodic and Electronic Currents at High Fields in Oxide Films	4
Gratzel, M.	Interfacial Charge Transfer Reactions in Colloidal Dispersions and Their Application to Water Cleavage by Visible Light	15
Green, M.	Electrochemistry of the Semiconductor-Electrolyte Interface	2



Author	Title	Number
Gregory, D. P.	Electrochemistry and the Hydrogen Economy	10
Gu, Z. H.	Recent Advance in the Study of the Dynamics of Electrode Processes	27
Gurevich, Y. Y.	Electrochemistry of Semiconductors: New Problems and Prospects	16
Gutiérrez, C.	Potential-Modulated Reflectance Spectroscopy Studies of the Electronic Transitions of Chemisorbed Carbon Monoxide	28
Gutmann, F.	Charge-Transfer Complexes in Electrochemistry	12
Gutmann, F.	The Electrochemical Splitting of Water	15
Gutmann, F.	An Introduction to the Electrochemistry of Charge Transfer Complexes II	13
Habib, M. A.	Solvent Dipoles at the Electrode-Solution Interface	12
Haering, R. R.	Physical Mechanisms of Intercalation	15
Hamann, S. D.	Electrolyte Solutions at High Pressure	9
Hamelin, A.	Double-Layer Properties at sp and sd Metal Single-Crystal Electrodes	16
Hamnett, A.	Surface States on Semiconductors	22
Hansma, P. K.	Scanning Tunneling Microscopy: A Natural for Electrochemistry	21
Hanington, D. A.	Ultrahigh-Vacuum Surface Analytical Methods in Electrochemical Studies of Single-Crystal Surfaces	28
Heiland, W.	The Structure of the Metal-Vacuum Interface	11
Herman, P. J.	Critical Observations on the Measurement of Adsorption at Electrodes	7
Hickling, A.	Electrochemical Processes in Glow Discharge at the Gas-Solution Interface	6
Hine, F.	Chemistry and Chemical Engineering in the Chlor-Alkali Industry	18
Hoar, T. R.	The Anodic Behavior of Metals	2
Hopfinger, A. J.	Structural Properties of Membrane Ionomers	14
Humffray, A. A.	Methods and Mechanisms in Electroorganic Chemistry	8
Hunter, R. J.	Electrochemical Aspects of Colloid Chemistry	11
Jaegermann, W.	The Semiconductor/Electrolyte Interface: A Surface Science Approach	30

Author	Title	Number
Jaksic, M. M.	The Electrochemical Activation of Catalytic Reactions	29
Johnson, C. A.	The Metal–Gas Interface	5
Jolieoeur, C.	Hydration Effects and Thermodynamic Properties of Ions	5
Jović, V. D.	Electrochemical Deposition and Dissolution of Alloys and Metal Components—Fundamental Aspects	27
Jurkiewicz-Herbich, M.	Metal/Solution Interface: An Experimental Approach	31
Kebarle, P.	Gas-Phase Ion Equilibria and Ion Solvation	9
Kelbg, G.	The Present State of the Theory of Electrolytic Solutions	2
Kelly, E. I.	Electrochemical Behavior of Titanium	14
Kahn, S. U. M.	Photoelectrochemical Kinetics and Related Devices	14
Kahn, S. U. M.	Quantum Mechanical Treatments in Electrode Kinetics	31
Kahn, S. U. M.	Some Fundamental Aspects of Electrode Processes	15
Koczorowski, Z.	Voltaic Cells in Electrochemistry and Surface Chemistry of Liquids	34
Krischer, K.	Principles of Temporal and Spatial Pattern Formation in Electrochemical Systems	32
Krstajic', N.V.	The Mechanism of Coarse and Disperse Electrodeposits	30
Lamy, C.	Direct Methanol Fuel Cells: From a Twentieth Century Electrochemist's Dream to a Twenty-First Century Emerging Technology	34
Lasia, A.	Electrochemical Impedance Spectroscopy and Its Applications	32
Lefebvre, M. C.	Establishing the Link Between Multistep Electrochemical Reaction Mechanisms and Experimental Tafel Slopes	32
Léger, J.-M.	Direct Methanol Fuel Cells: From a Twentieth Century Electrochemist's Dream to a Twenty-First Century Emerging Technology	34
Little, B. J.	Application of Electrochemical Techniques to the Study of Microbiologically Influenced Corrosion	34
Lust, E.	The Potential of Zero Charge	33

Author	Title	Number
Lyklema, J.	Interfacial Electrostatics and Electrodynamics in Disperse Systems	17
Lynn, K. G.	The Nickel Oxide Electrode	21
Lyons, M. E. G.	Electrochemistry of Hydrrous Oxide Films	18
MacDonald, D. D.	The Electrochemistry of Metals in Aqueous Systems at Elevated Temperatures	11
MacDonald, D. D.	Impedance Measurements in Electrochemical Systems	14
Maksimovic, M. D.	Theory of the Effect of Electrodeposition at a Periodically Changing Rate on the Morphology of Metal Deposits	19
Mandel, L. J.	Electrochemical Processes at Biological Interfaces	8
Marchiano, S. L.	Transport Phenomena in Electrochemical Kinetics	6
Marincic, N.	Lithium Batteries with Liquid Depolarizers	15
Markin, V. S.	Thermodynamics of Membrane Energy Transduction in an Oscillating Field	24
Martinez-Duart, J. M.	Electric Breakdown in Anodic Oxide Films	23
Matthews, D. B.	The Mechanism of Charge Transfer from Metal Electrodes to Ions in Solution	6
Mauritz, K. A.	Structural Properties of Membrane Ionomers	14
McBreen, J.	The Nickel Oxide Electrode	21
McKinnon, W. R.	Physical Mechanisms of Intercalation	15
McKubre, M. C. H.	Impedance Measurements in Electrochemical Systems	14
Mizuno, T.	Sorption of Hydrogen on and in Hydrogen-Absorbing Metals in Electrochemical Environments	30
Modi, V.	Analysis of Mass Transfer and Fluid Flow for Electrochemical Processes	32
Murphy, O. J.	The Electrochemical Splitting of Water	15
Nagarkan, P. V.	Electrochemistry of Metallic Glasses	21
Nágy, Z.	DC Electrochemical Techniques for the Measurement of Corrosion Rates	25
Nágy, Z.	DC Relaxation Techniques for the Investigation of Fast Electrode Reactions	21
Neophytides, S. G.	The Electrochemical Activation of Catalytic Reactions	29

Author	Title	Number
Newman, J.	Photoelectrochemical Devices for Solar Energy Conversion	18
Newman, J.	Determination of Current Distributions Governed by Laplace's Equation	23
Newman, J.	Metal Hydride Electrodes	27
Newman, K. E.	NMR Studies of the Structure of Electrolyte Solutions	12
Nielsen, L. V.	Automated Methods of Corrosion Measurement	31
Nisancioglu, K.	Design Techniques in Cathodic Protection Engineering	23
Novak, D. M.	Fundamental and Applied Aspects of Anodic Chlorine Production	14
Okada, I.	Transport Properties of Molten Salt	34
O'Keefe, T. J.	Electrogalvanizing	26
Orazem, M. E.	Photoelectrochemical Devices for Solar Energy Conversion	18
Oriani, R. A.	The Metal-Gas Interface	5
Otero, T. F.	Conducting Polymers, Electrochemistry, and Biomimicking Processes	33
Padova, J. I.	Ionic Solvation in Nonaqueous and Mixed Solvents	7
Paik, Woon-kie	Ellipsometry in Electrochemistry	25
Parkhutik, V.	Electrochemistry of Aluminum in Aqueous Solutions and Physics of Its Anodic Oxide	20
Parkhutik, V. P.	Electric Breakdown in Anodic Oxide Films	23
Parsons, R.	Equilibrium Properties of Electrified Interphases	1
Pavlovic, M. G.	Electrodeposition of Metal Powders with Controlled Particle Grain Size and Morphology	24
Perkins, R. S.	Potentials of Zero Charge of Electrodes	5
Pesco, A. M.	Theory and Applications of Periodic Electrolysis	19
Pickup, P. G.	Electrochemistry of Electronically Conducting Polymer Films	33
Piersma, B.	The Mechanism of Oxidation of Organic Fuels	4
Pilla, A. A.	Electrochemical Mechanisms and the Control of Biological Growth Processes	10

Author	Title	Number
Pintauro, P. N.	Transport Models for Ion-Exchange Membranes	19
Pleskov, Y. V.	Electrochemistry of Semiconductors: New Problems and Prospects	16
Plonski, I.-H.	Effects of Surface Structure and Adsorption Phenomena on the Active Dissolution of Iron in Acid Media	29
Plzak, v.	Advanced Electrochemical Hydrogen Technologies: Water Electrolyzers and Fuel Cells	26
Pons, S.	Interfacial Infrared Vibrational Spectroscopy	17
Popov, K. I.	Electrodeposition of Metal Powders with Controlled Particle Grain Size and Morphology	24
Popov, K. I.	The Mechanism of Formation of Coarse and Disperse Electrodeposits	30
Popov, K. I.	Theory of the Effect of Electrodeposition at a Periodically Changing Rate on the Morphology of Metal Deposits	19
Popov, K. I.	Transport-Controlled Deposition and Dissolution of Metals	7
Pound, B. G.	Electrochemical Techniques to Study Hydrogen Ingress in Metals	25
Power, G. P.	Metal Displacement Reactions	11
Reeve, J. C.	Automated Methods of Corrosion Measurement	31
Reeves, R. M.	The Electrical Double Layer: The Current States of Data and Models, with Particular Emphasis on the Solvent	9
Revie, R. W.	Environmental Cracking of Metals: Electrochemical Aspects	26
Ritchie, I. M.	Metal Displacement Reactions	11
Rohland, B.	Advanced Electrochemical Hydrogen Technologies: Water Electrolyzers and Fuel Cells	26
Roscoe, S. G.	Electrochemical Investigations of the Interfacial Behavior of Proteins	29
Rusling, J. F.	Electrochemistry and Electrochemical Catalysis in Microemulsions	26
Russell, J.	Interfacial Infrared Vibrational Spectroscopy	17

Author	Title	Number
Rysselberghe, P. Van	Some Aspects of the Thermodynamic Structure of Electrochemistry	4
Sacher, E.	Theories of Elementary Homogeneous Electron-Transfer Reactions	3
Saemann-Ischenko, G.	Low-Temperature Electrochemistry at High-T <sub>2</sub> Superconductor/Ionic Conductor Interfaces	28
Salvarezza, R. C.	A Modern Approach to Surface Roughness Applied to Electrochemical Systems	28
Sandstede, G. S.	Water Electrolysis and Solar Hydrogen Demonstration Projects	27
Savenko, V. I.	Electric Surface Effects in Solid Plasticity and Strength	24
Scharifker, B. R.	Microelectrode Techniques in Electrochemistry	22
Schmickler, W.	Electron Transfer Reactions on Oxide-Covered Metal Electrodes	17
Schneir, J.	Scanning Tunneling Microscopy: A Natural for Electrochemistry	21
Schultze, J. W.	Electron Transfer Reactions on Oxide-Covered Metal Electrodes	17
Scott, K.	Reaction Engineering and Digital Simulation in Electrochemical Processes	27
Searson, P. C.	Electrochemistry of Metallic Glasses	21
Sepa, D. B.	Energies of Activation of Electrode Reactions A Revisited Problem	29
Seversen, M.	Interfacial Infrared Vibrational Spectroscopy	17
Shchukin, E. D.	Electric Surface Effects in Solid Plasticity and Strength	24
Sides, P. J.	Phenomena and Effects of Electrolytic Gas Evolution	18
Snook, I. K.	Models for Molten Salts	9
Sobkowski, J.	Metal/Solution Interface: An Experimental Approach	31
Somasundaran P.	Electrochemical Aspects of Adsorption on Mineral Solids	13
Sonnenfeld, R.	Scanning Tunneling Microscopy: A Natural for Electrochemistry	21
Soriaga, M. P.	Ultrahigh Vacuum Surface Analytical Methods in Electrochemical Studies of Single-Crystal Surfaces	28

Author	Title	Number
Spiro, M.	A Critique of the Additivity Principle for Mixed Couples	34
Srinivasan, S.	Direct Methanol Fuel Cells: From a Twentieth Century Electrochemist's Dream to a Twenty-First Century Emerging Technology	34
Stickney, J. L.	Ultrahigh-Vacuum Surface Analytical Methods in Electrochemical Studies of Single-Crystal Surfaces	28
Stonehart, P.	Preparation and Characterization of Highly Dispersed Electrocatalytic Materials	12
Szklarczyk, M.	Electrical Breakdown of Liquids	25
Taniguchi, I.	Electrochemical and Photoelectrochemical Reduction of Carbon Dioxide	20
Tarasevich, M. R.	Electrocatalytic Properties of Carbon Materials	19
Thirsk, H. R.	The Study of Simple Consecutive Processes in Electrochemical Reactions	5
Tilak, B. V.	Chemistry and Chemical Engineering in the Chlor-Alkali Industry	18
Tilak, B. V.	Fundamental and Applied Aspects of Anodic Chlorine Production	14
Trasatti, S.	The Potential of Zero Charge	33
Trasatti, S.	Solvent Adsorption and Double-Layer Potential Drop at Electrodes	13
Tributsch, H.	Microwave (Photo)electrochemistry	33
Tributsch, H.	Photoelectrolysis and Photoelectrochemical Catalysis	17
Tsong, T. Y.	Thermodynamics of Membrane Energy Transduction in an Oscillating Field	24
Uosaki, K.	Theoretical Aspects of Semiconductor Electrochemistry	18
Van Leeuwen, H. P.	Interfacial Electrostatics and Electrodynamics in Disperse Systems	17
Vayenas, C. G.	The Electrochemical Activation of Catalytic Reactions	29
Velichko, G. I.	Phase Transitions in the Double Layer at Electrodes	26
Verbmge, M. W.	Transport Models for Ion-Exchange Membranes	19

Author	Title	Number
Vijh, A. K.	Electro-Osmotic Dewatering of Clays, Soils, and Suspensions	32
Vijh, A. K.	Perspectives in Electrochemical Physics	17
Viswanathan, K.	Chemistry and Chemical Engineering in the Chlor-Alkali Industry	18
Von Goldammer, E.	NMR Studies of Electrolyte Solutions	10
Vorotyntsev, M. A.	Modern State of Double Layer Study of Solid Metals	17
Wachter, R.	Temperature Dependence of Conductance of Electrolytes in Nonaqueous Solutions	13
Wagner, P. A.	Application of Electrochemical Techniques to the Study of Microbiologically Influenced Corrosion	34
Wendt, H.	Advanced Electrochemical Hydrogen Technologies: Water Electrolyzers and Fuel Cells	26
Wenglowski, G.	An Economic Study of Electrochemical Industry in the United States	4
West, A. C.	Analysis of Mass Transfer and Fluid Flow for Electrochemical Processes	32
West, A. C.	Determination of Current Distributions Governed by Laplace's Equation	23
Wieckowski, A.	Ultrahigh-Vacuum Surface Analytical Methods in Electrochemical Studies of Single-Crystal Surfaces	28
Wieckowski, A.	<i>In Situ</i> Surface Electrochemistry: Radioactive Labeling	21
Willig, E.	Spin-Dependent Kinetics in Dye-Sensitized Charge-Carrier Injection into Organic Crystal Electrodes	19
Wojtowicz, J.	Oscillatory Behavior in Electrochemical Systems	8
Woods, R.	Chemisorption of Thiols on Metals and Metal Sulfides	29
Wroblowa, H. S.	Batteries for Vehicular Propulsion	16
Wurster, R.	Water Electrolysis and Solar Hydrogen Demonstration Projects	27
Yang, J. D.	Analysis of Mass Transfer and Fluid Flow for Electrochemical Processes	32
Yeager, E. B.	Ultrasonic Vibration Potentials	14



Author	Title	Number
Yeager, H. L.	Structural and Transport Properties of Perfluorinated Ion-Exchange Membranes	16
Yeo, R. S.	Structural and Transport Properties of Perfluorinated Ion-Exchange Membranes	16
Young, L.	Anodic and Electronic Currents at High Fields in Oxide Films	4
Zana, R.	Ultrasonic Vibration Potentials	14
Zobel, F. G. R.	Anodic and Electronic Currents at High Fields in Oxide Films	4

## Cumulative Title Index for Numbers 1–34

Title	Author	Number
Adsorption of Organic Compounds at Electrodes	Frumkin, A. A. N. Damaskin, B. B.	3
Adsorption of Organic Species on Platinum Metal Electrodes	Breiter, M. W.	10
Advanced Electrochemical Hydrogen Technologies: Water Electrolyzers and Fuel Cells	Plzak, v. Rohland, B. Wendt, H.	26
Analysis of the Capacitance of the Metal-Solution Interface. Role of the Metal and the Metal-Solvent Coupling	Amokrane, S. Badiali, J. P.	22
Analysis of Mass Transfer and Fluid Flow for Electrochemical Processes	Yang, J. D. Modi, V. West, A. C.	32
The Anodic Behavior of Metals	Hoar, T. P.	2
Anodic and Electronic Currents at High Fields in Oxide Films	Young, L. Goruk, W. S. Zobel, F. G. R.	4
Application of Auger and Photoelectron Spectroscopy to Electrochemical Problems	Augustynski, J. Balsenc, L.	13
Application of Electrochemical Techniques to the Study of Microbiologically Influenced Corrosion	Little, B. J. Wagner, P. A.	34
Automated Methods of Corrosion Measurement	Bech-Nielsen, G. Andersen, J. E. T. Reeve, J. C. Bisgård, A. D. Nielsen, L. V.	31
Batteries for Vehicular Propulsion	Wroblowa, H. S.	16
The Behavior of Intermediates in Electrochemical Catalysis	Gileadi, E. Conway, B. E.	3
Bioelectrochemical Field Effects: Electrostimulation of Biological Cells by Low Frequencies	Berg, H.	24

Title	Author	Number
Bioelectrochemistry-Electrophysiology- Electrobiolgy	Findl, E.	14
Charge Transfer across Liquid-Liquid Interfaces	Girault, H. H.	25
Charge-Transfer Complexes in Electrochemistry	Farges, J.-P. Gutmann, F.	12
Chemisorption of Thiols on Metals and Metal Sulfides	Woods, R.	29
Chemistry and Chemical Engineering in the Chlor-Alkali Industry	Hine, E Tilak, B. V. Viswanathan, K.	18
Computed Thermodynamic Properties and Distribution Functions for Simple Models of Ionic Solutions	Friedman, H. L.	6
Conducting Polymers, Electrochemistry, and Biomimicking Processes	Otero, T. F.	33
Critical Observations on the Measurement of Adsorption at Electrodes	Bauer, H. H. Herman, P. J. Elving, P. J.	7
A Critique of the Additivity Principle for Mixed Couples	Spiro, M.	34
DC Relaxation Techniques for the Investigation of Fast Electrode Reactions	Nagy, Z.	21
DC Electrochemical Techniques for the Measurement of Corrosion Rates	Nagy, Z.	25
Design Techniques in Cathodic Protection Engineering	Nisancioglu, K.	23
Determination of Current Distributions Governed by Laplace's Equation	West, A. C. Newman, J.	23
Direct Methanol Fuel Cells: From a Twentieth Century Electrochemist's Dream to a Twenty-First Century Emerging Technology	Lamy, C. Uéger, J.-M. Srinivasan, S.	
Double-Layer Properties at sp and sd Metal Single-Crystal Electrodes	Hamelin, A.	16
An Economic Study of Electrochemical Industry in the United States	Wenglowski, G.	4
The Effect of Magnetic Fields on Electrochemical Processes	Fahidy, T. Z.	32

Title	Author	Number
Effect of Surface Structure and Adsorption Phenomena on the Active Dissolution of Iron in Acid Media	Plonski, I.-H.	29
Electrical Breakdown of Liquids	Szklarczyk, M.	25
The Electrical Double Layer: The Current Status of Data and Models, with Particular Emphasis on the Solvent	Reeves, R. M.	9
Electric Breakdown in Anodic Oxide Films	Parkhutik, V. P. Albella, J. M. Martinez-Duart, J. M.	23
Electric Surface Effects in Solid Plasticity and Strength	Shchukin, E. D. Kochanova, L. A. Savenko, V. I.	24
Electroanalytical Methods for Determination of $Al_2O_3$ in Molten Cryolite	Djokić, S. S. Conway, B. E.	26
Electrocatalysis	Appleby, A. I.	9
Electrocatalytic Oxidation of Oxygenated Aliphatic Organic Compounds at Noble Metal Electrodes	Beden, B. Léger, J.-M. Lamy, C.	22
Electrocatalytic Properties of Carbon Materials	Tarasevich, M. R. Khrushcheva, E. I.	19
The Electrochemical Activation of Catalytic Reactions	Vayenas, C. G. Jaksic, M. M. Bebelis, S. I. Neophytides, S. G.	29
Electrochemical Aspects of Adsorption on Mineral Solids	Somasundaran, P. Goddart, E. D.	13
Electrochemical Aspects of Colloid Chemistry	Hunter, R. J.	11
Electrochemical Behavior of Titanium	Kelly, E. J.	14
Electrochemical Investigations of the Interfacial Behavior of Proteins	Roscoe, S. G.	29
Electrochemical Mechanisms and the Control of Biological Growth Processes	Becker, R. O. Pilla, A. A.	10
Electrochemical and Photoelectrochemical Reduction of Carbon Dioxide	Taniguchi, I.	20
Electrochemical Processes at Biological Interfaces	Mandel, L. J.	8
Electrochemical Processes in Glow Discharge at the Gas-Solution Interface	Hickling, A.	6

Title	Author	Number
Electrochemical Properties of Nerve and Muscle	Floyd, W. F.	1
The Electrochemical Splitting of Water	Gutmann, E. Murphy, O. J.	15
Electrochemical Techniques to Study Hydrogen Ingress in Metals	Pound, B. G.	25
Electrochemistry and Electrochemical Catalysis in Microemulsions	Rusling, J. F.	26
Electrochemistry and the Hydrogen Economy	Gregory, D. P.	10
Electrochemistry of Aluminum in Aqueous Solutions and Physics of its Anodic Oxide	Despić, A. Parkhutik, V.	20
Electrochemistry of Electronically Conducting Polymer Films	Pickup, P. G.	33
Electrochemistry of Hydrrous Oxide Films	Burke, L. D. Lyons, M. E. G.	18
Electrochemistry of Metallic Glasses	Searson, P. C. Nagarkan, P. V. Latanision, R. M.	21
The Electrochemistry of Metals in Aqueous Systems at Elevated Temperatures	Macdonald, D. D.	11
Electrochemistry of Nerve Excitation	Blank, M.	24
Electrochemistry of Semiconductors: New Problems and Prospects	Pleskov, Y. V. Gurevich, Y. Y.	16
Electrochemistry of the Semiconductor-Electrolyte Interface	Green, M.	2
Electrochemistry of Sulfide Minerals	Koch, D. F. A.	10
Electrochemical Aspects of Stress Corrosion Cracking	Galvele, J. R.	27
Electrochemical Deposition and Dissolution of Alloys and Metal Components—Fundamental Aspects	Despić, A. R. Jović, V. D.	27
Electrochemical Impedance Spectroscopy and Its Applications	Lasia, A.	32
Electrode Kinetics	Bockris, J. O'M.	1
Electrodeposition of Metal Powders with Controlled Particle Grain Size and Morphology	Popov, K. I. Pavlovic, M. G.	24

Title	Author	Number
Electrodeposition of Nickel-Iron Alloys	Djokic, S. S. Maksimovic, M. D.	22
Electrogalvanizing	Lindsay, J. H. O'Keefe, T. J.	26
Electrolyte Solutions at High Pressure	Hamann, S. D.	9
Electron Transfer Effects and the Mechanism of the Membrane Potential	Boguslavsky, L. I.	18
Electron Transfer Reactions on Oxide-Covered Metal Electrodes	Schmickler, W. Schultze, J. W.	17
Electro-Osmotic Dewatering of Clays, Soils, and Suspensions	Vijh, A. K.	32
Ellipsometry in Electrochemistry	Paik, Woon-kie	25
Energies of Activation of Electrode Reactions: A Revisited Problem	Šepa, D. B.	29
Environmental Cracking of Metals: Electrochemical Aspects	Revie, R. W.	26
Equilibrium Properties of Electrified Interphases	Parsons, R.	1
Establishing the Link Between Multistep Electrochemical Reaction Mechanisms and Experimental Tafel Slopes	Lefebvre, M. C.	32
Fundamental and Applied Aspects of Anodic Chlorine Production	Novak, D. M. Tilak, B. V. Conway, B. E.	14
Gas-Phase Ion Equilibria and Ion Solvation	Kebarle, P.	9
Hydration Effects and Thermodynamic Properties of Ions	Desnoyers, J. B. Jolietoeur, C.	5
Impedance Measurements in Electrochemical Systems	Macdonald, D. D. McKubre, M. C. H.	14
Improvements in Fluorine Generation	Bauer, G. L. Childs, W. V.	33
Improvements upon the Debye-Hückel Theory of Ionic Solutions	Andersen, H. C.	11
<i>In Situ</i> Surface Electrochemistry: Radioactive Labeling	Wiekowski, A.	21

Title	Author	Number
Interfacial Charge Transfer Reactions in Colloidal Dispersions and Their Application to Water Cleavage by Visible Light	Grätzel, M.	15
Interfacial Electrostatics and Electrostatics in Disperse Systems	Van Leeuwen, H. P. Lyklema, J.	17
Interfacial Infrared Vibrational Spectroscopy	Pons, S. Foley, J. K. Russell, J. Seversen, M.	17
An Introduction to the Electrochemistry of Charge Transfer Complexes II	Gutmann, F. Farges, J.-P.	13
Ion and Electron Transfer across Monolayers of Organic Surfactants	Lipkowski, J.	23
Ionic Solvation	Conway, B. E. Bockris, J. O'M.	1
Ionic Solvation in Nonaqueous and Mixed Solvents	Padova, J. I.	7
Iron and Its Electrochemistry in an Active State	Drazic, D. M.	19
Lithium Batteries with Liquid Depolarizers	Marincic, N.	15
Low-Temperature Electrochemistry at High-T <sub>2</sub> Superconductor/Ionic Conductor Interfaces	Lorenz, W. J. Saemann-Ischenko, G. Breiter, M. W.	28
The Manganese Dioxide Electrode in Aqueous Solution	Andersen, T. N.	30
The Mechanism of Charge Transfer from Metal Electrodes to Ions in Solution	Matthews, D. B. Bockris, J. O'M.	6
The Mechanism of the Electrodeposition of Metals	Bockris, J. O'M. Damjanovic, A.	3
The Mechanism of Formation of Coarse and Disperse Electrodeposits	Popov, K. O. Krstajić, N.V.	30
Mechanism of the Hydrogen Electrode Reaction as Studied by Means of Deuterium as a Tracer	Enyo, M.	11
The Mechanism of Oxidation of Organic Fuels	Gileadi, E. Piersma, B.	4
Mechanisms of Stepwise Electrode Processes on Amalgams	Losev, V. V.	7

Title	Author	Number
Mechanistic Analysis of Oxygen Electrode Reactions	Damjanovic, A.	5
Membrane Chlor-Alkali Process	Burney, H. S.	24
Metal Displacement Reactions	Power, G. P. Ritchie, I. M.	11
The Metal-Gas Interface	Oriani, R. A. Johnson, C. A.	5
Metal Hydride Electrodes	Fuller, T. H. Newman, J.	27
Metal/Solution Interface: An Experimental Approach	Sobkowski, J. Jurkiewicz-Herbich, M.	31
Methods and Mechanisms in Electroorganic Chemistry	Humffray, A. A.	8
Microelectrode Techniques in Electrochemistry	Scharifker, B. R.	22
Microwave (Photo)electrochemistry	Tributsch, H.	33
Models for Molten Salts	Bloom, H. Snook, I. K.	9
A Modern Approach to Surface Roughness Applied to Electrochemical Systems	Salvarezza, R. C. Arvia, A. J.	28
Modern State of Double Layer Study of Solid Metals	Vorotyntsev, M. A.	17
Molecular Dynamic Simulations in Interfacial Electrochemistry	Benjamin, I.	31
Molten Electrolytes	Bloom, H. Bockris, J. O'M.	2
The Nickel Oxide Electrode	McBreen, J. Lynn, K. G.	21
NMR Studies of Electrolyte Solutions	von Goldammer, E.	10
NMR Studies of the Structure of Electrolyte Solutions	Covington, A. K. Newman, K. F.	12
Nonequilibrium Fluctuations in the Corrosion Process	Aogaki, R.	33
Oscillatory Behavior in Electrochemical Systems	Wojtowicz, J.	8
Perspectives in Electrochemical Physics	Vijh, A. K.	17



Title	Author	Number
Phase Transitions in the Double Layer at Electrodes	Benderskii, V. A. Brodskii, A. N. Daikhin, L. I. Velichko G. I.	26
Phenomena and Effects of Electrolytic Gas Evolution	Sides, R. J.	18
Photoelectrochemical Devices for Solar Energy Conversion	Orazem, M. E. Newman, J.	18
Photoelectrochemical Kinetics and Related Devices	Khan, S. U. M. Bockris, J. O'M.	14
Photoelectrolysis and Photoelectrochemical Catalysis	Tributsch, H.	17
Photovoltaic and Photoelectrochemical Cells Based on Schottky Barrier Heterojunctions	Badawy, W. A.	30
Physical Chemistry of Ion-Exchange Resins	Kitchener, J. A.	2
Physical Chemistry of Synthetic Polyelectrolytes	Eisenberg, H. Fuoss, R. M.	1
Physical Mechanisms of Intercalation	McKinnon, W. R. Haering, R. R.	15
Physics and Applications of Semiconductor Electrodes Covered with Metal Clusters	Allongue, P.	23
Potential-Modulated Reflectance Spectroscopy Studies of the Electronic Transitions of Chemisorbed Carbon Monoxide	Gutiérrez, C.	28
The Potential of Zero Charge	Trasatti, S. Lust, E.	33
Potentials of Zero Charge Electrodes	Perkins, R. S. Andersen, T. N.	5
Power Sources for Electric Vehicles	Kordesch, K. V.	10
Principles of Temporal and Spatial Pattern Formation in Electrochemical Systems	Krischer, K.	32
Preparation and Characterization of Highly Dispersed Electrocatalytic Materials	Kinoshita, K. Stonehart, R.	12
The Present State of the Theory of Electrolytic Solutions	Falkenhagen, H. Kelbg, G.	2
Proton Solvation and Proton Transfer Processes in Solution	Conway, B. E.	3

Title	Author	Number
Proton Transfer in Solution	Erdey-Grúz, T. Lengyel, S.	12
Quantum Chemical Treatment of Adsorbed Species	Blyholder, G.	8
Quantum Mechanical Treatments in Electrode Kinetics	Khan, S. U. M.	31
Quantum Theory of Charge-Transfer Processes in Condensed Media	Christov, S. G.	28
Reaction Engineering and Digital Simulation in Electrochemical Processes	Scott, K.	27
Reaction Kinetics and Mechanism on Metal Single Crystal Electrode Surfaces	Adžić, R.	21
Recent Advances in the Study of the Dynamics of Electrode Processes	Fahidy, T. Z. Gu, Z. H.	27
Recent Advances in the Theory of Charge Transfer	Kuznetsov, A. M.	20
Recent Developments in Faradaic Rectification Studies	Aganval, H. P.	20
The Role of Electrochemistry in Environmental Control	Kuhn, A. T.	8
The Role of the Electronic Factor in the Kinetics of Charge-Transfer Reactions	German, E. D. Kuznetsov, A. M.	24
Scanning Tunneling Microscopy: A Natural for Electrochemistry	Sonnenfeld, R. Schneir, J. Hansma, P. K.	21
The Semiconductor/Electrolyte Interface: A Surface Science Approach	Jaegermann, W.	30
Small-Particle Effects and Structural Considerations for Electrocatalysis	Kinoshita, K.	14
Solvated Electrons in Field- and Photo-Assisted Processes at Electrodes	Conway, B. E.	7
Solvent Adsorption and Double-Layer Potential Drop at Electrodes	Trasatti, S.	13
Solvent Dipoles at the Electrode-Solution Interface	Habib, M. A.	12
Some Aspects of the Thermodynamic Structure of Electrochemistry	Rysselberghe, P. van	4

Title	Author	Number
Some Fundamental Aspects of Electrode Processes	Khan, S. U. M.	15
Sorption of Hydrogen on and in Hydrogen-Absorbing Metals in Electrochemical Environments	Mizuno, T. Enyo, M.	30
Spin-Dependent Kinetics in Dye-Sensitized Charge-Carrier Injection into Organic Crystal Electrodes	Charle, K.-P. Willig, F.	19
Structural and Transport Properties of Perfluorinated Ion-Exchange Membranes	Yeo, R. S. Yeager, H. L.	16
Structural Properties of Membrane Ionomers	Mauritz, K. A. Hopfinger, A. J.	14
The Structure of the Metal-Vacuum Interface	Heiland, W.	11
The Study of Simple Consecutive Processes in Electrochemical Reactions	Bewick, A. Thirsk, H. R.	5
Surface Analysis by Electron Spectroscopy	Baker, B. G.	10
Surface-Enhanced Raman Scattering (SERS)	Efrima, S.	16
Surface Potential at Liquid Interfaces	Llopis, J.	6
Surface States on Semiconductors	Batchelor, R. A. Hamnett, A.	22
Temperature Dependence of Conductance of Electrolytes in Nonaqueous Solutions	Barthel, J. Wachter, R. Gores, H.-J.	13
The Temperature and Potential Dependence of Electrochemical Reaction Rates, and the Real Form of the Tafel Equation	Conway, B. E.	16
Theoretical Aspects of Semiconductor Electrochemistry	Uosaki, K. Kita, H.	18
Theories for the Metal in the Metal-Electrolyte Interface	Goodisman, J.	20
Theories of Elementary Homogeneous Electron-Transfer Reactions	Sacher, E. Laidler, K. J.	3
Theory and Applications of Periodic Electrolysis	Pesco, A. M. Cheh, H. Y. Popov, K. I.	19
Theory of the Effect of Electrodeposition at a Periodically Changing Rate on the Morphology of Metal Deposits	Maksimovic, M. D.	19

Title	Author	Number
Thermodynamics of Membrane Energy Transduction in an Oscillating Field	Markin, V. S.	24
Transport-Controlled Deposition and Dissolution of Metals	Tsong, T. Y. Despic', A. R. Popov, K. I.	7
Transport Models for Ion-Exchange Membranes	Verbrugge, M. W. Pintauro, P. N.	19
Transport Phenomena in Electrochemical Kinetics	Arvia, A. J. Marchiano, S. L.	6
Transport Properties of Molten Salt	Okada, I.	34
Ultrahigh-Vacuum Surface Analytical Methods in Electrochemical Studies of Single-Crystal Surfaces	Soriaga, M. P. Harrington, D. A. Stickney, J. L. Wieckowski, A.	28
Ultrasonic Vibration Potentials	Zana, R. Yeager, E. B.	14
Underpotential Deposition on Single-Crystal Metals	Aramata, A.	31
Voltaic Cells in Electrochemistry and Surface Chemistry of Liquids	Koczorowski, Z.	34
Water Electrolysis and Solar Hydrogen Demonstration Projects	Sandstede, G. Wurster, R.	27
X-Rays as Probes of Electrochemical Interfaces	Abrtina, H. D.	20

*This page intentionally left blank.*

## Index

- Acetonitrile, 46
- Acids
- adsorption potentials, 43
  - fuel cell catalysts and electrolytes, 66–67, 102
- Additivity principle, 1–11
- corrosion and electroless plating studies, 4–6
  - earlier tests, 3–4
  - principle, 1–3
  - recent research, 9–11
- Adsorption potentials, Voltaic cells
- of dipolar compounds, 36–41
  - of inorganic ions, 42–43
  - of surface-active electrolytes, 4142
- Agitation effect, molten salt transport properties, 135, 138
- Air–water interface, Voltaic cells, 40
- Alcohols, 46
- Aliphatic alcohols, 46
- Alkali ion systems, transport properties of molten salts, 125, 131–132, 135–136
- Alkali metal salts, surface potential of water, 43
- Alkaline earth salts, molten salt transport properties, 144–145, 160
- Alkaline electrolytes, fuel cell development, 65–66
- Alkaline fuel cells, status of technologies, 56, 58, 60
- Alkoxyethanols, 46
- Analytical transport-coupled methods, 158–159
- Anions
- adsorption potentials, 42–43
  - molten salt transport publications, 122
- Arrhenius equation, 172
- Associated species model, molten salt transport properties, 146–149
- Autocorrelation method, molten salt transport properties, 150–152
- Battery, biological, 226
- Biofilm formation, 205–207
- Biological battery, 226
- Biological corrosion: *see* Microbiologically influenced corrosion
- Birnessite, 214
- Bode plots, 234–236
- Bonding energy, molten salt, bulk viscosity and, 176
- Born–Haber–Fajans cycle, 29–30
- Bulk viscosity, molten salt transport measurement, 174–176
- Butanediols, 40
- $\gamma$ -Butyrolactone, 41
- Calomel electrode Volta potential, 30
- Capacitance, microbiologically influenced corrosion, 216–223

- Capillary methods, molten salt transport measurement, 159, 171–173, 176
- Carbonate systems  
 fuel cells: *see* Molten carbonate fuel cells  
 molten salt transport properties, 131
- Carbon dioxide and monoxide, fuel cells, 54–55
- Carbon-supported catalysts and electrodes, fuel cell, 85, 86–87, 103
- Cell stack development, direct methanol fuel cells, 111–114
- Ceramic electrolytes, fuel cell, 106–107, 108, 109
- Cerium, heterogeneous catalysis, 8
- Chemlaeffect, 129–132, 133, 134  
 association (dissociation) model, 147–149  
 response function method, 151  
 self-exchange velocity, 153
- Chromatography, molten salt transport measurement, 159
- Chronoamperometry, 158
- Circuit model, microbiologically influenced corrosion measurements, 220–221
- Cobalt, fuel cell oxygen reduction catalysts, 96–97
- Compensation voltage, 18–19, 34
- Concentric cylinder method, molten salt transport property measurement, 194
- Condenser method, 25, 27–28
- Condensers, vibrating, 21–22
- Conductance, molten salt transport properties, 120, 121, 124–154  
 Chemla effect, 129–132, 133, 134  
 electrically conducting species, 146–149  
 electrolytic conductivity, 124–125  
 empirical equation for internal mobility, 131–146  
 isotherm pattern in binary monovalent cation systems, 127–129
- Conductance, molten salt transport properties (*cont.*)  
 molecular dynamics simulation, 149–154  
 transport number measurement methods, 125–127
- Conductivity, electrical  
 molten salt standards  
 recommendations, 123, 124–125  
 transport properties of molten salts, 120, 121
- Conductivity, thermal: *see* Thermal conductivity, molten salt transport properties
- Contact (Volta) potential, 16–20, 31–33
- Copper, additivity principle, 4–6
- Corresponding states, law of, 196
- Corrosion  
 additivity principle, 4–6  
 fuel cell development, 66–67  
 microbiologically influenced: *see* Microbiologically influenced corrosion
- Corrosion potential  
 additivity principle, 4  
 microbiologically influenced corrosion, 213–216
- Cost, fuel cells  
 comparison of energy conversion methods, 62, 63, 64, 65  
 status of technologies, 58
- Crossover, methanol in fuel cells, 109–111
- Current density, microbiologically influenced corrosion, 209
- Current-potential curves, 2–3; *see also* Additivity principle
- Debye–Hückel equation, 121
- Debye–Onsager equation, 121
- Density, molten salt standards  
 recommendations, 123
- Dialkylethers, 40
- Diaphragm cell method, 159  
 1,2-Dichloroethane, 33, 35, 46, 47

- Diffusion, molten salt transport properties, 119, 120–121, 154–167  
macroscopic description, 154–157  
measurement methods, 157–165  
chronopotentiometry, 160  
linear sweep voltammetry, 160–161  
spin-echo method, 162–165  
wave-front shearing  
interferometry, 161–162  
molecular dynamics simulation, 165–167
- Diffusion coefficients, molten salts, 157–159, 160
- Diffusion-coupled methods, 159
- N,N*-Dimethyl-*p*-phenylenediamine (DMPDD), 9, 10
- Dimethylsulfoxide, 40, 41
- Dinitriles, 40
- Direct methanol fuel cells, 53–114  
development and principles, 62–73  
challenges, technical, 73  
historical development, 65–67  
principles, 67–73  
electrode kinetics and electrocatalysis of methanol oxidation, 73–92  
electrode structure and composition, and electroactivity, 83–92; *see also* Electrodes, direct methanol fuel cells  
mechanisms, 92–93  
oxidation kinetics, increasing, 82–83  
reaction products and adsorbed intermediates, 75–82  
overview of technologies, 53–62  
comparison of electrochemical with other energy conversion methods, 62–73  
incentives for development, 53–54  
natural gas, importance of, 55–57  
status of technologies, 57–62  
types of fuel cells, 54–55  
oxygen electroreduction and proton exchange membrane, 93–100  
catalyst innovations, 96–98  
electroreduction reaction, 93–96
- Direct methanol fuel cells (*cont.*)  
oxygen electroreduction and proton exchange membrane (*cont.*)  
proton exchange membrane development, 99–100  
progress in technology, 100–114  
cell stack development and demonstration, 111–114  
single-cell investigations for high performance levels, 100–111
- Dissociation model, molten salt transport properties, 147–149
- DMPPD (*N,N*-dimethyl-*p*-phenylenediamine), 9, 10
- Donnan potentials, 19
- Dual-cell technique, microbiologically influenced corrosion, 226–227
- Dynamic condenser (vibrating plate/condenser method), 21–22
- Dynamic dissociation model, 149
- Dynamic jet method, 22–23
- Dysprosium, molten salt transport properties, 143, 144, 145
- EDTA, 5–6
- Efficiency, fuel cells, 62, 64
- Einstein equation, 165, 195
- Electrical conductance: *see* Conductance, molten salt transport properties
- Electrical conductivity: *see* Conductivity, electrical
- Electrical potentials, Voltaic cells, 14–16
- Electrochemical impedance spectroscopy, microbiologically influenced corrosion, 233–240, 241
- Electrochemical noise analysis, microbiologically influenced corrosion, 227–233
- Electrode potentials, Voltaic cells  
absolute, 29–31  
*ex situ* and non-*situ* electrodes, 31–33
- Electrodes  
direct methanol fuel cells  
bimetallic, 87–92



- Electrodes (*cont.*)  
  direct methanol fuel cells (*cont.*)  
    crystallographic structure and, 83–84  
    mechanisms, 92–93  
    oxidation kinetics, increasing, 82–83  
    particle size and carbon support effects, 84–87  
    reaction products and adsorbed intermediates, 75–82  
  electroless plating, 6  
  fuel cell; *see also* Electrodes, direct methanol fuel cells  
    development of, 65–67  
    optimization of, 103–107, 108, 109  
  microbiologically influenced corrosion  
    biofilm redox potential, 208–209  
    scanning vibrating electrode techniques, 240  
  molten salt transport measurement, 158
- Electroless plating, additivity principle, 4–6
- Electrolytes  
  corrosion, microbiologically influenced, 211  
  fuel cell  
    ceramic, 106–107, 108, 109  
    development of, 65–67  
    performances achieved in single cells, 108  
    superacid, 102  
  Voltaic cells  
    immiscible solutions, 33–36  
    real ion activity, 26–27  
    real potentials of ions in solids, 27–28  
    real potentials of ions solutions, 24–26
- Electrolytic conductivity, molten salt standards recommendations, 123
- Emersion process, 31–33
- Environmental safety, fuel cells, 62, 64
- Equivalent conductivity, molten salts, 125
- E-TEK, 85
- Ethanol, 46, 47
- Ethylene glycol, 41, 47
- Ethylene-tetrafluoroethylene films (ETFE), 99, 100
- Falling ball measurement, viscosity measurement, 173–174, 176
- Faradic impedance, 158
- Ferricyanide–iodidesystem, heterogeneous catalysis, 6–7
- Fick, first law of, 119, 120
- Fick, second law of, 183
- Forced Rayleigh scattering method, molten salt thermal conductivity measurement, 188–190
- Formaldehyde  
  copper deposition, 5–6  
  fuel cell electrooxidation, 72
- Formyl species, fuel cell intermediates, 72, 91–92
- Fourier equation, 182
- Fourier's law, 119, 120
- Fractal behavior, molten salt transport properties, 165–167
- Free energy of solvation in different solvents, 31
- Free space effect, molten salt transport properties, 125, 135, 136–138
- Fuel cells: *see* Direct methanol fuel cells
- Galvani potential, 15, 17
- Galvanostatic reduction techniques, 222
- Galvanostatic transient method, 216, 217
- Gibbs–Duhem relation, 155
- Gibbs isotherm, 36
- Gouy–Chapman diffuse layer, adsorption potential of surface-active electrolytes, 41–42
- Graphite, high surface area, 85
- Gravimetry, molten salt transport measurement, 159
- Green–Kubo relation, 165, 195
- Halides, molten salt transport publications, 122
- Heat transmission, transport properties of molten salts, 121

- Helmholtz equation, 38, 44  
Hexadecylamine hydrochloride, 42  
High surface area graphite, 85  
Hittorf method, 125  
Hot-wire method, molten salt thermal conductivity measurement, 184–185, 194  
Hybrid electric vehicles, 60–61  
Hydrogen, fuel cell technology, 54, 56, 57
- Interface phenomena, Voltaic cells  
  immiscible electrolyte solutions, 33–36  
  metal/solution interface, 23–24  
  Volta potentials of *ex situ* and non-*situ* electrodes, 31–33
- Interferometry, molten salt transport property measurement, 158, 161–162, 190–192, 194
- Internal mobility, molten salt transport  
  agitation effect, 135, 138  
  anomalous behavior of Ag(I) and Tl(I), 138–143  
  charge asymmetric binary mixture, 144–145  
  empirical equation for, 131–132, 135  
  free space effect, 135, 136–138  
  multivalent charge symmetric binary mixture, 143–144, 145, 146  
  self-exchange velocity, 153–154  
  tranquilization effect, 132, 135, 138
- Iodide, heterogeneous catalysis, 7–8
- Ionic interactions  
  adsorption potential of surface-active electrolytes, 41–42  
  transport properties of molten salts, 121
- Ionization method, Voltaic cells, 25, 27–28  
Ionizing electrode method, 20–21  
Ionizing gap, 22
- Iridium, fuel cell bimetallic electrodes, 88
- Iron  
  fuel cell oxygen reduction catalysts, 96–97  
  heterogeneous catalysis, 8  
  microbiologically influenced corrosion measurements, 222, 224
- Isobutyl methyl ketone (IBMK), 46, 47
- Jet method, 22–23
- Kelvin probes, scanning, 22–23  
Klemm method, 126, 129
- Langmuir monolayers, 42
- Large signal polarization techniques, microbiologically influenced corrosion, 240, 242–244
- Laser flash method, molten salt thermal conductivity measurement, 186–188, 194
- Latent image, photographic, 9
- Law of corresponding states, 196
- Layer method, transport properties in molten salts, 125
- Lennard-Jones spline function, 196
- Lifetime of fuel cells, 58, 62
- Linear response theory, molten salt transport properties, 150
- Linear sweep voltammetry, 158, 160–161
- Liquid junction potential, Voltaic cells, 45–46
- Liquid surface chemistry: *see* Voltaic cells
- Macrocyclic compounds, fuel cell oxygen reduction catalysts, 97–98
- Manganese  
  fuel cell oxygen reduction catalysts, 96–97  
  microbiologically influenced corrosion, 214, 215, 216
- Markov rule, 125
- Mass activity, platinum fuel cell electrocatalysts, 76
- MCFC: *see* Molten carbonate fuel cells
- Mean-square displacement, 165
- Mercury  
  adsorption at water interface, 40  
  heterogeneous catalysis, 8
- Metal-reducing bacteria (MRB), 208

- Metals
- corrosion, microbiologically influenced: *see* Microbiologically influenced corrosion
  - fuel cell oxygen reduction catalysts, 96–97
  - molten salt properties, 124
- Methanediolate, 6
- Methanol, 46,47
- Methoxyethanol, 47
- Microbiologically influenced corrosion, 205–245
- biofilm formation, 205–207
  - MIC mechanisms, 207–208
  - techniques, 208–244
    - capacitance, 216–223
    - dual-cell technique, 226–227
    - electrochemical impedance spectroscopy 233–240
    - electrochemical noise analysis, 227–233
    - large signal polarization techniques, 240,242–244
    - microsensors, 223–226
    - open circuit potential, 213–216
    - polarization resistance, 209–213
    - redox potential, 208–209
    - scanning vibrating electrode techniques, 240
- Microsensors, microbiologically influenced corrosion, 223–226
- Mixed potential theory: *see* Additivity principle
- Mixed species biofilms, microsensors, 224
- Mobility ratio, molten salt transport properties, 126
- Molar conductivity, molten salt transport properties, 125
- Molecular dynamics simulations, molten salt transport properties, 121, 125
- diffusion, 165–167
  - electrical conductance, 149–154
  - self-exchange velocity and Chemla effect, 130–132, 133, 134
  - thermal conductivity, 195–196
  - viscosity, 180–182
- Molecular interactions, transport
- properties of molten salts, 121
- Molten carbonate fuel cells (MCFC), 55, 56
- comparison of energy conversion methods, 62
  - status of technologies, 58,59
- Molten salt transport properties, 119–196
- database, 121–124
  - diffusion, 154–167
    - macroscopic description, 154–157
    - measurement methods, 157–165; *see also* Diffusion, molten salt transport properties
    - molecular dynamics simulation, 165–167
  - electrical conductance, 124–154
    - Chemla effect, 129–132, 133, 134
    - electrically conducting species, 146–149
    - electrolytic conductivity, 124–125
    - empirical equation for internal mobility, 131–146
    - isotherm pattern in binary monovalent cation systems, 127–129
    - molecular dynamics simulation, 149–154
    - transport number measurement methods, 125–127
  - thermal conductivity, 182–196
    - evaluation of experimental data, 192–195
    - measurement methods, 184–192; *see also* Thermal conductivity, molten salt transport properties
    - molecular dynamics simulation, 195–196
  - viscosity, 167–182
    - bulk, 174–176
    - factors determining, 177–180
    - measurement methods, 168–174; *see also* Viscosity, molten salt transport properties

- Molten salt transport properties (*cont.*)  
viscosity (*cont.*)  
molecular dynamics simulation,  
180–182  
recommended values, 176–177
- Molybdenum alloys, fuel cell  
electrodes/catalysts, 87–92, 99,  
100, 102
- Monoalkyl ethers, 40
- Monte Carlo simulations, molten salt  
transport properties, 149
- Nafion, 86, 99  
fuel cell oxygen electroreduction  
reaction, 95–96  
optimization of fuel cell electrodes,  
103
- Natural gas  
direct methanol fuel cell technologies,  
55–57  
hydrogen for fuel cells, 54
- Nernst–Einstein relation, diffusion and  
conductivity, 120
- Nernst potential, 2
- Nickel, fuel cell catalysts, 89, 96–97
- Nitrates, molten salt transport properties,  
126, 127  
associated species model, 146–147  
internal mobility in alkali ion systems,  
131–132, 135–136  
internal mobility isotherms, 138–143  
publications, 122
- Nitriles, 40
- Nitrobenzene, Voltaic cells, 33, 35, 45–46,  
47
- Nitroethane, 46, 47
- Noise analysis, microbiologically  
influenced corrosion, 227–233
- Nuclear magnetic resonance, molten salt  
transport measurement, 159,  
162–165
- Ohm's law, 119
- Oil/water interface, adsorption potentials  
at, 42
- Onsager reciprocal relation, 155–156
- Open circuit potential, microbiologically  
influenced corrosion, 213–216
- Operating system optimization, fuel cell  
performance, 104
- Optical interferometry, molten salt  
transport property measurement,  
158, 161–162, 190–192, 194
- Organic solvents, Voltaic cells  
free energy of solvation, 31  
with immiscible electrolyte interfaces,  
33–35  
surface potentials of, 41, 43–47
- Organic species  
copper plating, 6  
fuel cell, 54  
oxygen reduction catalysts, 96–98  
tape casting, 107
- oscillating cup method, molten salt  
viscosity measurement, 169–170,  
176
- Oscillating cylinder method, molten salt  
viscosity measurement, 168–69,  
176
- Osmium, fuel cell bimetallic electrodes, 88
- overvoltages  
fuel cell, 73, 102  
microbiologically influenced corrosion  
measurements, 216
- Oxygen, and microbiologically influenced  
corrosion, 214, 223–226
- Oxygen electroreduction, direct methanol  
fuel cells, 93–100  
catalyst innovations, 96–98  
electroreduction reaction, 93–96
- PAFC: *see* Phosphoric acid fuel cell
- Parallel plate methods, molten salt thermal  
conductivity measurement, 186
- Parallel resistance-capacitance  
measurement, microbiologically  
influenced corrosion  
measurements, 217
- Partnership for a New Generation of  
Vehicles, fuel cell technology,  
60–61, 65

- PEMFC: *see* Proton exchange membrane fuel cells
- Perfluorodecanoic acid, 42
- PH
- copper plating, 6
  - microbiologically influenced corrosion, 224
- Phosphoric acid fuel cell (PAFC), 55,56, 57
- comparison of energy conversion methods, 62, 63, 64
  - status of technologies, 57, 58, 59
- Photographic processing, heterogeneous catalysis, 8–9
- Plating, electroless, additivity principle, 4–6
- Plating potential, 4
- Platinum catalysts and electrodes; *see also* specific electrochemical systems
- additivity principle research, 10
  - biofilm redox potential, 208–209
  - fuel cell, 68, 74, 99–100
    - chemical analysis of reaction products and intermediates, 76–82
    - mass activity and specific activity, 85
    - optimization of, 103–107, 108, 109
    - organic fuel cell oxygen reduction catalysts vs., 98
    - performances achieved, 108
    - specific and mass activity, 86, 87
    - heterogeneous catalysis by, 6–8
- Polarization curves, 4
- Polarization resistance, microbiologically influenced corrosion, 209–213
- Polarography, 158
- Polybenzimidazole (PBI) fuel cell membranes, 99
- Polymers
- fuel cell catalysts, 86, 97–98, 99
  - protection from microbial activity, 237–240
- Poly(tetrafluoroethylenehexafluoropropylene) copolymers, 99
- Poly-tetra-(*o*-aminophenyl) porphyrin (Poly CoTAPP), 97–98
- Porous frit technique, 159
- Porphyrins, fuel cell oxygen reduction catalysts, 97–98
- Power, fuel cells
- comparison of energy conversion methods, 64
  - status of technologies, 58, 60, 62
- Pressure, fuel cell performance optimization, 104
- Primers, protection from microbial activity, 237–240
- Propargyl alcohol, 40
- Propylene glycol, 47
- Proton exchange membrane fuel cells (PEMFC), 56,57, 102
- comparison of energy conversion methods, 63, 64
  - development of technology, 67,69
  - minimization of methanol permeability, 107, 109–110
  - optimization, 106–107, 108, 109
  - oxygen electroreduction reaction, 94–96
  - platinum catalysts, 74
  - status of technologies, 58, 60–61
- Proton hopping process, 107, 109
- Quadratic temperature equation, 172
- p*-Quinonedimine, 9
- Radioactive probe, ionizing electrode method, 20–21
- Raman scattering, molten salt viscosity measurement, 177–180
- Randles–Sevcikequation, 160
- Rayleigh scattering method, molten salt thermal conductivity measurement, 188–190
- Redox couple fuel cell catalysts, 102
- Redox potential, microbiologically influenced corrosion, 208–209
- Relaxation, thermal, molten salt bulk viscosity, 176
- Renewable energy sources, fuel cells, 55

- Response function method, molten salt transport properties, 151, 152
- Rhenium alloy fuel cell catalysts, 102
- Rhenium fuel cell bimetallic electrodes, 88
- Rotating cylinder viscometers, 170–171, 176
- Rotating disk electrode, 158
- Ruthenium alloy fuel cell catalysts and electrodes, 76, 90–93, 99, 100, 103
- bimetallic electrodes, 87–92
- performances, 108
- Safety, fuel cells, 62, 64
- Salt bridges, 34, 45–46
- Salts: see Molten salt transport properties
- Scanning Kelvin probes, 22–23
- Scanning vibrating electrode techniques, microbiologically influenced corrosion, 240
- Self-diffusion coefficients, molten salt transport studies, 163, 164
- Self-exchange velocity, molten salt transport properties, 130–132, 133, 134, 149, 153–154
- p*-Semiquinonediimine, 9
- Silver salts
- halides, heterogeneous catalysis, 8–9
- molten, anomalous behavior of, 138–140, 142–143
- Volta potential in solid electrolyte systems, 27–28
- Simulations: see Molecular dynamics simulations, molten salt transport properties
- Single-cell fuel cells, 103, 104, 105, 100–111
- Single-electrode potential, 30
- Single-ion activity, 26
- Slag melt viscosity, 174
- Solid oxide fuel cells (SOFC), 55
- comparison of energy conversion methods, 62
- status of technologies, 58.59
- tape casting organic formulations, 107
- Solvation free energy, comparison of solvents, 31
- Solvent interfaces: see Voltaic cells
- Sound absorption in binary molten salts, 174–176
- Specific activity, platinum fuel cell electrocatalysts, 76
- Specific conductivity, molten salts, 125
- Specific power, fuel cell
- comparison of energy conversion methods, 64
- performances achieved, 108
- Spectroscopic methods
- fuel cells
- catalyst studies, bimetallic alloys, 89, 90–91
- reaction product analysis, 75–76
- microbiologically influenced corrosion, 233–240
- molten salt viscosity, 177–180
- Spin-echo method, molten salt transport studies, 162–165
- Split-cell (biological battery) technique, 226
- Standard potentials, electrolyte solutions, 24–26
- Standard salts, molten salt bulk viscosity, 176–177
- Static capacitor method, 22
- Static condenser method, 22
- Steam reforming, fuel cell technology, 56
- Stepwise heating, molten salt thermal conductivity measurement, 185
- Stem modification of Gouy–Chapman system, 42
- Stokes–Einstein–Debye relation, molten salt viscosity, 177–180
- Stokes–Einstein relation, diffusion and viscosity, 120
- Stokes equation, 173
- Sulfate-reducing bacteria (SRB), 208, 211, 234
- Sulfide, microbiologically influenced corrosion, 224
- Superacid fuel cell electrolytes, 102
- Superionic electrolyte Volta potentials, 28
- Superposition theory: see Additivity principle
- Surface chemistry: see Voltaic cells

- Surface potential method, 13
- Surface potentials, Voltaic cells  
adsorption potentials of dipolar  
compounds, 36–41  
water and organic solvents, 43–47
- Surface tension  
adsorption potentials of dipolar  
compounds, 36  
molten salt standards  
recommendations, 123
- Tafel behavior, 4  
fuel cell  
oxygen electroreduction reaction,  
94.95  
single cell DMFC, 109  
microbiologically influenced corrosion  
measurements, 209, 217
- Tape casting, 107
- Temperature  
and molten salt transport, 175–176  
molten salt viscosity, 172–173  
transport properties of molten salts, 121
- Tetraethylammonium picrate salt bridge,  
45–46
- Thallium, molten salt transport properties,  
138–139, 141–143, 144
- Thermal conductivity, molten salt  
transport properties, 121, 182–196  
evaluation of experimental data,  
192–195  
measurement methods, 184–192  
hot-wire, 184–185  
laser flash, 186–188  
parallel-plate, 186  
Rayleigh scattering, forced,  
188–190  
stepwise heating, 185  
variable gap, 184  
wave-front shearing  
interferometry, 190–192  
molecular dynamics simulation,  
195–196
- Thermal diffusivity of molten salts: see  
Diffusion, molten salt transport  
properties
- Thermal relaxation, molten salt bulk  
viscosity, 176
- Tin alloys, fuel cell electrodes and  
catalysts, 87–92, 99, 100
- Titanium  
fuel cell catalysts, 102  
heterogeneous catalysis, 7–8
- Tosi–Fumi potentials, 152, 196
- Tranquilization effect  
charge asymmetric binary mixture,  
144–145  
molten salt transport properties, 132,  
135, 138
- Transient hot wire method, molten salt  
transport property measurement,  
194
- Transport properties: *see* Molten salt  
transport properties
- Trifluoromethane sulfonic acid, 102
- Tungsten carbide fuel cell catalysts, 89
- Variable gap method, molten salt thermal  
conductivity measurement, 184
- Velocity autocorrelation function, 165
- Vernadite, 214
- Vibrating plate/condenser method, 21–22
- Vibrational motions, transport properties  
of molten salts, 121
- Viscosity, molten salt transport properties,  
120, 121, 167–182  
bulk, 174–176  
factors determining, 177–180  
measurement methods, 168–174  
capillary, 171–173  
falling ball, 173–174  
industrial viscometers, 174  
oscillating cup, 169–170  
oscillating cylinder, 168–169  
rotating cylinder, 170–171  
molecular dynamics simulation,  
180–182  
recommended values, 176–177  
standards recommendations, 123
- Voltaic cells, 13–48  
and absolute electrode potentials,  
29–31

- Voltaic cells (*cont.*)
- adsorption potentials
    - of dipolar compounds, 36–41
    - of inorganic ions, 42–43
    - of surface-active electrolytes, 41–42
  - electrified interfaces and electrical potentials, 14–16
  - experimental methods, 20–23
  - with interfaces of immiscible electrolyte solutions, 33–36
  - metal/solution interface, 23–24
  - real ion activity, 26–27
  - real potentials of ions
    - in electrolyte solutions, 24–26
    - in solid electrolytes, 27–28
  - surface potentials of water and organic solvents, 43–47
  - Volta potential and, 16–20
  - Volta potentials of *ex situ* and *non-situ* electrodes, 31–33
  - Voltammetry, linear sweep, 160–161
  - Vulcan, 85
  - Wagner and Traud principle: *see* Additivity principle
  - Water/aqueous solution interfaces, Voltaic cells
    - adsorption potentials at oil water interface, 42
    - with immiscible electrolyte interfaces, 33–35
    - nitrobenzene–waterpartition system, 33–35, 45–46
    - surface potentials, 43–47
  - Wave-front shearing interferometry, 161–162, 190–192
  - Yttrium, molten salt transport properties, 143, 144, 145
  - Zone electromigration method, 125